Studies on novel phase behavior of ionic amphiphile-water systems

by

Santosh Prasad Gupta

Thesis submitted to the Jawaharlal Nehru University

for the award of the degree of Doctor of Philosophy

April 2014

Raman Research Institute

Bangalore 560080

India

DECLARATION

I, hereby, declare that this thesis is composed independently by me at Raman Research Institute, Bangalore, India, under the supervision of Prof. V. A. Raghunathan. I further declare that the subject matter presented in this thesis has not previously formed the basis of the award of any degree, diploma, associateship, fellowship or any other similar title in any other University.

V. A. Raghunathan
Raman Research Institute

Santosh Prasad Gupta

CERTIFICATE

This is to certify that the thesis entitled **Studies on novel phase behavior of ionic amphiphile-water systems** submitted by Santosh Prasad Gupta for the award of the degree of DOCTOR OF PHILOSOPHY of Jawaharlal Nehru University is his original work. This has not been published or submitted to any other University for any other degree or diploma.

Director	V. A. Raghunathan
Raman Research Institute	Thesis Supervisor

Dedicated to my

MAA & BABUJI

ACKNOWLEDGEMENTS

I am deeply indebted to my supervisor Prof. V. A. Raghunathan for his invaluable guidance, support, encouragement and help. I thank him for everything that I learnt from him. Without his inspiring guidance this thesis would not have been possible. I consider myself fortunate to have worked with him.

I will forever be thankful to Dr. Yashodhan Hatwalne and Dr. Reji philip for their constant interest in this work. I thank Dr. V. Lakshminarayanan, Dr. Arun Roy, Dr. Ranjini Bandyopadhyay, Dr. Pramod and Dr. R. Pratibha for many pleasant discussions with them. I express my gratitude to Prof. N. V. Madhusudana for his valuable comments and suggestions about my work. I am also thankful to all other faculty members of the soft condensed matter group for their encouragement and help. I express my gratitude to Prof. Ravi Subrahmanyan for his encouragement and support.

I thank Mr. H. Ram, Mr. Ravishankar and Mr. Ishaq for their help in carrying out the experiments. A special thanks to Mr. Mani from whom I have had various technical support for my experimental work. Also the technical support from Ms. K. N. Vasudha is sincerely acknowledged. I thank Mr. Dhason and Mr. Durai Chelvan for their help in carrying out the cryo-SEM experiments. I also thank the Chemistry lab for the help received at various stages of this work. I am thankful to Dr. Satyam, Srinivasa, Dr. Radhika, Swami, Avinash and Marichandran for their help in preparing some of the chemicals in the chemistry laboratory. I thank Raja and Murali for all the help that I received from them.

I thank all the library staff for their help, especially Patil, Meera, Girija, Manjunath, Nagaraj, Geetha, Vrinda, Hanumanthappa and Chowdappa.

I would like to thank everyone at the computer section for their help. I thank everyone in the administrative department. Special thanks to Mr. Krishnamaraju, Mr. K. Radhakrishna, Ms. Marisa and Ms. Radha for their administrative help.

My sincere thanks goes to Dr. RK for helping me familiarize with the Hecus MicroS3 in my initial days in X-ray lab. I thank Dr. Bibhu for all the discussions

that I have had with him and for his friendship. I would like to thank Dr. Antara and Dr. Arif for the help I received from them.

I am fortunate to have a senior and friend like Madhukar who has been a constant source of encouragement and support. I express my heartfelt thank to him. I thank to my close friend Shabeeb, with whom I had many evening tea and valuable discussion. I thank Meera, Sreeja, Jayesh and Surya for all the help I received from them. I also thank Rajib, Debasish and Samim for their help at various occasions. I thank to all the present and past regular members of SCM students room where I had a great time. I also thank all my friends from other labs and groups.

I thank JK, Dr. Rakesh, Dr. Nagaraju, Dr. Barat, Dr. Harikrishn and Dr. Suresh for their encouragement and help. My thanks goes to all my hostel friends specially, Kanhaiya, Mahaveer, Jagdeesh, Sanjay, Renu, Karmveer, Priyanka, Deepshikha, Aushutosh, Sushil and Amit for their wonderful company at hostel and mess.

I sincerely thank all my other friends with whom I enjoyed many evenings on the RRI football ground and badminton court.

I enjoyed very much my stay at RRI in the wonderful natural surroundings. My sincere thanks to all canteen staff, cooks at the hostels, security personnel and everyone at RRI for making my stay enjoyable.

I thank Usha, Divya, Maya and Swati for the time I enjoyed with them.

I am thankful to all my batch mates, seniors and juniors at Gorakhpur university who kept a warm relation with me, indeed Seraj, Iswarchandra, Shashank and Bind ji have been sources of inspiration.

I take this opportunity to express my gratitude to my school teachers Mr. Mohit Prasad Yadaw ji, Mr. Munshi ji, Mr. Shivpujan Prasad ji, Mr. Mohan lal Gupta ji, Mr. K. D. Rai ji, Dr. S. S. Prasad ji, Dr. K. K. Gupta ji and Mr. R. B. Singh ji for helping me shape my academic career.

My heartfelt thanks goes to my elder brother Umesh ji, who help me during the tough time of my academic life. My sincere thanks goes to Om bhaiya and Mani

ji for their encouragement and help. I thank my younger brother Shyambihari for his support through all these years.

Last but not the least, I extend my thanks to all my brothers and sisters and brothers in law and family members for their constant support. I express my heartfelt thanks to my loving parents who have sacrificed a lot for helping me realize my dreams.

SYNOPSIS

This thesis deals with the influence of strongly bound counterions on the phase behavior of some ionic amphiphile-water systems. Small angle x-ray scattering (SAXS), polarizing optical microscopy (POM) and cryogenic scanning electron microscopy (cryo-SEM) techniques have been used to identify the different structures formed in these systems. The strongly binding counterion is introduced by the dissociation of a water soluble aromatic salt. The effect of such counterions on the self-assembled structures of ionic amphiphiles has been extensively studied in the dilute limit, where they have been shown to lead to interesting viscoelastic behavior. However, there have been only a few studies on these systems at higher amphiphile concentrations, where they form ordered anisotropic phases. The present studies demonstrate the very rich phase behavior exhibited by these systems.

In **chapter 1** we introduce amphiphilic molecules and their self-assembled structures. Amphiphilic molecules are made up of one or more hydrophobic chains attached to a hydrophilic head group. They self-assemble in aqueous solutions to form aggregates above a critical micellar concentration (CMC). Various types of aggregates are formed depending upon the geometric shape of the molecules (Fig. 1). At higher concentrations they exhibit liquid crystalline phases with long range orientational order and some degree of translational order. Most commonly observed structures are the hexagonal phase consisting of long cylindrical micelles arranged on a two-dimensional hexagonal lattice and the lamellar phase, consisting of a periodic stack of bilayers separated by water layers. Many studies indicate that the morphological transformation from cylinders to bilayers does not take place abruptly, but through a sequence of intermediate shapes, giving rise to a sequence of so-called intermediate phases between the hexagonal and lamellar phases. Frequently bi-continuous cubic phases, which are optically isotropic, have been identified between the hexagonal and lamellar phases. In some systems a number of birefringent phases namely ribbon and mesh phases are seen instead at these intermediate compositions. In many systems the isotropic (L_3) sponge

phase is observed in narrow phase regions adjacent to the domain of stability of the lamellar phase. A brief description of all the phases exhibited by amphiphile-water systems is given in this chapter. We also present the basic principles of x-ray diffraction and optical polarizing microscopy techniques employed to determine the liquid crystalline structures. Cryogenic scanning electron microscopy (cryo-SEM) technique which is a powerful tool for characterizing the microstructure of liquid containing specimens, which are ordinarily unstable in the high vacuum of the electron microscope is also described in this chapter. Detailed modeling of the SAXS data required for the determination of the various structures has also been discussed in this chapter.

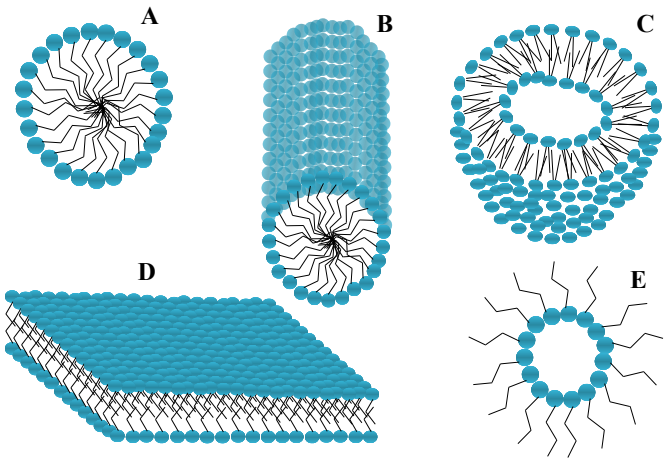

FIGURE 1: Schematics of various self assembled structures of amphiphilic molecules : (**A**) spherical micelle, (**B**) cylindrical micelle, (**C**) vesicle, (**D**) bilayer and (**E**) inverted micelle.

In **chapter 2** we describe the influence of two structurally isomeric organic salts, namely, 2- sodium-3-hydroxy naphthoate (SHN) and 1-sodium-2-hydroxy naphthoate (SHN1), on the phase behavior of the cationic surfactant cetylpyridinium chloride (CPC). For comparison, the effect of 2,3-dihydroxy naphthalene (DHN) on the same surfactant-water system was also studied. Both the CPC-SHN-Water and the CPC-SHN1-Water systems are found to exhibit a variety of intermediate phases, depending on the salt-to-surfactant molar ratio, α, and the water content. Both these systems show ribbon and bicontinuous cubic phases at low values of

α. At α=0.4 and 0.5, the CPC-SHN system exhibits a transition between two ordered mesh phases, as a function of both temperature and water content (Fig. 2). On the other hand, only the tetragonal mesh phase is observed in the CPC-SHN1 system at similar values of α. The parameter γ which is the ratio of the mesh size to the lamellar periodicity increases with surfactant concentration in the random mesh phase and the transition to the ordered mesh phase occurs at around $\gamma \sim$1.5. At $\alpha \sim 1$ phase diagrams of both systems are dominated by the lamellar phase. Two nematic phases are also observed with SHN, with the one at lower values of α consisting of cylindrical micelles and the one seen at higher values of α being made up of disc-like micelles. In contrast, DHN has a negligible effect on the phase behavior of CPC, and the micelles remain cylindrical up to α=0.75. These results show that strongly binding counterions, provided by the organic salts, can be used to tune the curvature of the micellar interface and stabilize different intermediate phases.

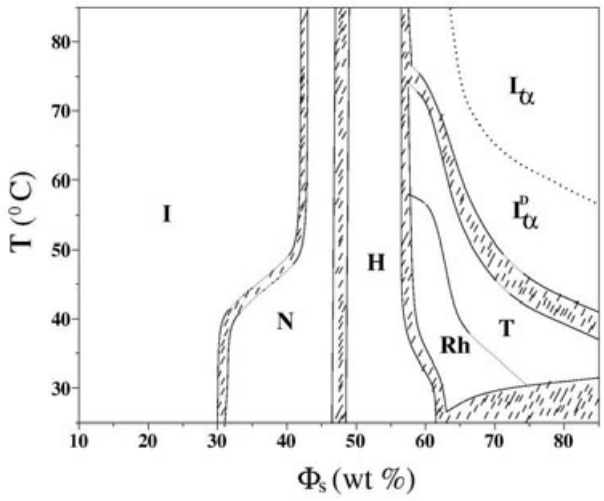

FIGURE 2: Partial phase diagram of the CPC-SHN-Water system at α=0.4. I, N, H, Rh, T, L_α^D and L_α denote the isotropic, nematic, hexagonal, rhombohedral mesh, tetragonal mesh, random mesh and lamellar phases, respectively. The dotted line indicates the continuous L_α^D - L_α transition. Shaded areas correspond to multiphase regions.

Chapter 3 describes a novel isotropic phase of bilayers observed in the CPC-SHN-water system at high SHN concentration. This system exhibits three phases- a dispersion of of multilamellar vesicles at high water content, an isotropic (L_x)

phase at moderate water content and lamellar (L_α) phase at low water content (Fig. 3).

Observation of flow-birefringence in the L_x phase and the fact that the average spacing in this phase is comparable to the periodicity of the low-temperature lamellar phase, suggest that the L_x phase consists of bilayer-like amphiphile aggregates. SAXS pattern of the L_x phase is found to exhibit a broad peak corresponding to the bilayer form factor at high water content and positional correlations between bilayers develop with decreasing water content. The much larger peak width in this phase, compared to the lamellar phase, can arise from an irregular stacking of bilayers. Since the number of correlated bilayers is a tunable parameter in the model used to describe scattering from the lamellar (L_α) phase, it can also be used to describe scattering from an irregular stack of bilayers. The number of correlated bilayers in the L_x phase turns out be of the order of 3, whereas it is ~ 10 in the L_α phase. The small and gradual variation of the electron density profile across the L_α-L_x transition obtained from fitting the data to the model, confirms that the L_x phase is made up of bilayers, with short range positional correlations.

Observed decrease in the inter-bilayer correlations across the L_α-L_x transition can be qualitatively understood in terms of the formation of pores or passages in the bilayer. At lower water content, L_x phase is suppressed, and L_α phase becomes stable again. This situation is similar to the suppression of bilayer curvature defects with decreasing water content seen in some lamellar phases, and the theoretically predicted suppression of dislocation loops in smectic films confined between two rigid boundaries.

Chapter 4 deals with the influence of oils and alcohols of different chain lengths on the stability of the L_x phase found in aqueous solutions of the anionic surfactant, sodium dodecyl sulfate (SDS) in the presence of the organic salt, p-toluidine hydrochloride (PTHC). Oils of shorter and alcohols of comparable chain length to the surfactant are found to stabilizes the lamellar (L_α) phase at the expenses of the L_x phase over a range of concentration, which decreases with increasing temperature (Fig. 4). Cryo-SEM micrographs of the L_x phase are found to show

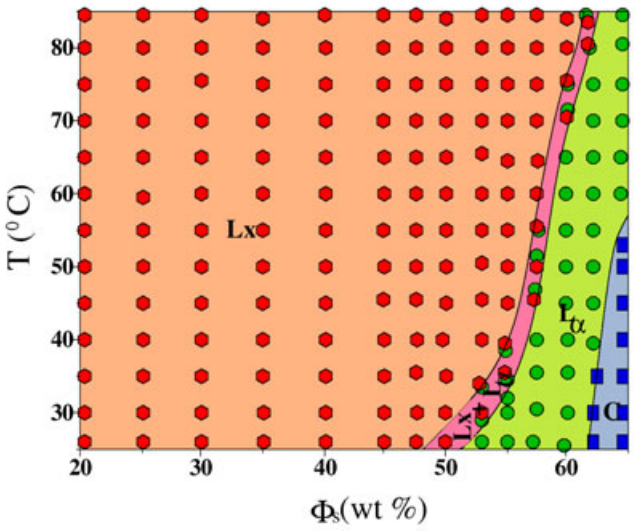

FIGURE 3: Partial phase diagram of the CPC-SHN-Water system at α=2. L_x and L_α denote the isotropic phase of bilayers and the lamellar phase, respectively.

bilayers with pore like features (Fig. 5A). Further, the ionic conductivity is found to be much higher in the L_x phase. These observations suggest that this phase has a connected bilayer structure with continuous water channels, in agreement with the detailed analysis of the SAXS data presented in the previous chapter.

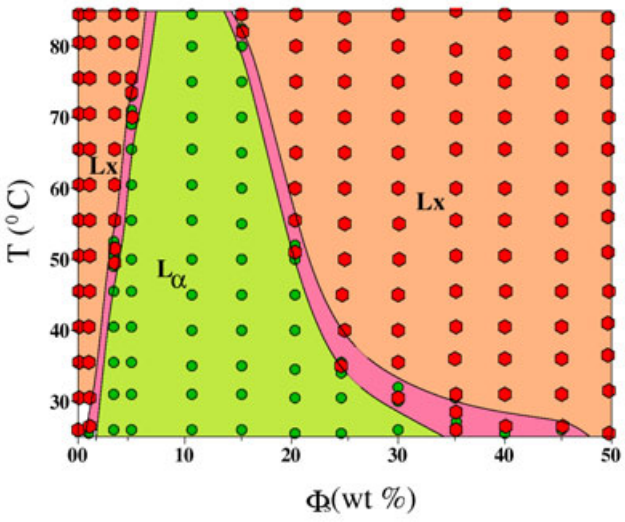

FIGURE 4: Partial phase diagram of the SDS-PTHC-Hexane-Water system. ϕ_s is the concentration of hexane. L_x and L_α denote the isotropic phase of bilayers and the lamellar phase, respectively.

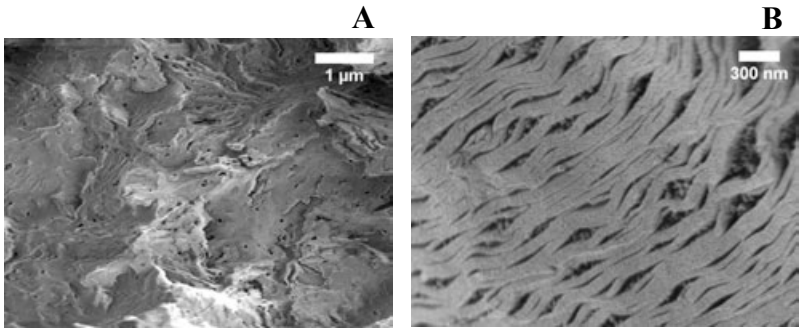

FIGURE 5: (**A**) Typical cryo-SEM micrograph of the L_x phase. It shows bilayers with pore like features. (**B**) Typical cryo-SEM micrograph of the L_α phase. It shows a regular stack of bilayers.

The lamellar (L_α) phase has been shown to be unstable against the formation of bilayer passages when the ratio of the moduli of Gaussian and mean curvatures $\frac{\bar{\kappa}}{\kappa}$ becomes weakly negative. Proliferation of such defects are also known to destroy long-range positional correlations in the lamellar phase. The re-entrant behavior of the L_x phase, observed in the present system suggests a non-monotonic variation of the above ratio.

$$\frac{\bar{\kappa}}{\kappa} = -a(\phi_s) + b(\phi_s)^2 + (\frac{\bar{\kappa}}{\kappa})_{\phi_s=0} \tag{1}$$

where a and b are positive constants depending on the system and ϕ_s is the weight fraction of oil or alcohol. Detailed understanding of this behavior is currently lacking.

Chapter 5 deals with structures exhibited by complexes of poly acrylic acid, sodium salt (PAANa) with didodecyldimethyl ammonnium bromide (DDAB) and the effect of poly acrylic acid (PAA) on the phase behavior of CPHN (complex of cetylpyridinium chloride (CPC) and 3- hydroxy-2-sodium naphthoate (SHN)). As we have discussed above, some ionic surfactants form an isotropic (L_x) phase of bilayers at very high concentrations of strongly binding counterions. Our motive was to see whether this phase could be stabilize in a system where the strongly binding counterion is replaced by an absorbing polyelectrolyte.

DDAB-PAANa-Water system exhibits only collapsed lamellar phase and swollen sponge phase. However, L_x phase is not found in this system (Fig. 6). Addition of salt (NaBr) to the collapse lamellar phase is found to show-collapsed lamellar phase → swollen sponge phase → collapsed lamellar phase transition sequence.

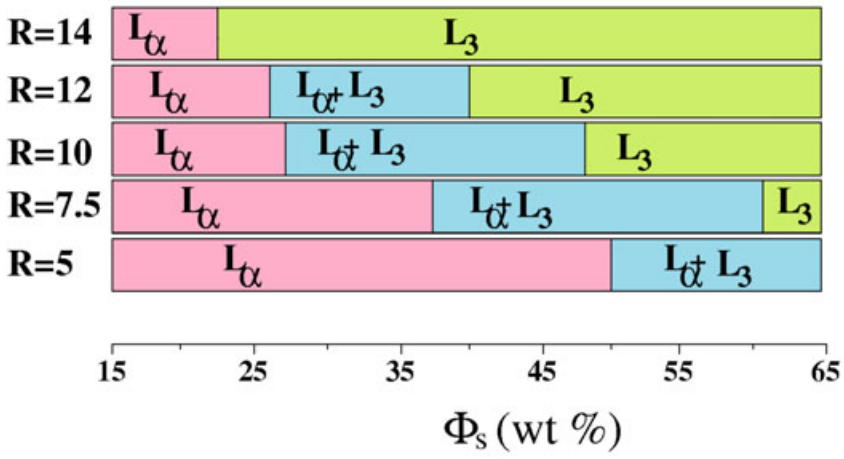

FIGURE 6: Partial phase diagram of the DDAB-PAANa-water system at 30°C. R is the weight ratio of PAANa to DDAB. Lα and L_3 are the lamellar and sponge phases respectively. The molecular weight of PAANa used was 2100.

The sponge phase found at all compositions in this system is highly swollen. The presence of large amounts of dissociated salt in the present system makes the Debye length extremely short. Hence, one can ruled out the role of electrostatic interaction in the swelling of the sponge phase. Swelling in the sponge phase might also arise from Helfrich repulsion. This repulsion originates from thermal undulations of the bilayers and is inversely proportional to the bending rigidity of the bilayer. It has been theoretically shown that homogeneous adsorption of polymers on both sides of the bilayer, leads to a decrease in the bending rigidity. Since, in the present system the concentration of polyelectrolyte is very high, it could lead to a drastic decrease in the bending rigidity of the bilayer, which in turn could give rise to a highly swollen phase. However, this does not explain the observed transformation of the microstructure from lamellar to sponge.

CPHN is found to show a lamellar phase coexisting with isotropic phase over a wide range of water content. Addition of PAA is found to tune the spontaneous

curvature of the micelles, leading to a transition from lamellar phase of bilayers to an inverted isotropic phase of spherical micelles via hexagonal phase of inverted cylindrical micelles.

In **Chapter 6** we study the influence of 6-hydroxy-2-sodium naphthoate (SHN2) on the phase behavior of cetylpyridinium chloride (CPC). Earlier studies on similar system suggest that the addition of a strongly binding counterion to CPC results in an increase in the length of CPC cylindrical micelles at low surfactant concentration and leads to a highly viscous entangled worm-like micellar solution on further increasing the salt concentration.

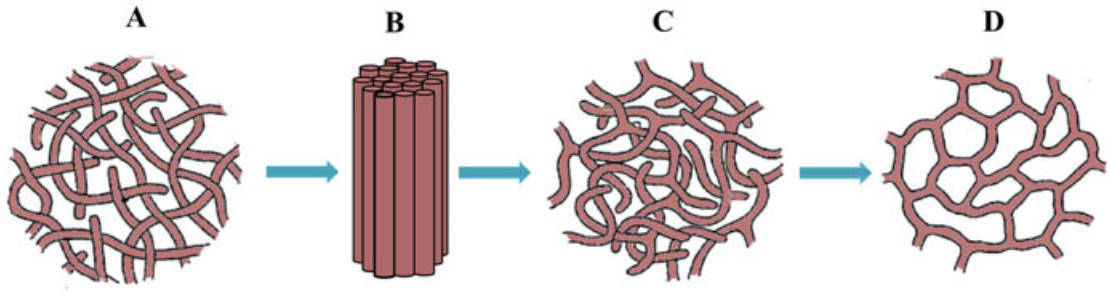

FIGURE 7: Schematic drawing of the proposed changes in the CPC aggregate morphology with increasing SHN2 concentration.

At low amounts of SHN2, the phase behavior of CPC-SHN2-Water system is similar to that of the CPC-Water system, except that the low-viscosity isotropic phase of spherical micelles at higher water content is replaced by a viscous isotropic solution (I_1) of worm-like micelles. With increasing concentration of SHN2, the hexagonal phase with excess water is found. At still higher concentration of SHN2, a low viscous isotropic (I_2) phase is found which seems to be made up of a branched and multi-connected network of cylindrical micelles. This isotropic phase transforms into the hexagonal phase at lower water content and low temperatures. On increasing the concentration of SHN2 the following sequence of transitions is found: $I_1 \rightarrow I_1$+excess water $\rightarrow$ H +excess water $\rightarrow I_2$+excess water $\rightarrow I_2$. The observed phase sequence can be explained as follows. Addition of very low amounts of SHN2 to CPC, transforms the spherical micelles of CPC to worm-like micelles and

leads to the formation of the viscous isotropic (I_1) phase (Fig. 7A). Further addition of SHN2, leads to additional growth of the micelles . The $\pi - \pi$ interactions between counterions ($HN2^-$) as well as interactions between the counterions and the cationic head-groups, mediated by the $HN2^-$ counterions embedded within the micelles, become dominant and lead to an attractive interaction between the worm-like micelles. This attractive interaction, gives rise to the (I_1+excess water) phase separation. Micelles become longer, on further addition of SHN2 and leads to the formation of hexagonal phase with excess water (H +excess water) (Fig. 7B). Further addition of SHN2 gives rise to branched micelles. Formation of branched micelles destroys positional order of the hexagonal phase and gives rise to the isotropic phase with excess water (I_2+excess water) (Fig. 7C). (Fig. 7D). Disappearance of excess water and swelling of the I_2 phase might result from osmotic pressure due to a non-uniform distribution of salt as found in the case of some polymer gels. So, this phase sequence is consistent with a gradual transformation of the aggregate topology from entangled worm-like micelles to branched and connected network of cylindrical micelles with increasing SHN2 concentration (Fig. 7).

In **Chapter 7** we describe the influence of p-toluidine hydrochloride (PTHC) on the phase behavior of sodium dodecyl sulfate (SDS). Effect of chirality on the phase behavior of this system has also been studied.

Phase behavior of SDS-PTHC-Water system has been studied at various molar ratios of PTHC to SDS, α. This system is found to exhibit- isotropic, nematic, hexagonal, lamellar and cubic phases. Two nematic phases are also observed, with the one at lower values of α, consisting of cylindrical micelles (N_c) and the other seen at higher values of α being made up of disc-like micelles (N_d).

Following phase sequence is seen in the SDS-PTHC-Water system at α=0.14. *Isotropic (I)* $\rightarrow$ *Nematic* (N_c) $\rightarrow$ *Hexagonal(H)* $\rightarrow$*Isotropic (I)*$\rightarrow$ *Lamellar* (L_α) as a function of increasing ϕ_s (Fig. 8). This phase sequence is unusual and consistent with a gradual transformation of the aggregate shape from cylindrical to disc-like with increasing ϕ_s. The apparent viscosity of the sample also shows a

non-monotonic behavior. It is found to increase gradually upto a maximum in the hexagonal phase and then decreases in the isotropic phase, on decreasing the water content. This is consistent with an initial gradual increase in the length of the cylindrical micelles and then a subsequent decrease. This sequence of phases suggests a gradual prolate to oblate change in the aggregate morphology with increasing ϕ_s. Such a morphological change seems to prevent the formation of other intermediate phases usually seen between the hexagonal and lamellar phases. Further experiments are needed to understand the proposed change in the morphology of the aggregates.

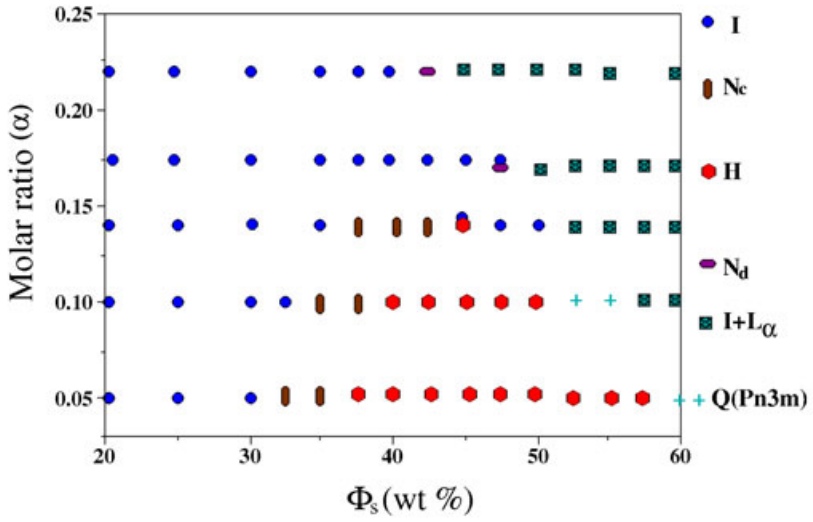

FIGURE 8: α-temperature phase diagram of the SDS-PTHC-Water system at T=45°C. I, N_c, H, N_d, Lα and Q(Pn3m), denote the isotropic, nematic of rod-like micelles, hexagonal, nematic of disc-like micelles, lamellar and cubic phases, respectively.

Our results suggest formation of the line hexatic phase in between the nematic and hexagonal phases over a narrow temperature and composition range. These transitions seem to be driven by a change in the degree of branching of the worm-like micelles with temperature. Further, the structure of the chiral line hexatic phase is consistent with the theoretically predicted Moiŕe structure. However, further detailed measurement of the evolution of the hexatic order parameter is needed to unambiguously confirm the existence of the hexatic phase.

In **Chapter 8** we present studies on an undulation instability observed in the nematic phase of worm-like micelles under dilation. For comparison, this instability was also studied in the hexagonal phase of worm-like micelles.

Striations were observed perpendicular to the long axis of the worm-like micelles in samples under dilation (Fig. 9A). The wave length λ of the striation pattern was measured for different sample thickness (d). λ was found to be proportional to $\sqrt{d}$, as in the case of the Helfrich-Hurault instability (Fig. 9B). A characteristic length (m) defined as: m=$\sqrt{\frac{K}{B}}$ where B and K are and curvature moduli of the system, can be estimated from the data.

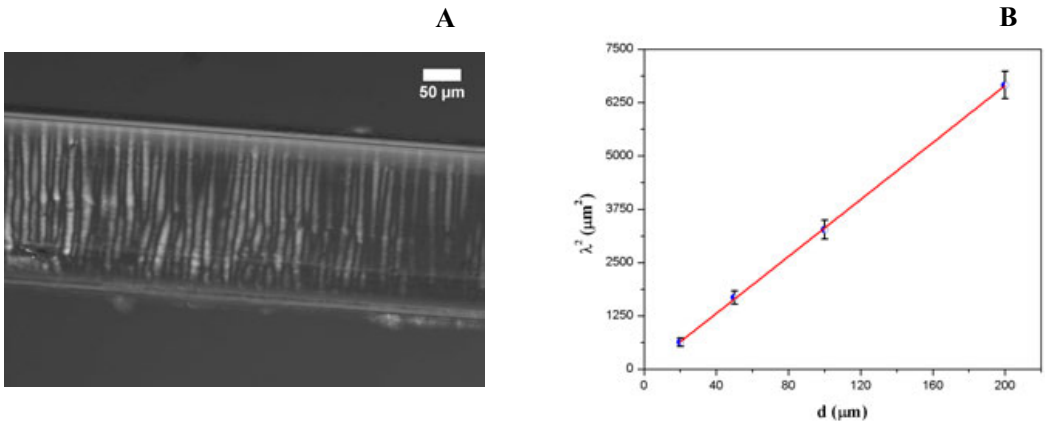

FIGURE 9: (**A**) Striation pattern in the chiral nematic phase of the SDS-PTHC-Cholesterol-Water system. (**B**) Variation of the square of the wavelength with sample thickness (d).

On increasing the temperature, the lateral separation between the micelles changes in all theses systems. Hence a sudden change in the temperature leads to a dilation (rate of heating is faster than the relaxation of the worm-like micelles). There are two possible ways of relaxing the imposed dilation. One must either increase the number of worm-like micelles or tilt them if their number is maintained constant. Since the dilation is too sudden for the system to be able to adjust the number of micelles, it has no other choice but to tilt the cylinders with respect to the bounding plates. This fast process leads to a periodic undulation of the micelles, resulting in a striation pattern. However, this instability does not occur in nematics made up of small micelles. The main difference between the two cases is the presence

of a free energy cost for locally compressing or dilating the system made up of worm-like micelles.

The characteristic length comparable to the diameter of worm-like micelles in the hexagonal phase but is about two orders of magnitude larger in the nematic phase. The reason for this difference is presently not clear. Independent measurements of K and B in the nematic phase could give a better understanding of this behavior.

In **chapter 9** a summary of our findings is given and some directions for future research are proposed.

V. A. Raghunathan
Raman Research Institute

Santosh Prasad Gupta

Publications

- Santosh Prasad Gupta and V. A. Raghunathan,
  Controlling the thermodynamic stability of intermediate phases in a cationic-amphiphile-water system with strongly binding counterions, Phys. Rev. E **88**, 012503 (2013).

Contents

Chapter 1

Introduction

This chapter gives a brief introduction to amphiphiles and their self assembly and also describes the experimental techniques used to identify their structure in aqueous medium. Thermodynamics of amphiphile self-assembly is described in section 1.1. Their general phase behavior in aqueous media is given in section 1.2. Basic theory of x-ray diffraction and a brief description of the experimental set up used for studying lyotropic liquid crystalline phases are contained in section 1.3. Section 1.4 describes the principles of polarizing optical microscopy. Cryogenic scanning electron microscopy (cryo-SEM) technique used to visualize structure of lyotropic phases is discussed in section 1.5. Characterization of different liquid crystalline phases using optical polarizing microscopy and x-ray diffraction is described in section 1.6. Procedure to analyze x-ray diffraction data from specific phases is described in the last section.

1.1 Amphiphiles

The word amphiphile comes from the Greek prefix amphi, which means both or double, and the word phile, which means like or love. In general, an amphiphile is any molecule that consists of two parts, one which is soluble in a specific fluid and the other insoluble. When the fluid is water one usually talks about hydrophilic

and hydrophobic parts, respectively. The hydrophilic part is referred to as the 'head group' and hydrophobic part as the 'tail'. Examples of amphiphiles are surfactants, block copolymers, lipids, bile acids, and cholesterol [1–3]. Synthetic amphiphiles are often referred to as surfactants, whereas those of biological origin are usually called lipids. However, this classification is not standard, but this is the sense in which these two terms are used here. Amphiphilic molecules can be classified depending on the nature of their head groups as ionic, non-ionic and zwitterionic. The head groups of ionic amphiphiles dissociate in water and acquire an electric charge. For example, cetyltrimethylammonium bromide (CTAB) is a cationic surfactant (Fig. 1.1A) and sodium dodecylsulfate (SDS) is an anionic surfactant (Fig. 1.1B). The nonionic surfactant n-dodecyl tetra (ethylene oxide) ($C_{12}E_4$) does not contain any charge but its head group is polar (Fig. 1.1C). In the case of a zwitterionic amphiphile the head group acquires a dipole moment in aqueous solutions (Fig. 1.1D).

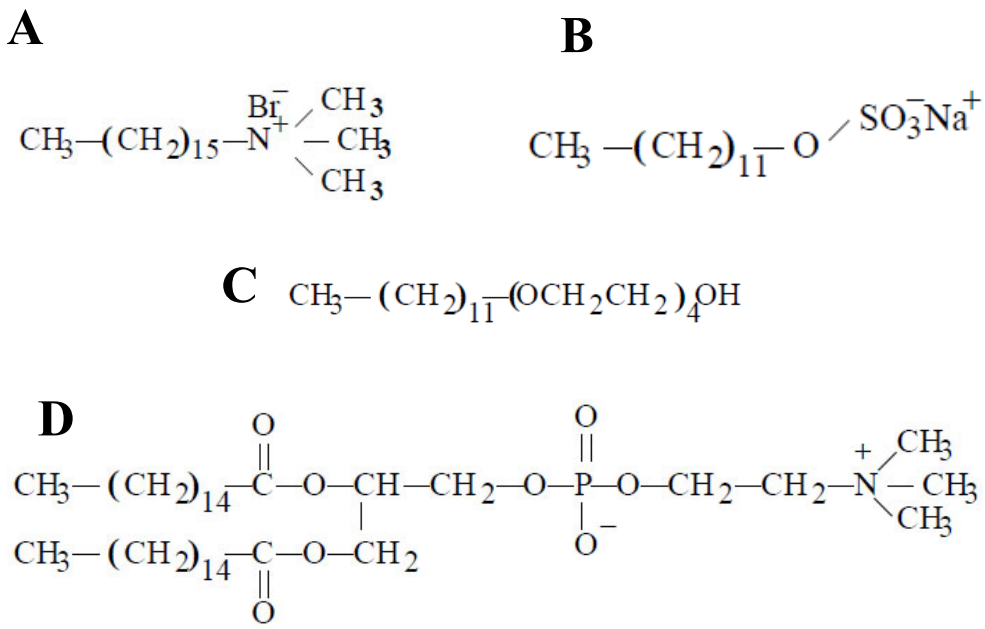

FIGURE 1.1: Chemical structure of (**A**) cationic surfactant cetyltrimethylammonium bromide (CTAB), (**B**) anionic surfactant sodium dodecylsulfate, (**C**) nonionic surfactant n-dodecyl tetra (ethylene oxide) (C_12E_4) and (**D**) zwitterionic lipid dipalmitoyl phosphatidylcholine (DPPC).

1.1.1 Hydrophobic effect

The interaction between water molecules involve orientation dependent hydrogen bonds. Molecules that have high water solubility are known as hydrophilic molecules. These molecules are believed to a have disordering effect on the water matrix around it, which in turn increases the entropy of the system and favors the molecules to be in contact with water [1]. On the other hand, molecules which are not capable of hydrogen bonding such as hydrocarbons and fluorocarbons, do not like to be in contact with water and are known as hydrophobic molecules. When such a molecule is placed in water, the water molecules around it, have to create a cavity to accommodate it. Since non-polar molecules cannot form hydrogen bonds, the creation of the cavity requires either breakage of hydrogen bonds, or rearrangement of the water molecules in a way that breaking of hydrogen bonds is avoided. Which process takes place depends on the details of the solute molecule. The shape of water molecules allows them to arrange themselves around most solutes to form cage-like structures, without breaking hydrogen bonds but in this process the water molecules become even more ordered than in bulk water which is entropically unfavorable. When many such molecules are present in water the loss of entropy becomes too great and it becomes more favorable to break hydrogen bonds and create larger cavities to accommodate an assembly of solute molecules. This leads to an effective attraction between the solute molecules, called the hydrophobic interaction [1, 4]. Due to the hydrophobic interaction, the solute molecules have stronger mutual attraction in water than they do in free space.

Hydrophobic effect is very important in nature. It is the reason behind the formation of lipid membrane and affect many other biological process, e.g. protein folding. It is an important effect which governs many phenomenon in soft matter systems, in particular, it is the driving force for amphiphilic self-assembly.

1.1.2 Amphiphilic self-assembly

At very low concentrations, amphiphiles form a monolayer at the air-water interface, by positioning their head groups at the water surface and keeping away the hydrocarbon part in the air. At higher concentrations, Many of them self-assemble into aggregates of different structures in water, such that their hydrophobic parts are screened from water molecules by their hydrophilic parts. This phenomena is referred as self assembly and aggregates formed are called micelles. The amphiphile concentration at which self-assembly occurs is called the critical micellar concentration (CMC). Below CMC the amphiphiles are dispersed in water as monomers, whereas above CMC micelles coexist with monomers.

1.1.2.1 Thermodynamics of self assembly

From a thermodynamic point of view, the system can be modeled using mass-action considerations. That is, an analogy can be drawn between micellization and chemical equilibrium among reactants. Aggregates of different sizes can be treated as distinct chemical species and aqueous solution of an amphiphile can be considered as a multicomponent system with several phases in equilibrium. Each phase is taken to consist of aggregates of a given aggregation number, which is the number of molecules in an aggregate. For a very dilute solution, the interaction between the aggregates may be neglected and one can apply the theory of dilute solutions to this system. The chemical potential of an amphiphile in an N-aggregate is given by [1, 5],

$$\mu_N = \mu_N^0 + \frac{k_B T}{N} log \frac{X_N}{N} \tag{1.1}$$

The first term is the reference chemical potential arising from the mean interaction free energy per molecule (μ_N^0) and the other one comes from the entropy of mixing. X_N is the mole fraction of amphiphiles that form N-aggregates. The total mole fraction of the amphiphiles $X = \sum_{N=1}^{\infty} X_N << 1$. In chemical equilibrium, the

chemical potential of the amphiphile (μ_N) remains the same for all N. Thus,

$$\mu_1^0 + \frac{k_B T}{1} log \frac{X_1}{1} = \mu_2^0 + \frac{k_B T}{2} log \frac{X_2}{2} = ... = \mu_N^0 + \frac{k_B T}{N} + log \frac{X_N}{N} \tag{1.2}$$

This gives the equilibrium distribution of the N-aggregates

$$\frac{X_N}{N} = X_1 (exp[\frac{\mu_1^0 - \mu_N^0}{k_B T}]) \tag{1.3}$$

If we define $\alpha = \frac{\mu_1^0 - \mu_N^0}{k_B T}$, then $X_N = N X_1 exp(\alpha)$

Therefore, aggregation can take place only if α>0. Hence the energy per molecule must be lower in aggregates of size M, for some M>1. In practice, M ∼50, and is determined by the optimal packing of the hydrocarbon chains within the micelles.

Since X_N cannot exceed unity, the limiting value of monomer concentration, $X_1 \sim e^{-\alpha}$. The critical micellar concentration (CMC), is the amphiphile concentration at which X_1 saturates and further addition of amphiphiles leads to the formation of micelles (fig. 1.2A). It is given by, CMC $\approx e^{-\alpha}$.

Experimentally, CMC is determined by studying the variation of certain physical quantities. Below the CMC value, some physical parameters such as turbidity, osmotic pressure and equivalent conductivity increase with concentration and surface tension decreases with concentration, but show a rather abrupt change in the concentration dependence above the CMC value [6], as in (fig. 1.2B).

The CMC depends on the chemical structure of the surfactant and many external factors, e.g., pH, temperature and pressure [7]. For example, it decreases strongly with increasing the hydrocarbon chain length of the surfactant. This is because the critical chemical potential, k_BT log(CMC), decreases linearly with chain length, with each methyl group contributing about 2-3 k_BT. The CMC of ionic surfactants (typically 10^{-3}-10^{-2}M) is orders of magnitude higher than that of nonionic amphiphiles (typically 10^{-5}-10^{-4}M). This is due to the smaller repulsion between the head-groups in the nonionic case. However, the CMC for lipids is typically ∼

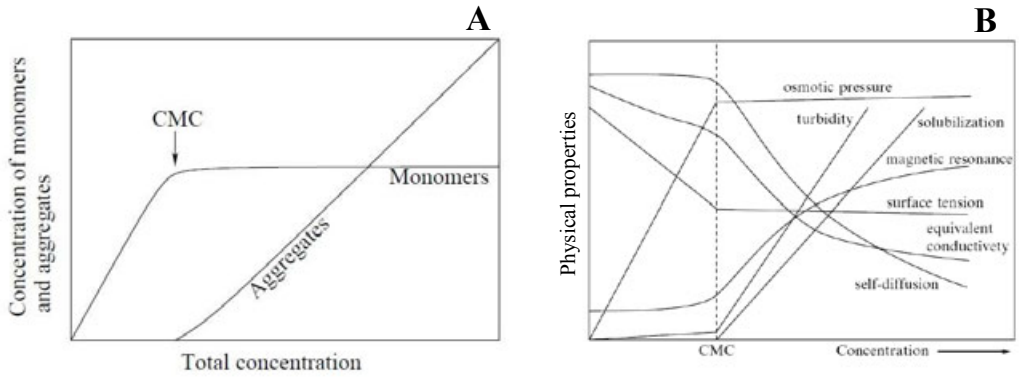

FIGURE 1.2: (**A**) Variation of monomers (X_1) and aggregates concentration (X_N) as a function of the amphiphile concentration (X) (from ref. [1]) and (**B**) Schematic representation of the concentration dependence of some physical properties of micelle forming surfactant solutions (from ref. [6]).

10^{-9}M, which is due to the large hydrophobic effect caused by their two chains. The addition of salt decreases the CMC of ionic surfactants by up to an order of magnitude. This effect is due to the electrostatic screening caused by the salt ions, which reduces the repulsion between the ionic head groups. However, salt has little effect on the CMC of nonionic amphiphiles and it can either increase or decrease.

1.1.2.2 Shapes of aggregates

The shape of aggregates in isotropic micellar solutions, just above CMC is usually spherical. In a mesomorphic state, aggregates can have different shapes, such as cylindrical, rod-like or disc-like. These shapes are subjected to a geometrical constraint; one of the three dimensions must be limited by the value 2l, where l is the length of the amphiphilic molecule.

To classify and study these structures, the packing parameter p is introduced,

$$p = \frac{v}{al} \tag{1.4}$$

TABLE 1.1: The packing parameter and shape of different aggregates of amphiphilic molecules.

$p = \frac{v}{al}$	Shape of the molecule	Shape of the aggregate
<1/3	cone	spherical micelles
1/3-1/2	truncated cone	cylindrical micelles
1/2-1	truncated cone	three fold junction of cylindrical micelles
∼1	cylinder	planer bilayer
>1	inverted truncated cone	inverted micelles

where a is the optimal head group area, v the hydrocarbon chain volume and l the chain length. For $p<$ 1/3, the molecules have a conical shape, which would force the aggregate to have a spherical shape. For other values of this parameter (p), the molecules can form cylindrical micelles, planer bilayer or inverted micelles (Figs. 1.3 and 1.4 and Tab. 1.1). However, the shape of amphiphiles depends upon concentration, pH, temperature, etc.

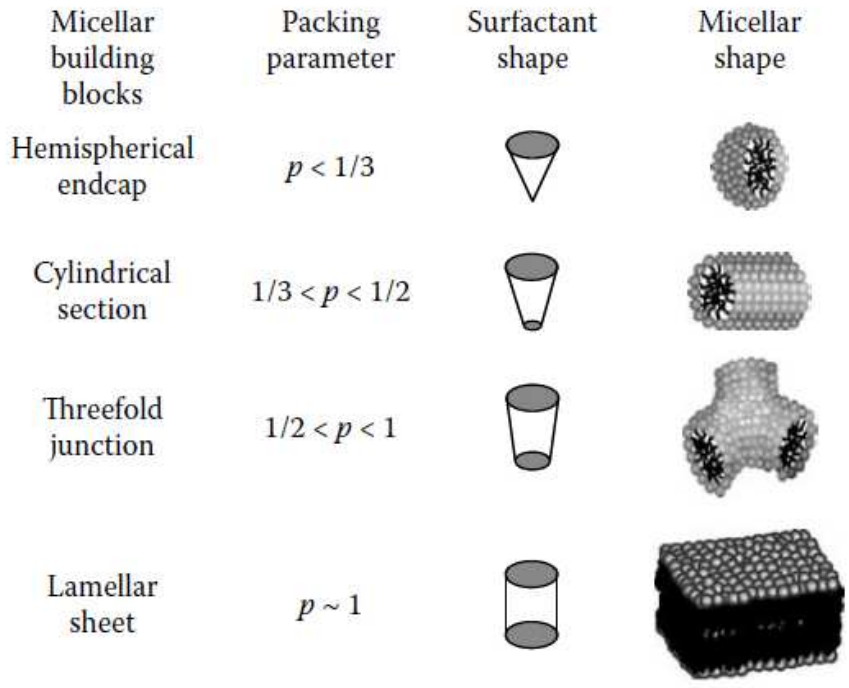

FIGURE 1.3: Dependence of aggregate morphology on the packing parameter (from ref. [8]).

In the case of spherical micelles, radius of the micelles is determined by chain length of amphiphilic molecule. As a result the size distribution of spherical micelles is fairly mono-disperse. The radius of a cylindrical micelle is again set by

the length of the amphiphile. Cylindrical micelles have hemispherical end-caps, which cost additional energy to create. This end-cap energy is clearly independent of the length of the cylinder. The length distribution of cylindrical micelles is determined by the competition between entropy, which would favor shorter and hence larger number of micelles, and end-cap energy, which would favor longer and hence smaller number of micelles. Since the end-cap energy is independent of the length of the cylinder, this results in a very broad length distribution of these micelles. The end-cap energy can be made very large by adding certain salts and alcohols to the amphiphile solution. This results in the formation of very long, flexible micelles that become entangled to form a viscoelastic gel. These are known as 'worm-like' micelles and these micelles may be microns long and have either a circular or elliptical cross section of a few nanometers. They behave in many ways similar to polymers [9]. Another kind of micelles is disc-like, have semi-toroidal rims in order to prevent the hydrocarbon chains from being in contact with water. The formation of these curved edges, however cost energy. The difference in the behavior of disc-like and rod-like micelles arises from the fact that the perimeter of the rim of a disc increases with the disc radius, whereas the size of the end cap on a cylinder is independent of the length of the cylinder. Generally, disc-like micelles are unstable and coalesce to form an infinite bilayer in order to decrease the edge energy. However, disc-like micelles are found in some multi-component amphiphilic systems [10–12].

Micelles are very useful in many fields of science and technology [3, 13, 14]. In chemistry micelles are used as catalysts and solubilizing agents in many organic and inorganic reactions. In colloid chemistry spherical micelles are used as a model system for studying many problems, for example the various interactions between colloid particles. They are very important in cosmetics and oil industry. Viscoelastic solutions of amphiphiles are widely used as lubricants. They are also used in medicine for encapsulating drugs in their hydrocarbon cores, in oil recovery for solubilizing oil droplets. Some of these systems have also been used for protein crystallization [15]. The recent development of nanotechnology has again expanded their field of application. For example, various liquid crystalline

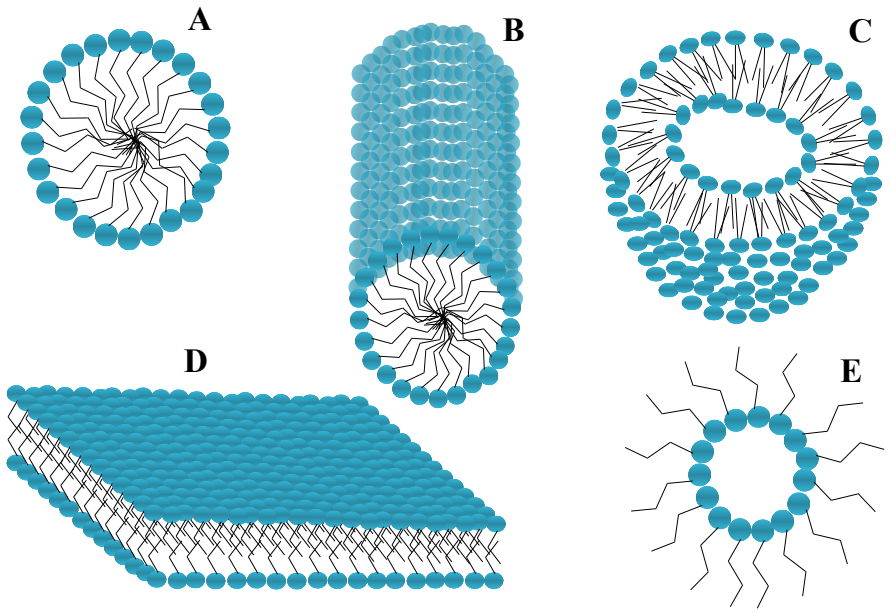

FIGURE 1.4: Schematics of various self assembled structures of amphiphilic molecules : (**A**) spherical micelle, (**B**) cylindrical micelle, (**C**) vesicle, (**D**) bilayer and (**E**) inverted micelle.

phases exhibited by these molecules have been used as templates for the synthesis of mesoporous materials and nano particles.

1.2 Phase behavior of aqueous solutions of amphiphiles

Figure 1.5 presents the generic temperature-composition phase diagram of binary surfactant-water systems.

Below the CMC, amphiphiles form an isotropic molecular solution. However, just above the CMC, they usually form a solution of spherical micelles. The next phase is a cubic phase built up of discrete globular micelles. Due to the free energy penalty of packing globular micelles at high volume fractions, the micelles deform and become elongated into cylindrical micelles to form finally a 2D hexagonal lattice, with their long axes aligned normal to the plane of the lattice. This hexagonal phase is usually observed over a wide range of composition. Thereafter,

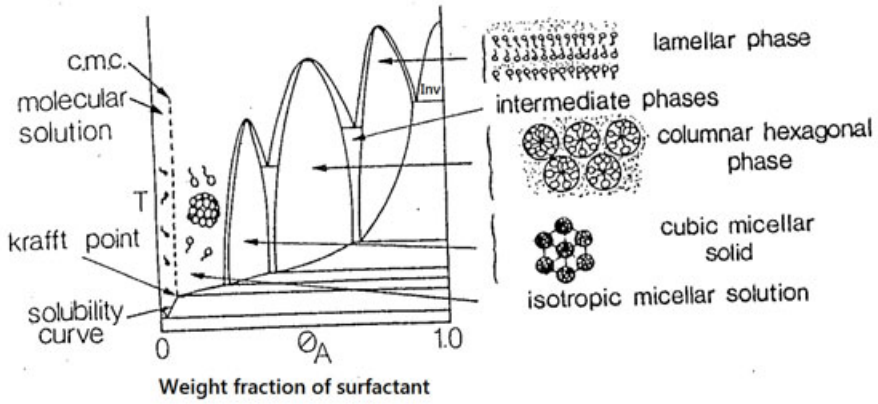

FIGURE 1.5: Schematic of phase diagram of amphiphile-water system (from ref. [16]).

the hexagonal phase transform to a lamellar phase (L_α), consisting of a periodic stack of bilayers separated by water layers; due to free energy penalty of packing cylindrical micelles at high volume fractions. This lamellar L_α phase is a one dimensional (1-D) lattice of bilayers, with liquid-like short range positional ordering of the molecules within the bilayers. Further increase of surfactant concentration gives-rise to a hexagonal phase of inverted micelles in some systems. This hexagonal phase can be looked at as consisting of a 2D lattice of water columns in the hydrocarbon matrix . The Kraft point or Kraft temperature shown in figure 1.5 is the temperature below which the amphiphile is in the crystalline phase and is insoluble in water. Schematics of various lyotropic liquid crystalline phases are shown in figure 1.6.

For double chain surfactants the phase diagram looks different as in the case of dioctyl sodium sulfosuccinate (Aerosol OT or AOT) and dioctadecyldimethylammonium chloride (DODMAC) [17, 18]. As for the single chain surfactant, the chain melting temperature strongly depends on the chain length. In the case of DODMAC the chains are long, which leads to a high melting temperature. The important feature of phase diagram of this class of surfactant is the stability of the lamellar phase over a wide composition range. In addition, this type of surfactant generally shows bicontinuous cubic phase and inverted hexagonal phase at

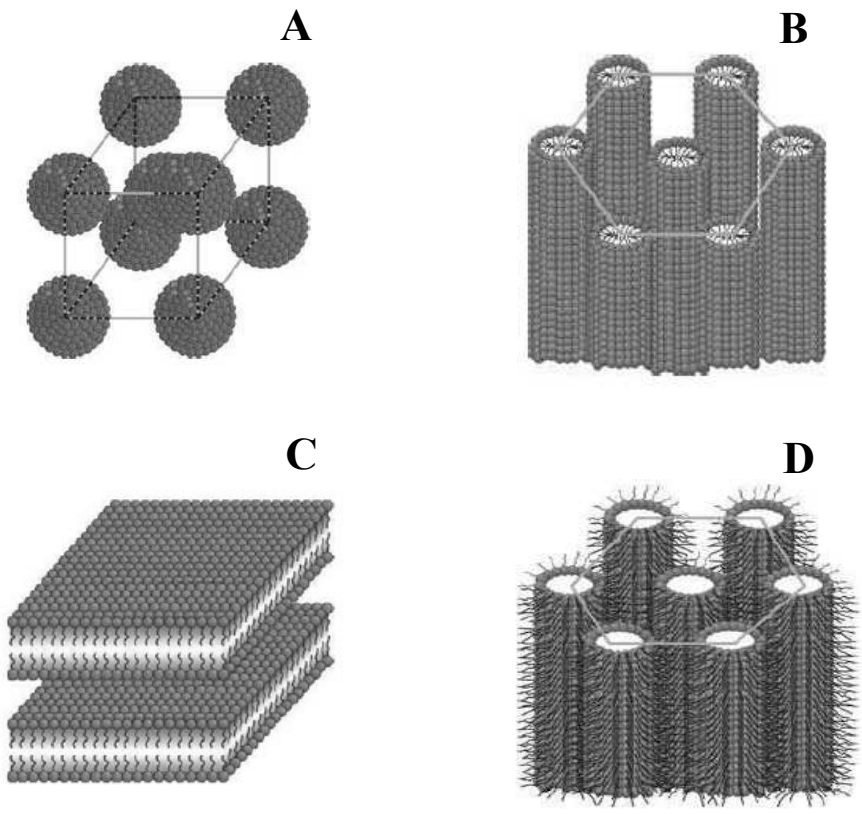

FIGURE 1.6: Schematics of various lyotropic liquid crystalline phases: (**A**) micellar cubic (bcc) phase, (**B**) direct hexagonal (H) phase, (**C**) lamellar (L_α) phase and (**D**) Inverted hexagonal (H_{II}) phase (from ref. [24])

higher surfactant concentrations. Double-chained lipids, such as Dipalmitoylphosphatidylcholine (DPPC), form only bilayers at all concentrations, except at extremely low water content. Hence, lamellar phases are very common in these systems. Above, the chain melting temperature, fluid lamellar (L_α) phase is found in this system and lamellar 'gel' phase is seen at lower temperatures, where the hydrocarbon chains are mainly in the all-trans conformation and arranged on a 2-D lattice within each bilayer.

In some systems, in between the isotropic and hexagonal phases, the rod-like micelles acquire long range orientational order to form a nematic phase denoted as N_c [19, 20]. Disc-like micelles, in between isotropic and lamellar phase, also exhibit the nematic phase [21], referred as N_d. Here, rod like (disc-like) micelles

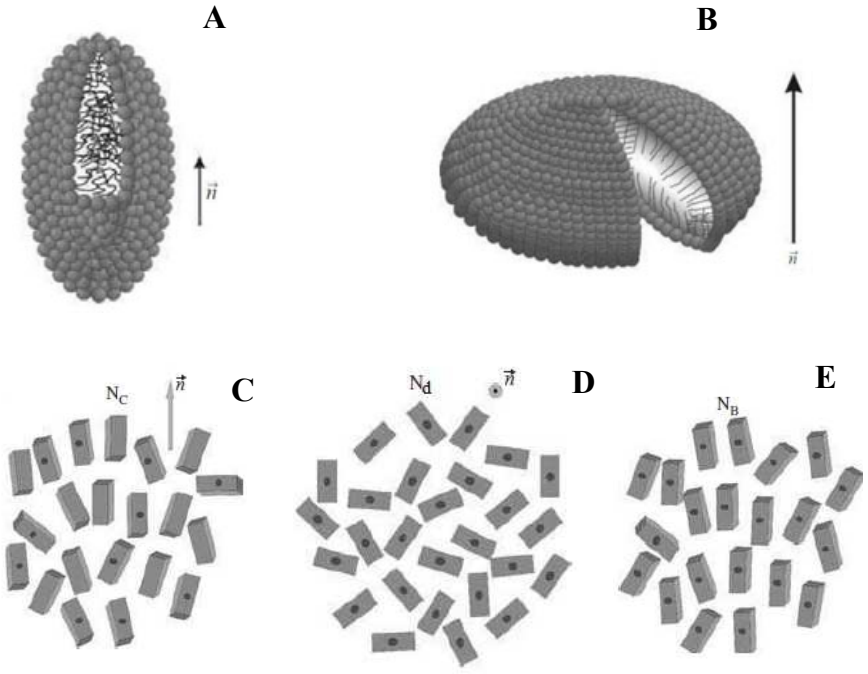

FIGURE 1.7: Schematics of micelles in lyotropic mixtures: (**A**) prolate ellipsoid or rod-like, (**B**) oblate ellipsoid or disc-like; $\vec{n}$ is the director and cuts show the paraffinic chains in inner part of micelles. Sketch of the order in the context of the intrinsically biaxial (brick-like) micelles model. The dots represent a particular surface of the micelles: (**C**) N_c phase, (**D**) N_d phase and (**E**) N_B phase(from ref. [24]).

has a preferred direction of orientation which is referred to as the nematic director ($\vec{n}$). These nematics are uniaxial in character. Another kind of nematic of biaxial character, so called 'biaxial nematic' N_B has also been reported in the literature [22, 23] (Fig. 1.7). Generally, these three nematics are not found in one amphiphile. However, the potassium laurate/ decanol/water [25] system displays all the three nematic phases.

A cholesteric phase can be formed if a nematic phase is doped with a chiral molecule. Three types of lyotropic cholesterics have been reported in the literature, Ch_c, Ch_d, and Ch_B [26]. The labels c, d, and B refer to the original nematic phases (calamitic, discotic, and biaxial), which were cholesterized by the addition of the chiral dopant. It has been observed that micelles spontaneously pack in a helicoidal structure (Fig. 1.8) whose pitch depends on the physico-chemical parameters [27], such as temperature, concentration of the chiral dopant (c_m) and

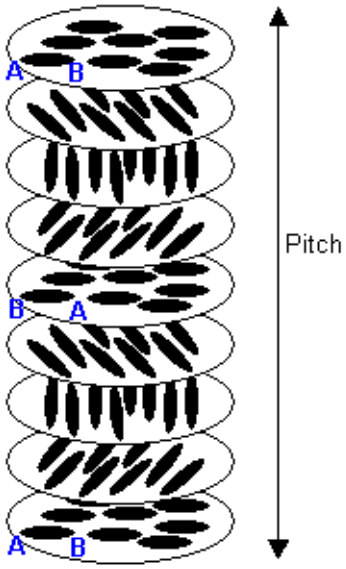

FIGURE 1.8: Sketch of a sequence of micelles in a cholesteric structure. A and B denote the two end of the rod-like micelles.

micellar shape anisotropy (S_a). In cholesterics, the typical length scale of the pitch is of the order of micrometers.

As described above, the hexagonal phase consists of cylindrical micelles with uniform curvature of the surfactant-water interface (neglecting the hemispherical end caps), whereas the lamellar phase is made up of planar bilayers. Many studies indicate that the morphological transformation from cylinders to bilayers does not take place abruptly, but through a sequence of intermediate shapes, giving rise to a sequence of so-called intermediate phases between the hexagonal and lamellar phases [28]. In ionic surfactants the intermediate phases usually occur only over very narrow ranges of composition. Further, the phase boundaries in these systems are almost independent of temperature [29]. Intermediate phases are frequently observed in the presence of a co-surfactant over a wide range of composition [30].

Frequently a bi-continuous cubic phases, which are optically isotropic, have been identified between the hexagonal and lamellar phases [28, 31, 32]. They form the first class of intermediate phases (Fig. 1.9A). Their identification is made easier by the fact that they are optically isotropic, unlike all other phases found at comparable surfactant concentrations. Hence, their formation can be easily visualized

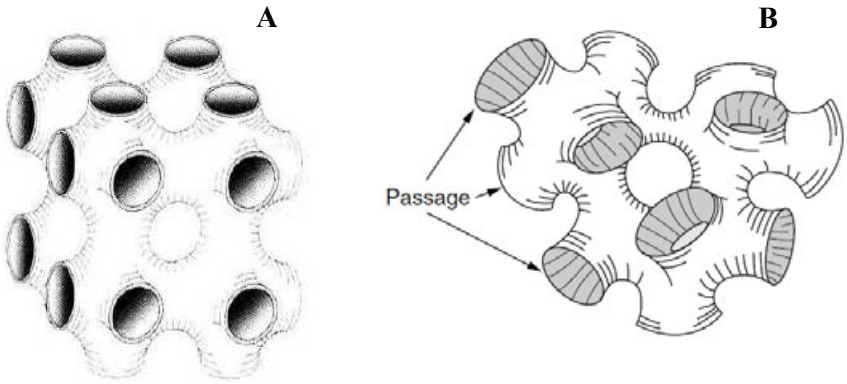

FIGURE 1.9: Schematic of (**A**) a bicontinuous cubic phase and (**B**) a sponge (L_3) phase (from ref. [33]).

using polarizing optical microscopy observations. Cubic phases can be classified into two types. Type I cubic phases consist of two interpenetrating, topologically identical networks of cylindrical micelles, separated by water. In type II cubic phases two interpenetrating water channels are separated by a surfactant bilayer. Interestingly, the surface separating the two networks into two equal volumes can be described as a triply periodic minimal surface characterized by vanishing mean curvature everywhere on the surface. Three cubic structures have been reported belonging to the space groups Im3m, Ia3d and Pn3m, usually associated with the P, gyroid and D triply periodic minimal surfaces respectively. Although some bicontinuous non-cubic intermediate phases have been proposed in the literature, their existence has not yet been unambiguously established [28].

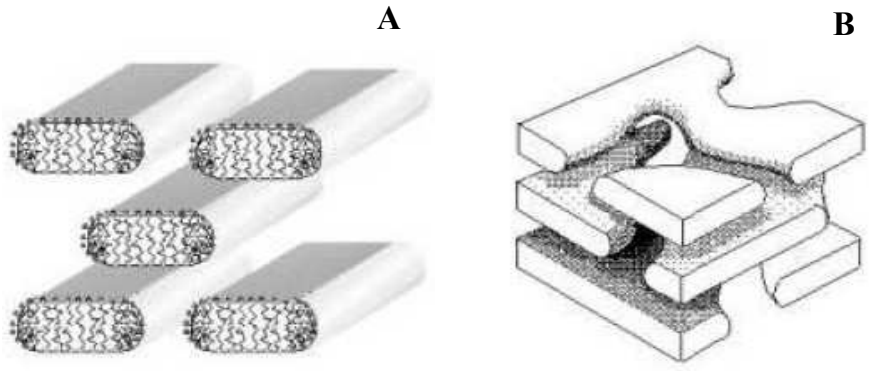

FIGURE 1.10: Schematic diagram of (**A**) centered rectangular lattice made up of ribbon-like aggregates, (**B**) a random mesh phase (from ref. [28]).

Another type of intermediate phase seen in some surfactants is the ribbon phase consisting of long micelles with roughly elliptical cross-section (Fig. 1.10A). These arrange on a two-dimensional rectangular lattice. Two types of structures have been reported, corresponding to the plane groups cmm and pgg [34–36].

Mesh phases are the third type of intermediate phases seen in many surfactant systems. They consist of two-dimensional mesh-like aggregates, which can also be described as bilayers with a regular array of mono-disperse pores. Mesh phases are of two types-ordered and random mesh phase. In the ordered mesh phase the mesh-like aggregates lock into a three-dimensional lattice. On the other hand, the random mesh phase consists of a periodic stacking of these aggregates with no long-range positional correlations of the in-plane structure (Fig. 1.10B). All known structures of ordered mesh phases are either rhombohedral (space group: $R\bar{3}m$) or tetragonal (space group: I4mm). The former consists of a 3-layer stacking of 3-coordinated hexagonal mesh, whereas the latter has a 2-layer stacking of 4-coordinated square mesh (Fig. 1.11).

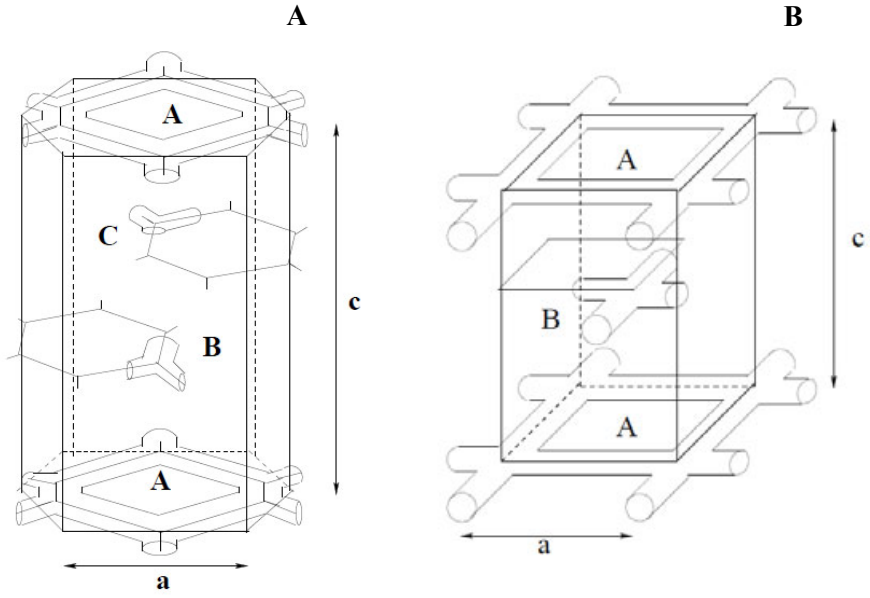

FIGURE 1.11: Schematic of an ordered mesh phase: (**A**) hexagonal unit cell and (**B**) a tetragonal unit cell (from ref. [37]).

Most of the studies on mesh phases, reported in the literature, have been carried out on the non-ionic surfactants, poly(oxyethylene glycol) alkyl ethers (C_nEO_m),

where they occur over a rather wide range of composition [38–46]. The role of the length of the hydrocarbon chain of the surfactant in stabilizing different intermediate phases has been well studied in this class of surfactants. Shorter hydrocarbon chains are found to favor the bi-continuous cubic phase, whereas longer ones induce mesh phases [45]. The structures of both these bi-continuous and mesh phases are consistent with the theoretical predictions of Hyde [47, 48]. However the theory does not explain the role of chain length in determining the structure. It has been conjectured that the increase in micellar curvature due to an increase in the head group size gives rise to the cubic phase, whereas the decrease in the flexibility of the aggregate due to an increase in the chain length induces the intermediate mesh phase. A variety of intermediate phases, such as ribbon, ordered mesh and bi-continuous cubic, have been seen in the sodium dodecylsulphate (SDS)-water system, albeit over very narrow ranges of composition.

Worm-like micelles that occur most frequently upon increasing the concentration of the surfactant or of an added salt, or in the presence of specific counterions. These micelles can be cross-link into a network and break and reform spontaneously or under stress, and so are often called 'living polymers' [49].

In many systems the isotropic (L_3) sponge phase observed in narrow phase regions adjacent to the domain of stability of the L_α phase [50]. Sponge phase exhibits no long range order and consists of one extended bilayer in a convoluted morphology, which is randomly interconnected throughout space and divides the sample volume into two equivalent strongly interwoven subvolumes (Fig. 1.9B). The relative stability of the isotropic L_3 and L_α structures depends critically on the membrane flexibility which can be tuned by varying temperature, electrolyte concentration, and co-surfactant surfactant ratio. The confinement of a sponge phase between two rigid macroscopic walls of a surface forces apparatus can lead to a first-order transition to a lamellar phase [51].

1.3 Theory of X-ray diffraction

X-rays are transverse electromagnetic radiation with wave length in the range (∼0.01-10nm), lying between ultraviolet (UV) and gamma radiation. They are scattered by the electrons in the irradiated material. Therefore, the intensity of scattered radiation depends upon the electron density distribution in the material. The interference of x-rays scattered by different electrons gives rise to the observed diffraction pattern [52]. Therefore, we consider only coherent, elastic scattering events.

Let us consider a monochromatic planar wave incident on a point scatterer, such as an electron, sitting at the origin. It can be written as, [53]

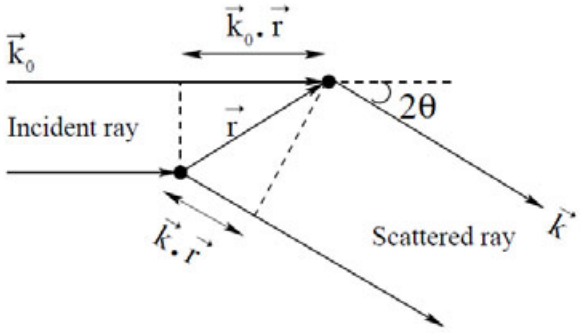

FIGURE 1.12: Geometric arrangement of scattering event from two scattering centers separated by a distance r.

$$\phi_{in} = \phi_o e^{i\vec{k_o}\vec{r}} \tag{1.5}$$

where ϕ_o is the amplitude of the plane wave with wave vector $\vec{k_o}$. The amplitude of the scattered spherical wave at a distance R can be written as,

$$\phi_{sc} = \frac{\phi_o a}{R} e^{ikR} \tag{1.6}$$

where a is the 'scattering length', which determines the strength of scattering. Now consider another electron at a distance r from the first one (Fig. 1.12). The

phase difference between the rays scattered by the two electrons can be expressed as $(\vec{k} - \vec{k_o}) \cdot \vec{r}$ where $\vec{k}$ is the wave vector in the direction of scattering. $\vec{q} = \vec{k} - \vec{k_o}$ is known as the scattering vector and its magnitude is given by $|\vec{q}| = (4\pi \sin\theta)/\lambda$, where 2θ is the scattering angle between $\vec{k}$ and $\vec{k_o}$. The amplitude of the scattered wave at R (>> r) where the scattered rays can be treated as parallel is given by,

$$\phi_{sc} = \frac{\phi_o a}{R} e^{i(kR - \vec{q}\cdot\vec{r})} \tag{1.7}$$

For an assembly of N scatterers at $\vec{r_n}$ (n= 1, 2, 3, . . . N), the above expression can be summed up to get the total amplitude of the scattered beam.

$$\phi_{tot} = \frac{\phi_o a}{R} e^{ikR} \sum_{n=1}^{N} e^{(-i\vec{q}\cdot\vec{r_n})} \tag{1.8}$$

For a material of electron density

$$\rho(\vec{r}) = \sum_{n} \delta(\vec{r} - \vec{r_n}) \tag{1.9}$$

the above equation can be modified to

$$\phi_{tot} = \frac{\phi_o a}{R} e^{ikR} \int \rho(\vec{r}) e^{(-i\vec{q}\cdot\vec{r})} d\vec{r} \tag{1.10}$$

This expression shows that the amplitude of the scattered wave is proportional to the Fourier transform of the electron density function of the scattering medium. The expression is derived based on the assumption that multiple scattering from the medium is negligible. The intensity of scattered radiation is the square of its amplitude and hence is given by,

$$I(q) = |\phi_{tot}|^2 = |\frac{\phi_o a}{R} e^{ikR} \int \rho(\vec{r}) e^{(-i\vec{q}\cdot\vec{r})} d\vec{r}|^2 \tag{1.11}$$

In the following chapters of this thesis x-ray diffraction technique has been used to identify various lyotropic liquid crystalline phases. For such periodic structures, the electron density $\rho(\vec{r})$ can be written as the convolution of a lattice function $\rho_l(\vec{r})$, describing the periodic lattice, and a basis function $\rho_b(\vec{r})$, describing the electron density within each unit cell.

$$\rho(r) = \rho_l(\vec{r}) \otimes \rho_b(\vec{r}) \tag{1.12}$$

Since the Fourier transform of the convolution of two functions is the product of their Fourier transforms, from Eq. (1.12) we get,

$$\int \rho(r) e^{(-i\vec{q}\cdot\vec{r})} d\vec{r} = \int \rho_l(\vec{r}) e^{(-i\vec{q}\cdot\vec{r})} d\vec{r} \int \rho_l(\vec{r}) e^{(-i\vec{q}\cdot\vec{r})} d\vec{r} = F_l F_b \tag{1.13}$$

where $\mathrm{F}_l(\vec{q})$ and $\mathrm{F}_b(\vec{q})$ are the Fourier transforms of the lattice and basis functions, respectively. From Eq. (1.11) the scattered intensity can be expressed as,

$$I(q) \sim |F_l(\vec{q})|^2 |F_b(\vec{q})|^2 = S(\vec{q}) f(\vec{q}) \tag{1.14}$$

Here $S(\vec{q}) = |F_l(\vec{q})|^2$, called the 'structure factor', determines the points in the reciprocal lattice, and $f(\vec{q}) = |F_b(\vec{q})|^2$, the 'form factor' determines the intensity at these points. For an infinite 3-D lattice defined by the crystallographic unit vectors $\vec{a}$, $\vec{b}$ and $\vec{c}$, the lattice function will be a 3D array of δ functions, given by [54],

$$\rho_l(\vec{r}) = \sum_{m,n,p} \delta(\vec{r} - [m\vec{a} + n\vec{b} + p\vec{c}]) \tag{1.15}$$

where m, n and p are integers. The Fourier transform of this function is,

$$F_l(\vec{q}) = \sum_{h,k,l} \delta(\vec{q} - [h\vec{a^*} + k\vec{a^*} + l\vec{c^*}]) \tag{1.16}$$

where a*, b* and c* are the basis vectors in the reciprocal lattice and h, k and l are integers. Finally the scattered intensity can be written as,

$$I(q) \sim \frac{1}{(\vec{a}.(\vec{b} \times \vec{c}))^2} |F_b(\vec{q})|^2 | \sum_{h,k,l} \delta(q - [h\vec{a^*} + k\vec{a^*} + l\vec{c^*}])|^2 \tag{1.17}$$

From this expression, it can again be seen that the diffraction pattern of an infinite lattice is another infinite 3D lattice. The position of the diffraction peaks are determined by the Miller indices (hkl) and their intensities by the value of the form factor at these reciprocal lattice points.

1.3.1 Polarization, Geometric and Multiplicity corrections to the Intensity

The scattered intensity from a sample is affected by certain factors, that depend on the scattered angle, nature of the sample and the type of the detector used for the experiment. Therefore, the observed intensities have to be corrected for these effects before they can be put on a relative scale. The corrected scattered intensity is given by,

$$I(q) = Ap(q)g(q)I_o(q) \tag{1.18}$$

where A is a q independent scale factor, p is the polarization factor, g is the geometric factor and I_o is the observed intensity.

The polarization factor,

$$p = \frac{1}{1 + cos^2(2\theta)}$$

and arises from the fact that the incident x-ray beam is unpolarized while scattered x-ray beam is polarized [54].

$$cos(2\theta) \sim 1$$

in the small angle region and hence, this correction can be ignored for small angle scattering.

The geometric factor depends both on the type of the sample and geometry of the detector used to record the data. In case of unoriented samples, the scattered intensities corresponding to each peak is distributed over a spherical shell of radius q. If the detector used to collect the data, is one dimensional (1D) such as a position sensitive detector (PSD), then the observed intensity has to be multiplied by a factor $4\pi q^2$; the area of the shell, in-order to get the total intensity, because 1D detector intersect the spherical shell at two points. On the other hand, a 2D detector, such as image plate, cuts the spherical shell along a plane, resulting in a ring. If the observed intensities are integrated over these then they have to further multiplied by q to get the total intensity.

In-order to construct the electron density map from the diffraction data, intensities of the peaks corresponding to the different lattice planes have to be calculated, this requires an additional correction factor called the multiplicity factor along with the above mentioned intensity corrections. In the case of unoriented samples, reflections from equivalent lattice planes can overlap, at the same value of q in the diffraction pattern. The observed intensity has to be scaled (divided) by a multiplicity factor to get the intensity of any one of the overlapping peaks, corresponding to a particular lattice plane. The multiplicities are lower in lower symmetry systems and very high in highly disordered systems. For example, the peaks corresponding to the lattice planes (100), (010), (001), $(\bar{1}00)$, $(0\bar{1}0)$ and $(00\bar{1})$ from a cubic lattice overlap in the diffraction pattern of unoriented samples. Therefore, we have to divide the intensity by 6 to obtain the intensity of the (100) peak.

1.3.2 Experimental setup

The experimental set up used for x-ray diffraction studies is shown in figure 1.13. X-rays were produced from a rotating anode x-ray generator (Rigaku, UltraX

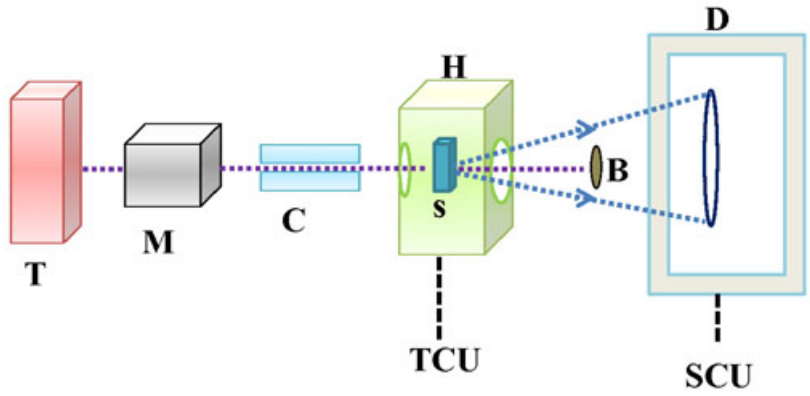

FIGURE 1.13: Schematic of the experimental set up used for x-ray diffraction study. T, M, C, H, B, S, D, TCU and SCU denotes the x-ray generator, monochromator, collimator, the heater, beam-stop, sample, detector (image plate), temperature control unit, and the scanning control unit respectively. The dashed violet and blue lines represents the incident and scattered rays respectively.

18) operating at 50 kV and 80 mA. CuK_α radiation of wavelength 0.154 nm was selected using a multilayer focusing mirror (Xenocs). The sample taken in a glass capillary (Hampton Research, outer diameter 0.5 to 1mm, wall thickness 0.01 mm) was placed in a locally built temperature controlled heater with a stability of 0.1 K. Experiments were carried out in the temperature range (25°C to 90°C). The data were collected using an image plate (Marresearch, diameter 80mm). The sample to detector distance varied from 200mm to 350mm. Typical exposure time was 30minutes to one hour.

We have also used the S3-Micro small angle scattering system (Hecus). In the SAXS S3-Micro system, we used mainly a 1-dimensional position sensitive detector (PSD), the sample to detector distance(D) was fixed at $\sim$ 265mm and was calibrated using the first order diffraction peak of the lamellar structure of silver behanate which has a spacing of 5.838nm. This system has a built-in temperature controller, which has a range from -20°C to 120°C. Typical exposure time was 20minutes.

1.4 Polarizing optical microscopy (POM)

Polarizing optical microscopy is widely used to identify different liquid crystalline phases [55]. Liquid crystalline phases are birefringent and show characteristic textures between crossed polarizers under an optical microscope, which arise due to the defects in the medium. These defects create deformations in the medium over length scales of the order of tens of micrometers due to the low elastic constants of the system. Since, the type of defect in the medium is determined by the symmetry of the structure, the textures resulting from these defects are characteristic of the phase. Therefore, these textures can be used as fingerprints to identify different liquid crystalline phases as discussed in the last section.

As an example, we shall briefly discuss the defects and corresponding texture in a nematic liquid crystal. Nematic phase is characterized by long range orientational order and short range positional order. Orientational ordering in the medium is described in terms of an apolar unit vector, called the director($\vec{n}$).

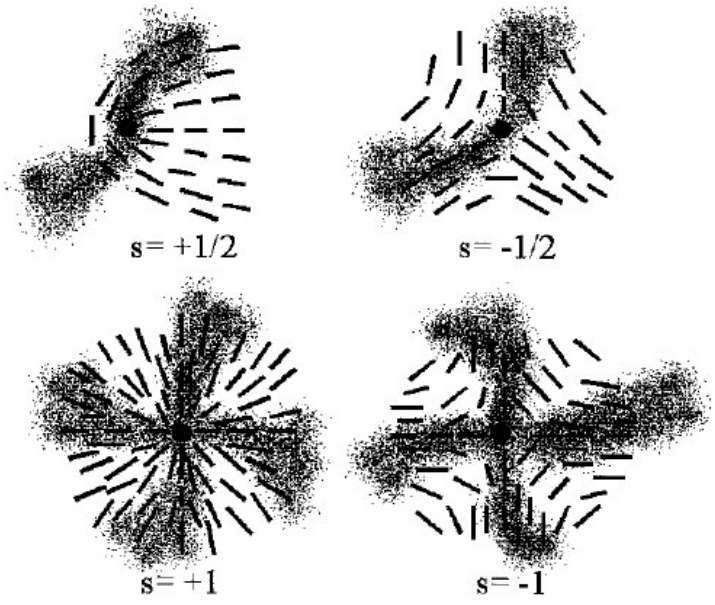

FIGURE 1.14: Director configurations in the vicinity of defect lines observed in nematic Schlieren textures (from ref. [60]).

Nematics between untreated glass plates often orient with their director parallel to the substrates. If this orientation is not homogeneous, but varies slowly in the plane of the substrate, so-called Schlieren textures [56–58] are observed between crossed polarizers (Fig. 1.15). Schlieren textures exhibit characteristic sets of often curved dark brushes. These correspond to the extinction position of the nematic director field, with $\mathrm{n}(\vec{r})$ coinciding with the direction of either the polarizer or the analyzer. A closer look reveals that the brushes come together in a singular point and can be twofold or fourfold [59]. The singularities are topological defects, called disclinations, which are assigned a certain strength s. The absolute value of the strength of the disclination is obtained by dividing by four the number of brushes cutting a 2π circle around the center, i.e. $|s|=$ number of brushes/4. The sign of the defect strength can be obtained by rotation of the polarizers: the defect is assigned a plus (+) sign if the dark brushes rotate in the same direction as the polarizers, and a minus (-) sign if they rotate in the opposite direction. Note that in any case the point singularities do not move and the rotation of the brushes is continuous, due to a continuous variation of the director field $\mathrm{n}(\vec{r})$. Experimentally, only $\mathrm{s}\pm\frac{1}{2}$ and $\mathrm{s}\pm1$ defects are observed for nematic liquid crystals. Twofold and fourfold singularities, also of different sign, generally occur simultaneously in the same sample. The corresponding director configurations are schematically shown in figure 1.14 as a top view on the substrate plane.

If the disclination lines make a large angle with the direction of observation they give rise to the 'threaded' texture. These disclination lines either form closed loops in the medium or end at the surfaces. In fact these thread-like structures are responsible for the name nematic [58, 61].

1.4.1 POM set-up

A typical setup of a polarizing optical microscope is shown in figure 1.16. It consists of a light source, which is generally a halogen lamp emitting white light with a wavelength characteristic provided by the producer. The light is reflected upwards by a mirror, passes through a lens, and is linearly polarized by a polarizer, which

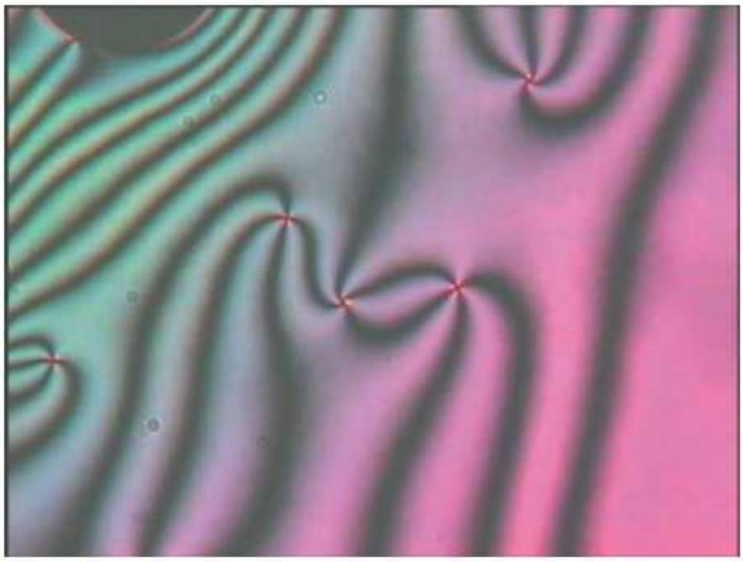

FIGURE 1.15: Typical Schlieren texture of nematic phase (from ref. [60]).

can often be rotated by 360°. The condenser collects the light from the light source and assures a uniform illumination of the sample. For this, the aperture iris must be adjusted correctly. Additionally, the distance between the condenser and the sample has to be adjusted to focus the light beam correctly and to assure proper illumination. Microscopes for liquid crystal research are generally equipped with a rotatable stage onto which a hot stage, containing the sample, can be securely mounted, to assure a precise rotation of the sample in a plane perpendicular to the direction of light propagation. The transmitted light then passes into the objective. This is another fundamental part of the microscope, as it crucially determines the quality of the image. After passing through the objective, the light passes through the analyzer, a second polarizer that is often rotatable by 360° and is also removable. For texture studies the analyzer is usually oriented at right angles to the polarizer, i.e. with no birefringent sample present, the field of view is black. The ocular or eyepiece serves to magnify the image further. Often a magnification of 10x is used. The ocular also determines the field of view. Alternatively, after opening a shutter or by use of a semi-transmitting mirror, the image can also be projected onto a camera mounted on the microscope.

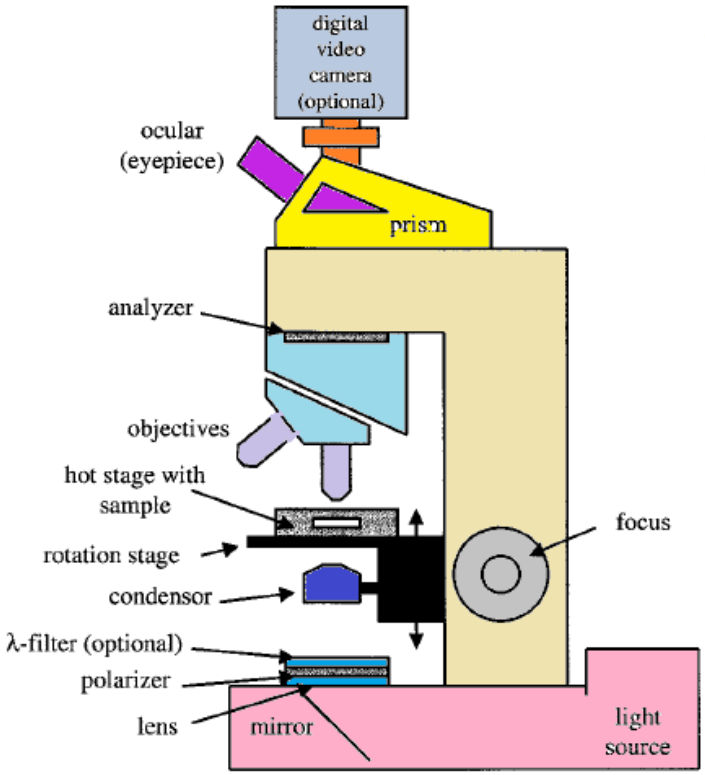

FIGURE 1.16: Schematic setup of a polarizing optical microscope as used for texture studies of liquid crystalline phases (from ref. [60]).

1.5 Cryo-SEM Technique

Cryogenic scanning electron microscopy (cryo-SEM) is a powerful tool for characterizing the microstructure of liquid containing specimens, which are ordinarily unstable in the high vacuum of the electron microscope. Cryo-SEM is widely used to explore the hydrated microstructures of biological specimens [62–64], and is finding increasing application in materials science [65–69]. For example, the technique has been used to investigate microstructures of concentrated ceramic particle suspensions [65], microstructures of self-assembled organic hydrogels [66], distributions of polymer nanoparticles on fractured surfaces of bitumen/polymer blends [67, 68], and distributions of silica nanoparticles in an immiscible polymer blend [69]. In these studies, cryo-SEM provided direct evidence of colloidal structures.

1.5.1 Cryo-SEM set-up

The experimental set up used for cryo-SEM studies is the scanning electron microscope (ZEISS, ULTA PLUS) fitted with the cryo preparation system (PP3000T, from Quorum Technologies). The details of the experimental procedure is given below.

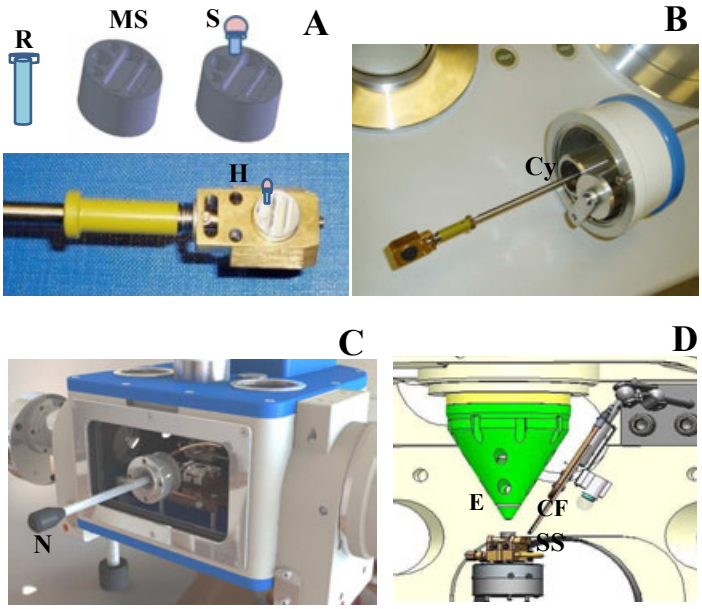

FIGURE 1.17: Schematic setup of cryo-SEM: (**A**) R-rivet, MS-master stub, S-sample is taken inside the rivet which in turn is kept in the master stub H is the sample holder (**B**) Cy-cylindrical container to accommodate the sample holder after cryo-freezing the sample, (**C**) Preparation chamber; N-knife to fracture the sample and (**D**) SEM chamber; SS-sample stage, CF-cold finger (cold traps) and E-aperture for electron beam (from ref. [70]).

The material is fixed on a holder inside the rivet with a layer of carbon-rich conductive glue (to allow discharge of electrons) (Fig. 1.17). It is rapidly frozen with liquid nitrogen or 'nitrogen slush'. The holder with frozen material held under liquid nitrogen is to be coupled to a rod and pulled back into a small cylindrical container. This has been done to transfer the sample to the high vacuum cryo-unit and prevent contamination with gas particles while sliding the sample into the cryo-chamber. At all stages of the procedure the specimen is maintained at a temperature typically lower than -160°C. The cryo-chamber was equipped with a knife that can be handled from outside to fracture the sample. Humidity from

the sample is sublimated and then sample fractured by using cold knife. Thin layer of platinum is sputtered on the material, for good conductance of electrons. Finally the entire or fractioned material is inserted into the observation chamber with a rod. To ensure contamination by ice is eliminated, cold traps are located close to the cold stages in the SEM, and are typically maintained at close to liquid nitrogen temperature (-190°C).

Image formation in SEM is dependent on the acquisition of the signal produced from the electron beam and specimen interactions. These interactions can be divided in to two major categories: elastic scattering and inelastic scattering. Inelastic scattering occurs through a variety of interactions between the incident electrons and electrons and atoms of the sample and result in the primary electron beam transferring substantial energy to the atoms in the sample. As a result, the excitation of the specimen electrons during the ionization of the specimen atoms leads to the generation of mainly secondary electrons (SE) and many other signals, including the emission of characteristic x-rays, Auger electrons and cathode luminescence. On other other hand, elastic scattering results from the deflection of the incident electron by the specimen atomic nucleus or outer shell electrons without changing its energy. Incident electrons that are elastically scattered through an angle more than 90° are called back scattered electrons (BSE).

Analysis of characteristic x-rays provides chemical information and is the most widely used microanalytical technique in SEM. Detection of BSE, provides both compositional and topographic information in SEM. On other hand, SE is used principally for topographic contrast in SEM i.e. for the visualization of surface texture and roughness. SE images have better lateral resolution over BSE images. In cryo-SEM studies electron beam of energy ranging from 0.4 to 1keV has been used to irradiate the sample and secondary electrons (SE) were collected by using in-lens detector which gives rise to resolved surface structures. Cryo-SEM micrograph of the lamellar phase of the DDAB-Water system is shown in figure 1.18. The details of the experimental parameters are on the image.

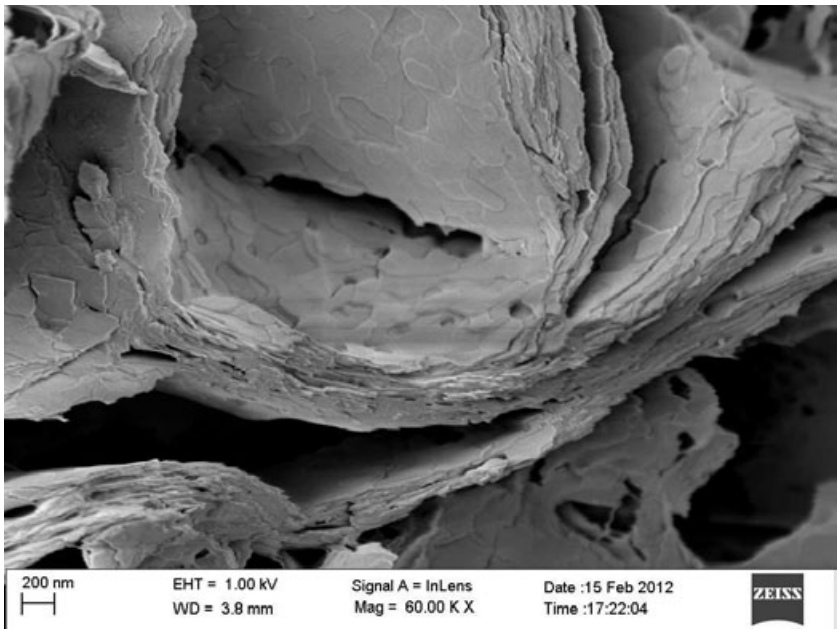

FIGURE 1.18: Typical cryo-SEM micrograph of lamellar (L_α) phase.

1.6 Characterization of lyotropic liquid crystalline phases

In this section we briefly describe the characterization of some of the commonly observed lyotropic liquid crystalline phases using polarizing optical microscopy and x-ray diffraction.

1.6.1 Nematic phase

Lyotropic nematic phases is usually located between the well ordered phases (lamellar, hexagonal) and the completely disordered (micellar solutions). The calamitic (N_c) phase is formed by rod-like micelles and occur close to the hexagonal phase. The discotic (N_d) phase is formed by disc-like micelles and occur close

to the lamellar phase. In the N_c phase there is long-range correlation in the orientation of the long axes of the rods, whereas in the N_d phase there is long-range correlation in the orientation of the normal to the discs. Under crossed polarizers, this phase exhibits, either a schlieren or thread-like texture (Fig. 1.19). In the N_d phase disc-like micelles naturally align parallel to the substrates and gives rise to large pseudo isotropic regions, on the other hand the N_c phase consisting of rod-like micelles naturally orient with their long axis parallel to the glass substrates and exhibit planer texture.

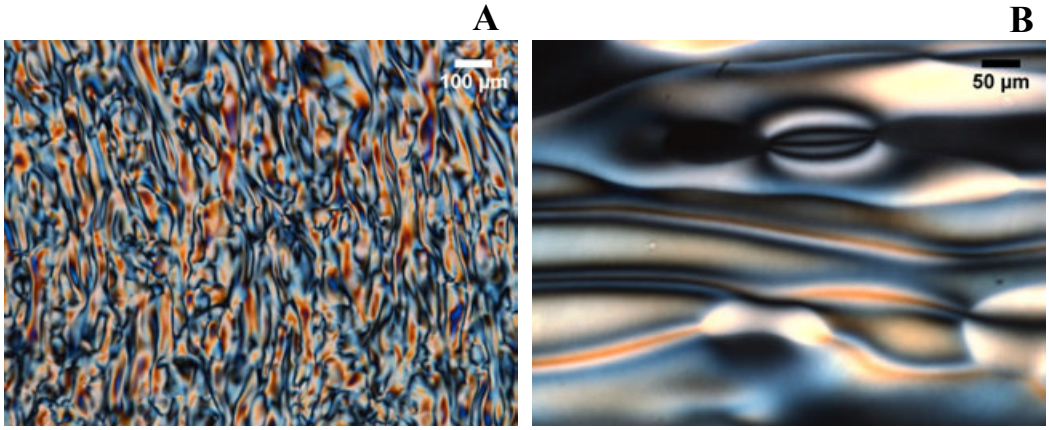

FIGURE 1.19: Polarizing optical microscopy texture of nematic phase: (**A**) schlieren texture in the N_c phase and (**B**) schlieren texture along with homeotropic region in the N_d phase

When the nematic phase is subjected to homeotropic boundary conditions the director orients perpendicular to the substrates. In this case the direction of light propagation coincides with the optic axis of the phase. Rotation of the sample does not produce any change in color or intensity. This is called the pseudo-isotropic texture, because the sample appears like the isotropic phase. To distinguish between the real isotropic and the pseudo-isotropic texture of the nematic phase, one can gently press on the top glass substrate. In doing so, a bright flash will appear in the case of the nematic phase, due to mechanical reorientation of the director and therefore also the optic axis.

There are two length scales associated with a nematic phase. One corresponds to the 'face to face' separation (d_1) of the micelles along the nematic director and

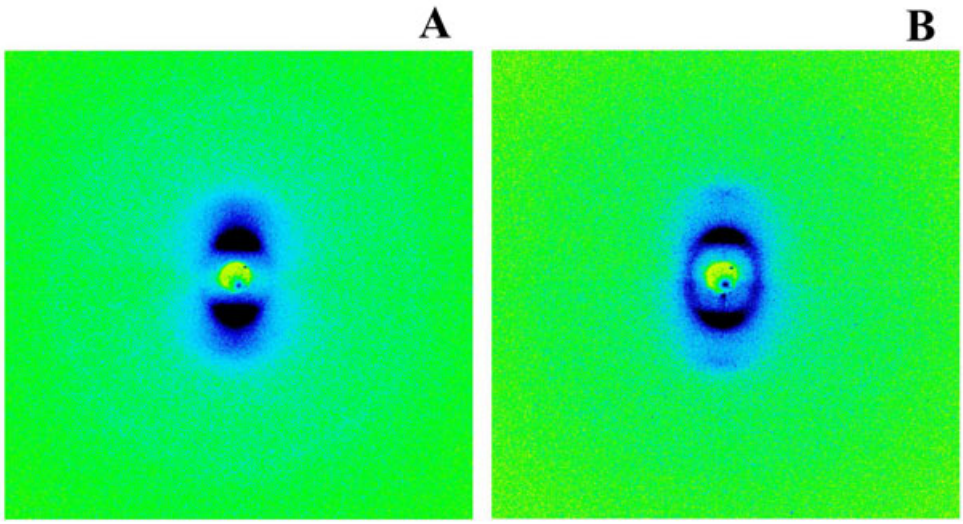

FIGURE 1.20: Typical diffraction pattern of nematic phases (**A**) N_c and (**B**) N_d.

other related to the 'side by side' separation (d_2) in the plane perpendicular to the director. X-ray scattering pattern of a single domain sample shows two sets of broad reflections on a 2-D detector which are perpendicular to each other and corresponding to these two length scales. These broad peaks, reflect the short range positional order in the system. Peak related to separation d_2 in the N_c phase is sharper than the one corresponding to d_1; the d_1 peak is usually very broad in these systems due to the highly poly-disperse length distribution of the rod-like micelles. d_1 peak in N_c and d_2 peak in N_d appear in the very small angle region due the larger dimension of these aggregates along these directions. Therefore, very often, only the d_2 peak is observed from a N_c phase (along with a very diffuse peak with spacing $d_2/\sqrt{3}$, due to short-range hexagonal order of the rod-like micelles), and the d_1 (along with a very diffuse peak with spacing $d_1/2$, due to short-range lamellar order of the disc-like micelles) from a N_d phase. Typical diffraction patterns of the N_c and N_d phase are shown in figures 1.20A and B, respectively.

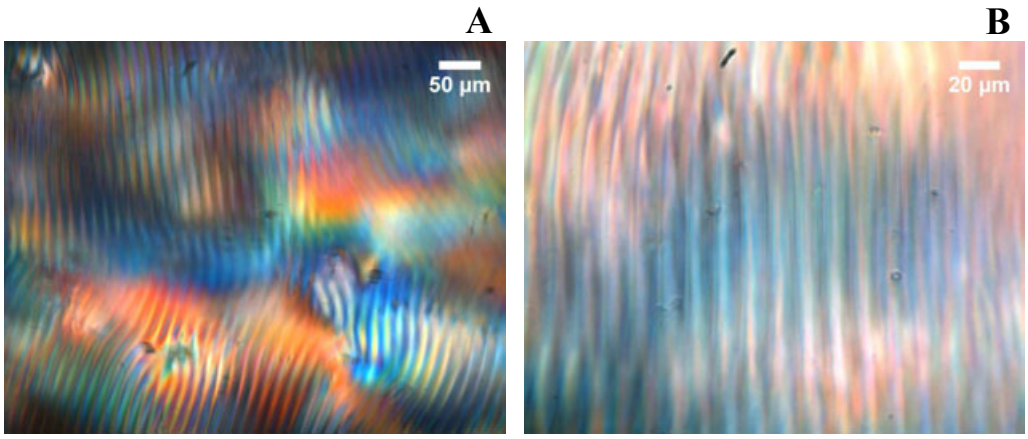

FIGURE 1.21: Typical fingerprint texture of cholesteric N_c phase.

1.6.2 Cholesteric phase

In cholesterics, the typical length scale of the pitch is of the order of micrometers. Between crossed polarizers, a film of cholestric presents the fingerprint texture (Fig. 1.21).

1.6.3 Hexagonal phase

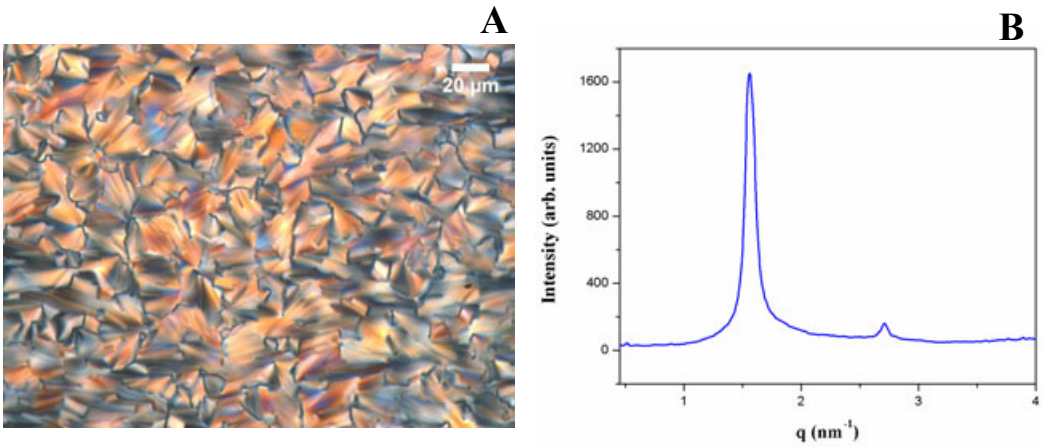

FIGURE 1.22: Characterization of 2D hexagonal phase: (**A**) 'Fan-like texture' and (**B**) x-ray diffraction pattern showing two peaks with q in the ratio 1:$\sqrt{3}$.

This phase consists of long cylindrical aggregates arranged on a 2D hexagonal lattice. Two types of lyotropic hexagonal phases have been reported in the literature,

direct (H_I) and inverted (H_{II}) hexagonal phases. The viscosity of the hexagonal phase is much larger than of the lamellar phases.

Small-angle X-ray diffraction patterns of hexagonal phase present Bragg peaks, with their scattering vector (q) values in the ratios $1{:}\sqrt{3}{:}\sqrt{4}{:}\sqrt{7}$..., which corresponds to the (1 0), (1 1), (2 0), (2 1)...planes of a hexagonal two-dimensional lattice (Fig. 1.22B). At high q, the diffraction pattern shows a typical band due to the mean distance between the carbon chains (∼0.5 nm). This phase shows a typical fan-like texture (Fig. 1.22A) under a polarizing optical microscope.

1.6.4 Lamellar phase

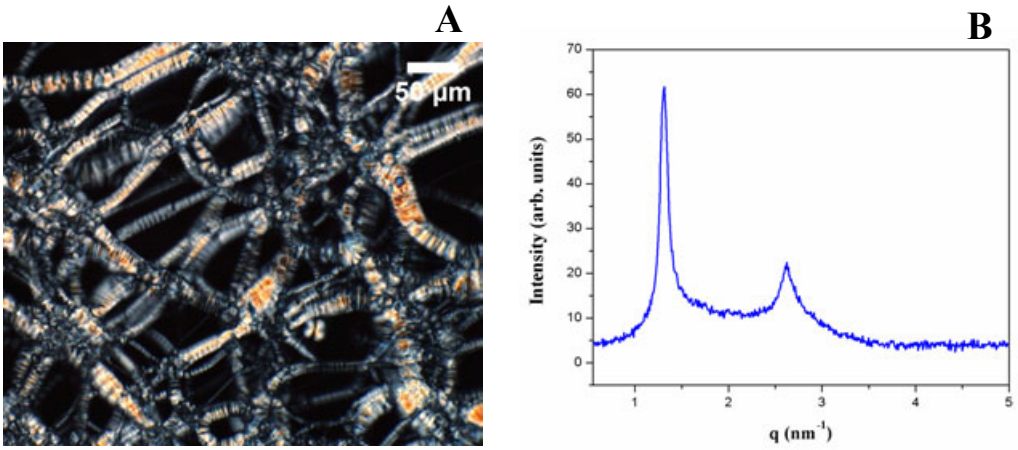

FIGURE 1.23: Characterization of lamellar phase: (**A**) 'oily streak' texture and (**B**) x-ray diffraction pattern showing two peaks with q in the ratio 1:2.

Lamellar phase is one of the commonly observed phase in lyotropic systems. The structural unit of the lamellar phase is the bilayer. The bilayers are stacked periodically alternating with water layers. In the fluid lamellar (L_α) phase the hydrocarbon chains of the amphiphiles are molten and the in-plane order within each bilayer is liquid-like. Like all the anisotropic phases, lamellar phases exhibit distinct optical textures, when confined in a thin slab between crossed polarizers and viewed through an optical microscope, reflecting the type of defects in the medium. Focal conics texture is often seen in the system. In the case of dilute lamellar phases the bilayers have a strong tendency to orient parallel to the bounding surfaces, which

produces a pseudo-isotropic texture with birefringent oily streaks separating the dark regions (Fig. 1.23A). In some cases, when lamellar phase coexists with excess water, bilayers normally curl up into multilamellar vesicles and show characteristic maltese-cross texture.

Diffraction pattern of the lamellar phase consists of a set of reflections in the small angle region, with their q values in the ratio 1:2:3:4..., which is characteristic of a one dimensional crystal (Fig. 1.23B). L_α shows a broad peak in the wide angle region (∼0.5nm) corresponding to the hydrocarbon chain-chain separation. The repeating distance (sum of the bilayer and water layer thickness) $d=2\pi/q_o$, where q_o is the position of the first peak.

1.6.5 Intermediate phases

Intermediate phases in lyotropic systems provide a topological link between the hexagonal and lamellar phases. Here we shall discuss the experimental identification of ribbon phase, random and ordered mesh phases and also of bi-continuous cubic phases which we will come across in different chapters of this thesis.

1.6.5.1 Ribbon phase

Ribbon phases consist of long micelles with roughly elliptical cross-section, ordered on a two-dimensional rectangular lattice. This phase is birefringent. Unoriented samples of the R phase, between crossed polarizers, present a mosaic-like texture with many pseudo-isotropic regions (Fig. 1.24A). X-ray diffraction patterns of these phases show a number of sharp peaks which can be indexed on a rectangular lattice (Fig. 1.24B). Two types of structures have been reported, corresponding to the plane groups cmm and pgg.

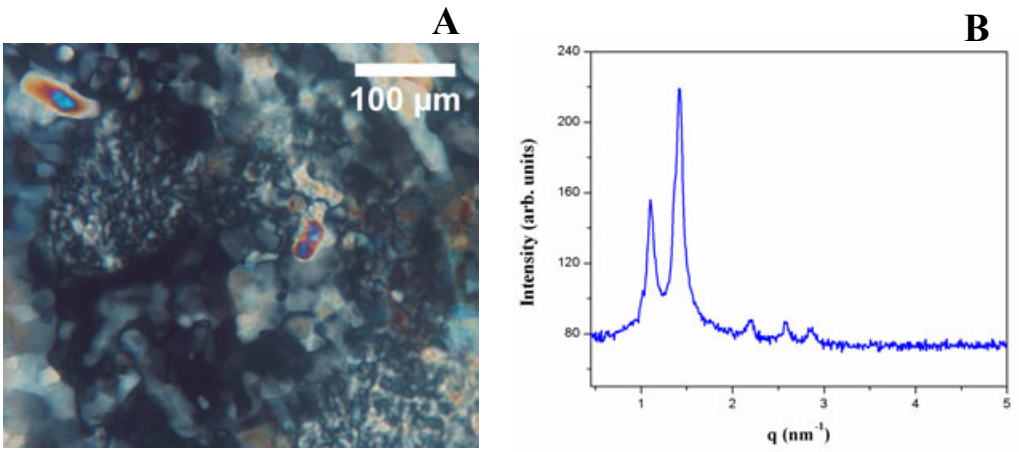

FIGURE 1.24: Characterization of ribbon phase: (**A**) 'mosaic texture' along with 'homeotropic' region and (**B**) x-ray diffraction pattern showing many reflections that can be indexed on a 2D lattice of space group cmm.

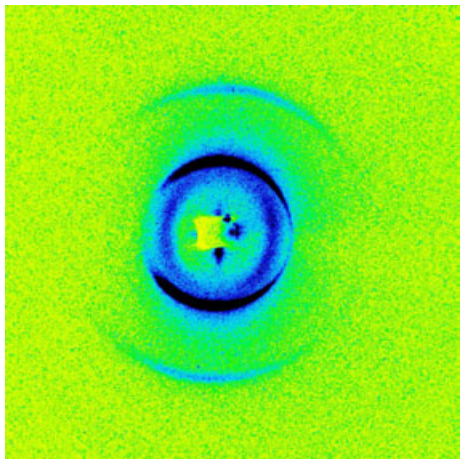

FIGURE 1.25: Typical diffraction pattern of random mesh phase. The horizontal diffuse spots arise from structural inhomogeneities in the amphiphilic bilayers

1.6.5.2 Mesh phases

Mesh phases are structurally very similar to the classical lamellar phase, since they consist of stacked surfactant bilayers. However, they possess water-filled pores within the bilayers. Mesh phase are two of types; Random mesh phase and ordered mesh phase.

In the random mesh phase, the positions of the pores are uncorrelated between and within the layers. Due to their lamellar structure, they show textures similar

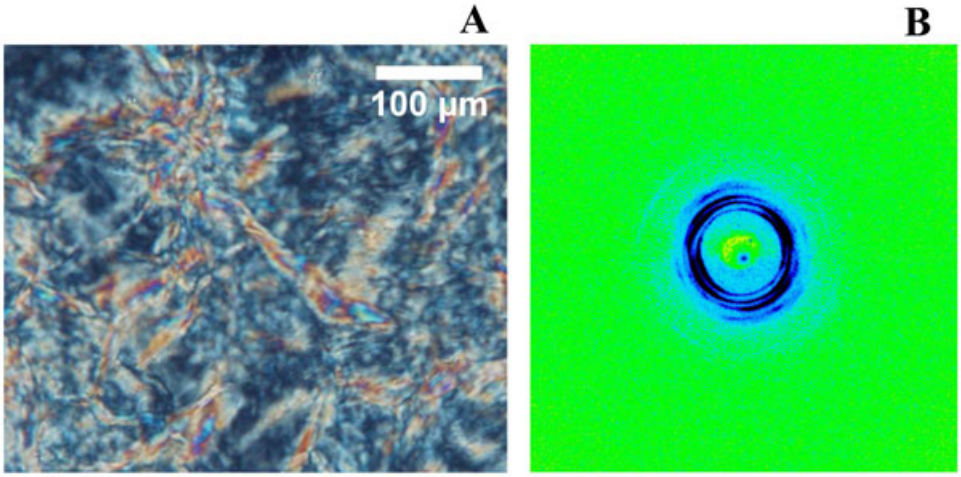

FIGURE 1.26: Characterization of ordered mesh phase: (**A**) mosaic texture along with homeotropic region and (**B**) x-ray diffraction pattern showing many reflections that can be indexed on a 3D lattice of space group R$\bar{3}$m.

to those of regular lamellar phases with continuous bilayers. The random mesh phase can be distinguished from a lamellar phase consisting of regular bilayers by the presence of an additional diffuse peak in the small angle region of the X-ray diffraction pattern (Fig. 1.25). Diffraction patterns of oriented samples show that the diffuse peak occurs in a direction normal to that along which the set of peaks corresponding to the lamellar periodicity appears, indicating that the former indeed arises from in-plane inhomogeneities with short-range positional correlations.

In the ordered mesh phases the mesh-like aggregates lock into a three-dimensional lattice. This phase exhibits typical mosaic texture under POM, which often contains pseudo isotropic-regions (Fig. 1.26A and 1.27A). This texture is quite different from that observed in random mesh phase, reflecting the change in order in the system. Diffraction pattern of the ordered mesh phase shows many reflection corresponding to the 3D structure of the system (Fig. 1.26B and 1.27B). Structure of the phase can be deduced from the positions of peaks by indexing it on a suitable lattice. For example, the diffraction patterns shown in figures 1.26B and 1.27B correspond to space groups R$\bar{3}$m and I4mm, respectively. All known structures of ordered mesh phases are either rhombohedral (Rh) (space group: R$\bar{3}$m)

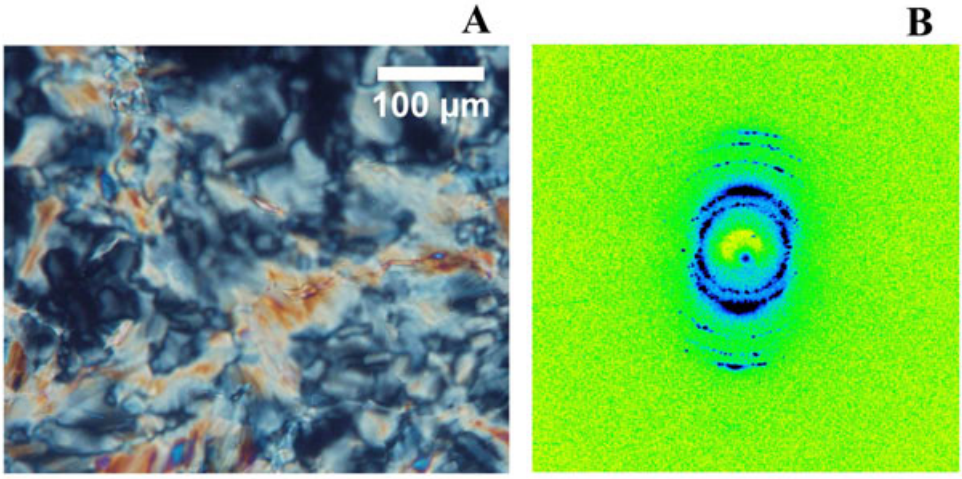

FIGURE 1.27: Characterization of ordered mesh phase: (**A**) mosaic texture along with homeotropic region and (**B**) x-ray diffraction pattern showing many reflections that can be indexed on a 3D lattice of space group I4mm.

or tetragonal (T) (space group: I4mm). The former consists of a 3 layer stacking of 3-coordinated hexagonal mesh, whereas the latter has a 2-layer stacking of 4-coordinated square mesh.

1.6.5.3 Cubic phase

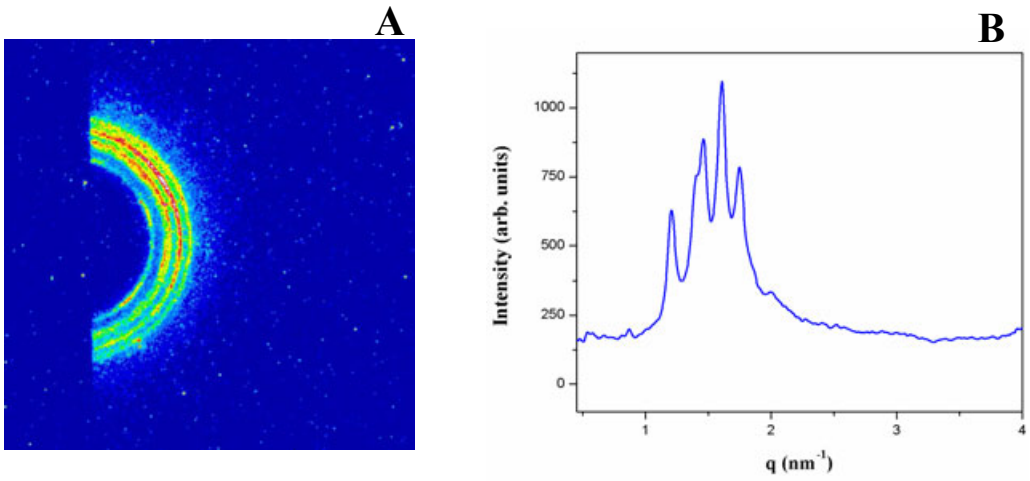

FIGURE 1.28: Typical diffraction pattern of the cubic phase. X-ray diffraction pattern showing many reflections that can be indexed on a 3D lattice of space group Pn3m.

Cubic micellar phases are not so commonly observed in lyotropic mixtures. But bi-continuous cubic phases are usually observed in narrow regions of the phase diagrams, between lamellar and hexagonal phases. Cubic phases, can be easily identified by the fact that they are optically isotropic, unlike all other phases found at comparable surfactant concentrations, which are birefringent. However, they show little flow birefringence. Diffraction patterns of these phases consist of many peaks which could be indexed on a cubic lattice and the space group symmetry of the structure can be deduced from the systematic absence of certain peaks. For example, the diffraction pattern shown in figure 1.28 corresponds to the space group Pn3m. Cubic bi-continuous structures with space groups Ia3d, Im3m, and Pn3m have been reported in lyotropic systems.

1.6.6 Sponge phase

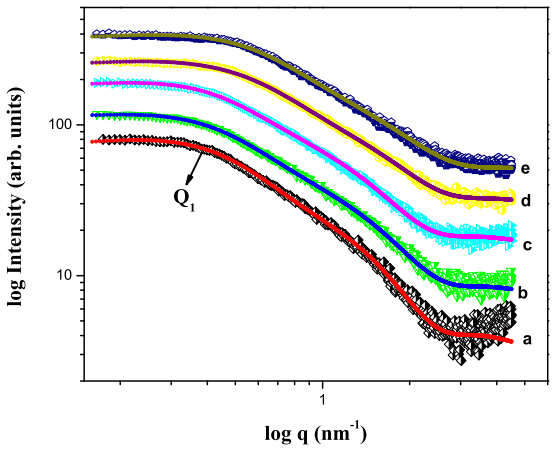

FIGURE 1.29: Typical diffraction pattern of sponge phase. Q_1, the position of the broad structure peak, corresponds to the characteristic size of the cell.

Sponge (L_3) phase exhibits isotropic texture under polarizing optical microscopy. However, it shows flow birefringence due to flow induced alignment. The diffraction pattern of the L_3 phase, at larger q is characteristic of the scattering from randomly oriented discs. However, in the small q range, it shows a broad peak, which

corresponds to a characteristic distance (Fig. 1.29), related to the average size of the cell, with short range positional ordering.

1.7 X-Ray Data Analysis

1.7.1 Lamellar (L_α) phase

Diffraction data of the lamellar (L_α) phase were analyzed using the procedure described by Pabst et al. [71]. The scattered intensity is given by

$$I(q) = \frac{S(q)|F(q)|^2}{q^2} + \frac{N_d|F(q)|^2}{q^2} \tag{1.19}$$

where S(q) is the structure factor and F(q) is the form factor of the bilayers. F(q) is given by the Fourier transform of the bilayer electron density profile ρ(z), which is described by two Gaussians, representing the head-groups, of width σ_h centered at z=$\pm z_h$, and a third Gaussian of width σ_c at the bilayer center(z=0) representing the terminal methyl groups,

$$\rho(z) = \rho_{CH_2} + \bar{\rho_h}[exp(-\frac{(z-z_h)^2}{2{\sigma_h}^2}) + exp(-\frac{(z+z_h)^2}{2{\sigma_h}^2})] + \bar{\rho_c}[exp(-\frac{z^2}{2{\sigma_c}^2})] \tag{1.20}$$

where the electron densities of the head group ρ_h and hydrocarbon tails ρ_c are defined relative to the methylene electron density ρ_{CH_2}. This leads to the form factor

$$F(q) = 2\sqrt{2\pi}\sigma_h\bar{\rho_h}[exp(-\frac{{\sigma_h}^2q^2}{2})]cos(qz_h) + \sqrt{2\pi}\sigma c\bar{\rho_c}[exp(-\frac{{\sigma_c}^2q^2}{2})] \tag{1.21}$$

The last term in eq. 1.19 is due to diffuse scattering from uncorrelated bilayers. According to modified Caille theory S(q) is given by [72]

$$S(q) = N + 2\sum_{k=1}^{N-1}(N-k)cos(qkd) \times e^{-(d/2\pi)^2q^2\eta\gamma}\pi k^{-(d/2\pi)^2q^2\eta} \tag{1.22}$$

where N is the mean number of coherent scattering bilayers in the stack, γ is the Euler's constant, and d the lamellar periodicity. The Caille parameter $\eta = q^2kBT/(8\pi\sqrt{KB})$, where K and B are the bending and bulk moduli of the lamellar stack, respectively. The model parameters such as σ_h, σ_c, ρ_h, ρ_c, z_h, η, N & N_d are adjusted to get the best fit between the observed and calculated intensity.

1.7.2 Sponge (L_3) phase

Diffraction data of the sponge (L_3) phase were analyzed using the procedure described by Porcar [73]. The observed coherent scattering intensity (after background subtraction) is given by,

$$I(q) = NS(q)P(q) \tag{1.23}$$

where S(q) is the structure factor and P(q) is the form factor of the bilayer discoids and N is the effective density of these discoids. We have used the structure factor due to Lei et al. [74] which may be expressed as,

$$S(q) = 1 + (A\frac{arctan((q\xi_1)/2)}{q}) + (\frac{B}{((\xi_2)^2 + (q - Q_1)^2)}) \tag{1.24}$$

The first two terms of this expression are the structure factor derived by Roux et al., [75, 76] which describes the membrane correlations on a length scale much larger than the pore size in terms of an inside-outside correlation length ξ_1. Third term B describes the cell-cell correlation with correlation length ξ_2 and an average cell-cell distance L=2pi/Q_1.

We have used the form factor ($P(q)$) for scattering from membrane discoids of thickness (w) with a Gaussian distribution of transverse scattering length density characterized by a radius of gyration σ as described in ref [73, 77]. An analytical approximation for the form factor ($P(q)$) of these discoids averaged over random orientations is given by;

$$P(q) \approx 4(\pi\sigma^2 Nm)^2(\frac{((1-((Cos[qw])(Exp[-q^2w^2/32])))/q^2)}{((q^2\sigma^2)+(2Exp[-((q^2\sigma^2))/6]))}) \tag{1.25}$$

The model parameters such as A, ξ_1, B, ξ_2, w & σ are adjusted to get the best fit between the observed and calculated intensity.

Bibliography

[1] J. Israelachvili, *Intermolecular and Surface Forces*, 2nd Ed., Academic Press, London (1992).

[2] F. Evans and H. Wennerstr̈om, it The Colloidal Domain), 2nd Ed., Wiley, New York (1999).

[3] K. Holmberg, B. Jonsson, B. Kronberg and B. Lindman, *Surfactants and Polymers in Aqueous Solution*, 2nd Ed. Wiley and Sons Ltd: Chichester (2002).

[4] C. Tanford, *The Hydrophobic Effect*, 2nd edition, Wiley, New York (1980).

[5] A. Ben-Shaul and W. M. Gelbart *in Micelles, Membranes, Microemulsions and Monolayers*, Eds. W. M. Gelbert, A. Ben-Shaul and D. Roux, Springer-Verlag, New York (1994).

[6] B. Lindman and H. Wennerstrom, *Micelles*, Springer-Verlag, Berlin (1980).

[7] R. J. Hunter, *Foundations of Colloid Science*, Oxford University Press, USA (1987).

[8] Florian Nettesheim and Eric W. Kaler, in *Giant Micelles Properties and Applications*, edited by Raoul Zana, Eric W. Kaler, CRC Press, **vol. 140** of *Surfactant science series*, pp. 223-247 (2007).

[9] M. E. Cates and S. J. Candau, *J. Phys. Condens. Matter*, **2**, 6869 (1990).

[10] M. S. Leaver and M. C. Holmes, *J. Phys. II France*, **3**, 105 (1993).

[11] M. C. Holmes, A. M. Smith and M. S. Leaver, *J. Phys. II France*, **3**, 1357 (1993).

[12] M. C. Holmes, P. Sotta, Y. Hendrix and B. Deloche, *J. Phys. II France*, **3**, 1735 (1993).

[13] D. Myers, *Surfactant Science and Technology*, 3rd Ed. Wiley and Sons Ltd, Hoboken, New Jersey (2006).

[14] A. Patist, S. G. Oh, R. Leung and D. O. Shah, *Coll. Surf. A*, **176**, 3 (2000).

[15] E. M. Landau and J. P. Rosenbusch, *Proc. Natl. Acad. Sci. USA*, **93**, 14532 (1996).

[16] William M Gelbart, Avinoam Ben-Shaul and D. Roux, in *Micelles, Membranes, Microemulsions, and Monolayers*, ed. New York, NY : Springer New York (1994).

[17] J. Rogers and P. A. Winsor, *J. Colloidal Interface Sci.*, **30**, 247 (1969).

[18] R. G. Laughlin, *The Aqueous Phase Behavior of Surfactants*, Academic Press, London, p-29 (1994)

[19] P. G. de Gennes and J. Prost, *The Physics of Liquid Crystal*, 2nd edition, Oxford University Press, Oxford (1994).

[20] L. Coppola, R. Gianferri, I. Nocotera, C. Oliviero and G. A. Ranieri, *Phys. Chem. Chem. Phys*, **6**, 2364 (2004).

[21] N. Boden, K. W. Jolley, and M. H. Smith, *Liq. Cryst.*, **6**, 481 (1989).

[22] Y. Hendrikx and J. Charvolin, *J. Phys.(Paris)*, **42**, 1427 (1981)

[23] A. M. Figueiredo Neto, Y. Galerne, A. M. Levelut, and L. Liébert, *J. Phys. (Paris) Lett.*, **46**, L-499 (1985).

[24] Antônio M. Figueiredo Neto and Silvio R. A. Salinas, in *The Physics of lyotropic liquid crystals Phase transitions and structural properties*, ed. Oxford university press (2005).

[25] A. M. Figueiredo Neto, L. Liébert, and Y. Galerne, *J. Phys. Chem.*, **89**, 3737 (1985).

[26] A. M. Figueiredo Neto, Y. Galerne, and L. Liébert, *J. Phys. Chem.*, **89**, 3939 (1985).

[27] M. C. Valente Lopes and A.M. Figueiredo, *Phys.Rev.A*, **38**, 1101 (1988).

[28] M. C. Holmes and M. S. Leaver, in *Bicontinuous liquid crystals*, edited by M. L. Lynch and P. T. Spicer (CRC Press, Boca Raton, FL), **vol. 127** of *Surfactant science series*, pp. 15-39 (2005).

[29] P. Kékicheff and B. Cabane, *J. Phys.*, **48**, 1571 (1987).

[30] S. K. Ghosh and V. A. Raghunathan, *Langmuir*, **25**, 2622 (2009).

[31] G. Lindblom and L. Rilfors, *Biochem. Biophys. Acta*, **988**, 221 (1989).

[32] K. Fontell, *Adv. Colloid Interface Sci.*, **41**, 127 (1992).

[33] G. Porte, M. Delsanti, I. Billard, M. Skori, J. Appell, J. Marignan, F. Debeauvais, *J. Phys. II France*, **1**, 1101 (1991).

[34] V. Luzzati, H. Mustachhi, A. E. Skoulios, and F. Husson, *Acta Crystallogr.*, **13**, 660 (1960).

[35] Y. Hendrikx and J. Charvolin, *J. Phys.*, **42**, 1427 (1981).

[36] G. Chidichimo, N. A. P. Vaz, Z. Yaniv, and J. W. Doane, *Phys. Rev. Lett.*, **49**, 1950 (1982).

[37] Sajal Kumar Ghosh, thesis in title *Influence of Strongly Bound Counterions on the Phase Behaviour of Ionic Amphiphiles* (2007).

[38] S. S. Funari, M. C. Holmes, and G. J. T. Tiddy, *J. Phys. Chem.*, **96**, 11029 (1992).

[39] S. S. Funari, M. C. Holmes, and G. J. T. Tiddy, *J. Phys. Chem.*, **98**, 3015 (1994).

[40] J. Burgoyne, M. C. Holmes, and G. J. T. Tiddy, *J. Phys. Chem.*, **99**, 6054 (1995).

[41] C. E. Fairhurst, M. C. Holmes, and M. S. Leaver, *Langmuir*, **13**, 4964 (1997).

[42] S. S. Funari and G. Rapp, *Proc. Natl. Acad. Sci. USA*, **96**, 7756 (1999).

[43] M. Leaver, A. Fogden, M. C. Holmes, and C. Fairhurst, *Langmuir*, **17**, 35 (2001).

[44] M. Imai, K. Nakaya, T. Kawakatsu, and H. Seto, *J. Chem. Phys.*, **119**, 8103 (2003).

[45] M. Imai, K. Sakai, M. Kikuchi, K. Nakaya, A. Saeki, and T. Teramoto, *J. Chem. Phys.*, **122**, 214906 (2005).

[46] M. Baciu, U. Olsson, M. S. Leaver, and M. C. Holmes, *J. Phys. Chem. B*, **110**, 8184 (2006).

[47] S. T. Hyde, *J. Physique (Coll.)*, **C-7**, 209 (1990).

[48] S. T. Hyde, *Colloid Surfaces A: Physicochem. Eng. Aspects*, **103**, 227 (1995).

[49] Cécile A. Dreiss, *Soft Matter*, **3**, 956 (2007).

[50] G. Porte, J. Appell, P. Bassereau, and J. Marignan, *J. Phys. (Paris)*, **50**, 1335 (1989).

[51] D. A. Antelmi, P. Kekicheff and P. Richetti, *J. Phys. II*, **5**, 103 (1995).

[52] B. E. Warren, *X-ray diffraction, Dover Publications*, New York (1990).

[53] D. C. Champeney, *Fourier Transforms and Thier Physical Applications*, Academic Press, London (1973).

[54] D. Sherwood, *Crystal, X-rays and Protein*, Longman, London (1976).

[55] P. J. Collings and M. Hird, *Introduction to Liquid Crystals Chemistry and Physics*, Taylor and Francis, Bristol (1997).

[56] G. Friedel, *Ann. Phys. (Fr.)*, **18**, 273 (1922).

[57] J. Nehring, A. Saupe, *J. Chem Soc., Faraday Trans. II*, **68**, 1 (1972).

[58] A. Saupe, *Mol. Cryst. Liq. Cryst.*, **21**, 211 (1973).

[59] H.-R. Trebin, *Adv. Phys.*, **31**, 195 (1982).

[60] Ingo Dierking, *Textures of Liquid Crystals*, WILEY-VCH, Verlag GmbH & Co. KGaA, Weinheim (2003).

[61] J. Nehring, *Phys. Rev. A*, **7**, 1737 (1973).

[62] J. Bastacky, C. Wodley, R. LaBrie and C. Backhus, *Scanning*, **9**, 219 (1987).

[63] R.P. Apkarian, *Microsc. Microanal.*, **9**, 272 (2003).

[64] S.L. Erlandsen, C. Ottenwaelter, C. Frethem and Y. Chen, *BioTechniques*, **31**, 300 (2001).

[65] H. M. Wyss, M. Hutter, M. Muller, L. P. Meier and L. J. Gauckler, *J. Colloid Interface Sci.*, **248**, 340 (2002).

[66] R. P. Apkarian, E. R. Wright, V. A. Seredyuk, S. Eustis, L. A. Lyon, V. P. Conticello, F. M. Menger and *Microsc. Microanal.*, **9**, 286 (2003).

[67] L. Champion, J.-P. Gerard, J.-P. Planche, D. Martin and D. Anderson, *J. Mater. Sci.*, **36**, 451 (2001).

[68] L. Champion-Lapalu, A. Wilson, G. Fuchs, D. Martin and J.-P. Planche, *Energy Fuels*, **16**, 143 (2002).

[69] J. Vermant, G. Cioccolo, K. Golapan Nair and P. Moldenaers, *Rheol. Acta*, **43**, 529 (2004).

[70] Images are taken from the PPT provided by Quorum Technologies.

[71] G. Pabst, M. Rappolt, H. Amenitsch, and P. Laggner, *Phys. Rev. E*, **62**, 4000 (2000).

[72] R. Zhang, R. M. Suter, and J. F. Nagle, *Phys. Rev. E*, **50**, 5047 (1994).

[73] L. Porcar, W. A. Hamilton, and P. D. Butler, *langmuir*, **19**, 10779 (2003).

[74] N. Lei, C. R. Safinya, D. Roux, and K. S. Liang, *Phys. Rev. E*, **56**, 608 (1997).

[75] D. Roux, M. E. Cates, U. Olsson, R. C. Ball, F. Nallet and A. M. Bellocq, *Europhys. Lett.*, **11**, 229 (1990).

[76] D. Roux and C. J. Coulon, *Phys. Chem.*, **96**, 4147 (1992).

[77] F. Nallet, R. Laversanne and D. Roux, *J. Phys. II*, **3**, 487 (1993).

Chapter 2

Stability of intermediate phases in a cationic amphiphile-water system

2.1 Introduction

Amphiphilic molecules self-assemble in water to form micellar aggregates above the critical micellar concentration (CMC) [1], as described in chapter 1. At much higher amphiphile concentrations (ϕ_s) these solutions exhibit a variety of thermodynamic phases, characterized by varying degrees of translational and orientational order of the micelles [2]. The phase diagrams of single chain amphiphiles is in general dominated by the hexagonal (H_I) phase, consisting of cylindrical micelles arranged on a two-dimensional (2D) hexagonal lattice, which occurs over a wide range of ϕ_s. At still higher ϕ_s a lamellar (L_α) phase is observed, made up of a periodic stack of planar amphiphile bilayers separated by water. Further increase in ϕ_s results in inverse structures, where water-filled regions surrounded by the hydrophilic head groups of the amphiphilic molecules are dispersed in the hydrocarbon matrix. These inverse micellar morphologies are referred to as type II, whereas the direct micellar morphologies are called type I.

The generic phase behavior of amphiphile-water systems, outlined above, can be rationalized in terms of a gradual decrease in the spontaneous mean curvature of the micelle-water interface with increasing ϕ_s, from being positive at low values of ϕ_s to being negative for high values of ϕ_s. Many studies indicate that the morphological transformation from cylinders to bilayers does not take place abruptly, but through a sequence of intermediate shapes, giving rise to a sequence of so-called intermediate phases between the hexagonal and the lamellar phases [3]. Nevertheless, the stability of these intermediate phases remains poorly understood, mainly because of the fact that amphiphile aggregates in many of these phases have non-uniform mean and/or Gaussian curvatures.

Intermediate phases are of three kinds-bicontinuous cubic phases, ribbon phases, and mesh phases; all of them can occur as type I and type II. Bicontinuous cubic phases can be easily identified by the fact that they are optically isotropic, unlike all other phases found at comparable surfactant concentrations, which are birefringent [4]. Type I bicontinuous cubic phases consist of two interpenetrating, topologically identical networks of cylindrical micelles, separated by water. In type II bicontinuous cubic phases two interpenetrating water channels are separated by a surfactant bilayer. Interestingly, the surface separating the two networks into two equal volumes can be described as a triply periodic minimal surface characterized by vanishing mean curvature everywhere on the surface. Three bicontinuous cubic structures have been reported in amphiphile-water systems, belonging to the space groups Im3m, Ia3d, and Pn3m, usually associated with the P, gyroid, and D triply periodic minimal surfaces, respectively. However, a given space group can, in principle, be realized by more than one triply periodic minimal surface [5].

Ribbon phases consist of long micelles with a roughly elliptical cross section, ordered on a 2D rectangular lattice. Two types of structures have been reported, corresponding to the plane groups cmm and pgg [6–8].

Mesh phases are made up of 2D mesh-like aggregates, which can also be described as bilayers with a regular array of mono-disperse pores. In the ordered mesh phases the mesh-like aggregates lock into a 3D lattice. On the other hand, the

random mesh phase consists of a periodic stacking of these aggregates with no long-range positional correlations of the in-plane structure; this phase can also be described as a lamellar phase with in-plane defects that are weakly correlated (L_α^D). All known structures of ordered mesh phases are either rhombohedral (Rh) (space group $R\bar{3}m$) or tetragonal (T) (space group I4mm). The former consists of a three-layer stacking of three-coordinated hexagonal mesh, whereas the latter has a two-layer stacking of four-coordinated square mesh.

In this chapter we describe the influence of two structurally isomeric organic salts, namely, 2-sodium-3-hydroxy naphthoate (SHN) and 1-sodium-2-hydroxy naphthoate (SHN1), on the phase behavior of the cationic surfactant cetylpyridinium chloride (CPC). For comparison, the effect of 2,3-dihydroxy naphthalene (DHN) on the same surfactant-water system was also studied. Earlier studies on similar systems are described in section 2.2. A short description of chemicals and experimental techniques has been given in section 2.3. The experimental results are described in section 2.4. Both the CPC-SHN-Water and the CPC-SHN1-Water systems are found to exhibit a variety of intermediate phases, depending on the salt-to-surfactant molar ratio, α, and the water content. Both these systems show ribbon and bicontinuous cubic phases at low values of α. At α=0.4 and 0.5, the CPC-SHN-Water system exhibits a transition between the two ordered mesh phases, as a function of both temperature and water content. On the other hand, only the tetragonal mesh phase is observed in the CPC-SHN1-Water system at similar values of α. At $\alpha \sim 1$ phase diagrams of both systems are dominated by the lamellar phase. Two nematic phases are also observed with SHN, with the one at lower values of α consisting of cylindrical micelles and the one seen at higher values of α being made up of disc-like micelles. In contrast, DHN has a negligible effect on the phase behavior of CPC, and the micelles remain cylindrical up to α=0.75. These results show that strongly binding counterions, provided by the organic salts, can be used to tune the curvature of the micellar interface and stabilize different intermediate phases. A detailed discussion of our results is given in section 2.5, and the conclusions that can be drawn from this study are given in section 2.6.

2.2 Earlier Studies

Most of the studies on mesh phases, reported in the literature, have been carried out on non-ionic surfactants, poly(oxyethylene glycol) alkyl ethers (C_nEO_m), where they occur over a rather wide range of composition [9–17]. The role of the length of the hydrocarbon chain of the surfactant in stabilizing different intermediate phases has been well studied in this class of surfactants. Shorter hydrocarbon chains are found to favor the bicontinuous cubic phase, whereas longer ones induce mesh phases [16]. Interestingly, the ordered mesh phase seen in all these systems has a rhombohedral (Rh) structure [13, 14, 16]. Mesh phases have also been seen in some anionic surfactants [18–21]. A variety of intermediate phases, such as ribbon, ordered mesh, and bicontinuous cubic, has been seen in the sodium dodecyl sulfate (SDS)-water system, albeit over very narrow ranges of composition [18]. On the other hand, mesh phases have been observed over wide composition ranges in aqueous solutions of some anionic surfactants with stiffer fluorocarbon chains [19–22]. In these systems the structure of the mesh phase is found to depend critically on the type of the counterion. For example, only a random mesh phase (L_α^D) is seen in cesium perfluoro-octanoate, whereas its lithium counterpart shows the T mesh phase in addition to the L_α^D phase. The Rh mesh phase is seen in tetramethylammonium perfluorodecanoate, but all mesh phases disappear upon increasing the hydrophobicity of the counterion. The above observations suggest that the balance between the aggregate flexibility, determined by the chain length or degree of fluorination, and the interfacial curvature, determined by the head-group size or the nature of the counterion, decides the relative stability of different intermediate phases [3].

Another system exhibiting mesh phases is cationic-amphiphile mixtures, where the Rh and L_α^D mesh phases have been observed for slightly differing chain lengths of the two components, indicating again the fine-tuning of the spontaneous curvature necessary to stabilize these phases [23]. Mesh phases have also been reported in some cationic surfactants in the presence of strongly binding counterions provided by organic salts [24–26]. Such counterions are known to adsorb at the micelle-water

interface and lead to a reduction in the spontaneous curvature of the aggregates, with cylindrical micelles formed by the pure surfactant transforming into bilayers as the salt-to-surfactant molar ratio (α) approaches 1. Thus the spontaneous mean curvature of the aggregates in these systems can be conveniently controlled by tuning the concentration of the counterions, and mesh phases are observed over an intermediate range of α. Interestingly, changes in the structure of the surfactant head group have been found to influence the stability of ordered mesh phases in these systems, with the Rh phase in the cetyltrimethylammonium bromide (CTAB)−3-hydroxy-2-naphthoate (SHN)water system being replaced by the T phase upon substituting CTAB with cetylpyridinium bromide (CPB) [25, 26].

2.3 Experimental

CPC, 3-hydroxy-2-naphthoic acid (HNA), 2-hydroxy-1-naphthoic acid (HNA1), 2,3-dihydroxy naphthalene (DHN), and sodium hydroxide (NaOH) were purchased from Sigma-Aldrich. Sodium salts of HNA and HNA1 were prepared by adding an equivalent amount of NaOH to an ethanol solution of the acid [27]. Chemical structures of CPC and the organic salts are shown in figure 2.1. Solutions of appropriate concentration ϕ_s (total wt of surfactant and organic salt) were prepared by adding deionized water (Millipore) to the surfactant-salt mixture. The sample tubes were then sealed and left in an oven at 40°C for more than 2 weeks. Samples with different molar ratios (α=[organic salt]/[surfactant]) were prepared to determine partial phase diagrams of the ternary systems.

Samples were taken between a glass slide and a cover-slip for polarizing optical microscopy (POM) observations. Phase transitions were monitored near the center of the sample, far from the edges. For x-ray diffraction studies, samples were taken in 0.5-mm-diameter glass capillaries (Hampton Research) and were flame-sealed. Some of the samples were found to align due to the shear flow at the time of filling the capillaries. Diffraction patterns were obtained using CuK_α radiation from a rotating anode x-ray generator (Rigaku UltraX 18) equipped with a collimating

multilayer mirror (Xenocs). Data were collected using a 2D image plate detector (Marresearch). Exposures lasted for 20−90 min. Spacings of the sharp peaks in the diffraction pattern could be measured to an accuracy of 0.03 nm, whereas the corresponding quantity for the diffuse peaks was 0.1 nm. Small-angle x-ray scattering (SAXS) studies, covering a range of scattering vector (q) values from 0.01 to 5.0 nm^{-1}, were also carried out using a Hecus S3-Micro system, equipped with a 1D position-sensitive detector (MBraun PSD50M). Typical exposure time was 20 min.

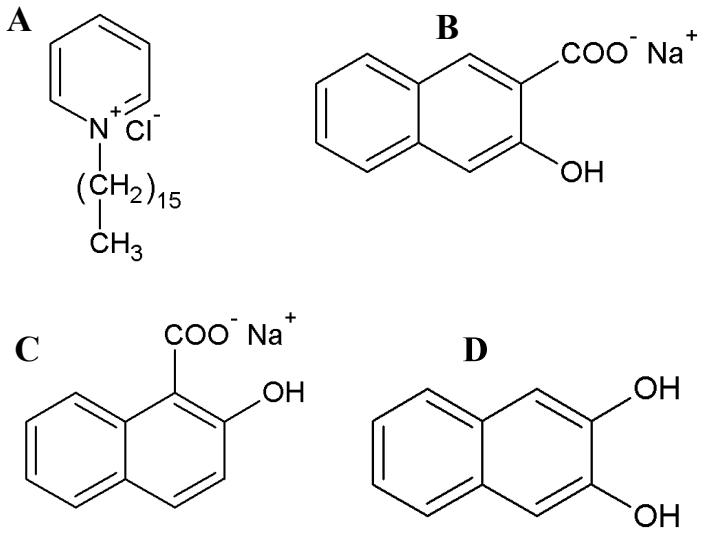

FIGURE 2.1: Chemical structures of cetylpyridinium chloride (CPC) (**A**), 2-sodium-3-hydroxy naphthoate (SHN) (**B**), 1-sodium-2-hydroxy naphthoate (SHN1) (**C**) and 2, 3 dihydroxy naphthalene (DHN) (**D**).

2.4 Results

2.4.1 CPC-SHN-Water system

The phase behavior of these mixtures was studied at α ([SHN]/[CPC])=0.25, 0.4, 0.5, 0.6, 1.0, and 1.25. For each α, (CPC+ SHN) concentration (ϕ_s) was varied from 10 to 80 wt%. Microscopy observations were made over the temperature

range from 25 to 85°C. Phases were identified from their characteristic microscopy textures and diffraction patterns.

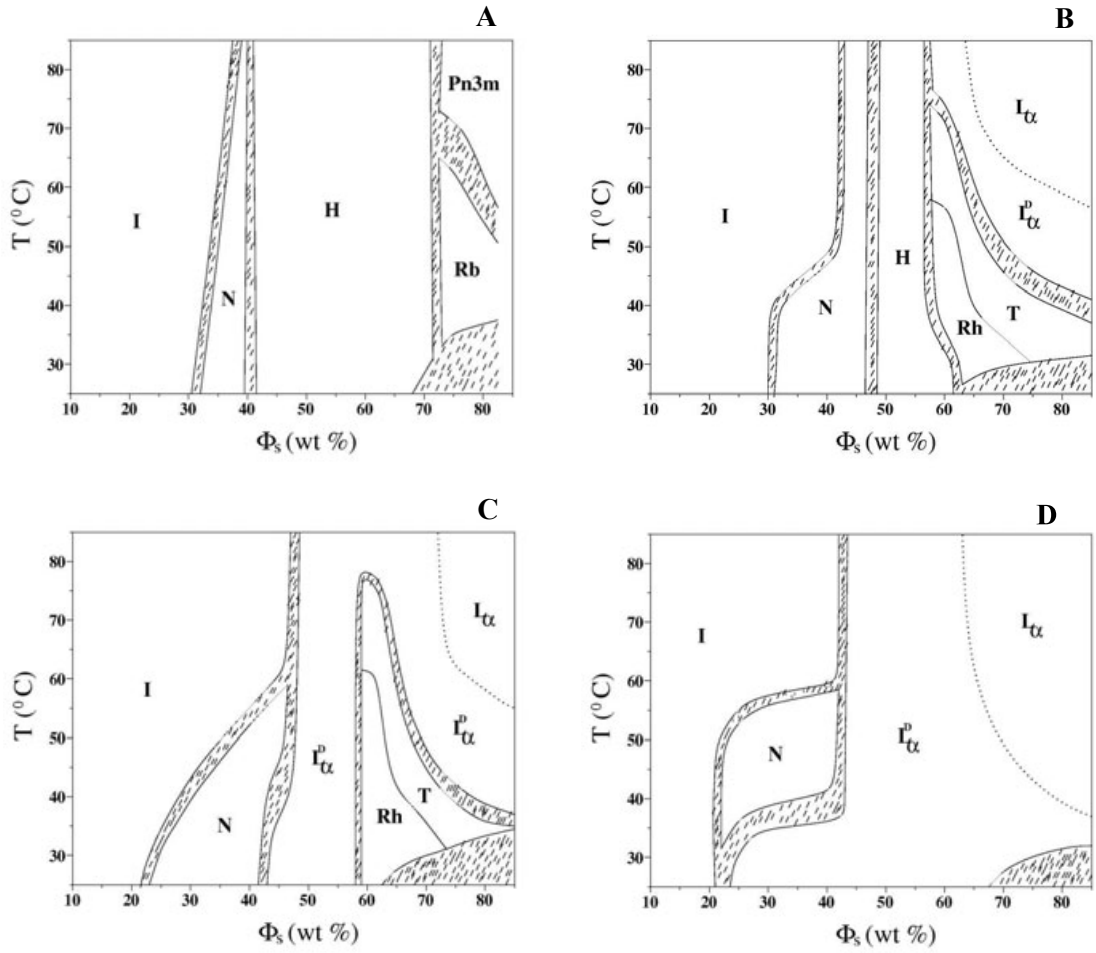

FIGURE 2.2: Partial phase diagram of the CPC-SHN-Water system at α=0.25 (**A**), 0.4 (**B**), 0.5 (**C**) and 0.6 (**D**). I, N, H, Rb, Pn3m, Rh, T, L_α^D and L_α denote the isotropic, nematic, hexagonal, ribbon, bicontinuous cubic, rhombohedral mesh, tetragonal mesh, random mesh and lamellar phases, respectively. The dotted line indicates the continuous L_α^D - L_α transition. The shaded regions in this and all the subsequent phase diagrams correspond to multiphase regions.

2.4.1.1 Phase behavior at α=0.25

At α=0.25 a flow-birefringent isotropic viscoelastic gel (I) is observed at low values of ϕ_s (Fig. 2.2A). Upon increasing ϕ_s beyond 30, the samples become birefringent and show POM textures typical of the nematic (N) phase (Fig. 2.4A). Diffraction

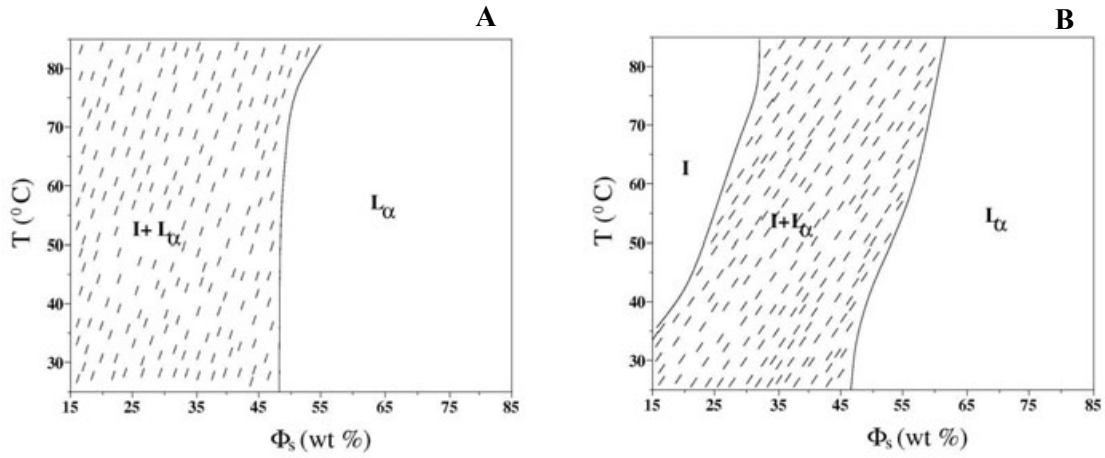

FIGURE 2.3: Partial phase diagram of the CPC-SHN-Water system at α=1 (**A**) and 1.25 (**B**). I and L_α denote the isotropic and lamellar phases, respectively.

patterns of these samples show one broad peak in the small-angle region, confirming the nematic structure (Figs. 2.5A and 2.6b). Upon further increase in ϕ_s, the samples exhibit the characteristic texture of the hexagonal (H) phase (Fig. 2.4B). Diffraction patterns of these samples show two peaks in the small-angle region with their spacings in the ratio 1:$\frac{1}{\sqrt{3}}$, consistent with the 2D hexagonal structure (Figs. 2.5B and 2.6d). The average spacing in the nematic phase and the lattice parameter of the hexagonal phase decrease with increasing ϕ_s. For $\phi_s > \sim 70$ a crystalline phase coexisting with another birefringent phase is observed at low temperatures. However, upon heating a pure phase with a different texture is observed (Fig. 2.4C). The x-ray diffraction patterns of this phase show five peaks (Fig. 2.7b), which can be indexed on a centered rectangular lattice corresponding to the plane group cmm (Tab. 2.1). We identify this as a ribbon (Rb) phase, which is transformed into an optically isotropic phase upon further increase in the temperature. The x-ray diffraction patterns of the latter phase (Fig. 2.7a) show three peaks with their spacings in the ratio $\frac{1}{\sqrt{2}} : \frac{1}{\sqrt{3}} : \frac{1}{\sqrt{4}}$, and can be indexed on a cubic lattice with space group Pn3m (Tab. 2.2).

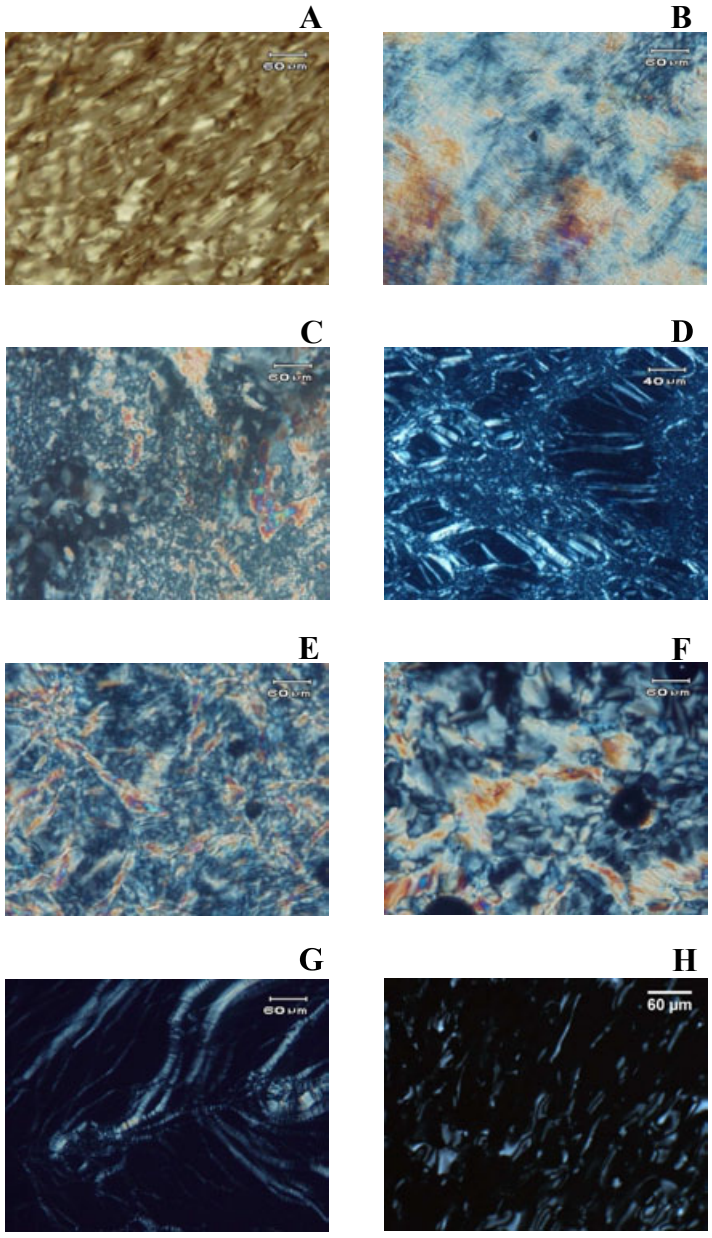

FIGURE 2.4: Typical polarizing optical microscopy (POM) textures of the N_c (**A**), H (**B**), Rb (**C**), L_α (**D**), Rh (**E**), T (**F**), L_α^D (**G**) and N_d (**H**) phases. The N_c phase is made up of cylindrical micelles, whereas the N_d phase is made up of disc-like micelles.

2.4.1.2 Phase behavior at α=0.4

Flow-birefringent isotropic, nematic, and hexagonal phases are also observed at lower values of ϕ_s at α=0.4 (Fig. 2.2B). However, the concentration range of the H phase is considerably reduced and the phase behavior at higher ϕ_s is very

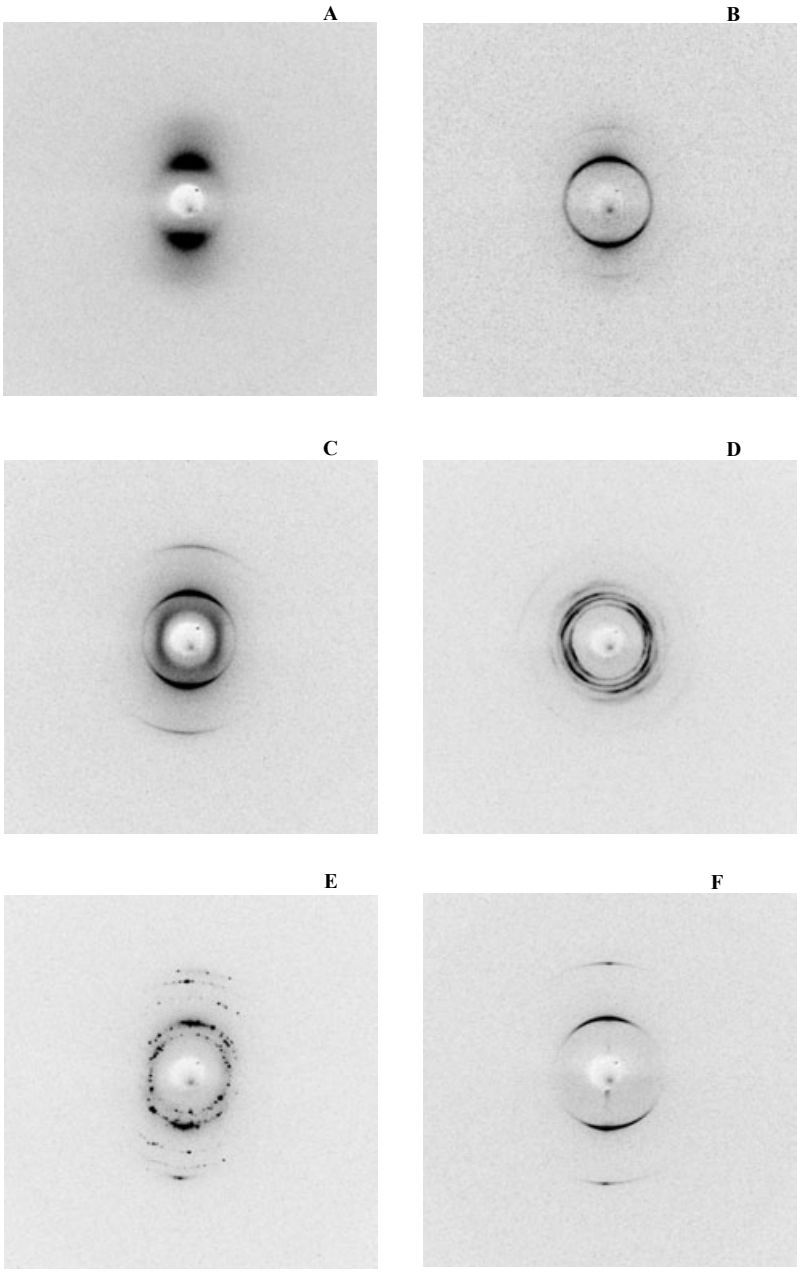

FIGURE 2.5: Partially oriented diffraction patterns of the N (**A**), H (**B**), L_α^D (**C**), Rh (**D**), T (**E**) and L_α (**F**) phases.

different. A lamellar (L_α) phase is observed in the high-ϕ_s, high-temperature limit. The diffraction patterns of this phase show two peaks with their spacings in the ratio 1:$\frac{1}{2}$ (Figs. 2.5F and 2.6e). Three intermediate phases are observed between the H and the L_α phases. Two of these phases (Rh and T) exhibit distinct mosaic POM textures, whereas the third (L_α^D) shows an oily-streak texture similar to the L_α phase (Figs. 2.4D-G). Diffraction patterns of the Rh phase typically show six

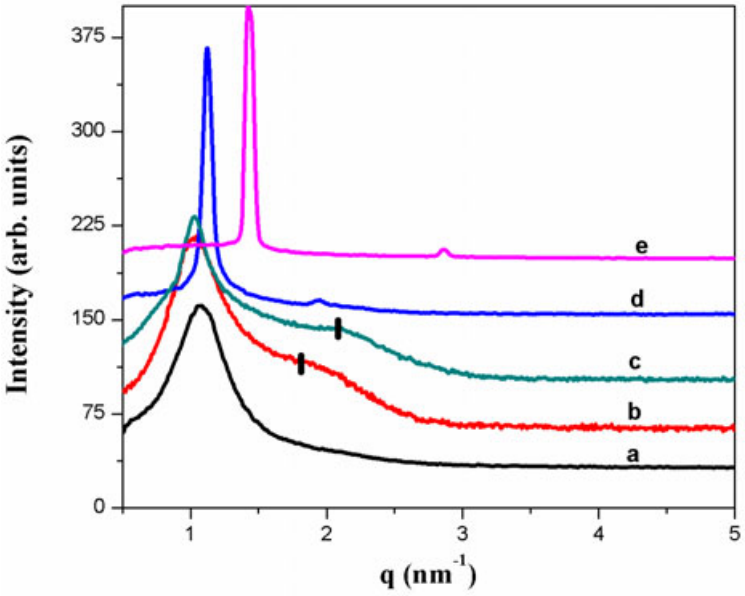

FIGURE 2.6: Typical diffraction patterns of the I (**a**), N_c (**b**), N_d (**c**), H (**d**) and L_α (**e**) phases of the CPC-SHN-Water system. The bars on curves b and c indicate secondary peaks at $\sqrt{3}q_o$ and $2q_o$, respectively, where q_o is the position of the primary peak.

TABLE 2.1: X-ray diffraction data from the Rb phase of the CPC-SHN-Water system at $\alpha = 0.25$, $\phi_s = 80$ and T= 40°C, indexed on a centered rectangular lattice corresponding to the space group cmm. The calculated spacings (d_c) are obtained using the relation $1/d^2 = h^2/a^2 + k^2/b^2$ with the condition $h + k = 2n$, where n is an integer. The unit cell parameters are: $a = 7.49$nm, $b = 8.84$nm.

d_o(nm)	d_c(nm)	(hk)	Intensity
5.71	5.71	(11)	60
4.42	4.42	(02)	100
2.86	2.86	(22)	10
2.42	2.40	(31)	10
2.21	2.21	(04)	8

peaks (Figs. 2.5D and 2.7d), which can be indexed on a rhombohedral lattice (Tab. 2.3) with space group R$\bar{3}$m. The T phase also typically shows six peaks in its diffraction pattern (Figs. 2.5E and 2.7e), which can be indexed on a body centered tetragonal lattice with space group I4mm (Tab. 2.4). Diffraction patterns of the L_α^D phase show a diffuse peak in the small-q region, in addition to two sharp peaks, whose spacings are in the ratio 1:1/2 (Figs. 2.5C and 2.7c). In oriented samples, the diffuse peak appears in the direction normal to the sharp peaks (Fig. 2.5C). The diffuse peak gradually disappears upon increasing the temperature at

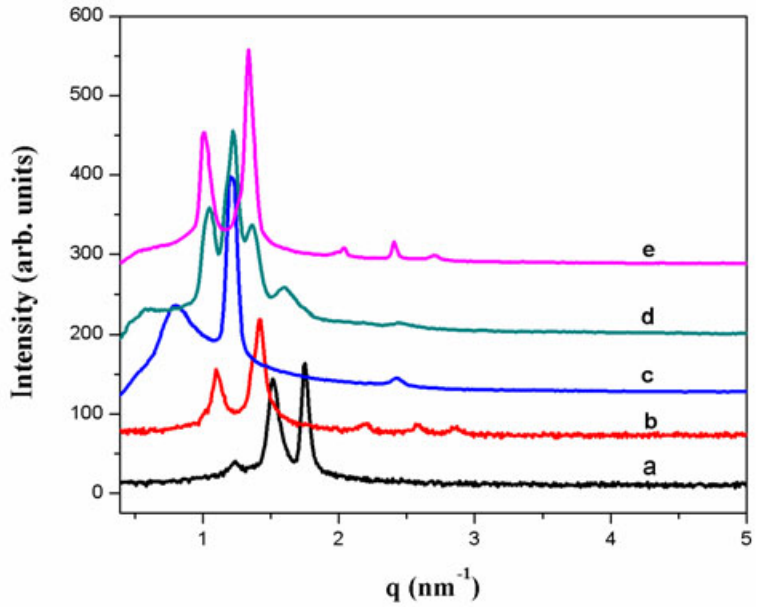

FIGURE 2.7: Typical diffraction patterns of the Pn3m (**a**), Rb (**b**), L_α^D (**c**), Rh (**d**) and T (**e**) phases of the CPC-SHN-Water system.

TABLE 2.2: X-ray diffraction data from the cubic phase of the CPC-SHN-Water system at $\alpha = 0.25$, $\phi_s = 80$ and T= 60°C, indexed on a cubic lattice corresponding to the space group Pn3m. The calculated spacings (d_c) are obtained from the relation $1/d^2 = (h^2 + k^2 + l^2)/a^2$, with $a = 7.17$nm.

d_o(nm)	d_c(nm)	(hkl)	Intensity
5.07	5.07	(110)	20
4.13	4.14	(111)	80
3.59	3.58	(200)	100

high values of ϕ_s and the L_α^D phase transforms continuously into the L_α.

2.4.1.3 Phase behavior at α=0.5

The phase behavior at α=0.5 is very similar to that observed at α=0.4, with the difference that the L_α^D phase is observed at intermediate values of ϕ_s instead of the H phase (Fig. 2.2C). Further, the nematic phase at this composition shows pseudo-isotropic regions in its POM texture, where the optic axis is oriented normal to the glass plates (Fig. 2.4H). Since rod-like micelles do not exhibit such an orientation, we conclude that this nematic phase is made of disc-like micelles, unlike the one

TABLE 2.3: X-ray diffraction data from the Rh phase of the CPC-SHN-Water system at $\alpha = 0.40$, $\phi_s = 60$ and T= 40°C, indexed on a rhombohedral ($R\bar{3}m$) lattice. The calculated spacings (d_c) are obtained using the relation $1/d^2 = 4(h^2 + hk + k^2)/3a^2 + l^2/c^2$ with the condition $-h + k + l = 3n$, where n is an integer. The unit cell parameters are: $a = 10.77$nm, $c = 15.28$nm.

d_o(nm)	d_c(nm)	(hkl)	Intensity
5.91	5.91	(012)	20
5.09	5.09	(003)	100
4.48	4.46	(021)	20
3.72	3.70	(013)	6
2.91	2.90	(015)	3
2.54	2.55	(006)	2

TABLE 2.4: X-ray diffraction data from the T phase of the CPC-SHN-Water system at $\alpha = 0.4$, $\phi_s = 60$ and T= 65°C, indexed on a body centered tetragonal lattice. The calculated spacings (d_c) are obtained using the relation $1/d^2 = (h^2 + k^2)/a^2 + l^2/c^2$ with the condition $h + k + l = 2n$, where n is an integer. The unit cell parameters are: $a = 6.69$nm, $c = 8.69$nm.

d_o(nm)	d_c(nm)	(hkl)	Intensity
5.30	5.30	(101)	55
4.33	4.35	(002)	100
2.84	2.83	(211)	5
2.38	2.37	(220)	4
2.15	2.17	(004)	3
1.42	1.45	(006)	2

seen at α=0.25 and 0.4, which is made up of long cylindrical micelles. The much lower viscosity of this phase at α=0.5 is in agreement with this conclusion.

2.4.1.4 Phase behavior at α=0.6

At α=0.6 the Rh and T phases seen at α=0.5 disappear and only the I, N, L_α^D , and L_α phases are observed with increasing ϕ_s (Fig. 2.2D).

2.4.1.5 Phase behavior at α=1 and α=1.25

The phase diagrams at α=1.0 and 1.25 are very similar and dominated by the L_α phase (Figs. 2.3A and 2.3B). It coexists with a low-viscosity isotropic phase at lower values of ϕ_s. A pure isotropic phase is obtained at α=1.25 upon heating.

2.4.2 CPC-SHN1-Water system

The phase behavior of these mixtures was studied at α= 0.25, 0.4, 0.5, and 1.0. For each α, the (CPC + SHN1) concentration (ϕ_s) was varied from 10 to 80 wt%. Observations were made over the temperature range from 25 to 85°C.

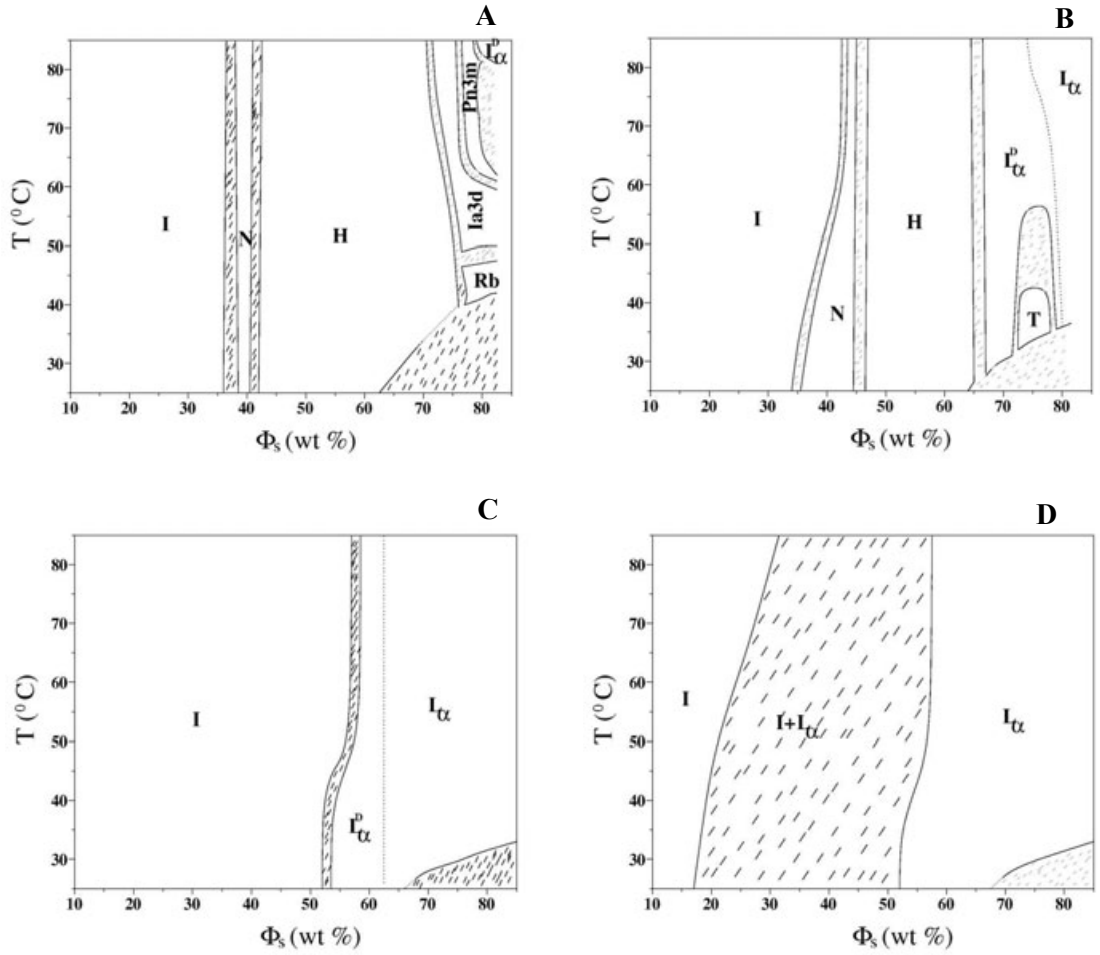

FIGURE 2.8: Partial phase diagram of the CPC-SHN1-Water system, at α = 0.25 (**A**), 0.4 (**B**), 0.5 (**C**) and 1.0 (**D**). I, N, H, Rb, Ia3d, Pn3m and L_α^D denote the isotropic, nematic, hexagonal, ribbon, cubic phase (Ia3d), cubic phase (Pn3m) and Random mesh phase respectively.

2.4.2.1 Phase behavior at α=0.25

The phase behavior of this system at α=0.25 is almost identical to that of the CPC-SHN-Water system at the same value of α, except for the fact that the L_α^D

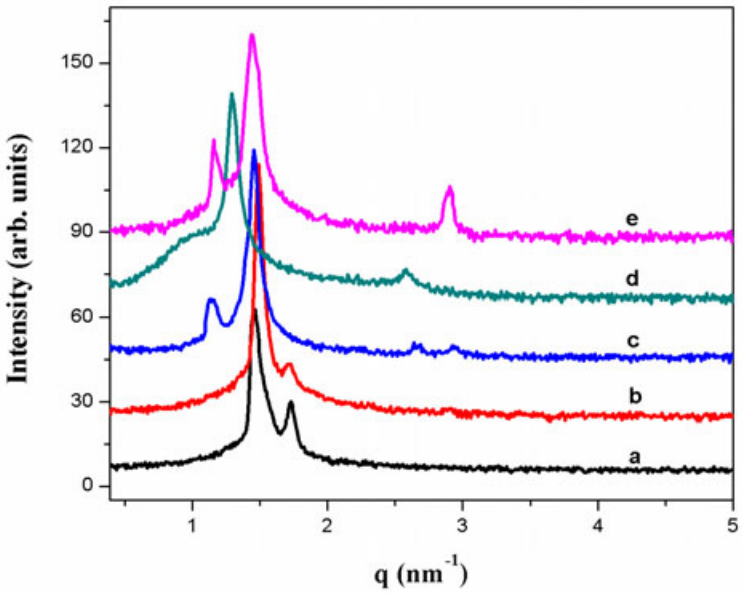

FIGURE 2.9: Typical diffraction patterns of the Ia3d (**a**) Pn3m (**b**), Rb (**c**), L_α^D (**d**) and T (**e**) phases of the CPC-SHN1-Water system.

phase and an additional cubic phase are observed at high values of ϕ_s at temperatures above the Rb phase (Fig. 2.8A). Diffraction data from the Rb phase are consistent with the cmm plane group as in the previous case (Tab. 2.5, Fig.2.9c). Diffraction patterns of the higher temperature cubic phase show four peaks, with their spacings in the ratio $\frac{1}{\sqrt{3}} : \frac{1}{\sqrt{4}} : \frac{1}{\sqrt{11}} : \frac{1}{\sqrt{14}}$, and can be indexed on a cubic lattice with the Pn3m space group (Tab. 2.6, Fig. 2.9b). The lower temperature cubic phase shows only two peaks, with their spacings in the ratio $\frac{1}{\sqrt{6}} : \frac{1}{\sqrt{8}}$; we tentatively assign it the space group Ia3d since these spacings correspond to the first two allowed reflections from it, although the other two possible space groups, namely, Pn3m and Im3m, are also consistent with the diffraction data (Tab. 2.7, Fig. 2.9a).

2.4.2.2 Phase behavior at α=0.4

The phase behavior of this system at α=0.4 is also very similar to that of the previous one, the only difference being that the Rh phase is absent (Fig. 2.8B). Diffraction data from the T phase is very similar to those obtained from the CPC-SHN-Water system (Tab. 2.8, Fig. 2.9e).

TABLE 2.5: X-ray diffraction data from the ribbon phase of the CPC-SHN1-Water system at $\alpha = 0.25$, $\phi_s = 80$ and T= 42°C, indexed on a 2-D centered rectangular lattice corresponding to the space group cmm. The unit cell parameters are: $a = 7.25$nm, $b = 8.60$nm.

d_o(nm)	d_c(nm)	(hk)	Intensity
5.54	5.54	(11)	10
4.30	4.30	(02)	100
2.34	2.33	(31)	1
2.14	2.15	(04)	1

TABLE 2.6: X-ray diffraction data from the cubic phase of the CPC-SHN1-Water system at $\alpha = 0.25$, $\phi_s = 77.5$ and T= 75°C, indexed on a 3-D cubic lattice corresponding to the space group Pn3m. The calculated spacings (d_c) are obtained using the relation $1/\mathrm{d}^2=(\mathrm{h}^2+\mathrm{k}^2+\mathrm{l}^2)/\mathrm{a}^2$, with $a = 7.17$nm.

d_o(nm)	d_c(nm)	(hkl)	Intensity
4.15	4.14	(111)	100
3.59	3.58	(200)	9
2.16	2.16	(311)	1
1.92	1.92	(321)	1

TABLE 2.7: X-ray diffraction data from the cubic phase of the CPC-SHN1-Water system at $\alpha = 0.25$, $\phi_s = 75$ and T= 75°C, indexed on a 3-D cubic lattice corresponding to the space group Ia3d. The calculated spacings (d_c) are obtained from the relation $1/d^2 = (h^2 + k^2 + l^2)/a^2$, with $a = 10.21$ nm.

d_o(nm)	d_c(nm)	(hkl)	Intensity
4.17	4.17	(211)	100
3.60	3.61	(220)	6

TABLE 2.8: X-ray diffraction data from the tetragonal mesh phase of the CPC-SHN1-Water system at $\alpha = 0.4$, $\phi_s = 75$ and T= 35°C, indexed on a 3-D body centered tetragonal (T)lattice corresponding to the space group I4mm. The unit cell parameters are: $a = 6.90$nm, $c = 8.64$nm.

d_o(nm)	d_c(nm)	(hkl)	Intensity
5.39	5.39	(101)	28
4.32	4.32	(002)	100
2.16	2.16	(004)	9

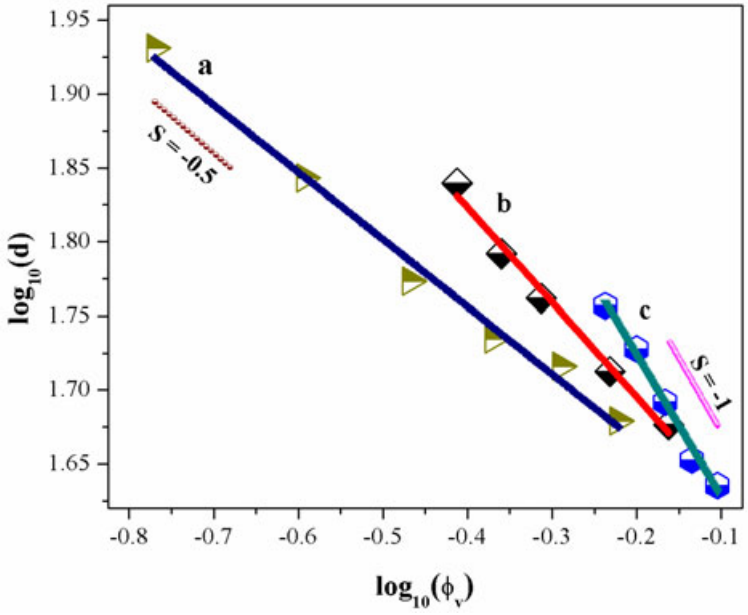

FIGURE 2.10: Variation of the lattice parameters with the volume fraction, of the H (curve **a**), L_α^D (curve **b**) and L_α (curve **c**) phases.

2.4.2.3 Phase behavior at α=0.5 and 1

Only the I, L_α^D , and L_α phases are observed at α=0.5 (Fig. 2.8C), and at α=1.0 the L_α^Dphase also disappears (Fig. 2.8D). The I phase at these compositions has a very low viscosity, unlike the one observed at lower values of α. Variation of d in the pure L_α is found to be described by the relation ($d \sim \phi_v^{-s}$) with s∼1, where ϕ_v is the volume fraction of the non-aqueous component estimated from ϕ_s, using the densities of the components (Fig. 2.10c). We have taken the densities of CPC, DHN and water as 0.980, 1.330 and 0.997g/cm^3 respectively to calculate ϕ_v.

2.4.3 CPC-DHN-Water system

The phase behavior of these mixtures was studied at α=0.5 and 0.75. For each α, the (CPC + DHN) concentration (ϕ_s) was varied from 10 to 80 wt% Microscopy observations were made over the temperature range from 25 to 85°C.

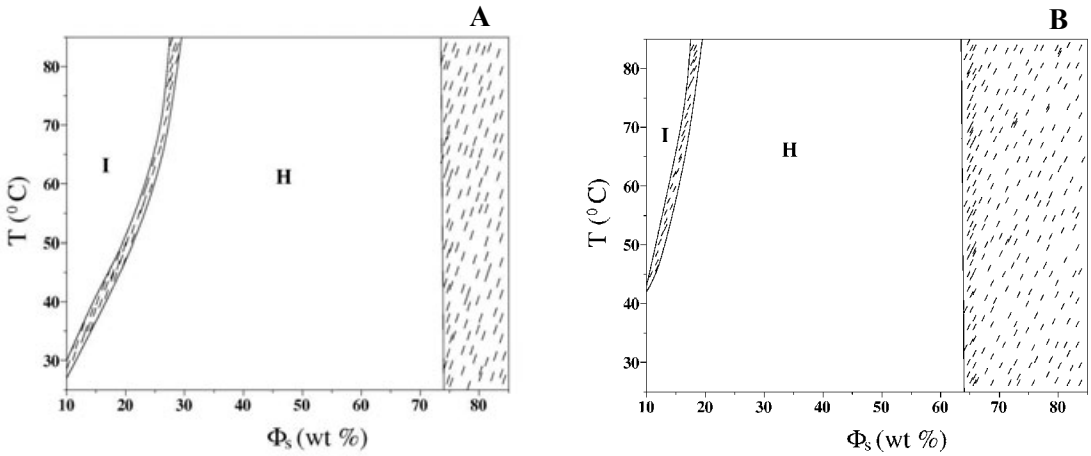

FIGURE 2.11: Partial phase diagram of the CPC-DHN-Water system, at α=0.5 (**A**) and 0.75 (**B**). I, and H denote the isotropic and hexagonal phase respectively.

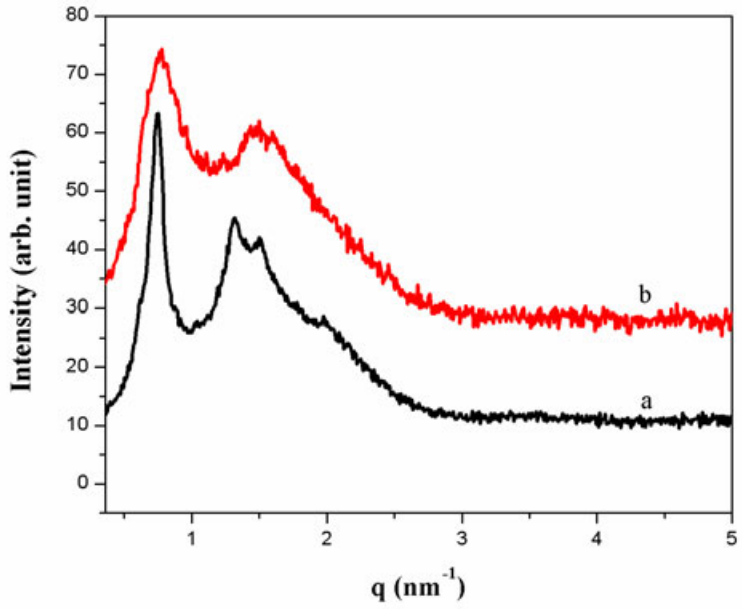

FIGURE 2.12: Typical diffraction patterns of the (**a**) Hexagonal (H) and (**b**) Isotropic (I) phases of the CPC-DHN-Water system.

2.4.3.1 Phase behavior at α=0.5 and 0.75

The phase behavior of this system is very similar for α=0.5 and α= 0.75(Fig. 2.11A and 2.11B). At low values of ϕ_s and low temperatures, a viscoelastic hexagonal phase is found, which transform to isotropic phase at higher temperature. The occurrence of hexagonal phase is confirmed by X-ray diffraction and POM studies.

The diffraction pattern of the hexagonal phase consists of four peaks in small angle region, with spacing in the ratio $1 : \frac{1}{\sqrt{3}} : \frac{1}{\sqrt{4}} : \frac{1}{\sqrt{7}}$ and corresponds to (1 0), (1 1) (2 0) and (1 2) planes of the hexagonal lattice. However, Isotropic phase also shows four peaks with their spacing in the ratio same as in hexagonal phase, but the peaks are broad, indicating that the local hexagonal order is maintained in this phase (Fig. 2.12). At higher values of ϕ_s the phase diagram is dominated by the H phase. At much higher values ofϕ_s, DHN crystallizes out of the solution. Figure 2.10a shows the variation of the lattice parameter of the H phase with ϕ_s. It is found to be described by the relation (d$\sim{\phi_v}^{-s}$) with s$\sim$0.5, where ϕ_v is the volume fraction of the non-aqueous component estimated from ϕ_s, using the densities of the components. Density of DHN is taken as 1.120g/cm^3.

2.5 Discussion

The high viscosity of the isotropic phase observed at low values of α in all three systems indicates the formation of long worm-like micelles. Such behavior is quite common in ionic surfactants upon the addition of simple inorganic as well as organic salts [28] and is very similar to that seen in mixtures of CTAB with salts such as KBr, sodium salicylate, sodium tosylate, and SHN [24, 29–31] and in the CPB-SHN-Water system [26]. The formation of these long flexible micelles is attributed to the decrease in the spontaneous curvature of the micelles in the presence of salt, which leads to an increase in the end-cap energy of the cylindrical micelles.

The nematic (N_c) phase that occurs in the CPC-SHN-Water and CPC-SHN1-Water systems at low values of α is made up of worm-like micelles that have a cylindrical shape on average. This conclusion is supported by the following observations. This phase occurs close to the hexagonal phase and is highly viscous. POM textures of this phase do not exhibit any homeotropic regions, where the optic axis is normal to the bounding plates (Fig. 2.4A). The x-ray diffraction patterns of this phase show a secondary maximum near $\sqrt{3}q_o$, where q_o is the

wave vector of the primary peak, which indicates short-range hexagonal order (Fig. 2.6b). A further increase in ϕ_s brings the cylindrical micelles closer, forcing them to order on a 2D hexagonal lattice.

In contrast, the nematic (N_d) phase that occurs at higher values of α in the CPC-SHN-Water system is made up of micelles that have a disc-like shape on average. This phase has a much lower viscosity in comparison and occurs close to the lamellar phase. POM textures of this phase show homeotropic regions, where the optic axis is normal to the bounding plates (Fig. 2.4H). The x-ray diffraction patterns of this phase show a secondary maximum near $2q_o$, indicating short-range lamellar order (Fig. 2.6c).

It is possible that a biaxial nematic phase might occur in between the above two uniaxial phases, as found, for example, in the potassium laurate-decanol-Water system [32]. Another possibility is that an isotropic phase made up of almost-spherical micelles intervenes between the two uniaxial nematic phases, as found in a closely related system [33]. Further work is needed to clarify this point.

The observation of a lamellar phase over an extended range of ϕ_s near α=1.0 in the CPC-SHN-Water and CPC-SHN1-Water systems is reminiscent of the behavior of mixtures of cationic and anionic surfactants [34–36]. Although HN^- and $HN1^-$ counterions are much shorter than the CPC molecule, their incorporation in the CPC micelle seems to have a similar effect as that of a much longer anionic surfactant.

The structure of the rhombohedral mesh phase can be described as a periodic stack of 2D networks of rod-like segments, with three rods meeting at each node [25]. Each unit cell of the 3D hexagonal lattice has a three-layer stacking (ABC) of these mesh-like aggregates. On the other hand, in the tetragonal mesh structure, four rods meet at each node. These are stacked with a two-layer repeat, with the centers of the squares in one layer placed on top of the nodes in the next [18, 19]. Upon dilution, the layers swell apart to form a lamellar structure where long-range positional correlations of the mesh structure are lost; heating also has a similar

effect. Hence, the basic structural unit of the random mesh phase (L_α^D) and the ordered mesh phases (Rh and T) can be expected to be the same.

To verify the above structure, the size of the surfactant aggregates can be calculated from the known surfactant volume fraction. The total volume of the rods in each unit cell can be equated to the surfactant volume fraction ϕ_v in the sample, resulting in the relation [12]

$$4(2-\pi)r_m^3 + 2\pi a r_m^2 - a^2 d\phi_v = 0 \tag{2.1}$$

whereas r_m is the micellar radius, d=$\frac{c}{3}$ for the Rh phase and d=$\frac{c}{2}$ for the T phase, a and c being the lattice parameters. ϕ_v was estimated from ϕ_s and densities of the constituent components. We have taken the densities of CPC, SHN and water as 0.98, 1.33 and 0.997g/cm^3 respectively to calculate ϕ_v. Density of SHN1 is taken to be the same as that of SHN. The above expression can also be used in the case of the L_α^D phase with a=d_d, given by the position of the diffuse peak, and the lamellar periodicity d. Values of r_m obtained from the above expression are listed in table 2.9. They are found to be comparable to the values of micellar radii of surfactants with the same chain length, reported in the literature [37], lending support to the proposed models of these phases.

Table 2.9 also lists the values of the ratio of the in-plane periodicity to the stacking periodicity, γ, which is defined as $\frac{d_d}{d}$ for the random mesh, $\frac{2a}{c}$ for the T phase, and $\frac{3a}{c}$ for the Rh phase. Variation of γ with ϕ_s at a few fixed values of α and temperature is shown in figure 2.13. Interestingly, the ordered mesh phases are found to occur only above a critical value of $\gamma \sim 1.5$. This behavior can be understood in terms of the spatially modulated part of the interaction potential between the layers (due to the mesh-like structure), which can be expected to decay almost exponentially with a decay length of the order of the in-plane periodicity [1]. Only when the separation between adjacent mesh-like layers is slightly lower than the mesh size will the interaction potential be strong enough to lock the layers into a 3D ordered phase. These data also show that the reappearance of the L_α^D phase at higher ϕ_s is a consequence of the decreasing in-plane periodicity (pore

TABLE 2.9: Values of micellar radius obtained using equation 1 at different composition at T=40 °C in the (a) CPC-SHN-Water and (b) CPC-SHN1-Water systems. d_d is the spacing of the diffuse peak in the L_α^D phase, d the lamellar periodicity, a and c the lattice parameters of the Rh and T phases. The ratio of the in-plane and out-of-plane periodicities, γ, is defined as d_d/d for the L_α^D phase, $3a/c$ for Rh phase and $2a/c$ for the T phase.

α	ϕ_s	ϕ_v	$d_d(nm)$	d(nm)	$a(nm)$	$c(nm)$	$r_m(nm)$	γ	phase
(a)									
0.4	65	0.64	–	–	7.49	8.96	2.07	1.67	T
–	70	0.69	–	–	7.49	8.75	2.13	1.71	T
–	80	0.79	–	–	7.28	8.65	2.27	1.68	T
0.5	45	0.44	7.633	5.62	–	–	1.91	1.36	L_α^D
–	50	0.49	7.413	5.42	–	–	1.96	1.37	L_α^D
–	54	0.53	7.393	5.32	–	–	2.03	1.39	L_α^D
–	56	0.55	7.371	5.27	–	–	2.06	1.40	L_α^D
–	60	0.59	–	–	10.18	14.62	2.36	2.09	Rh
–	65	0.64	–	–	8.03	9.22	2.16	1.74	T
–	70	0.69	–	–	6.70	8.41	1.98	1.60	T
–	80	0.79	5.096	4.17	–	–	1.92	1.22	L_α^D
0.6	50	0.48	7.398	5.69	–	–	2.01	1.30	L_α^D
–	60	0.58	7.234	5.28	–	–	2.13	1.37	L_α^D
–	70	0.69	6.561	4.72	–	–	2.10	1.39	L_α^D
(b)									
0.4	70	0.69	6.08	4.84	–	–	2.08	1.26	L_α^D
–	75	0.74	–	–	6.90	8.64	2.13	1.60	T

size), rather than being due to the screening of the inter-bilayer interactions, as proposed earlier [21]. The observed decrease in pore size with increasing ϕ_s at a low water content is consistent with earlier reports of the annealing of bilayer pores with increasing surfactant concentration [20].

Figure 2.10b shows the swelling behavior of the L_α^D phase in the CPC-SHN-Water system. It is found to be described by the relation ($d \sim {\phi_v}^{-s}$) with s∼0.63, where ϕ_v is the volume fraction of the non-aqueous components estimated from ϕ_s, using their densities. In the lamellar phase s=1.0 and in the hexagonal phase it is 0.5. The intermediate value of s found here reflects a micellar morphology in between a cylinder and a bilayer, and it is consistent with the presence of mesh-like aggregates [12, 38].

The CPC-SHN-Water system shows both kinds of ordered mesh phases, and the transformation from the ordered mesh phase to L_α via L_α^D occurs with increasing

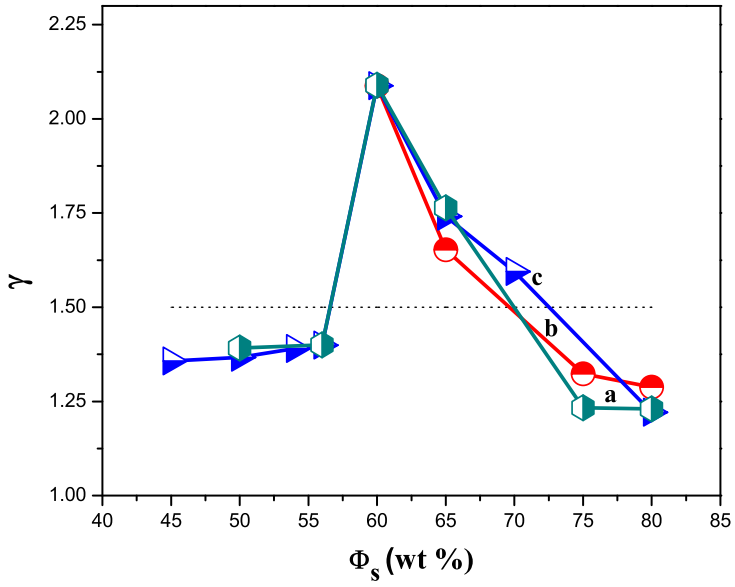

FIGURE 2.13: Variation of γ with composition in the CPC-SHN-Water system. Curves **a**, **b** and **c** correspond to α=0.5, T=50°C, α=0.4, T=50°C, and α= 0.5, T = 40°C, respectively. The dotted line indicates the boundary between the ordered and random mesh phases.

temperature, concentration, or molar ratio. Both the Rh and the T mesh phases are also seen in the SDS-water system, but unlike in the present case they occur on either side of a bicontinuous cubic phase [39]. Therefore, these two phases have been identified as being of type I and type II, respectively [5]. In contrast, all the intermediate phases reported here are of type I and are made up of networks of rod-like micelles.

The CPC-SHN1-Water system shows only the T and L_α^D mesh phases, and the Rh phase is absent here. Further, the intermediate phases in this system occur at relatively lower values of α compared to the CPC-SHN system. As mentioned earlier, counterions such as HN^- and $HN1^-$ are known to be anchored at the micellar-water interface. However, their orientations at the micellar interface will be dissimilar, due to differences in the positions of the hydrophilic moieties. This is probably responsible for the observed differences in the phase behavior of the two mixtures.

In contrast to SHN and SHN1, the addition of DHN to CPC is not able to induce any kind of intermediate phase, and the phase behavior of this system is very similar to that of pure CPC. Although the DHN molecule can also be expected to preferentially sit at the micellar interface, its negligible effect on the phase behavior suggests that the electrostatic interaction between the surfactant head groups is the dominant factor in determining the curvature of the micelle-water interface. However, the stability of the mesh phases in the CPC-SHN and CPC-SHN1 systems can not be attributed to the screening of the electrostatic repulsion between the head groups alone, since these phases are not usually seen with simple inorganic salts. Further, even some strongly binding counterions, such as salicylate and tosylate, do not induce these phases; for example, the phase diagram of the CPB-sodium salicylate and CPB-sodium tosylate systems at α=1.0 show only cylindrical worm-like micelles up to very high surfactant concentrations [40]. On the other hand, an alternative route between cylinders and bilayers, not involving any intermediate phases, has been observed in the SDS-p-toluidine hydrochloride-water system, with a gradual change of the micellar morphology from cylindrical to disc-like [33]. Thus fine tuning of many structural and interaction parameters seems to be necessary to stabilize the intermediate phases.

Theoretical considerations have shown the possibility of formation of type I mesh phases for values of the surfactant shape parameter p ($= v/al$, where v is the volume of the hydrocarbon chain, l its optimal length, and a the optimal area of the head group) between 1/2 and 2/3 [5]. These studies also indicate that the tetragonal and hexagonal mesh structures, made up of genus 2 surfaces, are also the ones energetically most favored. However, the relative stability of these two phases is still poorly understood.

Intermediate phases have also been observed in diblock copolymers, which resemble surfactant systems in many ways because of their two chemically distinct parts [41]. Experimental and theoretical studies have shown that the bicontinuous gyroid phase is stable in these systems in between the hexagonal and the lamellar phase. On the other hand, mesh phases are not stable in these systems, although a metastable hexagonal perforated lamellar phase corresponding to the

space group ($R\bar{3}m$), similar to the Rh mesh phase of surfactant-water systems, has been observed in some diblock copolymers.

2.6 Conclusion

The influence of two structurally isomeric organic salts, namely, SHN and SHN1, on the phase behavior of the cationic surfactant CPC has been investigated. Partial phase diagrams of the two systems have been constructed using POM and x-ray diffraction techniques. Intermediate phases are observed in both systems over a range of salt concentrations. All three known mesh phases are observed in the CPC-SHN-Water system, whereas only the T and L_α^D phases are seen in the CPC-SHN1-Water system. In addition, nematic phases made up of cylindrical and disc-like micelles are observed in one of the systems, for relatively low and high salt concentrations, respectively. These results show that the concentration of strongly binding counterions can be used as a control parameter to tune the spontaneous curvature of the micellar aggregates and stabilize different intermediate phases.

Bibliography

[1] J. Israelachvili, *Intermolecular and Surface Forces*, 2nd ed. Academic Press, London (1991).

[2] J. M. Seddon and R. H. Templer, *in Handbook of Biological Physics*, edited by R. Lipowsky and E. Sackmann, Elsevier,Amsterdam (1995).

[3] M. C. Holmes and M. S. Leaver, *in Bicontinuous Liquid Crystals*, edited by M. L. Lynch and P. T. Spicer, Surfactant Science Series, **Vol. 127**, CRC Press, Boca Raton, FL, pp. 1539 (2005).

[4] V. Luzzati, *in Biological Membranes*, edited by D. Chapman, Academic Press, London, (1968).

[5] S. T. Hyde, *Pure Appl. Chem.* **64**, 1617 (1992).

[6] V. Luzzati, H.Mustachhi, A. E. Skoulios, and F. Husson, *Acta Crystallogr.*, **13**, 660 (1960).

[7] Y. Hendrikx and J. Charvolin, *J. Phys.*, **42**, 1427 (1981).

[8] G. Chidichimo, N. A. P. Vaz, Z. Yaniv, and J. W. Doane, *Phys.Rev. Lett.*, **49**, 1950 (1982).

[9] S. S. Funari, M. C. Holmes, and G. J. T. Tiddy, *J. Phys. Chem.*, **96**, 11029 (1992).

[10] S. S. Funari, M. C. Holmes, and G. J. T. Tiddy, *J. Phys. Chem.*, **98**, 3015 (1994).

[11] J. Burgoyne, M. C. Holmes, and G. J. T. Tiddy, *J. Phys. Chem.*, **99**S, 6054 (1995).

[12] C. E. Fairhurst, M. C. Holmes, and M. S. Leaver, *Langmuir*, **13**, 4964 (1997).

[13] S. S. Funari and G. Rapp, *Proc. Natl. Acad. Sci. USA*, **96**, 7756 (1999).

[14] M. Leaver, A. Fogden, M. C. Holmes, and C. Fairhurst, *Langmuir*, **17**, 35 (2001).

[15] M. Imai, K. Nakaya, T. Kawakatsu, and H. Seto, *J. Chem. Phys.*, **119**, 8103 (2003).

[16] M. Imai, K. Sakai, M. Kikuchi, K. Nakaya, A. Saeki, and T. Teramoto, *J. Chem. Phys.*, **122**, 214906 (2005).

[17] M. Baciu, U. Olsson, M. S. Leaver, and M. C. Holmes, *J. Phys. Chem. B*, **110**, 8184 (2006).

[18] P. Kékicheff and B. Cabane, *J. Phys.*, 48, 1571 (1987).

[19] P. Kékicheff and G. J. T. Tiddy, *J. Phys. Chem.*, **93**, 2520 (1989).

[20] M. S. Leaver andM. C. Holmes, *J. Phys. II France*, **3**, 105 (1993).

[21] S. Puntambekar, M. C. Holmes, and M. S. Lever, *Liq. Cryst.*, **27**, 743 (2000).

[22] R. Zhou, M. C. Holmes, S. Puntambekar, M. S. Lever, and R. McCabe, *Soft Matter*, **8**, 5835 (2012).

[23] B. F. B. Silva, E. F. Marques, and U. Olsson, *Soft Matter*, **7**, 225 (2011).

[24] R. Krishnaswamy, S. K. Ghosh, S. Lakshmanan, V. A. Raghunathan, and A. K. Sood, *Langmuir*, **21**, 10439 (2005).

[25] S. K. Ghosh, R. Ganapathy, R. Krishnaswamy, J. Bellare, V. A. Raghunathan, and A. K. Sood, *Langmuir*, **23**, 3606 (2007).

[26] S. K. Ghosh and V. A. Raghunathan, *Langmuir*, **25**, 2622 (2009).

[27] R. Oda, J. Narayanan, P. A. Hassan, C. Manohar, R. A. Salkar, F. Kern, and S. J. Candau, *Langmuir*, **14**, 4364 (1998).

[28] M. E. Cates and S. J. Candau, *J. Phys.: Condens.Matter*, **2**, 6869 (1990).

[29] T. Shikata, H. Hirata, and T. Kotaka, *Langmuir*, **4**, 354 (1988).

[30] A. Khatory, F. Lequeux, F. Kern, and S. J. Candau, *Langmuir*, **9**, 1456 (1993).

[31] V. Hartmann and R. Cressely, *J. Phys II France*, **7**, 1087 (1997).

[32] L. J. Yu and A. Saupe, *Phys. Rev. Lett.*, **45**, 1000 (1980).

[33] S. K. Ghosh, V. Rathee, R. Krishnaswamy, V. A. Raghunathan, and A. K. Sood, *Langmuir*, **25**, 8497 (2009).

[34] E. W. Kaler, K. L. Herrington, A. K. Murthy, and J. A. N. Zasadzinski, *J. Phys. Chem.*, **96**, 6698 (1992).

[35] M. T. Yatcilla, K. L. Herrington, L. L. Brasher, and E.W. Kaler, *J. Phys. Chem.*, **100**, 5874 (1996).

[36] K. L. Herrington, E. W. Kaler, D. D. Millar, J. A. Zasadzinski, and S. Chiruvolu, *J. Phys. Chem.*, **97**, 13792 (1993).

[37] F. R. Husson and V. Luzzati, *J. Phys. Chem.*, **68**, 3504 (1964).

[38] S. T. Hyde, *J. Phys. Colloq.*, **51**, C7-209 (1990).

[39] P. Kékicheff and B. Cabane, *Acta Crystallogr.*, **B44**, 395 (1988).

[40] S. K. Ghosh, Ph.D. thesis, Jawaharlal University, New Delhi (2007).

[41] A. J. Meuler, M. A. Hillmyer, and F. S. Bates, *Macromolecules*, **42**, 7221 (2009).

Chapter 3

Salt-induced isotropic phase of amphiphile bilayers

3.1 Introduction

Due to their amphiphilic nature, surfactant molecules in an aqueous solution can form a large variety of different aggregates, as described in the first chapter. The shape of these aggregates is determined by that of the amphiphile, which is usually described in terms of the shape parameter $p = v/al$, where v is the volume of the hydrocarbon chain of the amphiphile, a the optimal head group area and l the typical chain length in the aggregate [1]. Bilayers are formed in dilute solutions by amphiphiles with $p \sim 1$, such as double-tailed phospholipids which are the major constituents of biomembranes. It is also the preferred aggregate morphology in mixtures of single-tailed cationic and anionic amphiphiles. In these 'catanionic' systems, bilayers in the form of unilamellar vesicles (ULV) are present in dilute solutions near the equimolar composition of the two amphiphiles [2]. Organic salts, such as 3-hydroxy-2-sodium naphthoate (SHN), can be considered as an extreme limit of an ionic amphiphile. While they do not self-assemble in water to form micelles, they have a preference to sit at the surface of the micelle and hence affect the properties of the micelle-water interface [3]. Such molecules, often called

hydrotropes, decrease the spontaneous curvature of the micellar surface leading to the formation of long worm-like micelles (WLM) in many amphiphiles [4]. In some cases the decrease in the spontaneous curvature is large enough to stabilize bilayers [5].

One of the most common phases formed by bilayers is the periodically stacked lamellar phase [6]. In the absence of any osmotic pressure, the lamellar periodicity (d) of these systems is determined by the balance between different inter-bilayer interactions, namely, electrostatic repulsion, van derWaals attraction, steric repulsion and hydration repulsion [1]. Steric repulsion arises from thermal undulations of the bilayers [7], whereas the short-ranged hydration force arises from the ordering of water molecules at the bilayer surface and from thermally excited protrusion of molecules out of the bilayer. Bilayers also exhibit isotropic phases without any long-range positional or orientational order, such as a dispersion of ULV and the sponge (L_3) phase [8]. The sponge phase, made up of a random network of bilayers, is found in some very dilute amphiphilic systems in the presence of a cosurfactant, such as a short-chain alcohol, and/or an inorganic salt, such as NaCl [9–11]. In these systems electrostatic interactions are screened out by the salt and the bilayer flexibility is enhanced by the cosurfactant; as a result inter-bilayer interactions are dominated by steric repulsion.

A variant of sponge phase, characterized by small average inter-bilayer spacing and short-range positional correlations, has been recently reported in a few systems dominated by attractive interaction [12, 13]. Our motive is to check whether the appearance of this kind of isotropic phase of bilayers is generic or specific to these system. For this purpose, we have studied the phase behavior of a aqueous solutions of cationic surfactant in the presence of very high salt concentration.

This chapter deals with structure and stability of a novel isotropic phase seen in the CPC-SHN-Water system at very high salt concentration. Before we discuss our experimental results, we summarize earlier studies on the sponge phase in section 3.2. Experimental methods and chemicals that we have used are described in section 3.3. Our experimental results on the CPC-SHN-Water system at high

salt concentration are described in section 3.4. We discuss our results in section 3.5. Section 3.6 contains conclusions that can be drawn from these studies.

3.2 Earlier Studies

The sponge phase (L_3) was discovered by J. Rang and R. Morgan in the $C_{10}E_4$-Water system [14]. Generally the L_3 phase is encountered when dilute L_α phase is made more lipophilic by changing the physico-chemical parameter of the system. It is easily done by changing the cosurfactant/surfactant ratio or increasing the salt concentration in the case of ionic surfactants or by increasing the temperature in the case of non-ionic surfactants [15–17]. But there are many known situations, where the L_3 phase is not observed by making the L_α phase more lipophilic [18]. L_3 phase is generally seen in zwitterionic surfactants with intermediate-chain alcohol, but not observed with alcohols of longer chain length or alcohol with perfluorinated chains [19]. L_3 phase is also reported in block copolymer systems [20]. The first experimental study proposing that the surfactant and cosurfactant molecules in the L_3 phase form a continuous network structure was done by Porte et al. [21], independently of a theoretical proposition by Cates et al. [22]. The phase can therefore be considered as a molten Lα phase in which the aqueous part and the surfactant part are continuous in nature; it is therefore a bicontinuous phase.

In ternary phase diagrams, the L_3 phase can usually be observed over a large concentration range or volume fraction but only over an extremely narrow cosurfactant/surfactant ratio [23, 24]. The existence of the phase is extremely sensitive to ionic charges. Usually it becomes unstable when in neutral cosurfactant/surfactant systems a few percent of the nonionic surfactant is replaced by an ionic surfactant. The phase also is shear sensitive, and high shear can transform the L_3 phase into a metastable L_α phase that relaxes back into the L_3 phase when the shear is stopped [25–27].

The sponge phase has also been found in the charged system consisting of calcium dodecylsulfate/alcohol and water [28, 29]. Interestingly, another variant of the L_3

phase has been reported in a ternary system consisting Ca-or Mg-salts of anionic surfactants, branched cosurfactants and water [30, 31] system. One important difference being that in this phase, a broad correlation peak, occurs at about the same position as the sharper peak in the L_α phase while in the L_3 sponge phase, the spacing corresponding to the broad correlation peak is about 1.5 times the corresponding lamellar phase spacing.

3.3 Experimental

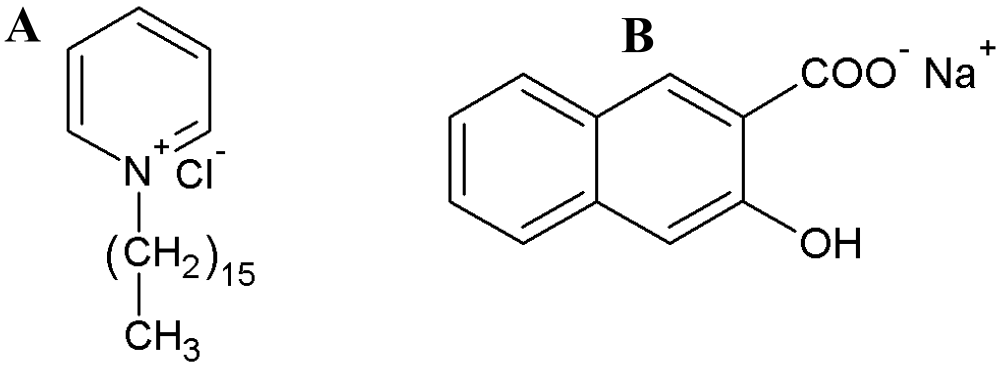

FIGURE 3.1: Chemical structure of (**A**) cetylpyridinium chloride (CPC) (**B**) 3-hydroxy-2-sodium naphthoate (SHN).

Cetylpyridinium chloride (CPC) and 3-hydroxy-2-naphthoic acid (HNA) were purchased from Sigma-Aldrich. 3-hydroxy-2-sodium-naphthoate (SHN) was prepared by adding equivalent amount of an aqueous solution of sodium hydroxide (NaOH) to an ethanol solution of HNA. The chemical structures of the molecules are shown in figure 3.1. Ternary solutions were prepared by adding appropriate amount of deionized water in the mixture of CPC and SHN. The sample tube was then sealed and left in an incubator at 40°C for more than two weeks to equilibrate. For polarizing optical microscopy (POM) studies samples were taken in between cover slip and glass slide. Small-angle X-ray scattering (SAXS) studies, covering a range of the scattering vector (q) from 0.01 to 5.0 nm^{-1}, were carried out using a Hecus S3-Micro system, equipped with a 1D position-sensitive detector (MBraun PSD50M).

Typical exposure time was 20 min. In the cryo-SEM experiments, samples were cryo-freezed by quickly dipping them into liquid nitrogen. The frozen samples were then transferred to a PP3000T cryo unit (Quorum Technologies) which is maintained at -160°C, where it is fractured with a cold knife. The fractured samples were sublimated at -90°C for 5 minutes and then sputtered with platinum for 90 seconds which lead to a coating of nanometer thickness on the fractured sample surface. The samples were imaged using a Zeiss Ultra Plus. Cryo-SEM setup maintained at -180°C. UV-vis absorption spectra were recorded with a Lambd25 spectrometer from PerkinElmer.

3.4 Results

3.4.1 CPC-SHN-Water system

The phase behavior of mixtures of CPC and SHN was studied at different values of the molar ratio ($\alpha = \frac{[SHN]}{[CPC]}$) of the two components. For each α the total concentration of the non-aqueous components ($\phi_s = \frac{(CPC+SHN)}{(CPC+SHN+Water)}$x100) was varied from 20 to 80 wt%. The polarizing optical microscopy (POM) texture of each sample was monitored from 25 to 80°C. The structure of the phases was confirmed by using diffraction studies and POM texture of the sample.

3.4.1.1 Phase behavior at α=1.5

Figure 3.2A shows the temperature$-\phi_s$ phase diagram of the system at α=1.5. For 20 $\leq\phi_s<$30 small angle x-ray scattering (SAXS) and polarizing optical microscopy (POM) studies indicate the occurrence of an isotropic phase over all the temperature range studied. Henceforth, we shall refer this isotropic phase as L_x. This phase shows an optically isotropic texture (Fig. 3.4B) and exhibits low birefringence under flow. Its SAXS pattern shows a broad peak (Fig. 3.3A(a and b)). For 50$<\phi_s<$75 it exhibits a lamellar (L_α) phase over all the temperature range studied. Its SAXS pattern shows two sharp peaks in the small wave vector (q)

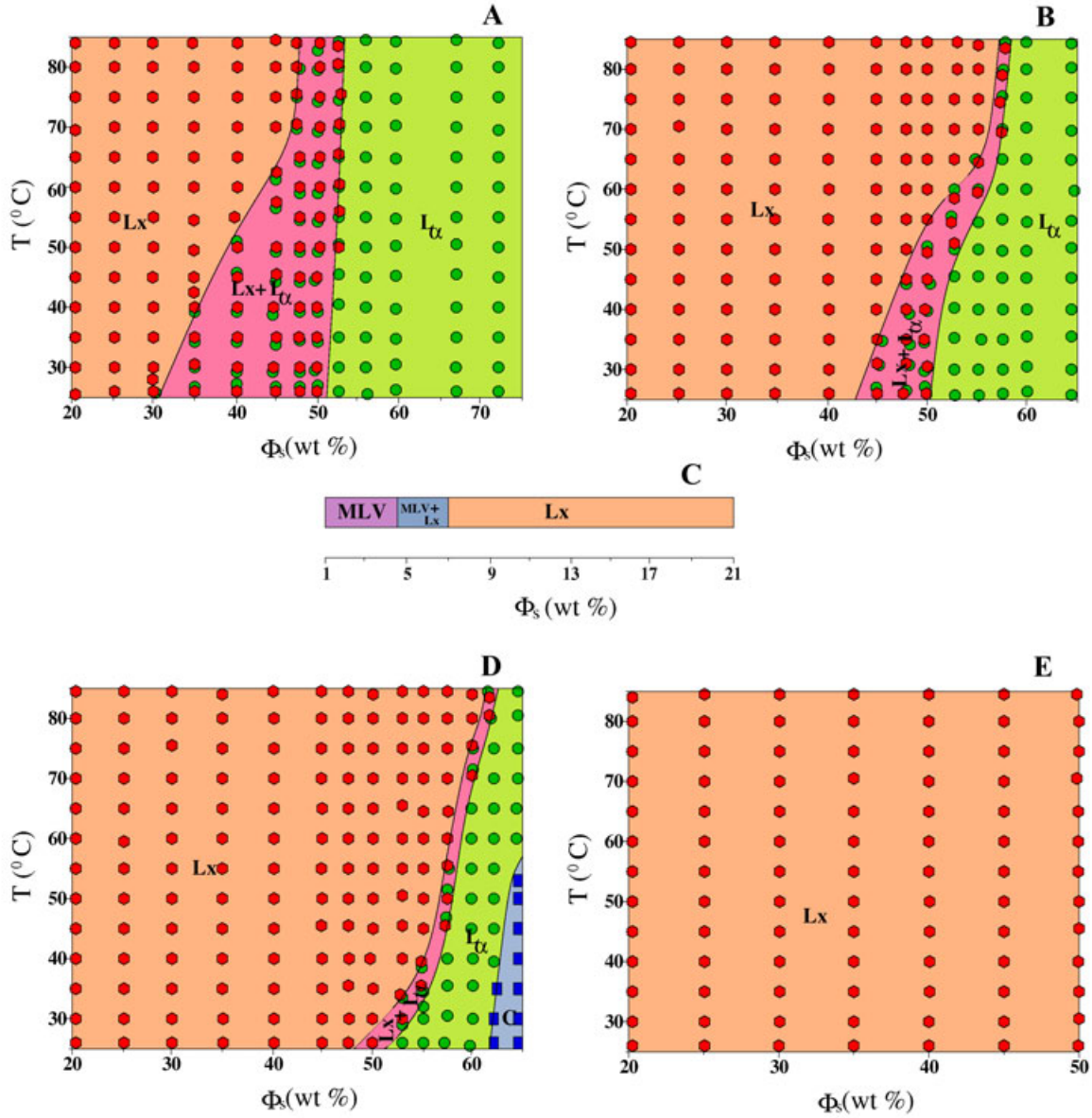

FIGURE 3.2: Partial phase diagram of the CPC-SHN-Water system at: α=1.5 (**A**), α=1.75 (**B**), α=2 (**C**), α=2 (**D**) and α=2.25 (**E**). L_x, L_α, MLV and C, denote the isotropic phase of the bilayer, lamellar, multilamellar vesicle and crystalline phases, respectively.

region with their q in the ratio 1:2 (Fig. 3.3A(c-f)). Oily streaks texture found under crossed POM (similar to Fig. 3.4D) confirms the occurrence of the lamellar phase. Figure 3.5A shows the variation of the lamellar periodicity (d) of the L_α phase with ϕ_s. It is found to be described by the relation ($d \sim \phi_v^{-s}$) with $s \sim 1$, where ϕ_v is the volume fraction of the non-aqueous component estimated from ϕ_s, by using the densities of the components. For $30 < \phi_s < 50$, L_α and L_x phases are

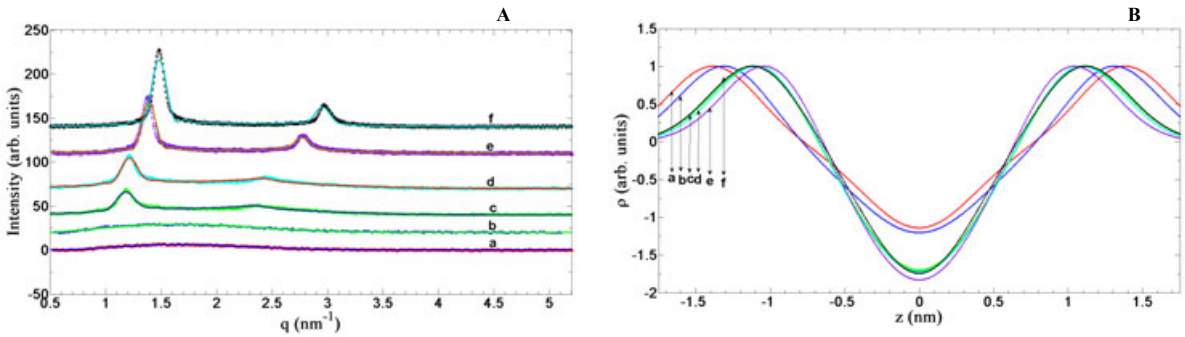

FIGURE 3.3: (**A**) X-ray diffraction patterns of the CPC-SHN-Water system at α=1.5, T=30°C corresponding to ϕ_s=20 (**a**), ϕ_s=30 (**b**),ϕ_s=56.8 (**c**), ϕ_s=60 (**d**), ϕ_s=67.19 (**e**), ϕ_s=72.15 (**f**). The solid lines are fits to the model, obtained as described in chapter 1. (**B**) Electron density profiles obtained from fitting the data to the model, corresponding to ϕ_s=20 (**a**), ϕ_s=30 (**b**) ϕ_s=56.8 (**c**), ϕ_s=60 (**d**), ϕ_s=67.19 (**e**), ϕ_s=72.15 (**f**).

TABLE 3.1: Values of parameters for the diffraction data at α=1.5 and T=30°C of the CPC-SHN-Water system obtained from the fit to the model of lamellar (L_α) phase.

ϕ_s	σ_h(nm)	σ_c(nm)	$(\rho_c)/(\rho_h)$	$z_h(nm)$	η	N	N_d	$d(nm)$	Phase
20	0.30 ±0.02	0.37±0.02	-1.14±0.08	1.38±0.04	–	–	0.77± 0.05	–	L_x
30	0.30 ±0.02	0.43±0.02	-1.19±0.08	1.30±0.04	–	–	0.82± 0.05	–	L_x
57	0.31 ±0.02	0.41±0.02	-1.63 ±0.08	1.08±0.04	0.29± 0.02	6±1	1.66± 0.02	5.31	L_α
60	0.30 ±0.02	0.41±0.02	-1.64±0.08	1.07±0.04	0.28± 0.02	7±1	1.83± 0.05	5.16	L_α
67	0.30 ±0.02	0.41±0.02	-1.70 ±0.08	1.00±0.04	0.11± 0.02	9±1	0.88± 0.02	4.52	L_α
72	0.30 ±0.02	0.36±0.02	-1.72 ±0.08	1.11±0.04	0.06± 0.02	9±1	2.05± 0.02	4.24	L_α

found to be coexisting at lower temperatures. This sample exhibits focal conics streaks with black droplets under crossed POM and these droplets are found to grow with increasing temperature (Fig. 3.4C). This coexistence region transforms into a pure L_x phase on heating.

3.4.1.2 Phase behavior at α=1.75

Figure 3.2B shows the temperature−ϕ_s phase diagram of the system at α=1.75. For 20 $\leq\phi_s<$40 it shows the isotropic (L_x) phase over the temperature range studied. For 50 $\leq\phi_s<$65 it exhibits a lamellar phase (L_α) phase at lower temperatures which transforms into an isotropic phase on heating. The L_α to L_x transition temperature increases with decreasing water content. Variation of the lamellar

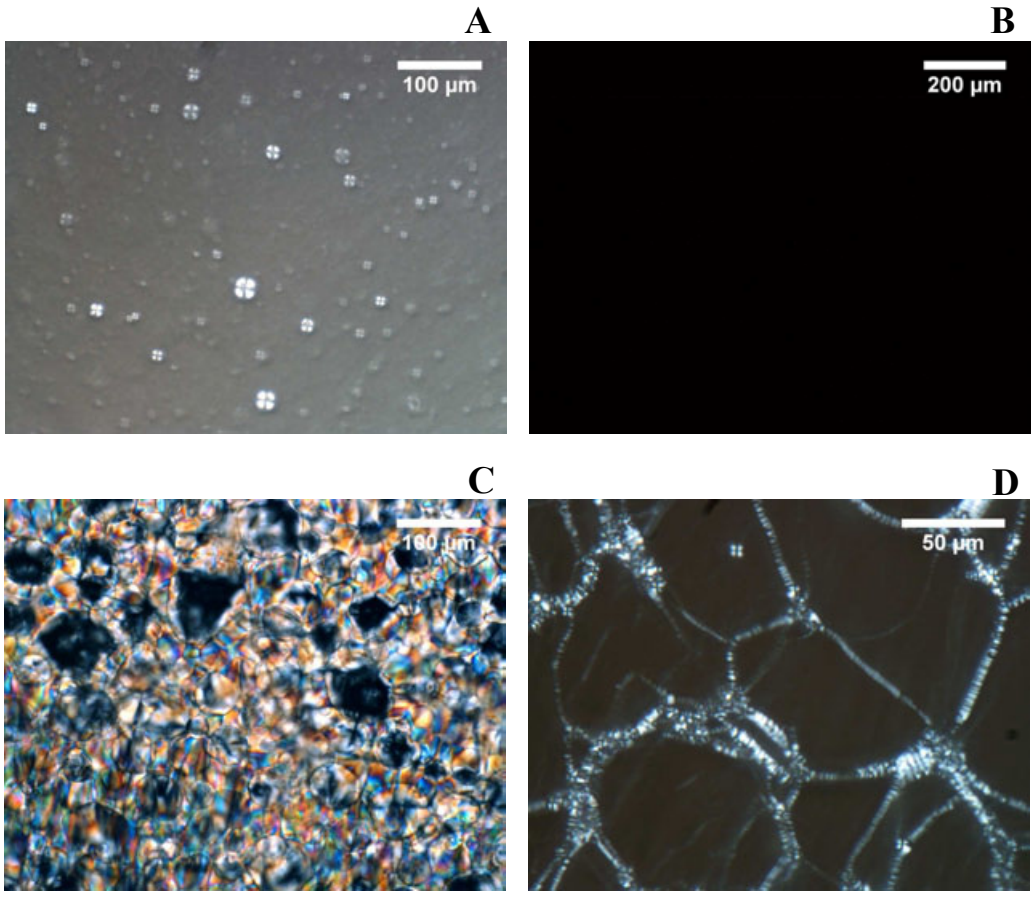

FIGURE 3.4: Polarizing optical microscopy textures of (**A**) MLV at α=2, ϕ_s=3 and T=30°C, (**B**) L_x phase at α=2, ϕ_s=40 and T=30°C, (**C**) L_x+L_α phase at α=1.5, ϕ_s=45 and T=40° and (**D**) L_α phase at α=2, ϕ_s=60 and T=30°C in the CPC-SHN-Water system

periodicity (d) of the L_α phase with ϕ_s is shown in figure 3.5B. It is found to be described by the relation d$\sim{\phi_v}^{-s}$ with s$\sim$1.

3.4.1.3 Phase behavior at α=2

Figure 3.2D shows the temperature$-\phi_s$ phase diagram of the system at α=2. For 20 $\leq\phi_s<$50 it shows the L_x phase over the temperatures range studied. SAXS pattern shows a broad peak at higher water content and an additional broad peak is found to develop with decreasing water content (Fig. 3.6A). For 55 $\leq\phi_s<$65 it exhibits a L_α phase at lower temperatures which transforms into a L_x phase on heating. This transition is found to be reversible on cooling. Lamellar phase

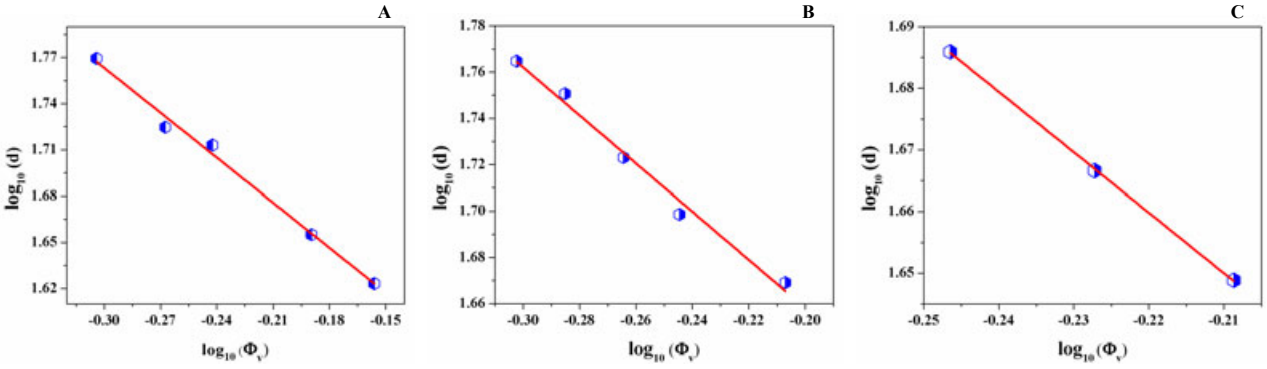

FIGURE 3.5: Variation of lattice spacing of the L_α phase with volume fraction in the CPC-SHN-Water system at: α=1.5 and T=30 °C (**A**), α=1.75 and T=30°C (**B**) and α=2 and T=57.5 °C (**C**).

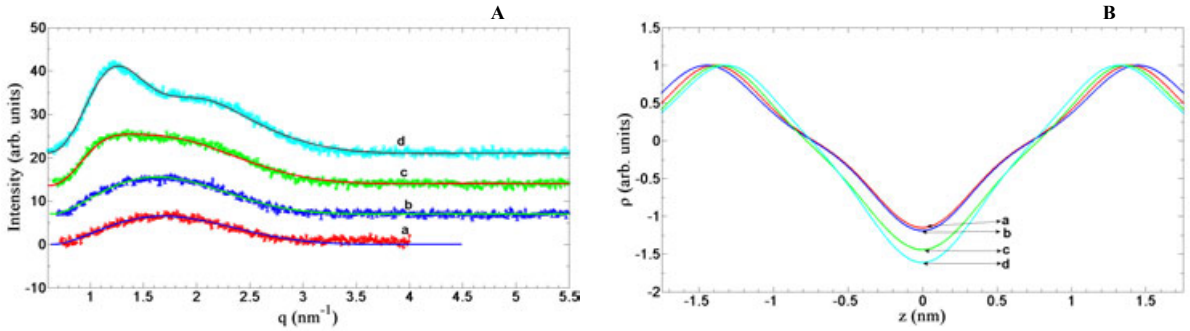

FIGURE 3.6: (**A**) X-ray diffraction patterns of the CPC-SHN-Water system at α=2, T=30°C corresponding to ϕ_s=20 (**a**), ϕ_s=30 (**b**), ϕ_s=40 (**c**), ϕ_s=50 (**d**). The solid lines are fits to the model. (**B**) Electron density profiles obtained from the fit corresponding to ϕ_s=20 (**a**), ϕ_s=30 (**b**), ϕ_s=40 (**c**), ϕ_s=50 (**d**).

appearing at lower water content, shows two sharp peaks in the small q region. The positions of the broad peak of the L_x phase and the sharp peak of the L_α phase are found to be the same (Fig. 3.7A). Figure 3.5C shows the variation of the lamellar periodicity (d) of the L_α phase with ϕ_s. It is found to be described by the relation $d \sim \phi_v^{-s}$ with $s \sim 1$.

Figure 3.2C shows the phase diagram of the system at α=2 and 30°C for $1 \leq \phi_s \leq 20$. For $1 \leq \phi_s \leq 4$, samples are turbid and exhibit maltese-cross texture under POM (Fig. 3.4A) confirming the occurrence of a multi-lamellar vesicle (MLV) dispersion. For $8 \leq \phi_s \leq 20$ samples are translucent and optically isotropic and their SAXS patterns show a broad peak similar to that of the figure 3.6A(a), confirming the

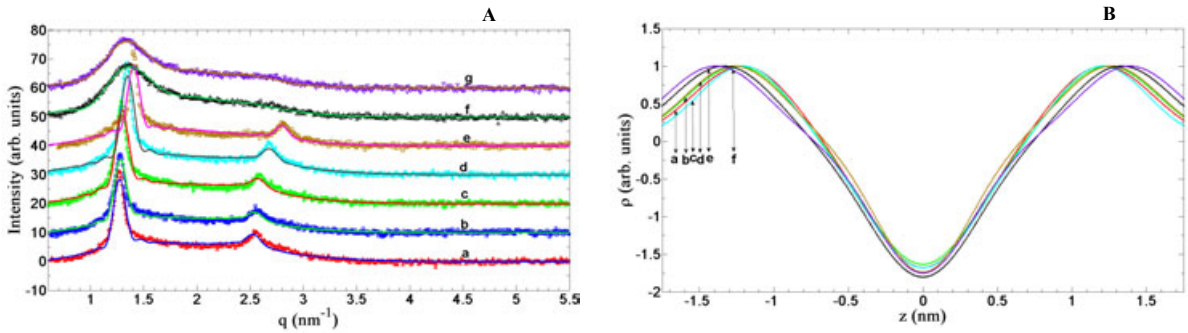

FIGURE 3.7: (**A**) X-ray diffraction patterns of the CPC-SHN-Water system at α=2, ϕ_s=60 corresponding to T=30°C (**a**), T=40°C (**b**), T=50°C (**c**), T=60°C (**d**), T=75°C (**e**), T=77°C (**f**), T=80°C (**g**). The solid lines are fits to the model. (**B**) Electron density profiles obtained from the fit corresponding to T=30°C (**a**), T=40°C (**b**),T=50°C (**c**), T=60°C (**d**), T=75°C (**e**), T=77°C (**f**), T=80°C (**g**).

TABLE 3.2: Values of parameters for the diffraction data at α=2 and T=30°C of the CPC-SHN-Water system obtained from the fit to the model of lamellar (L_α) phase.

ϕ_s	σ_h(nm)	σ_c(nm)	$(\rho_c)/(\rho_h)$	$z_h(nm)$	η	N	N_d	$d(nm)$	Phase
20	0.30 ±0.02	0.32±0.02	-1.15±0.08	1.07±0.04	–	–	-1.32± 0.02	–	L_x
30	0.32 ±0.02	0.32±0.02	-1.19±0.08	1.07±0.04	–	–	0.07± 0.02	–	L_x
40	0.30 ±0.02	0.37±0.02	-1.44±0.08	1.48±0.04	1.79± 0.02	2±0	-1.17± 0.02	4.79	L_x
50	0.31 ±0.02	0.36±0.02	-1.61±0.08	1.48±0.04	0.60± 0.02	2±0	-0.41± 0.02	5.08	L_x

TABLE 3.3: Values of parameters for the diffraction data at α=2 and ϕ_s=60 of the CPC-SHN-Water system obtained from the fit to the model of lamellar (L_α) phase.

T (°C)	σ_h(nm)	σ_c(nm)	$(\rho_c)/(\rho_h)$	$z_h(nm)$	η	N	N_d	$d(nm)$	Phase
30	0.34 ±0.02	0.36±0.02	-1.67±0.08	1.21±0.04	0.17± 0.02	9±1	7.70± 0.05	4.94	Lα
40	0.35 ±0.02	0.37±0.02	-1.62±0.08	1.24±0.04	0.18± 0.02	9±1	6.64± 0.05	4.91	Lα
50	0.34 ±0.02	0.36±0.02	-1.63±0.08	1.24±0.04	0.19± 0.02	9±1	6.87± 0.05	4.85	Lα
60	0.31 ±0.02	0.36±0.02	-1.67±0.08	1.20±0.04	0.16± 0.02	9±1	8.22± 0.05	4.66	Lα
75	0.33 ±0.02	0.31±0.02	-1.74±0.08	1.26±0.04	0.09± 0.02	10±1	15.68± 0.05	4.48	Lα
77	0.34 ±0.02	0.36±0.02	-1.80 ±0.08	1.33±0.04	0.39± 0.02	3±0	0.67± 0.02	4.59	L_x
80	0.34 ±0.02	0.36±0.02	-1.75 ±0.08	1.39±0.04	0.22± 0.02	3±0	1.89± 0.02	4.72	L_x

occurrence of the L_x phase. However, for 4<ϕ_s<8, MLV are found to be coexist with the L_x phase.

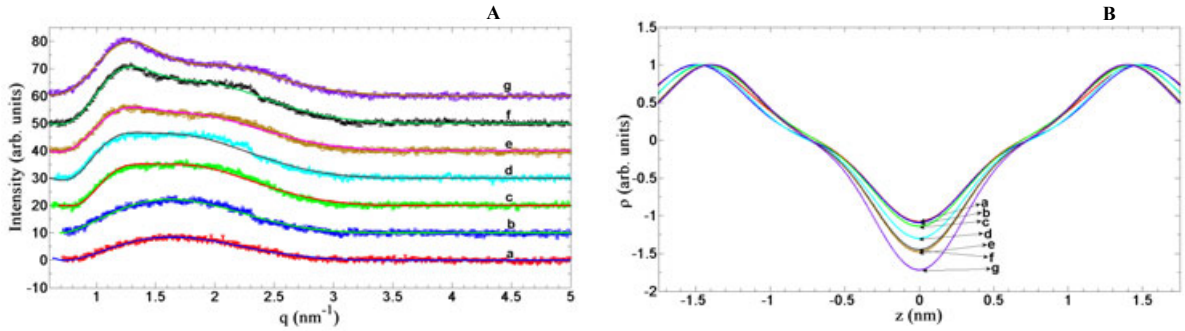

FIGURE 3.8: (**A**) X-ray diffraction patterns of the CPC-SHN-Water system at α=2.25, T=30 °C corresponding to ϕ_s=20 (**a**), ϕ_s=25 (**b**), ϕ_s=30 (**c**), ϕ_s=35 (**d**), ϕ_s=40 (**e**), ϕ_s=45 (**f**), ϕ_s=50 (**g**). The solid lines are fits to the model. (**B**) Electron density profiles obtained from the fit corresponding to ϕ_s=20 (**a**), ϕ_s=25 (**b**), ϕ_s=30 (**c**), ϕ_s=35 (**d**), ϕ_s=40 (**e**), ϕ_s=45 (**f**), ϕ_s=50 (**g**).

TABLE 3.4: Values of parameters for the diffraction data at α=2.25 and T=30°C of the CPC-SHN-Water system obtained from the fit to the model of lamellar (L_α) phase.

ϕ_s	σ_h(nm)	σ_c(nm)	$(\rho_c)/(\rho_h)$	$z_h(nm)$	η	N	N_d	$d(nm)$	Phase
20	0.35 ±0.02	0.30±0.02	-1.08±0.08	1.48±0.04	–	–	-0.29± 0.02	–	L_x
25	0.32 ±0.02	0.30±0.02	-1.09±0.08	1.49±0.04	–	–	-0.20± 0.02	–	L_x
30	0.33 ±0.02	0.30±0.02	-1.14±0.08	1.43±0.04	1.61± 0.02	2 ±0	-1.62± 0.02	5.01	L_x
35	0.30 ±0.02	0.30±0.02	-1.30±0.08	1.46±0.04	1.77± 0.02	2 ±0	-1.58± 0.02	4.97	L_x
40	0.30 ±0.02	0.30±0.02	-1.48±0.08	1.41±0.04	1.26± 0.02	2 ±0	-1.20± 0.02	4.93	L_x
45	0.30 ±0.02	0.30±0.02	-1.45±0.08	1.40±0.04	0.89± 0.02	2 ±0	-1.03 ± 0.02	5.00	L_x
50	0.30 ±0.02	0.30±0.02	-1.72±0.08	1.39±0.04	0.49± 0.02	2 ±0	-0.22 ± 0.02	5.00	L_x

3.4.1.4 Phase behavior at α=2.25

Figure 3.2E shows the temperature−ϕ_s phase diagram of the system at α=2.25. SAXS and POM studies confirm the occurrence of a L_x over the temperature and concentrations range studied. At higher water content SAXS patterns shows a broad peak. An additional broad peak is found to develop with decreasing water content (Fig. 3.8A).

3.4.1.5 Cryo-SEM studies

Cryo-SEM studies have been carried out in the MLV, L_x and L_α phases at α=2. Figures 3.10(D1&D2) show cryo-SEM micrographs of the L_α phase. It clearly

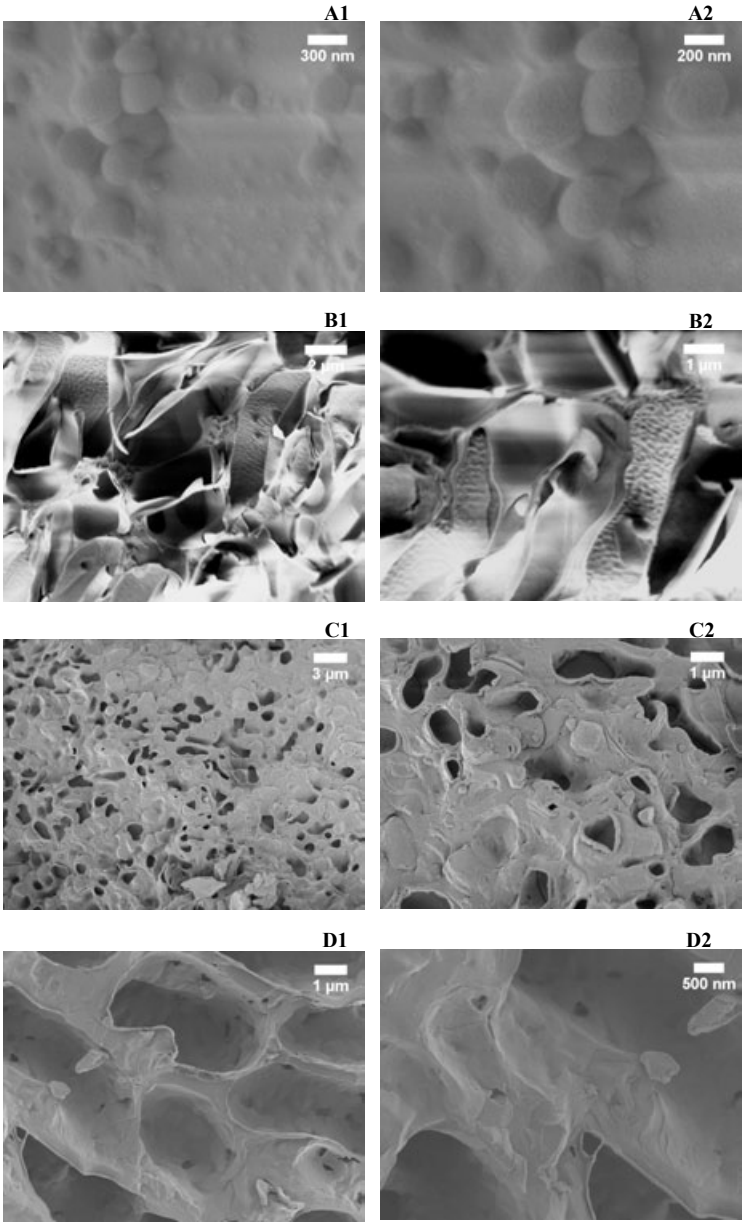

FIGURE 3.9: Cryo-SEM micrographs of MLV (**A1 and A2**) at ϕ_s=3, and L_x phase((**B1 and B2**), (**C1 and C2**) and (**D1 and D2**) at ϕ_s=10, 15 and 20 respectively) in the CPC-SHN-Water system at α=2

show the basic feature of the lamellar phase, i.e., a regular stack of bilayers. However, resolution is not enough to measure the thickness of the bilayer from the micrograph. Micrograph at higher water content in the L_x phase, show connected droplet structure and confirms that the average size of the droplets decreases on decreasing the water content(Figs. 3.9(C1&C2), 3.9(D1&D2), 3.10(A1&A2) and

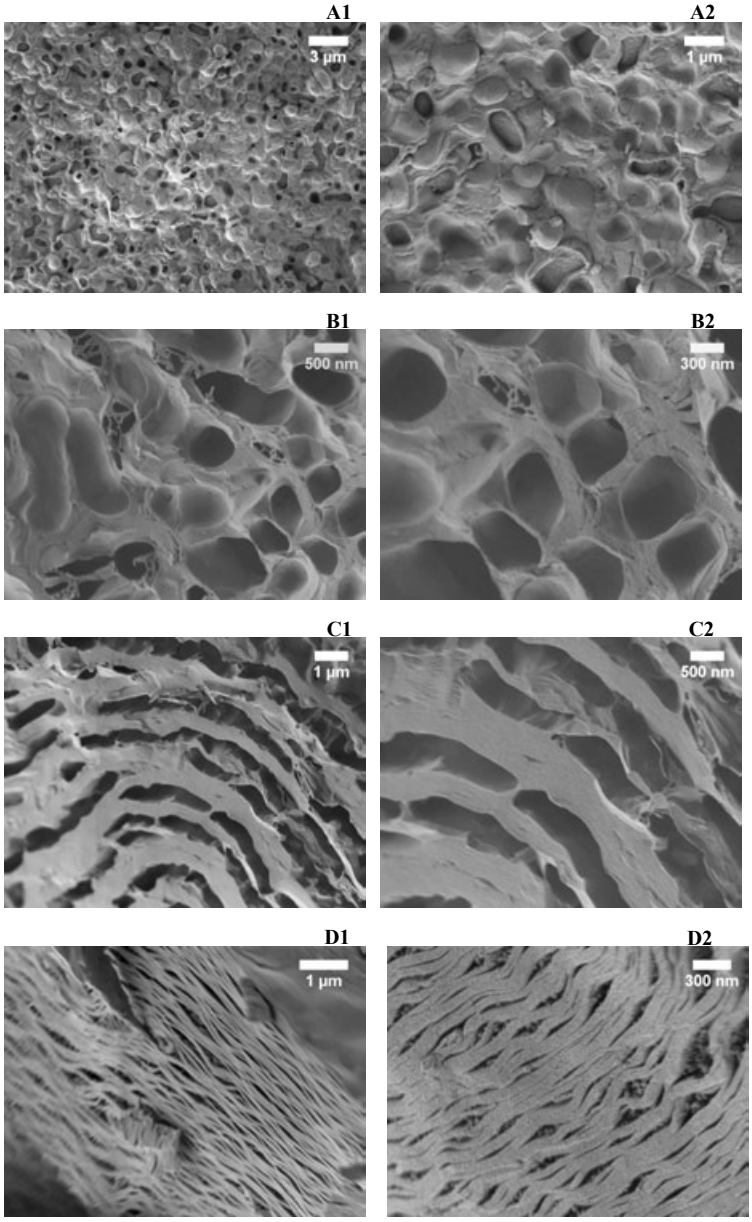

FIGURE 3.10: Cryo-SEM micrographs of L_x ((**A1 and A2**) and (**B1 and B2**) at ϕ_s=30 and 50 respectively) and L_α phase ((**C1 and C2**) and (**D1 and D2**) at ϕ_s=55, and 60 respectively) in the CPC-SHN-Water system at α=2.

3.10(B1&B2)). Still, at higher water content in the L_x phase, cryo-SEM micrographs (Figs. 3.9(B1&B2)) show uncorrelated bilayers or uncorrelated bilayer bundles. While, at very high water content cryo-SEM micrographs (Fig. 3.9(A1&A2)) show MLVs, which is consistent with SAXS and POM studies.

3.4.2 CPC-SHN-NaCl-Water system: Effect of salt

Effect of the salt (NaCl) on the phase behavior of the CPC-SHN-Water system has been studied at very high concentration of SHN. It has been done by varying the concentrations of the salt (NaCl) at α=2, ϕ_s=3 (starting from MLV dispersion) and at α=2, ϕ_s=20 (starting from L_x phase).

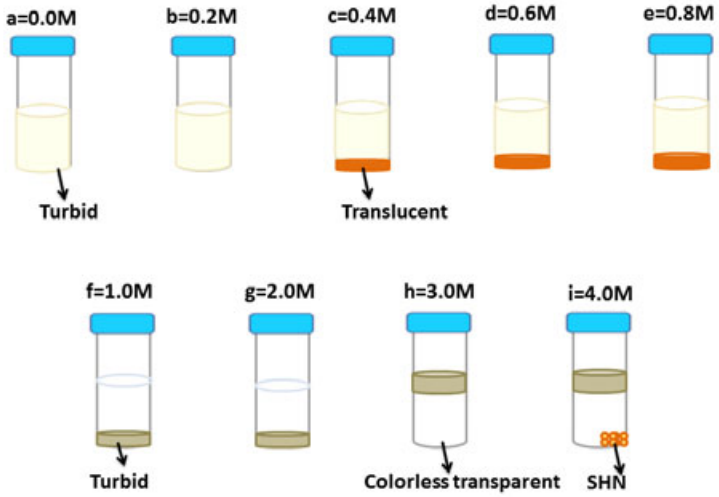

FIGURE 3.11: The different phases in the CPC-SHN-NaCl-water system at α=2, ϕ_s=3 and T=30°C: MLV phase at 0.0M (a), MLV phase at 0.2M (b), MLV phase coexisting with L_x phase at 0.4M (c), 0.6M (d) 0.8M (e), isotropic phase floating at the top at 1M (f) and at 2M (g), collapsed MLV phase floating at the top at 3M (h) and collapsed MLV phase floating at the top at 4M with the excess SHN at the bottom (i).

TABLE 3.5: Values of parameters for the diffraction data at α=2, ϕ_s=3 and T=30°C of the CPC-SHN-NaCl-Water system obtained from the fit to the model of lamellar (L_α) phase.

Nacl [M]	σ_h(nm)	σ_c(nm)	$(\rho_c)/(\rho_h)$	$z_h(nm)$	η	N	N_d	$d(nm)$	Phase
0.0	0.30 ±0.02	0.36±0.02	-1.23±0.08	1.17±0.04	–	–	-1.33± 0.02	–	MLV
0.6	0.30 ±0.02	0.36±0.02	-1.36±0.08	1.13±0.04	–	–	-0.66± 0.02	–	MLV+L_x
1.0	0.30 ±0.02	0.34±0.02	-1.57±0.08	1.26±0.04	1.31± 0.02	2±0	-0.56± 0.02	5.54	I+MLV
2.0	0.30 ±0.02	0.32±0.02	-1.92±0.08	1.28±0.04	0.86± 0.02	4±1	-1.12± 0.02	6.49	I+MLV
3.0	0.30 ±0.02	0.32±0.02	-1.96±0.08	1.41±0.04	0.61± 0.02	4±1	-0.47± 0.02	5.88	MLV+I

At α=2, ϕ_s=3 and for [NaCl]=0.0M and [NaCl]=0.2M samples are turbid (Figs. 3.11a and b). Their SAXS patterns show a broad peak (Fig. 3.12A(a)) and

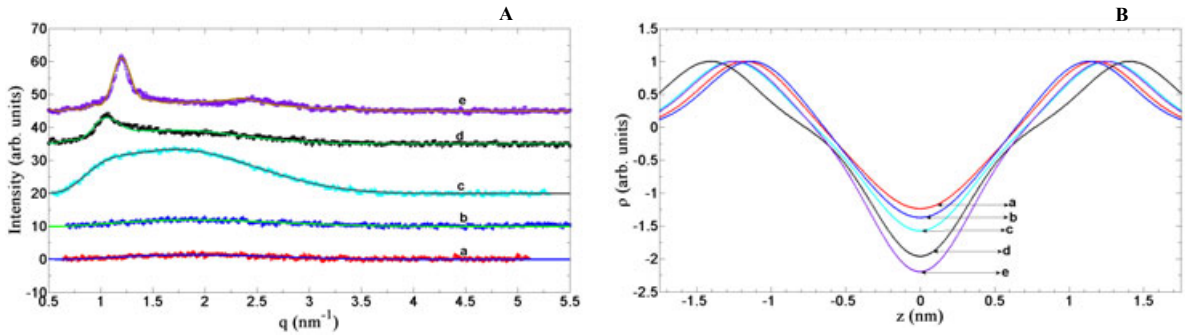

FIGURE 3.12: (**A**) X-ray diffraction patterns of the CPC-SHN-NaCl-Water system at α=2, ϕ_s=3, T=30°C corresponding to [NaCl]=0.0M (**a**), [NaCl]=0.6M (**b**), [NaCl]=1M (**c**), [NaCl]=2M (**d**), [NaCl]=3M (**e**), [NaCl]=4M (**f**). The solid lines are fits to the model. (**B**) Electron density profiles obtained from the fit corresponding to [NaCl]=0.0M (**a**), [NaCl]=0.6M (**b**), [NaCl]=1M (**c**), [NaCl]=2M (**d**), [NaCl]=3M (**e**), [NaCl]=4M (**f**).

maltese-cross texture is found under polarizing optical microscope (Fig. 3.13A and B), confirming the occurrence of MLV phase. Yet, at about [NaCl]=0.4M, two phases are found to coexist. The top one is turbid and shows maltese-cross texture under POM (similar to figure 3.13C) and the bottom part is translucent and exhibits an optically isotropic texture (Fig. 3.11c). SAXS pattern for both the phases (similar to figure 3.12A(b)) show a broad peak. From POM studies, we conclude that the turbid part is dilute dispersion of MLV and translucent part is L_x phase. These two phases coexist up to a salt concentration of 0.8M (Fig. 3.11d and e). For [NaCl]=1M, a transparent colorless isotropic phase (excess water) is found at the top with a turbid phase at the bottom(Fig. 3.11f). SAXS pattern of the bottom part shows a broad peak at about 5.5nm (Fig. 3.12A(a)). It exhibits maltese-cross texture under POM (Fig. 3.13D), indicating the occurrence of a MLV dispersion. Similar behavior is found at a salt concentration of 2M (Fig. 3.11g). However, for [NaCl]=3M a collapsed turbid part appeared at the top with excess water at the bottom (Fig. 3.11h). SAXS pattern of the turbid part shows two peaks in the small angle region with their q in the ratio 1:2 (Fig. 3.12A(e)) and maltese-cross texture is observed under polarizing optical microscope (Fig. 3.13F), confirming the occurrence of a MLV dispersion. Cryo-SEM micrograph of this phase is also consistent with POM and SAXS studies (Fig. 3.14A1&A2). Excess SHN is found to crystallize out at [NaCl]=4M (Fig. 3.11i).

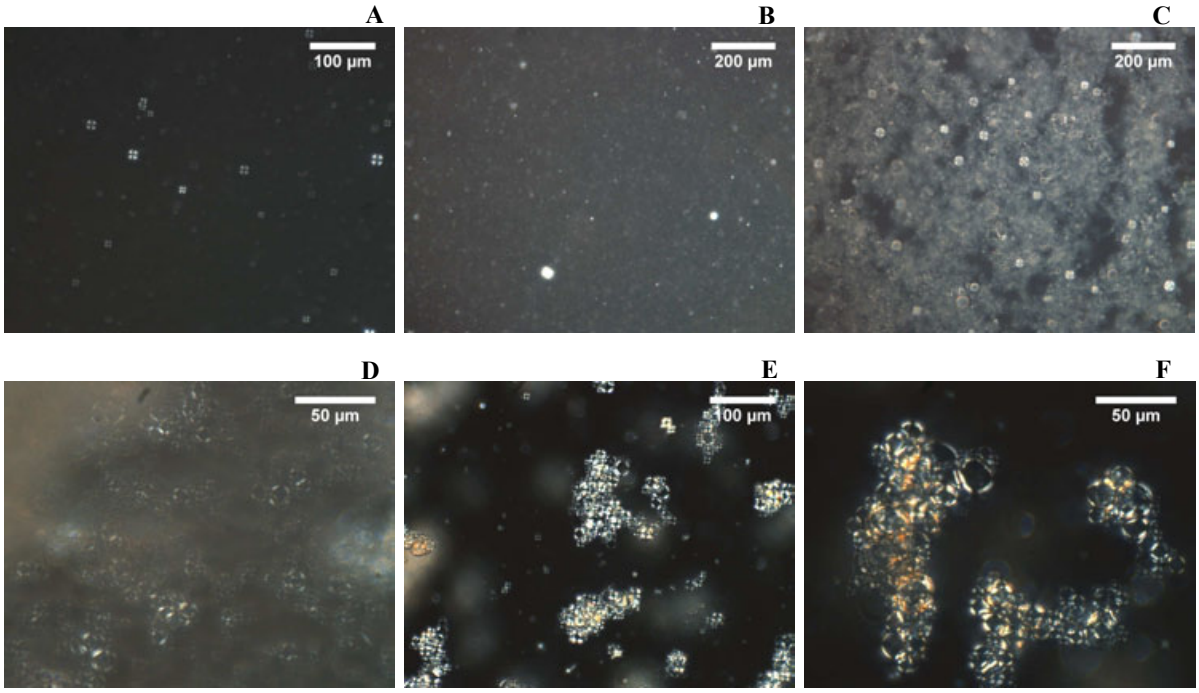

FIGURE 3.13: Polarizing optical microscopy texture of MLV of the CPC-SHN-NaCl-Water system at α=2, ϕ_s=3, T=30°C: [NaCl]=0.0M (**A**), [NaCl]=0.2M (**B**), [NaCl]=0.6M (**C**), [NaCl]=1M (**D**), [NaCl]=2M (**E**) and [NaCl]=3M (**F**).

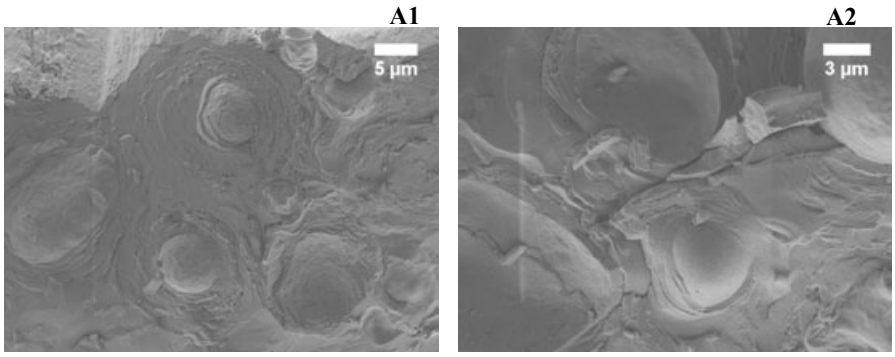

FIGURE 3.14: Cryo-SEM micrograph of MLV phase in the CPC-SHN-NaCl-Water system at α=2, ϕ_s=3, T=25°C and [NaCl]=3M (**A1 and A2**).

At α=2, ϕ_s=20 and T=30°C the sample is translucent and shows the L_x phase, it remains in the pure L_x phase on increasing the salt concentrations up to [NaCl]=0.2M (Fig. 3.15a). SAXS pattern shows a broad peak similar to that found at 0.0M (Fig. 3.16A(a)) and optically isotropic texture is observed under crossed POM, confirming that the L_x phase is stable over that range. At $\sim$ [NaCl]=0.4M, it shows a coexistence of two phases; a transparent colorless isotropic phase (excess

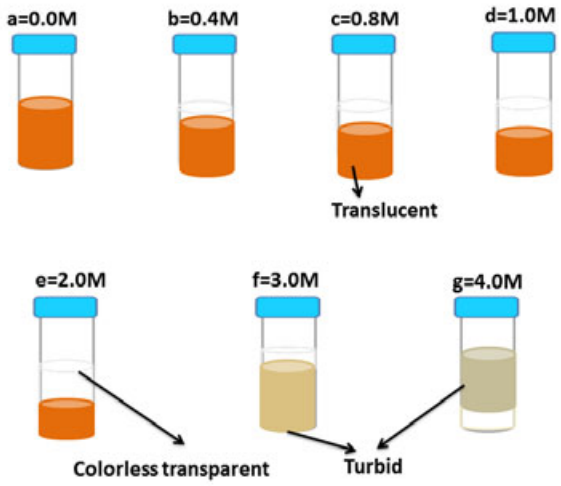

FIGURE 3.15: The different phases in the CPC-SHN-NaCl-water system at α=2, ϕ_s=20 and T=30°C: L_x phase at 0.0M (a), isotropic phase (excess water) floating at the top with L_x phase at the bottom at 0.4M (b), 0.8M (c), 1M (d) and 2M (e), isotropic phase floating at the top with MLV phase at the bottom at 3M (f) and MLV phase floating at the top at 4M (g).

TABLE 3.6: Values of parameters for the diffraction data at α=2, ϕ_s=20 and T=30°C of the CPC-SHN-NaCl-Water system obtained from the fit to the model of lamellar (L_α) phase.

Nacl [M]	σ_h(nm)	σ_c(nm)	$(\rho_c)/(\rho_h)$	$z_h(nm)$	η	N	N_d	$d(nm)$	Phase
0.0	0.30 ±0.02	0.30±0.02	-1.09±0.08	1.51±0.04	–	–	-0.09± 0.002	–	I+L_x
0.4	0.30 ±0.02	0.30±0.02	-1.20±0.08	1.47±0.04	–	–	-0.10± 0.002	–	I+L_x
0.8	0.30 ±0.02	0.30±0.02	-1.30±0.08	1.46±0.04	–	–	-0.15± 0.002	–	I+L_x
1.2	0.30 ±0.02	0.30±0.02	-1.55±0.08	1.41±0.04	0.82± 0.02	2±0	1.42± 0.02	6.27	I+L_x
1.5	0.30 ±0.02	0.30±0.02	-1.64±0.08	1.43±0.04	0.61± 0.02	2±0	2.55± 0.02	6.22	I+L_x
2.0	0.30 ±0.02	0.30±0.02	-1.93±0.08	1.42±0.04	0.98± 0.02	2±0	0.41± 0.02	5.78	I+L_x
3.0	0.30 ±0.02	0.41±0.02	-2.02±0.08	1.05±0.04	0.47± 0.02	6±0	3.54± 0.02	5.54	I+MLV

water) found at the top with a translucent (surfactant rich) phase at the bottom (Fig. 3.15b). Bottom part shows optically isotropic texture and its SAXS pattern is similar to that found at 0.2M. Amount of excess water is found to increase on increasing the salt concentration up to [NaCl]=2M (Fig. 3.15c-e). The bottom part is found to remain optically isotropic under POM (Fig. 3.17A) while SAXS patterns show an additional broad peak developing at about 5.5nm on increasing

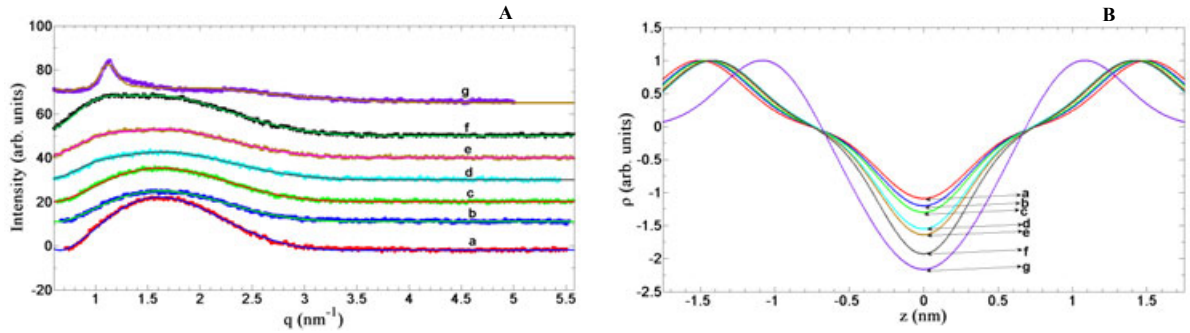

FIGURE 3.16: (**A**) X-ray diffraction patterns of the CPC-SHN-NaCl-Water system at α=2, ϕ_s=20, T=30°C corresponding to [NaCl]=0.2M (**a**), [NaCl]=0.4M (**b**), [NaCl]=0.8M (**c**), [NaCl]=1.2M (**d**), [NaCl]=1.5M (**e**), [NaCl]=2M (**f**), [NaCl]=3M (**g**). The solid lines are fits to the model. (**B**) Electron density profiles obtained from fit corresponding to [NaCl]=0.2M (**a**), [NaCl]=0.4M (**b**), [NaCl]=0.8M (**c**), [NaCl]=1.2M (**d**), [NaCl]=1.5M (**e**), [NaCl]=2M (**f**), [NaCl]=3M (**g**).

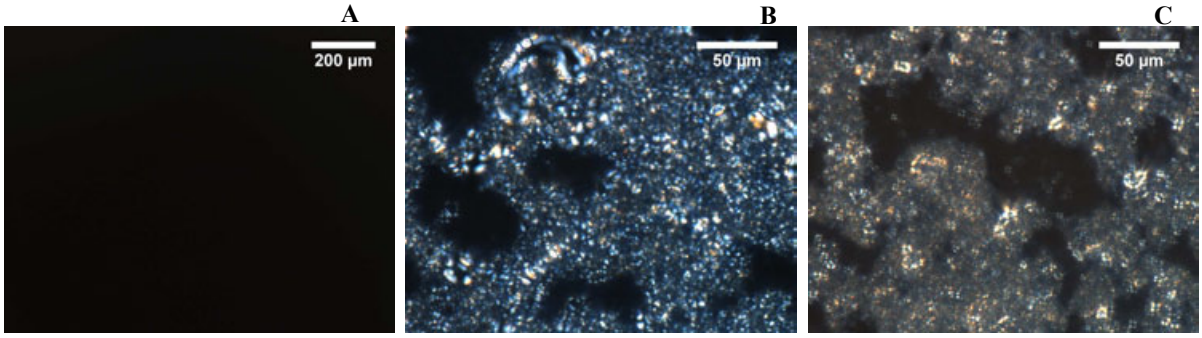

FIGURE 3.17: Polarizing optical microscopy texture of L_x phase at [NaCl]=2M (**A**), MLV phase at [NaCl]=3M (**B**) and [NaCl]=4M (**C**) in the CPC-SHN-NaCl-Water system at α=2, ϕ_s=20, T=30°C.

the salt concentration (Fig. 3.16A(c-f)). However, at [NaCl]=3M it shows a turbid lower part (surfactant rich) with excess water at the top (Fig. 3.15f) while at [NaCl]=4M the turbid part (surfactant rich) is found at the top with excess water at the bottom (Fig. 3.15g). The turbid part shows maltese-cross texture (Fig. 3.17B and C) and its SAXS pattern shows two peaks in the small angle region with their q in the ratio 1:2, confirming the occurrence of a MLV dispersion (Fig. 3.16A(g)).

3.4.3 CPC-SHN-1-Hexanol-Water system: Effect of Hexanol

Effect of hexanol on the phase behavior of CPC-SHN-Water system has been studied at very high concentration of SHN. It has been done by varying the weight ratio of hexanol/CPC (Hc) and fixing α=2, ϕ_s=30.

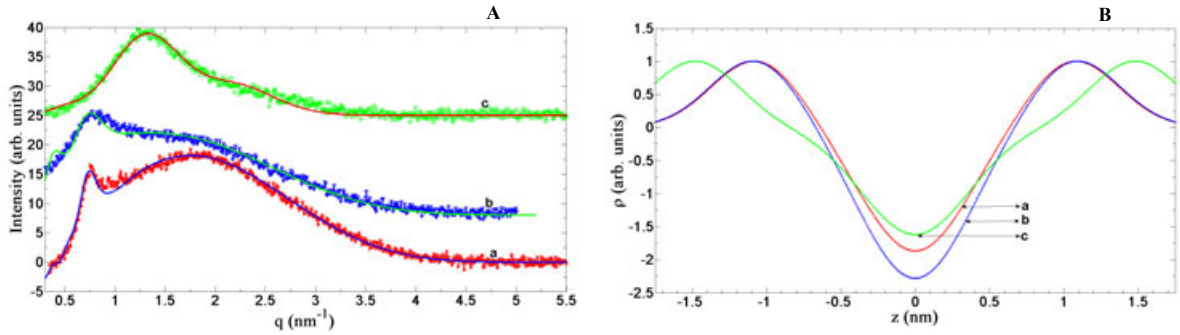

FIGURE 3.18: (**A**) X-ray diffraction patterns of the CPC-SHN-NaCl-Water system at α=2, ϕ_s=30, T=30°C corresponding to Hc=0.4381 (**a**), Hc=0.8333 (**b**), Hc=1.2829 (**c**). The solid lines are fits to the model. (**B**) Electron density profiles corresponding to Hc=0.4381 (**a**), Hc=0.8333 (**b**), Hc=1.2829 (**c**).

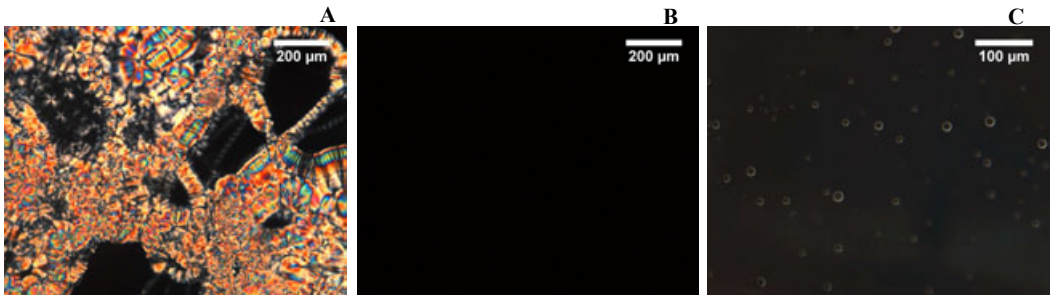

FIGURE 3.19: Polarizing optical microscopy texture of; (**A**) swollen lamellar phase at Hc=0.4381, (**B**) swollen L_x phase at Hc=0.8333 and (**C**) L_x phase at Hc=1.2829 in the CPC-SHN-Hexanol-Water system at α=2, ϕ_s=30, T=30°C.

At α=2, ϕ_s=30 (without hexanol) it exhibits the L_x phase. Low amounts of hexanol (at low Hc), is found to transform the translucent (L_x) phase into a slightly turbid phase. This turbid phase shows focal conic texture under polarizing optical microscope (Fig. 3.19A) and its SAXS pattern exhibits a narrow peak about at 8nm (Fig. 3.18A(a)), confirming the occurrence of a swollen lamellar phase. At higher Hc, an optically isotropic phase is found (Fig. 3.19B), which shows a broad

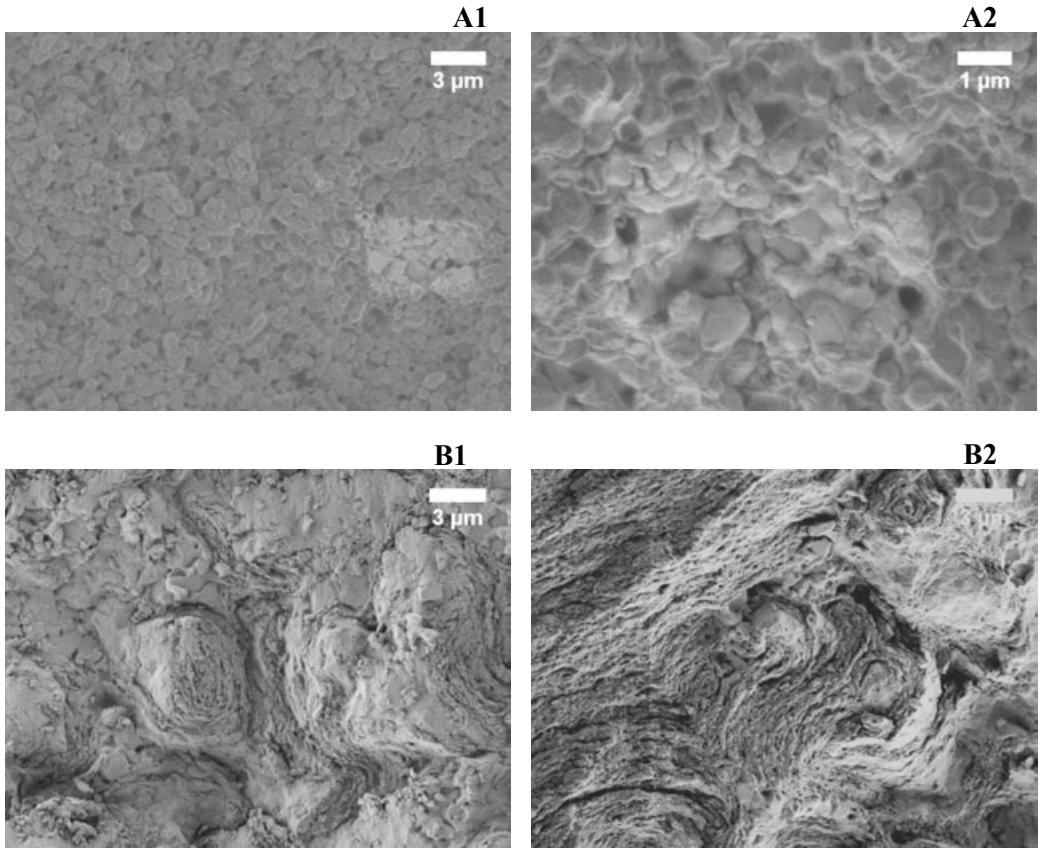

FIGURE 3.20: Cryo-SEM micrograph of (**A1 and A2**) swollen lamellar phase at Hc=0.4381 and (**B1 and B2**) swollen isotropic (L_x) phase at Hc=0.8333 in the CPC-SHN-Hexanol-Water system at α=2, ϕ_s=30, T=25°C

TABLE 3.7: Values of parameters for the diffraction data at α=2, ϕ_s=30 and T=30°C of the CPC-SHN-Hexanol-Water system obtained from the fit to the model of lamellar (L_α) phase.

Hc	σ_h(nm)	σ_c(nm)	$(\rho_c)/(\rho_h)$	$z_h(nm)$	η	N	N_d	$d(nm)$	Phase
0.4381	0.30 ±0.02	0.35±0.02	-1.84±0.08	1.07±0.04	1.19± 0.02	5±1	-2.39± 0.02	8.25	L_α
0.8333	0.30 ±0.02	0.36±0.02	-2.23±0.08	1.07±0.04	1.48± 0.02	3±0	-0.52± 0.02	7.89	swollen L_x
1.2829	0.30 ±0.02	0.36±0.02	-1.62±0.08	1.48±0.04	0.17± 0.02	2±0	3.02± 0.02	4.81	L_x +excess hexanol

peak at around 7.5nm in the diffraction pattern (Fig. 3.18A(b)) indicating the occurrence of swollen isotropic (L_x) phase. Still, at higher Hc, hexanol separates out and the surfactant rich part is found at the top of the sample tube. SAXS pattern of the top part exhibits a broad peak at about 5nm (Fig. 3.18A(c))similar to figure 3.6A(d) and it is found optically isotropic under POM (Fig. 3.19C), confirming the occurrence of L_x phase.

Cryo-SEM micrograph of the swollen lamellar phase is shown in figures 3.20(A1&A2), which indicate the occurrence of a vesicular structure. Figures 3.20(B1&B2) show Cryo-SEM micrograph of a swollen isotropic (L_x) phase.

3.4.4 CPC-SHN-NaCl-1-Hexanol-Water system: Effect of salt and alcohol

To examine the effect of NaCl along with that of hexanol on the phase behavior of CPC-SHN-Water system at very high SHN concentration, we have studied the system at α=2, ϕ_s=30 and [NaCl]=1.2M by varying the concentration of hexanol.

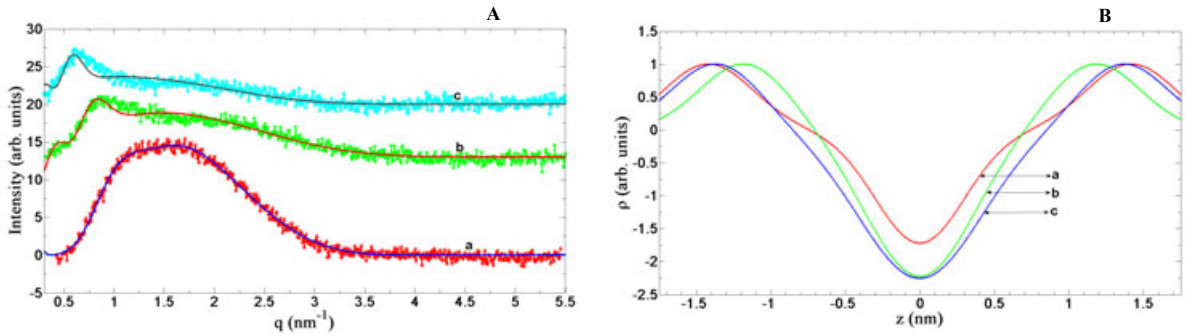

FIGURE 3.21: (**A**) X-ray diffraction patterns of the CPC-SHN-NaCl-Hexanol-Water system at α=2, ϕ_s=30, T=30°C, [NaCl]=1.2M corresponding to Hc=0.00 (**a**), Hc=0.3490 (**b**), Hc=0.5693 (**c**). The solid lines are fits to the model. (**B**) Electron density profiles corresponding to Hc=0.00 (**a**), Hc=0.3490 (**b**), Hc=0.5693 (**c**).

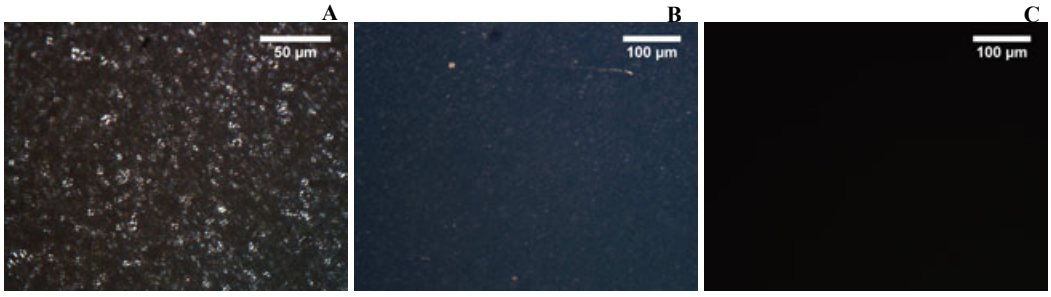

FIGURE 3.22: Polarizing optical microscopy texture of (**A**) swollen lamellar phase at Hc=0.1584 and (**B**) Hc=0.3490 and (**C**) swollen isotropic (L_x) phase at Hc=0.5693 in the CPC-SHN-NaCl-Hexanol-Water system at α=2, ϕ_s=30, T=30^0C and [NaCl]=1.2M.

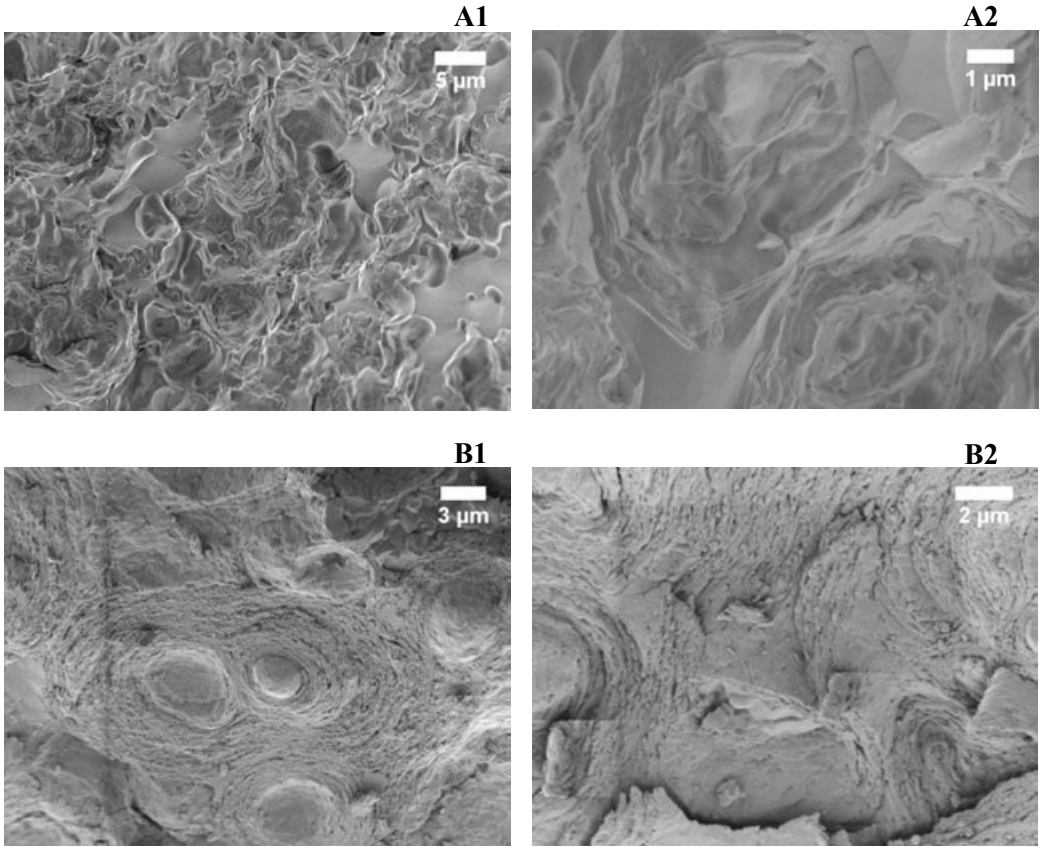

FIGURE 3.23: Cryo-SEM micrograph of swollen lamellar phase at Hc=0.1584 (**A1 and A2**) and swollen isotropic phase at Hc=0.5693 (**B1 and B2**) in the CPC-SHN-NaCl-Hexanol-Water system at α=2, ϕ_s=30, T=25°C and [NaCl]=1.2M.

TABLE 3.8: Values of parameters for the diffraction data at α=2, ϕ_s=30, [NaCl]=1.2M and T=30°C of the CPC-SHN-NaCl-Hexanol-Water system obtained from the fit to the model of lamellar (L_α) phase.

Hc	σ_h(nm)	σ_c(nm)	$(\rho_c)/(\rho_h)$	$z_h(nm)$	η	N	N_d	$d(nm)$	Phase
0.00	0.30 ±0.02	0.30±0.02	-1.72±0.08	1.42±0.04	0.92± 0.02	2±0	0.72± 0.02	5.87	I+L_x
0.3490	0.30±0.02	0.35±0.02	-2.21±0.08	1.18±0.04	1.13± 0.02	3±1	-1.01±0.02	7.07	MLV
0.5693	0.30±0.02	0.40±0.03	-2.24± 0.08	1.37±0.04	0.95±0.02	3±1	-0.77±0.3	9.74	swollen L_x

At α=2, ϕ_s=30 [NaCl]=1.2M the sample has excess water at the top and the translucent surfactant rich phase is at the bottom. Bottom part shows the L_x phase and its SAXS pattern shows a peak at about 6nm (Fig. 3.21A(a)). At low concentrations (Hc) of hexanol, It shows a maltese-cross texture (Fig. 3.22A) which confirms the occurrence of MLV. Cryo-SEM micrograph is shown in figures 3.23(A1&A2), show a vesicular structure which is consistent with POM results.

At higher Hc, SAXS patterns shows a peak at about 7nm (Fig. 3.21A(b)) and maltese-cross texture is found under POM (Fig. 3.22B), indicating the occurrence of MLV. Still at higher Hc, SAXS pattern shows a broad peak at about 9nm (Fig. 3.21A(c)) and an optically isotropic texture (Fig. 3.22C), confirming the occurrence of the swollen L_x phase. Figures 3.23(B1&B2) show the Cryo-SEM of this L_x phase which is similar to figures 3.20(B1&B2).

3.5 Discussion

3.5.1 Data analysis

Diffraction data of the lamellar phase (L_α) were analyzed using the procedure described in chapter 1.

Variation of the SAXS pattern with ϕ_s at α= 1.5 and T=30°C is shown in figure 3.3A. The patterns at ϕ_s=57, 60, 67 and 72 are well described by the model for the L_α phase. The electron density profiles obtained from the fit are shown in figure 3.3B; the corresponding model parameters are given in table 3.1. Variation of the SAXS pattern with temperature at α=2 and ϕ_s=60 is shown in figure 3.7A. The patterns at 30, 40, 50, 60 and 75°C are well described by the model for the L_α phase. The electron density profiles obtained from the fit are shown in figure 3.7B; the corresponding model parameters are given in table 3.3.

We tried to fit the SAXS data from the L_x phase to the scattering expected from the sponge phase [8, 32] as described in the introduction. But it was not possible to get a good fit for any reasonable values of the model parameters. The typical fit with the diffraction data is shown in figure 3.24 and the corresponding model parameters are given in table 3.9. Further, the mesh size in the sponge phase (given by the position of the broad peak) is typically 1.5 times the d-spacing of the L_α phase with the same water content [33]. On the other hand, the average periodicity in the L_x phase is comparable to the d-spacing of the low-temperature L_α phase. Due to these differences we can rule out the L_x phase being a conventional sponge

phase. Another possibility is that it is made up of inverted micelles. But it can also be ruled out on the basis of the phase diagram (Fig. 3.2), which shows a pure L_α phase occurring at lower water content than the L_x phase.

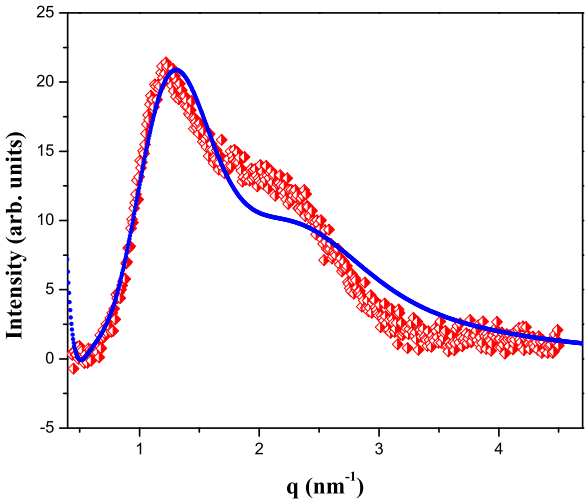

FIGURE 3.24: X-ray diffraction pattern of the L_x phase along with fit to the model of sponge (L_3) phase. Red and blue colors represent the data and fit respectively.

TABLE 3.9: Values of parameters for the diffraction data atα=2, ϕ_s=50 and T=30°C of the CPC-SHN-Water system obtained from the fit to the model of sponge (L_3) phase.

ξ_2(nm)	σ(nm)	w(nm)	L(nm)
0.98	4.90	3.12	5.11

Observation of flow-birefringence in the L_x phase and the fact that the average spacing in this phase is comparable to the periodicity of the low-temperature L_α phase, suggest that the L_x phase consists of bilayer-like amphiphile aggregates. The much larger peak width in this phase, compared to the L_α, can arise from an irregular stacking of such aggregates. Since the number of correlated bilayers is a tunable parameter in the model for the L_α phase, it can also be used to describe an irregular stack of bilayers. We have, therefore, used the same model to describe the SAXS data from the L_x phase. However, it should be stressed here that η, the Caille parameter would be just a fitting parameter in the case of the L_x phase, without the physical significance it has in the L_α phase.

Figure 3.7A(f and g) shows the good agreement between this model and the data; values of the model parameters obtained are shown in table 3.3. The number of correlated bilayers in the L_x phase turns out be of the order of 3, whereas it is ~ 10 in the Lα phase. Variation of the bilayer electron density profile across the Lα - L_x transition is shown in figure 3.7B. The small and gradual variation of the profile across this transition confirms that the L_x phase is made up of an irregular stack of bilayers, with short range positional correlations.

Figures 3.6A and 3.8A show the variation of the SAXS pattern with ϕ_s at α=2 and α=2.25 respectively. They show the good agreement between the model and the data; values of the model parameters obtained are shown in tables 3.2 & 3.4 and corresponding electron density profiles are shown in figures 3.6B & 3.8B respectively. Data from the L_x phase (at α=2 and 2.25) at higher water content (Figs. 3.6A (a and b), 3.8A (a and b)) can be fitted using only the bilayer form factor similarly to the L_x phase at higher water content at α=1.5 (Fig. 3.3A (a and b)), showing that this phase is made up of positionally uncorrelated bilayers (UB). However, the SAXS pattern at lower water content can be fitted only if S(q) is taken in account, showing that positional correlations between the bilayers is developing with decreasing water content. Electron density profiles vary smoothly in the L_x phase on decreasing the water content, further confirming the proposed model of the L_x phase.

The influence of dislocation loops on the structure of the lamellar phase has been studied theoretically in the context of the smectic A-nematic liquid crystal transition [34–36]. It has been shown that a finite density of unbound dislocations can destroy the (quasi) long-range positional order of the lamellar phase and make the inter-lamellar correlations short-range. In the case of a bilayer stack such dislocation loops correspond to pores or passages in the bilayer (Fig. 3.25).

Thus, the observed decrease in inter-bilayer correlations can be qualitatively understood in terms of the formation of dislocation-loops (pores or passages in this case) in the bilayer. However, at lower water content L_x phase is suppressed and the L_α phase becomes stable again. In the absence of excess water, the creation of

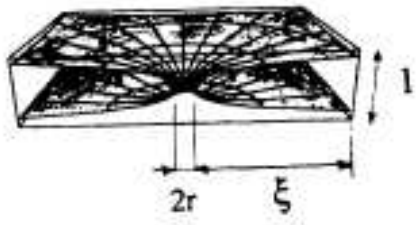

FIGURE 3.25: Schematic of a passage geometry in the bilayer. l is the inter-bilayer separation, r is the size of the passage neck, and ξ is the size of the passage deformation region (from ref. [37])

dislocation loops would lead to a decrease in the spacing of the stack far from the defect, since the material removed to create the defect has to be accommodated elsewhere. This will be resisted by the exponentially varying hydration repulsion between the bilayers. As a result such defects will be suppressed when there is no excess water and the inter-bilayer interaction becomes repulsive. This situation is similar to the suppression of bilayer curvature defects with decreasing water content seen in some lamellar phases [38], and the theoretically predicted suppression of dislocation loops in smectic films confined between two rigid boundaries [36].

The deformation energy of a bilayer is described in terms of two elastic moduli; the modulus of mean curvature κ and the modulus of Gaussian curvature $\bar{\kappa}$ [39]. As discussed earlier, theoretically it can be shown that the sponge phase consisting of a network of bilayers should be stable when the Gaussian rigidity modulus ($\bar{\kappa}$) is weakly negative; for lower values of ($\bar{\kappa}$) the lamellar phase is stable [37, 40]. In the case of bilayers made up of ionic amphiphiles there is an electrostatic contribution to ($\bar{\kappa}$) which is predicted to be negative [41, 42]. At high salt concentrations the electrostatic interaction will be screened out and $\bar{\kappa}$ can become weakly negative, favoring bilayer passages and hence stabilizing the sponge phase, as observed in many systems. Such passages can also be expected to form in the present system due to the high concentration of salt. However, the main difference between the present system and the ones where a sponge phase occurs is the difference in the inter-bilayer interactions. The present system is dominated by attractive van der Waals interaction leading to a weakly-swollen phase, whereas the sponge phase is

seen in highly swollen systems dominated by steric repulsion. The observation of a similar Lα-L$_x$ transition in some other amphiphile-water systems dominated by attractive inter-bilayer interactions leads us to believe that the L$_x$ phase may be rather common in such systems [43].

3.5.2 Phase transition: From MLV $\rightarrow$ L$_x$ $\rightarrow$ L$_\alpha$

The phase transition from the MLV to L$_\alpha$ phase is accompanied by changes in the aggregate topology from a isolated disconnected spherical object to disconnected bilayer via connected bilayer structure. Present investigations have revealed a transition sequence from MLV to L$_\alpha$ in the CPC-SHN-Water system at α=2 (Figs. 3.2C and D):

MLV $\rightarrow$ L$_x$ $\rightarrow$ L$_\alpha$ as function of decreasing water content (increasing ϕ_s).

Figures 3.2C and D show the phase diagram of the CPC-SHN-Water system at α=2. At higher water content MLV are found to coexist with excess water which give rise to the L$_x$ phase on decreasing the water content. L$_\alpha$ phase is found on further decreasing the water content. The observed phase sequence can be explained as follows. Initially, HN$^-$ ions are distributed between the micelles and water. On decreasing the water content, concentration of salt (NaCl due to released counterion; sodium from SHN and chlorine from CPC) in water increases, as result more and more HN$^-$ bind to micelles and lead to a decrease in the curvature of the hydrocarbon-water interface which give rise to L$_x$ phase [5]. Finally, at low water content, formation of defects (pores or passages) which is responsible for stabilizing the L$_x$ would be suppressed as discussed above (effect of confinement). So, Lamellar (L$_\alpha$) phase would be stable.

In order to check the first part of the hypothesis, that increasing the salt (NaCl) (due to released counterions) lead the MLV to L$_\alpha$ transition, we have studied the effect of salt (NaCl) on the phase behavior of CPC-SHN-Water system at various salt (NaCl) concentrations, by keeping α=2, ϕ_s=3 to be constant (starting from MLV). We found that MLV dispersion at α=2 and ϕ_s=3, is transform into

collapsed MLV via L_x phase on increasing the salt (NaCl) concentration(Fig. 3.11) (as discussed in section 3.4.2). Positional correlation between the bilayer is found to be developing on increasing the salt concentration. Figure 3.12A shows that a good agreement is found between the model and the data; values of the model parameters obtained are shown in table 3.5 and corresponding electron density profile is shown in figure 3.12B. A continuous variation is seen in the electron density profile across the transition.

Further, L_x to MLV (collapsed) phase transition is also found on increasing the salt (NaCl) concentrations in the L_x phase and keeping α=2 and ϕ_s=20 constant (Figs. 3.15) (as discussed in the section 3.4.2). Figure 3.16A, shows the good agreement between model and the data; values of the model parameters obtained are shown in table 3.6 and corresponding electron density profile is shown in figure 3.16B. So, its clear that, increasing the salt concentration could lead to MLV-L_x-MLV transition. However, we cannot draw any conclusion regarding the relative importance of salt (NaCl) and confinement in stabilizing the L_α phase at low water content.

In order to check the second part of the hypothesis that SHN concentration is increasing in the micelles on decreasing the water content, UV-visible absorption spectroscopy studies were carried out in the excess water part of CPC-SHN-NaCl-Water system of composition α=2, ϕ_s=20 at various salt (NaCl) concentrations. SHN is found to show a strong absorption peak at around 292nm (Fig. 3.26A(b)), along with three weaker peaks at 272nm, 283nm and 294nm whereas CPC exhibits three peaks at 253nm, 259nm and 265nm (Fig. 3.26A(a)). A strong absorption peak at 292nm along with three peaks at 272nm, 283nm and 294nm characteristic of SHN are observed in all these systems and the absorbance is found to decrease continuously on increasing the salt concentration, confirming that the SH^- concentration is increasing in the micelles (decreasing in the excess water) on increasing the salt (NaCl) concentration (Fig. 3.26B). Further, amounts of SH^- estimated from volume of excess water and absorbance, are found to increase in the micelles on increasing the salt (NaCl) concentration which further confirming the hypothesis (Tab. 3.10). Absorption peak corresponding to CPC, which is characteristic

for micellar solution is not found, indicating that the concentration of the micelles in the water rich part is not significant.

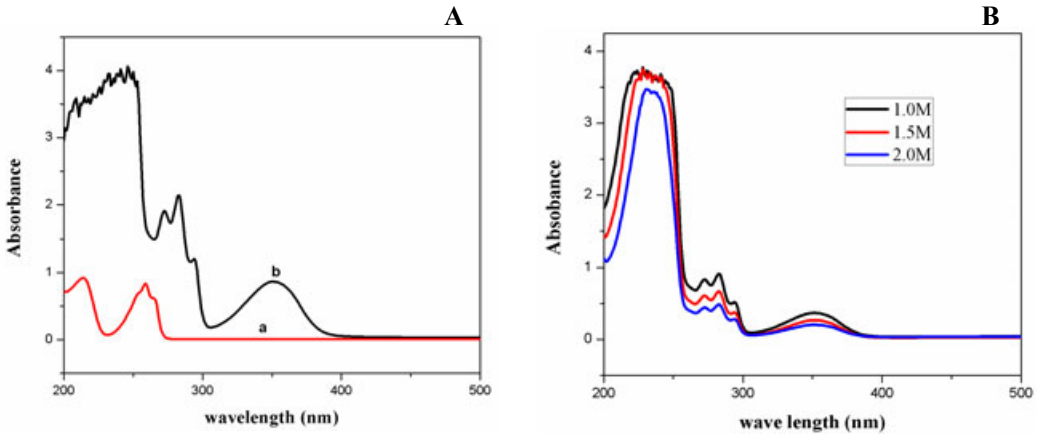

FIGURE 3.26: UV spectra of (**A**(a)) 0.174mM aqueous solution of CPC, (**A**(b)) 0.713mM aqueous solution of SHN (**B**), water rich part of the CPC-SHN-NaCl-Water system at α=2, ϕ_s=20 and [NaCl] 1M, 1.5M and 2M.

TABLE 3.10: Variation of SHN concentration in the excess water with salt (NaCl) concentration at α=2, ϕ_s=20 of the CPC-SHN-NaCl-Water system.

NaCl[M]	Volume of the excess water (cm^3)	Absorbance	Relative amount of SHN in excess water (g)
1.0	0.32	0.370	1.00
1.5	0.41	0.269	0.92
2.0	0.47	0.205	0.81

3.5.3 Phase transition: From $L_x \rightarrow L_\alpha \rightarrow$ swollen L_x

L_x phase is found to transform into swollen L_x phase via L_α phase on addition of hexanol (Fig. 3.18A) (as discussed in the section 3.4.3). SAXS data of these phases are found to fit very well to the model for the L_α (Fig. 3.18A). Values of the model parameter obtained from the fit are given in the table 3.7 and corresponding electron density profile are shown in figure 3.18B. The observed phase sequence: $L_x \rightarrow L_\alpha \rightarrow$ swollen L_x as function of increasing Hc, could be understood as follows.

L_x phase of this system is dominated by attractive van der Waals interaction and stability of this phase depends upon the ratio of two elastic moduli: modulus of

Gaussian curvature ($\bar{\kappa}$) and modulus of mean curvature (κ) [40]. Initially, this ratio is weakly negative which stabilize the L_x phase. Addition of low amounts of alcohol, initially leads to a decrease κ, which makes the ratio more negative and gives rise to the swollen lamellar phase (L_α), stabilized by Helfirch interaction [7]. Further addition of alcohol lead to increase in ($\bar{\kappa}$), which makes this ratio again weakly negative and gives rise to a swollen L_x phase stabilized by repulsive steric (Helfrich) interaction.

In the presence of salt, less amount of alcohol is required to transform the swollen lamellar phase into the swollen L_x phase (as discussed in the section 3.4.4), which is consistent with the fact that temperature, salt or alcohol alone can lead to Lα to L_x transition. SAXS data are found to fit very well to the model for the L_α (Fig. 3.21A). Values of the model parameters obtained from fit are given in table 3.8 and corresponding electron density profiles are shown in figure 3.21B.

3.6 Conclusion

The influence of the strongly bound anionic counterion HN^- on the phase behavior of concentrated aqueous solutions of the cationic surfactant CPC was studied at high concentration of SHN, using x-ray diffraction, polarizing optical microscopy and cryo-SEM techniques. A low viscous isotropic phase is observed. It is identified as a connected network of bilayers and referred to as L_x phase, a novel isotropic phase of bilayers. L_x phase is unstable on addition of salt (NaCl) and gives rise to L_α phase. L_x phase is also unstable on addition of short chain alcohol and found to transform into a swollen L_x phase via a L_α phase.

Bibliography

[1] J. Israelachvili, *Intermolecular and Surface Forces*, 2nd ed. Academic Press, London (1991).

[2] E. W. Kaler, A. K. Murthy, B. E. Rodriguez and J. A. N. Zasadzinski, *Science*, **245**, 1371 (1989).

[3] P. A. Hassan, S. R. Raghavan and E. W. Kaler, *Langmuir*, **18**, 2543 (2002).

[4] G. Porte, J. Appel, P. Bassereau and J. Marignian, *J. Phys.France*, **50**, 1335 (1989).

[5] S. K. Ghosh, R. Ganapathy, R. Krishnaswamy, J. Bellare, V. A. Raghunathan, A. K. Sood, *Langmuir*, **23**, 3606 (2007).

[6] D. Roux, F. Nallet and J. Prost in *Micelles, Membranes, Microemulsions and Monolayers*, Eds. W. M. Gelbart, A. Ben-Shaul, D. Roux, Springer (1994).

[7] W. Helfrich, *Z. Naturforsch.*, **A 33**, 305 (1978).

[8] D. Roux, C. Coulon and M. E. Cates, *J. Phys. Chem.*, **96**, 4174 (1992).

[9] G. Porte, J. Appel, P. Bassereau and J. Marignan, *J. Phys.*, **50**, 1335 (1989).

[10] D. Gazeau. A. M. Bellocq, D. Roux and T. Zemb, *Europhys.Lett.*, **9**, 447 (1989).

[11] M. Skouri, J. Marignan and R. May, *Colloid Polymer Sci.*, **269**, 929 (1991).

[12] A. Pal, G. Pabstb and V. A. Raghunathan, *Soft Matter*, **8**, 9069 (2012).

[13] A. Pal, P. Bharath, Sudipta G. Dastidarb and V. A. Raghunathan, *Soft Matter*, **8**, 927 (2012).

[14] J. Lang and R. D. Morgan, *J. Chem. Phys.*, **73**, 5849 (1980).

[15] D. J. Mitchell, G. J. D. Tiddy, L. Waring, T. Bostock and M. P. McDonald, *J. Chem. Soc. Faraday Trans. I*, **79**, 975 (1983).

[16] M. Jonströmer and R. Strey, *J. Phys. Chem.*, **96**, 5993 (1992).

[17] K. Fontell, in *Colloidal Dispersions and Micellar Behavior*, ACS Symposium Series 9, American Chemical Society, Washington, DC, p. 270 (1975).

[18] C. A. Miller, M. Gradzielski, H. Hoffmann, U. Krämer and C. Thunig, *Colloid. Polym. Sci.*, **268**, 1066 (1990).

[19] M. Bergmeier, H. Hoffmann, F. Witte and S. Zourab, *J. Coll. Interface. Sci.*, **203**, 1 (1998).

[20] E. Hecht, K. Mortensen and H. Hoffmann, *Macromolecules*, **28**, 5465 (1995).

[21] G. Porte, P. Bassereau, J. Marignan and J. May, *J. Phys. France*, **49**, 511 (1988).

[22] M. Cates, D. Roux, D. Andelman, S. C. Milner and S. Safran, *Europhys. Lett.*, **5**, 733 (1988).

[23] J. Marignan, F. Gauthier-Fournier, J. Appell, F. Akoum and J Lang, *J. Phys.Chem.*, **92**, 440 (1988).

[24] R. Gomati, J. Appell, P. Bassereau, J. Marignan and G. Porte, *J. Phys. Chem.*, **91**, 6203 (1987).

[25] H. Hoffmann, S. Hofmann, A. Rauscher and J. Kalus, *Progr. Colloid. Polym. Sci.*, **84**, 24 (1991).

[26] H. F. Mahjoub, K. M. McGrath and M. Kléman, *Langmuir*, **12**, 3131 (1996).

[27] J. Yamamoto and H. Tanaka, *Phys. Rev. Lett.*, **77**, 4390 (1996).

[28] U. Hornfeck, M. Gradzielski, K. Mortensen, C. Thunig and G. Platz, *Langmuir*, **14**, 2958 (1998).

[29] A. Zapf, U. Hornfeck, G. Platz and H. Hoffmann, *Langmuir*, **17**, 6113 (2001).

[30] R. Beck and H. Hoffmann, *Phys. Chem. Chem. Phys.*, **3**, 5438 (2001).

[31] R. Beck, Y. Abe, T. Terabayashi and H. Hoffmann, *J. Phys. Chem. B*, **106**, 3335 (2002).

[32] N. Lei, C. R. Safinya, D. Roux and K. S. Liang, *Phys. Rev. E*, **56**, 608 (1997).

[33] M. Skouri, J. Marignan, J. Apell and G. Porte, *J. Phys. II*, **1**, 1121 (1991).

[34] W. Helfrich, *J. Phys.*, **39**, 1199 (1978).

[35] D. Nelson and J. Toner, *Phys. Rev. B*, **24**, 363 (1981).

[36] R. Holyst, *Phys. Rev. B*, **50**, 12398 (1994).

[37] L. Golubović, *Phys. Rev. E*, **50**, R2419 (1994).

[38] M. C. Holmes, P. Sotta, Y. Hendrikx and B. Deloche, *J. Phys. II*, **3**, 1735 (1993).

[39] W. Helfrich, Z. *Naturforsch. C*, **28**, 693 (1973).

[40] D. C. Morse, *Phys. Rev. E*, **50**, R2432 (1994).

[41] M. Winterhalter andW. Helfrich, *J. Phys. Chem.*, **92**, 6865 (1988).

[42] D. J. Mitchell and B. W. Ninham, *Langmuir*, **5**, 1121 (1989).

[43] A. Pal, P. Bharath, S. G. Dastidar and V. A. Raghunathan, *Soft Matter*, DOI: 10.1039/C2SM06817F (2012).

Chapter 4

Effect of oil and alcohol on the stability of a novel isotropic phase of bilayers

4.1 Introduction

The novel isotropic (L_x) phase of bilayers has been seen in a few ionic surfactant systems in the presence of high salt concentration and has been discussed in the previous chapter [1, 2]. In these systems electrostatic interactions are screened out by the salt and the attractive van derWaals interaction is balanced by short range repulsive hydration interaction leading to a weakly-swollen phase. The L_x phase is characterized by small average inter-bilayer spacing and short-range positional correlations. It has been suggested that this phase could be made up of a connected network of the bilayers, as discussed in the previous chapter. However, structure of the L_x phase is still not unambiguously established. In-order to probe its structure, further effect of oils and alcohols have been investigated on the stability of this phase in the present study.

This chapter deals with the structure and stability of the L_x phase in the SDS (sodium dodecyl sulfate)-PTHC (p-toluidine hydrochloride)-water system. Earlier

studies on this system are described in section 4.2. A brief description of chemicals are given in section 4.3. Results of these studies are presented in section 4.4. A partial phase diagram of the various structures induced by oil/alcohol in the surfactant rich part of the SDS-PTHC-Water system (at α=2.5 and ϕ_s=20) as a function of chain length of oil/alcohol has been determined from x-ray diffraction and POM studies. Only the L_x and L_α phases are seen in all these systems. Oil of shorter and alcohol of comparable chain length to the surfactant are found to stabilizes the L_α phase at the expenses of the L_x phase at small to medium concentrations. Our results are discussed in section 4.5. The last section contains conclusions that can be drawn from these studies.

4.2 Earlier Studies

Phase behavior of the SDS-PTHC-Water system has been investigated previously [3]. Lamellar (L_α) and an isotropic (labeled as L_3) phases coexisting with excess water have been reported at high salt concentration (Fig. 4.1A). SAXS pattern show a sharp peak in the L_α phase and a broad peak in L_3 phase. The peak positions in the L_α and the L_3 phases are found to be the same (Fig. 4.1B). The structure of L_3 phase has not been probed in details. Henceforth, we called this L_3 phase as L_x phase.

Aim of the present studies is to understand the structure of the L_x phase. Detailed modeling of the SAXS data required for the confirmation of the structures has not been taken up in previous studies on the SDS-PTHC-Water system. Cryo-SEM studies done to probe the structure of the L_x phase is also described.

4.3 Experimental

Sodium dodecyl sulfate (SDS), p-toluidine hydrochloride (PTHC), hexane, decane, dodecane, tetradecane, 1-hexanol, and 1-dodecanol were purchased from Sigma-Aldrich. Structures of the chemicals are shown in figure 4.2. Solutions of molar

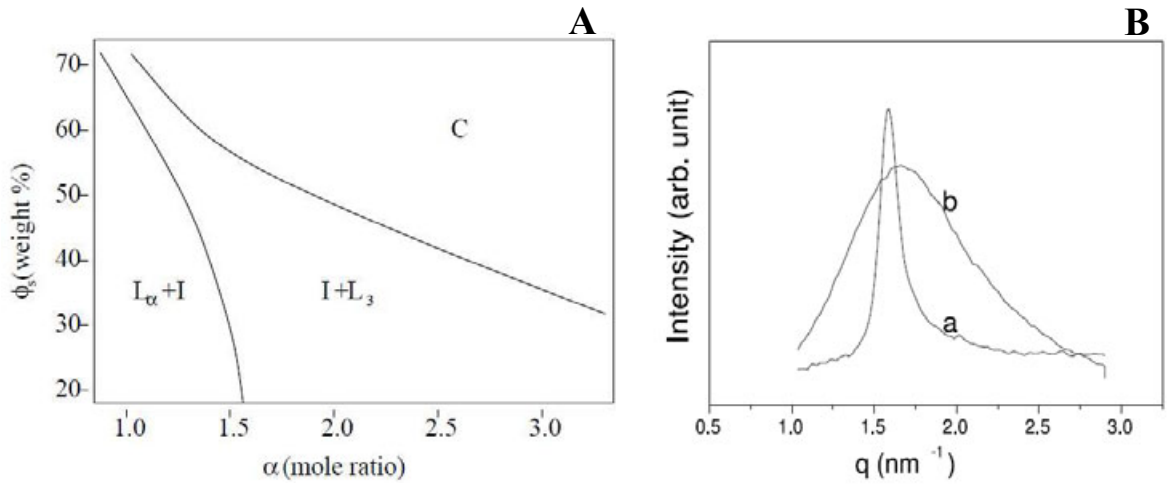

FIGURE 4.1: (**A**) Partial phase diagram of the SDS-PTHC-Water system at 30°C; I+L_α, I+L_3 and C denote the lamellar phase coexisting with excess water, sponge phase coexisting with excess water and crystalline phases, respectively. (**B**) X-ray diffraction patterns of the SDS-PTHC-water system at α= 1.25 and ϕ_s=30 (**a**) and ϕ_s=50 (**b**) corresponding to L_α and L_3 phases respectively [3].

ratio (α=[organic salt]/[surfactant]=2.5) and concentration (ϕ_s=20, total wt% of surfactant and organic salt) were prepared by adding deionized water (Millipore) to the surfactant-organic salt mixture. Sample tubes were then sealed and left in an oven at 40°C for more than one week to equilibrate. The L_x phase coexisting with excess water was taken out carefully. For further studies, solutions of appropriate concentration (ϕ_s total wt% of oil or alcohol) were prepared by adding oil or alcohol to the bottom part (L_x phase).

4.4 Results

4.4.1 SDS-PTHC-Dodecane-Water System

Figure 4.3C shows the temperature−ϕ_s phase diagram of the system. For $\phi_s = 0$, SAXS and POM studies indicate the occurrence of L_x phase over the temperature range studied. SAXS patterns show one broad peak with spacing of about 3.7 nm (similar to figure 4.4A(a)). For $2.59 \leq \phi_s \leq 16.12$ at low temperatures, SAXS pattern (Fig. 4.5A(a)) shows two quasi-Bragg peaks whose spacings are in the ratio

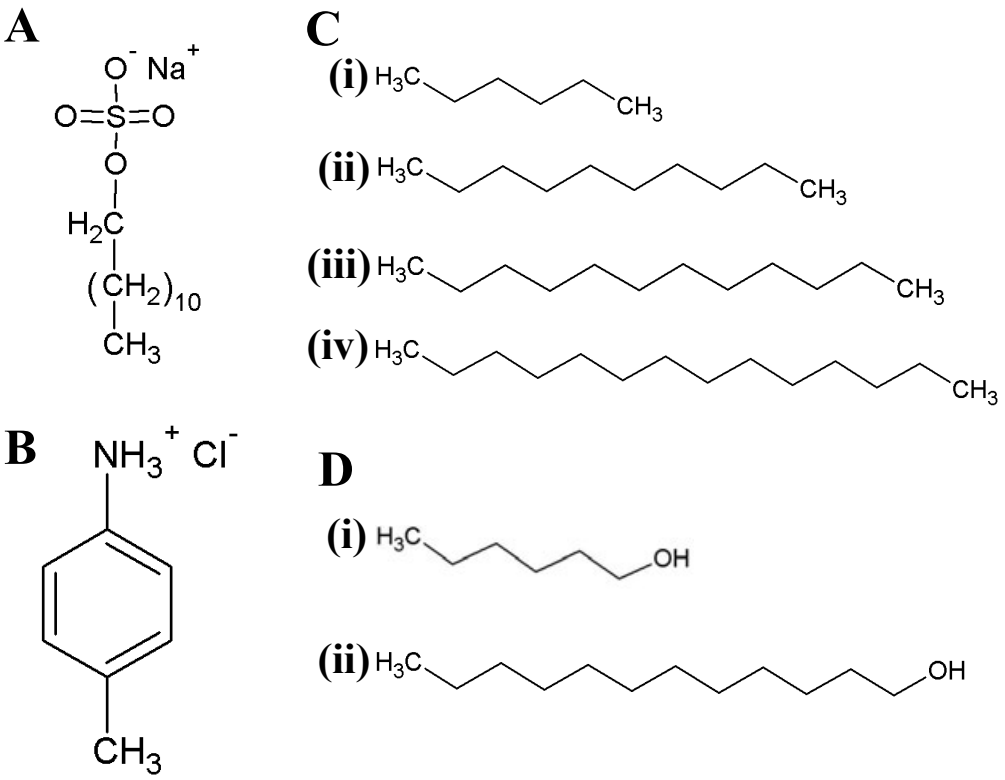

FIGURE 4.2: Chemical structure of (**A**) Sodium dodecyl sulfate (SDS) (**B**) p-toluidine hydrochloride (PTHC) (**C**) Oils; (i) Hexane (ii) Decane (iii) Dodecane and (iv) Tetradecane and (**D**) Alcohols; (i) 1-Hexanol and (ii) 1-Dodecanol.

1:2 and POM textures show oily streaks (Fig. 4.6B), confirming the occurrence of the lamellar (L_α) phase. This lamellar (L_α) phase transforms to L_x phase on heating via a two phase region. d-spacing is found to increase slowly in the L_α phase and then jumps to a high value in the L_x phase (Tab. 4.1). The ratio of spacing corresponding to the L_x and L_α phase, in the two phase region (L_x and L_α) is found to be in the range of 1.3 to 1.5 (Tab. 4.2). Transition is reversible on cooling and the transition temperature is found to initially increase and then decrease with increasing oil content. POM texture of L_α in the vicinity of the L_α-L_x transition shows oily streaks as focal conic chains (Fig. 4.6C). For $30 \leq \phi_s \leq 50$, L_x is found to swell with oil, however oil (dodecane) phase separates out from the solution at higher temperatures. For $\phi_s > 50$, oil phase separates out even at lower temperatures.

Figures 4.7C and 4.8C show the variation of d (d is the lamellar periodicity in

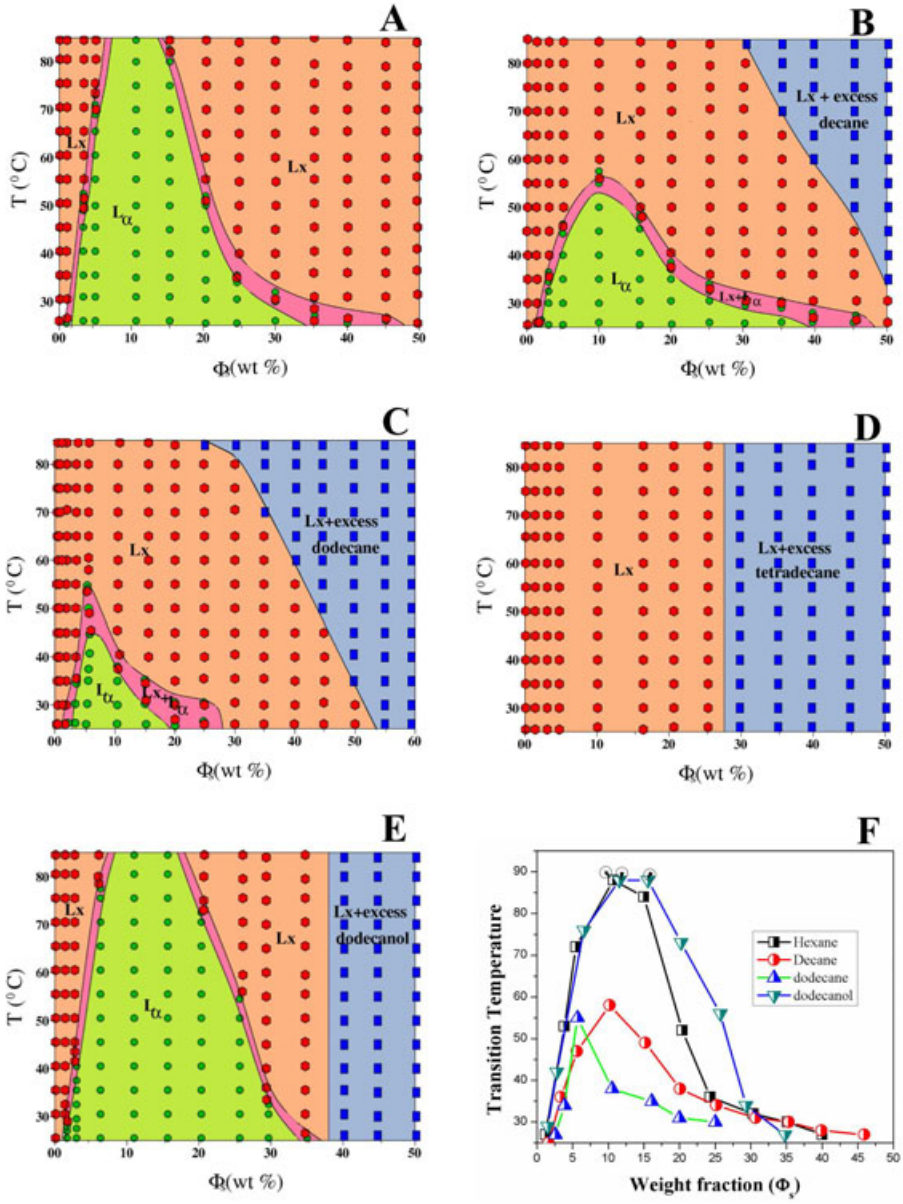

FIGURE 4.3: Partial phase diagram of the: SDS-PTHC-Hexane-Water system (**A**), SDS-PTHC-Decane-Water system (**B**), SDS-PTHC-Dodecane-Water system (**C**), SDS-PTHC-Tetradecane-Water system (**D**), SDS-PTHC-1-Dodecanol-Water system, (**E**) Region of stability of the L_α phase in the different systems (**F**); L_x is the isotropic phase of the bilayers and L_α is the lamellar phase. ϕ_s is the weight fraction of oil/alcohol.

the case of L_α phase or spacing corresponding to the broad peak in the case of L_x phase) with $1/\phi_v$, in the L_x and L_α phases, respectively; ϕ_v is the volume fraction of the L_x phase. ϕ_v is equal to (1-volume fraction of dodecane), volume fraction of dodecane is calculated from the weight fraction (ϕ_s), by using the densities of dodecane and L_x phase. Density of the L_x phase is estimated from its weight and

corresponding volume and it is found to be 1.0512 $\frac{g}{cm^3}$. Density of dodecane is taken as 0.750$\frac{g}{cm^3}$.

Variation of d with $1/\phi_v$ in the L_x and L_α phases could be fitted to straight lines with slopes 7.92 and 4.77 respectively. The ratio of these two slopes is 1.66 (Tab. 4.3)

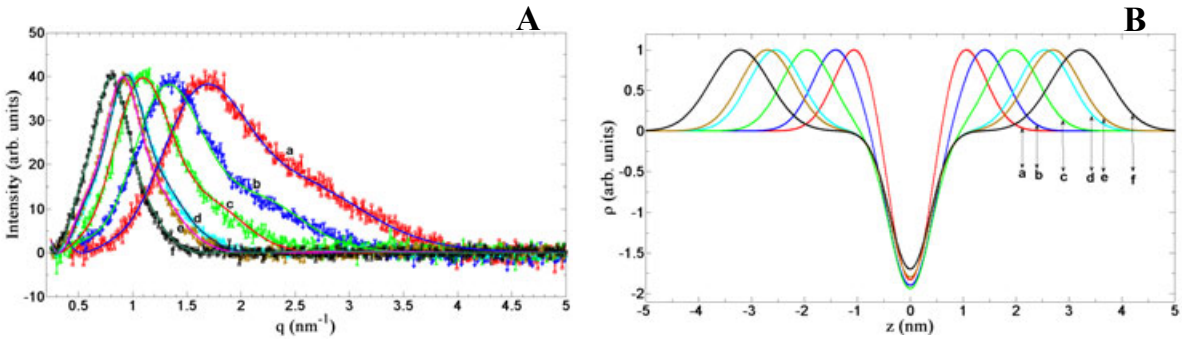

FIGURE 4.4: (**A**) X-ray diffraction patterns of the SDS-PTHC-Dodecane-Water system at T=60°C corresponding to ϕ_s=0.00 (**a**) ϕ_s=5.68 (**b**), ϕ_s=10.54 (**c**), ϕ_s=16.12 (**d**), ϕ_s=19.99 (**e**), ϕ_s=25.04 (**f**). The solid lines are fits to the model, obtained as described in chapter 1. (**B**) Electron density profiles obtained from fitting the data to the model corresponding to ϕ_s=0.00 (**a**) ϕ_s=5.68 (**b**), ϕ_s=10.54 (**c**), ϕ_s=16.12 (**d**), ϕ_s=19.99 (**e**), ϕ_s=25.04 (**f**).

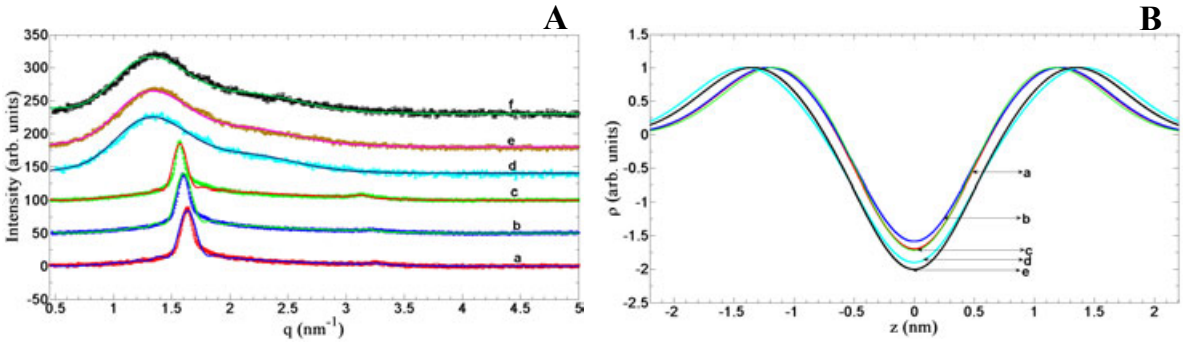

FIGURE 4.5: (**A**) X-ray diffraction patterns of the SDS-PTHC-Dodecane-Water system at ϕ_s=5.68 corresponding to T=25°C (**a**), T=30°C (**b**), T=40°C (**c**), T=60°C (**d**), T=70°C (**e**), T=80°C (**f**). The solid lines are fits to the model. (**B**) Electron density profiles obtained from fit corresponding to T=25°C (**a**), T=30°C (**b**), T=40°C (**c**), T=60°C (**d**), T=70°C (**e**), T=80°C (**f**).

Ionic conductivity studies have been done in the L_x phases at ϕ_s=0 and ϕ_s=30.09 and across the L_α-L_x transition (at ϕ_s=15.76). Conductivity at ϕ_s=0 is 15 mS/cm at 25°C and increases linearly with temperature (Fig. 4.9A). For ϕ_s=30.09, it is

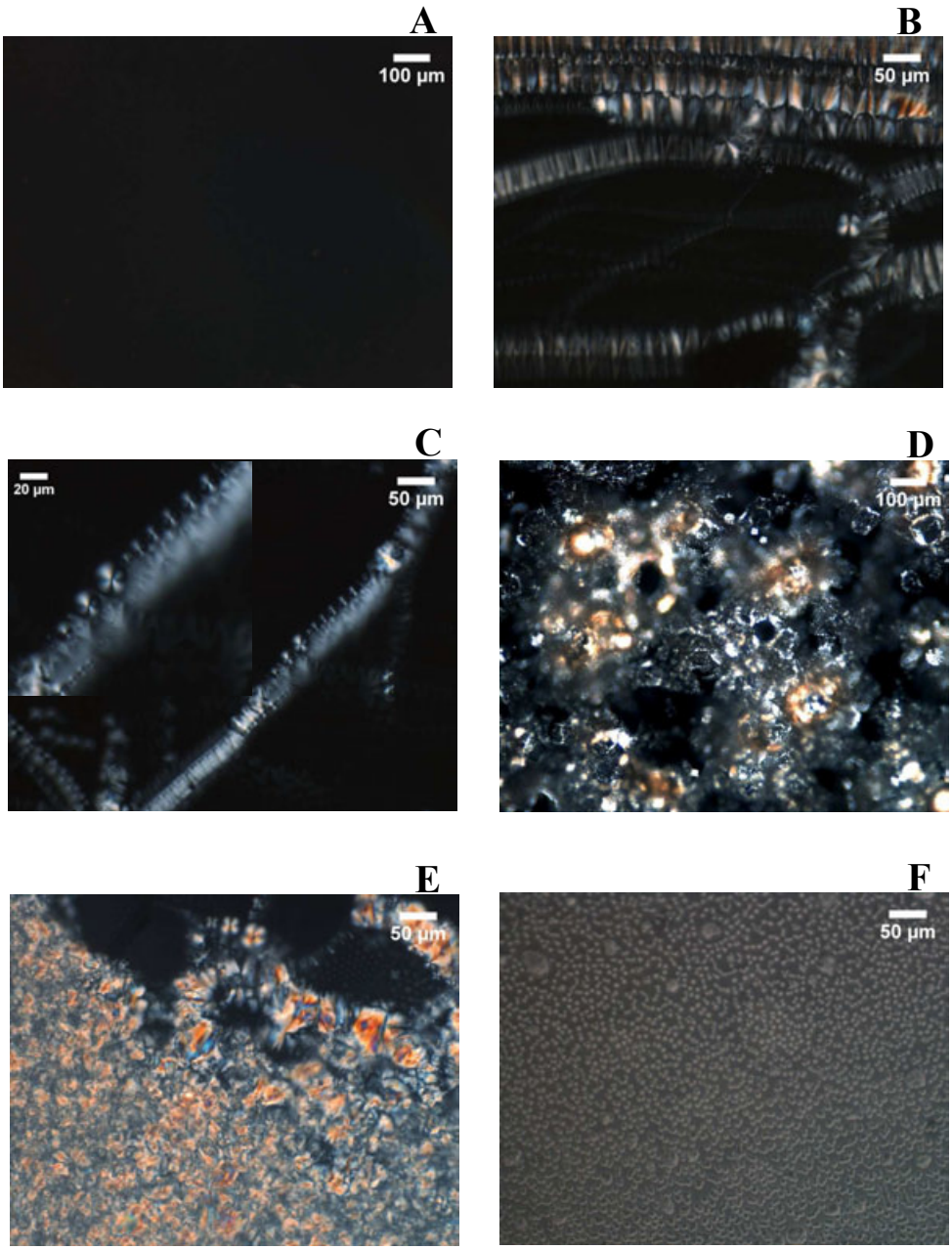

FIGURE 4.6: Polarizing Optical Microscopy textures of (**A**) L_x, **B** L_α, (**C**) $L_\alpha$phase in the vicinity of L_α-L_x transition showing oily streak as a chain of focal conic in the SDS-PTHC-Dodecane-Water system, (**D**) L_α, (**E**) L_α phase in the vicinity of L_α-L_x transition and (**f**) L_x phase with excess 1-Dodecanol in the SDS-PTHC-1-Dodecanol-Water system.

around 6 mS/cm at 25°C and increases slowly with temperature (Fig. 4.9C). At $\phi_s = 15.76$, across the L_α-L_x transition, its start at 3 mS/cm at 25°C in the L_α phase and rapidly changes to 8 mS/cm in the L_x phase, with a transition region of about 5°C (Fig. 4.9B).

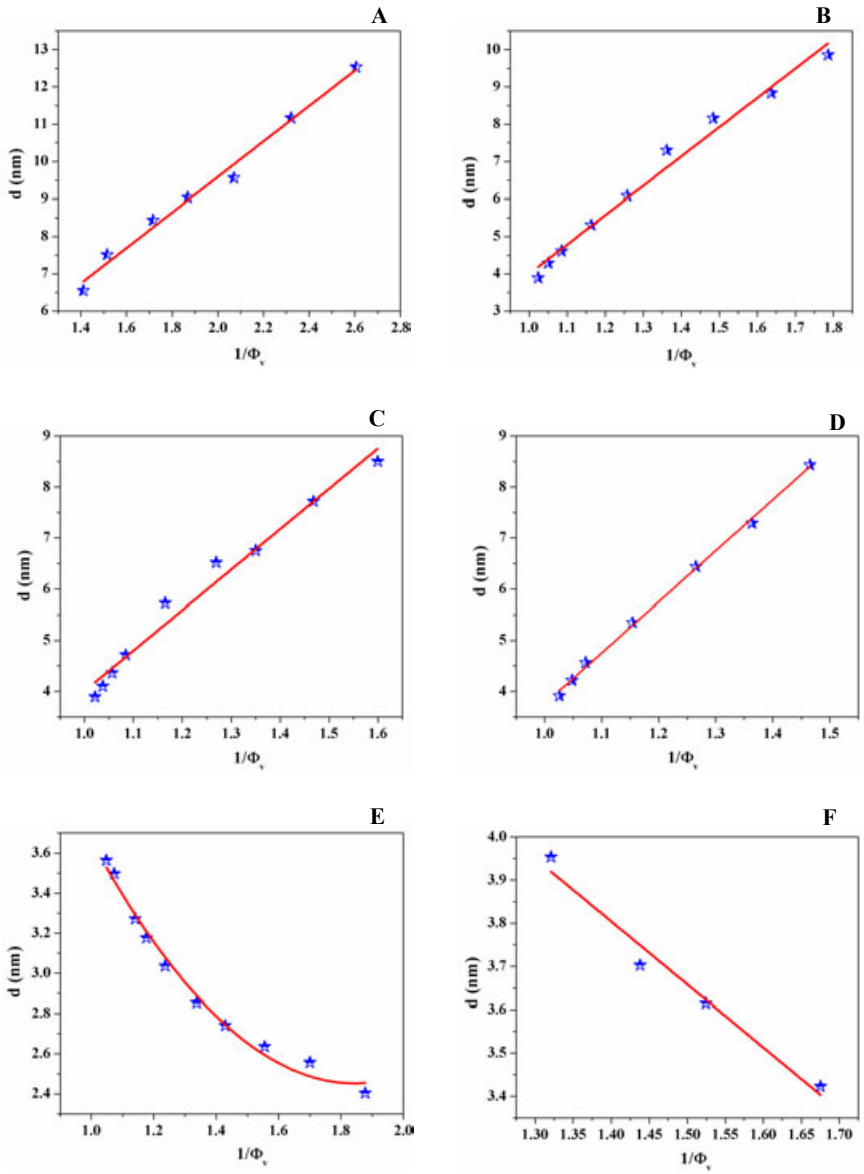

FIGURE 4.7: Variation of d-spacing with 1/volume fraction (ϕ_v) of oil/alcohol in the (L_x) phase of the (**A**) SDS-PTHC-Hexane-Water system, (**B**) SDS-PTHC-Decane-Water system, (**C**) SDS-PTHC-Dodecane-Water system, (**D**) SDS-PTHC-Tetradecane-Water system, (**E**) SDS-PTHC-1-Hexanol-Water system and (**F**) SDS-PTHC-1-Dodecanol-Water system.

Cryo-SEM studies have been done in the L_x phase at ϕ_s=0.00 and ϕ_s=29.85 and L_α phase at ϕ_s=5.71. Micrographs show bilayers with pore like features in the L_x phase (Fig. 4.10(A-D)). Stacks of the bilayers can be easily seen in the micrographs of L_α phase (Fig. 4.11(C and D)). However, the resolution of the micrograph is not sufficient to measure the bilayer thickness in the L_α phase and to investigate

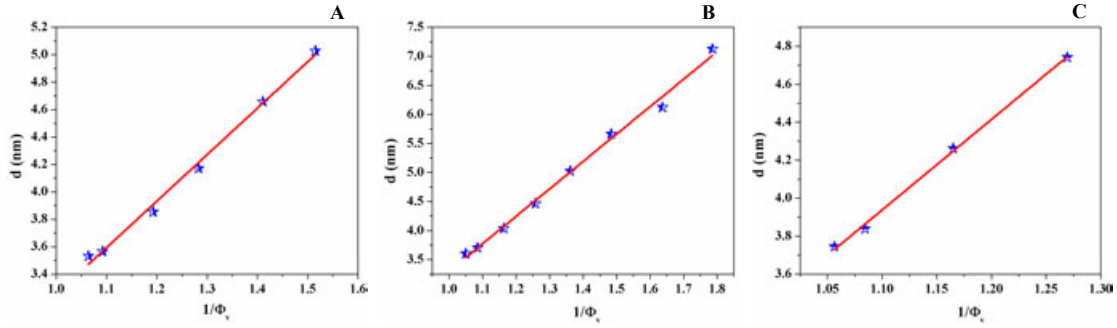

FIGURE 4.8: Variation of d-spacing with 1/volume fraction of oil in the L_α phase of the (**A**) SDS-PTHC-Hexane-Water system, (**B**) SDS-PTHC-Decane-Water system and (**C**) SDS-PTHC-Dodecane-Water system.

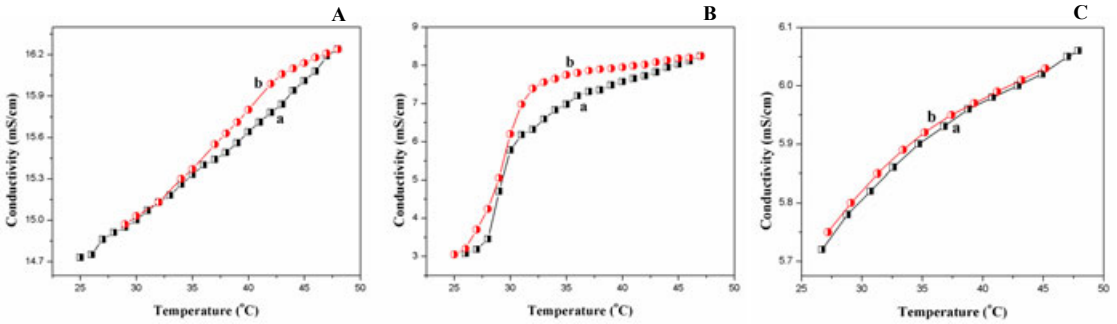

FIGURE 4.9: Variation of ionic conductivity with temperature in the SDS-PTHC-Dodecane-Water system at ϕ_s=0.00 **A**, ϕ_s=15.76 **B** and ϕ_s=30.09 **C**. Black (a) and red (b) colors show the heating and cooling cycle, respectively.

the nature of bilayer connections in the L_x phase.

4.4.2 SDS-PTHC-Hexane-Water system

Figure 4.3A shows the temperature−ϕ_s phase diagram of the system. For 1.2<ϕ_s<20, SAXS patterns (similar to figure 4.5A(a)) show two quasi-Bragg peaks whose spacings are in the ratio 1:2 and POM textures show oily streaks (similar to figure 4.6B), which confirm the occurrence of the lamellar (L_α) phase. For 20<ϕ_s<30, it shows the lamellar (L_α) phase at low temperatures, which transforms to isotropic (L_x) phase on heating via a two phase region. For ϕ_s>30, lamellar (L_α) phase coexists with the isotropic (L_x) phase at low temperatures and transforms to a pure isotropic (L_x) phase at higher temperatures.

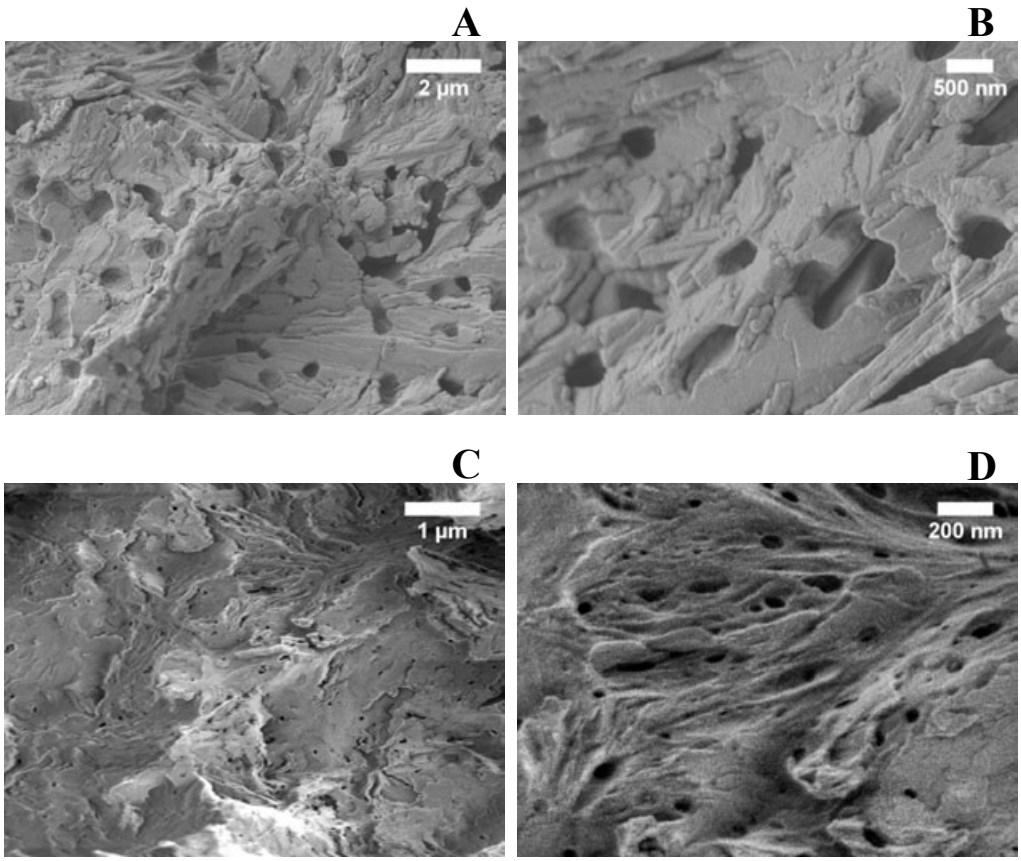

FIGURE 4.10: Cryo-SEM micrographs of L_x phase in the SDS-PTHC-Dodecane-Water system at T=25°C and ϕ_s=0.00 (**A and B**) and ϕ_s=29.85 (**C and D**).

L_x and L_α phases are found to swell with hexane. Figures 4.7A and 4.8A show the variation of d with $1/\phi_v$, in the L_x and L_α phase respectively, (ϕ_v=1-volume fraction of hexane). Volume fraction of hexane is calculated from the weight fraction (ϕ_s), by using the densities of hexane and the L_x phase, which are 0.6543 $\frac{g}{cm^3}$ and 1.0512 $\frac{g}{cm^3}$ respectively.

Variation of d with $1/\phi_v$ in the L_x and in Lα phases could be fitted to straight lines with slopes 4.75 and 3.39 respectively. The ratio of these two slopes is 1.40 (Tab. 4.3).

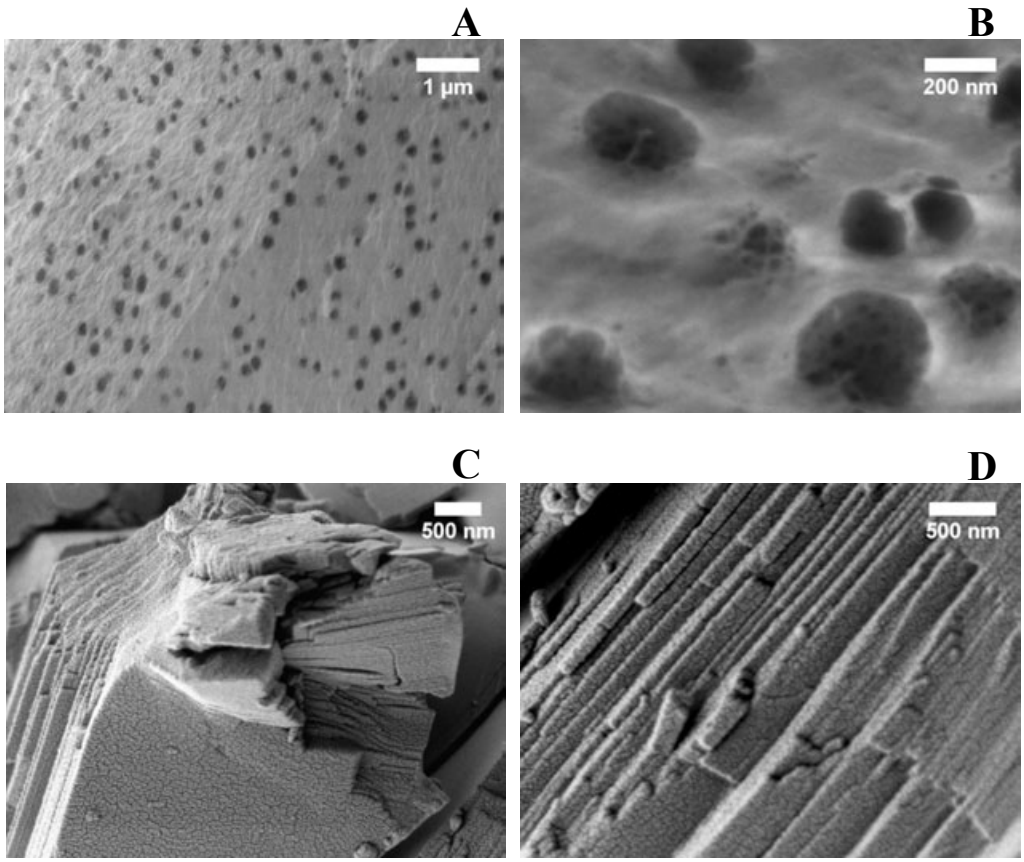

FIGURE 4.11: Cryo-SEM micrographs of L_x phase in the SDS-PTHC-1-Hexanol-Water system at T=25°C and ϕ_s=30.06 (**A and B**) and L_α phase in SDS-PTHC-Dodecane-Water system at T=25°C and ϕ_s=5.71 (**C and D**).

4.4.3 SDS-PTHC-Decane-Water system

Figure 4.3B shows the temperature$-\phi_s$ phase diagram of the system. For $1.7<\phi_s<35$, it shows the L_α phase at low temperatures which transforms to the L_x phase at higher temperatures. L_α phase is stable for a larger temperature range around $\phi_s\sim10$. For $\phi_s>35$, L_α phase coexists with a L_x phase at low temperatures, and transforms to the L_x phase at higher temperatures. At still higher temperatures, decane is found to phase separates out from the solution.

L_x and L_α phases are found to swell with decane. Figures 4.7B and 4.8B shows the variation of d with $1/\phi_v$ in the L_x and L_α phase respectively, ϕ_v=1-volume fraction of decane and is calculated from the decane weight fraction (ϕ_s), by using the densities of decane and the L_x phase. Density of decane is taken as $0.7030\frac{g}{cm^3}$.

Variation of d with $1/\phi_v$ in the L_x and in $L\alpha$ phases could be fitted to straight lines with slopes 7.86 and 4.73 respectively. The ratio of these two slopes is 1.66 (Tab. 4.3).

4.4.4 SDS-PTHC-Tetradecane-Water system

Figure 4.3D shows the temperature$-\phi_s$ phase diagram of the system. For $0<\phi_s<27$, the isotropic phase (L_x) is found to be stable over the whole temperature range studied. For $27<\phi_s<50$, tetradecane phase separates out from the solution.

L_x phase swells with tetradecane. Figure 4.7D shows the variation of d with $1/\phi_v$ in the L_x phase. Density of tetradecane is taken as 0.7635 $\frac{g}{cm^3}$.

Variation of d with $1/\phi_v$ in the L_x phase could be fitted to a straight line with a slope of 9.99 (Tab. 4.3).

4.4.5 SDS-PTHC-1-Hexanol-Water system

Addition of 1-hexanol to the L_x phase of the SDS-PTHC-Water system is found not to alter this phase, which is confirmed by SAXS and POM studies. POM studies show an optically isotropic texture (Fig. 4.6A). SAXS patterns show a broad peak (Fig. 4.12). However, the d-spacing corresponding to the broad peak is found to decrease on addition of 1-hexanol (Tab. 4.7).

Cryo-SEM studies have been done at ϕ_s=30.06 in the L_x phase. Micrographs show pore like features (Fig. 4.11A) which are found to have a substructure (Fig. 4.11B).

A de-swelling behavior is found in the L_x phase with 1-hexanol. Figure 4.7E shows the variation of d with $1/\phi_v$ in the L_x phase-ϕ_v is calculated from the hexagonal weight fraction (ϕ_s), by using the densities of 1-hexanol and the L_x phase. Density of 1-hexanol is taken as 0.8136$\frac{g}{cm^3}$.

Variation of d with $1/\phi_v$ in the L_x phase could be fitted to a quadratic equation. Parameters are given in table 4.3.

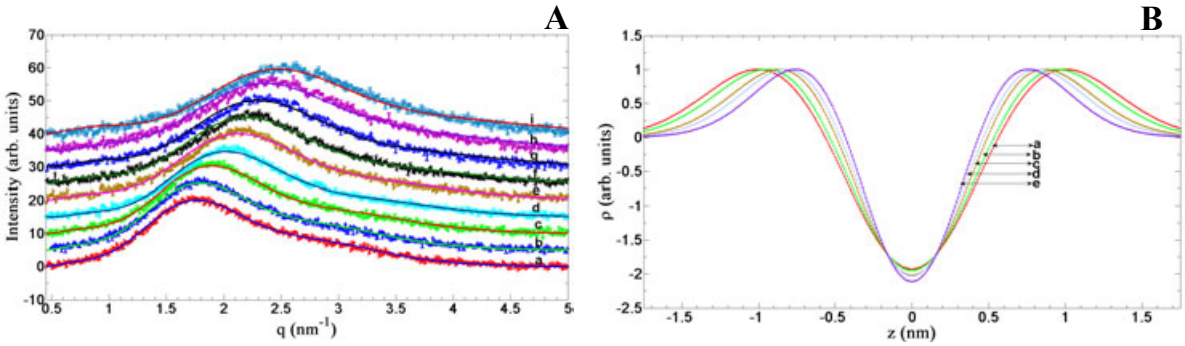

FIGURE 4.12: (**A**) X-ray diffraction patterns of the SDS-PTHC-1-Hexanol-Water system at T=30°C corresponding to ϕ_s=3.56 (**a**), ϕ_s=5.36 (**b**), ϕ_s=9.79 (**c**), ϕ_s=15.47 (**d**), ϕ_s=20.70 (**e**), ϕ_s=24.92 (**f**), ϕ_s=30.06 (**g**), ϕ_s=35.15 (**h**) and ϕ_s=40.45 (**i**). The solid lines are fits to the model. (**B**) Electron density profiles obtained from the fit corresponding to ϕ_s=3.56 (**a**), ϕ_s=9.79 (**b**), ϕ_s=20.70 (**c**), ϕ_s=30.06 (**d**) and ϕ_s=40.45 (**e**).

4.4.6 SDS-PTHC-1-Dodecanol-Water system

Figure 4.3E shows the temperature$-\phi_s$ phase diagram of the system. For $1.524 \leq \phi_s \leq 6.57$ at low temperatures, it shows the lamellar (L_α) phase which transforms to the isotropic (L_x) phase at higher temperatures-POM shows an oily streak texture which is characteristic of the $L_\alpha$phase (Fig. 4.6D and E). For $6.57 \leq \phi_s \leq 15.56$, it shows the L_α phase for the temperature range studied. For $15.56 \leq \phi_s \leq 34.80$, it shows L_α phase at low temperatures which transforms to the L_x phase at higher temperatures. For $\phi_s \geq 34.80$ excess 1-dodecanol comes out from the solution and POM shows droplet-like texture (Fig. 4.6F).

A de-swelling behavior is found in the L_x phase with 1-dodecanol. Figure 4.7F shows the variation of d with $1/\phi_v$, where ϕ_v is calculated from the weight fraction (ϕ_s), by using the densities of 1-dodecanol and the L_x phase. Density of 1-dodecanol is taken as $0.8309 \frac{g}{cm^3}$.

Variation of d with $1/\phi_v$ in the L_x phase could be fitted to a straight line with slope of -1.46 (Tab. 4.3).

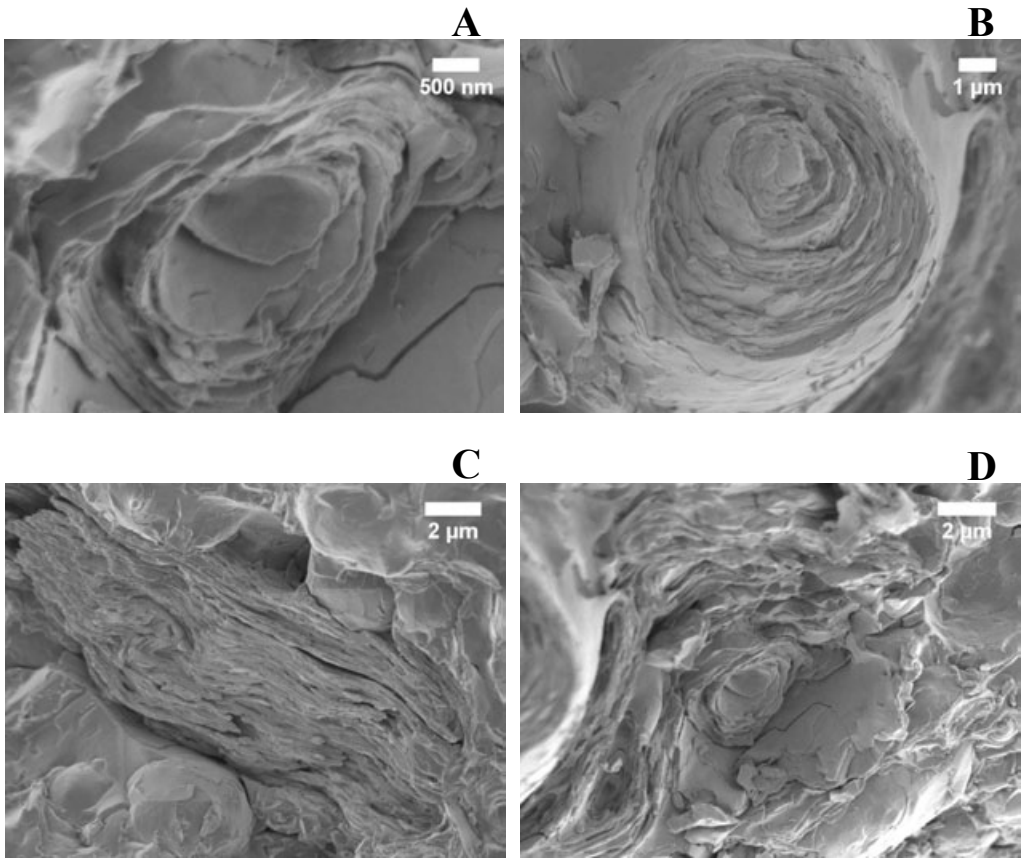

FIGURE 4.13: Cryo-SEM micrographs of L_α phase in the SDS-PTHC-1-Dodecanol-Water system at T=25^{0}C and ϕ_s=11.51 (**A-D**).

Cryo-SEM studies have been done in the lamellar (L_α) phase at ϕ_s=5.71. Micrographs show features of stacks of bilayers (Fig. 4.13(A-D)).

TABLE 4.1: Values of parameters for the diffraction data at ϕ_s=5.68 of the SDS-PTHC-Dodecane-Water system obtained from the fit to the model of lamellar (L_α) phase.

T (°C)	σ_h(nm)	σ_c(nm)	$(\rho_c)/(\rho_h)$	$z_h(nm)$	η	N	N_d	$d(nm)$	phase
25	0.44 ±0.02	0.40±0.02	-1.72±0.08	1.18±0.04	0.16± 0.02	9±1	6.5± 0.3	3.83	L_α
30	0.44±0.02	0.40±0.02	-1.61±0.08	1.19±0.04	0.15±,0.02	10±1	7.5±0.3	3.92	L_α
40	0.44±0.02	0.40±0.03	-1.74± 0.08	1.14±0.04	0.14±0.02	11±1	12.4±0.3	4.00	L_α
60	0.44±0.03	0.42±0.03	-1.90±0.09	1.40±0.05	0.27±0.03	2±0	1.4± 0.1	4.72	L_x
70	0.44±0.03	0.42±0.03	-1.9± 0.1	1.40±0.05	0.27± 0.03	2±0	1.3± 0.1	4.72	L_x
80	0.44±0.03	0.42± 0.03	-2.0± 0.1	1.33±0.05	0.30±0.03	2±0	1.0±0.1	4.71	L_x

TABLE 4.2: Ratios of spacing corresponding to L_x and L_α phases, in the L_α-L_x coexisting region of the SDS-PTHC-Dodecane-Water system

T(°C)	ϕ_s	$d(nm)_{L_\alpha}$	$d(nm)_{L_x}$	Ratio	Phase
55	5.68	3.90	5.08	1.30	$L_\alpha + L_x$
38	10.54	4.48	6.01	1.34	$L_\alpha + L_x$
35	16.12	4.88	7.07	1.45	$L_\alpha + L_x$
25	19.99	4.95	7.32	1.48	$L_\alpha + L_x$
25	25.04	5.61	8.14	1.45	$L_\alpha + L_x$

TABLE 4.3: Swelling behavior of L_x and L_α phases in the different systems.

Oil or Alcohol	Slope (L_x)	of the fit nature	T (°C)	Slope (L_α)	of the fit nature	T (°C)	Ratio ((Slope L_x) /(slope L_α))
Hexane	4.75	linear	60	3.39	linear	25	1.40
Decane	7.86	linear	60	4.73	linear	60	1.66
Dodecane	7.92	linear	60	4.77	linear	25	1.66
Tetradecane	9.99	linear	40	–	–	–	–
1-Hexanol	-6.25, 1.69	quadratic	25	–	–	–	–
1-Dodecanol	-1.46	linear	80	–	–	–	–

4.5 Discussion

4.5.1 Data analysis

SAXS data of the L_α phase were analyzed as described in chapter 1. Variation of the SAXS data with temperature at ϕ_s=5.68, of the SDS-PTHC-Dodecane-Water system is shown in figure 4.5A. The patterns are well described by the model for the L_α phase. The electron density profiles obtained from the fit are shown in figure 4.5B and the corresponding model parameters are given in table 4.1.

SAXS data from the L_x phase, at low oil content is found to be well described by the model of the L_α phase. Figure 4.5A(d-f) shows a good agreement between data and the model and the fitting parameters are given in table 4.1. The variation of the electron density profile across the transition L_α-L_x is found to be gradual (Fig. 4.5B).

The L_x phase found at higher oil content shows a broad peak which is sharper than the peak found at low oil content. The intensity at $q \to 0$ ($I_{q\to 0}$) is also found to increase with increasing the oil content (Fig. 4.14) and the SAXS data do not

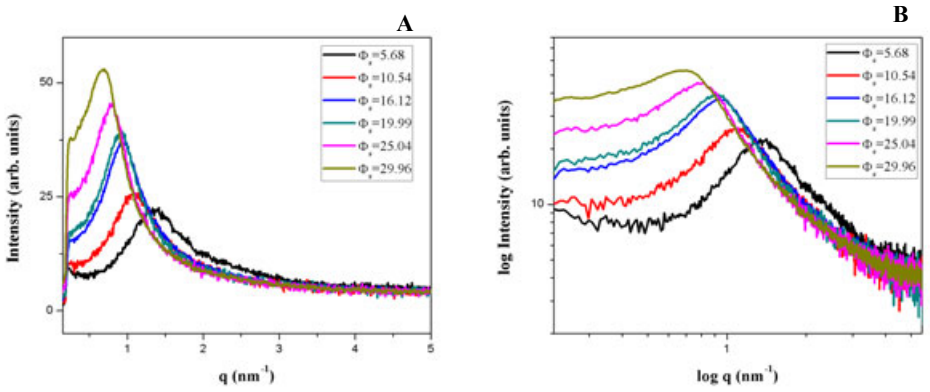

FIGURE 4.14: X-ray diffraction patterns of the L_x phase with increasing concentration of Dodecane in the SDS-PTHC-Dodecane-Water system at T=60°C; (**A**) linear scale (**B**) log scale. base of log is 10.

fit well to the model of L_α phase. Though, a good agreement is found between the model of Lα phase and data of L_x phase at low oil content, the fit becomes worse at higher oil content (Fig. 4.15 and Tab.4.4). Good agreement is also not found between the data and the model of the sponge (L_3) phase (as described in chapter 1) for reasonable values of the parameters as shown in figure 4.16. The obtained fitting parameters are given in table 4.5. The high value of ($I_{q\to 0}$), at higher oil content, may come from composition fluctuation as reported by many authors [4]. So, After removing background scattering at low q, we found a good agreement between model of Lα and data as shown in figure 4.4A. The parameters obtained from the model are given in table 4.6 and corresponding electron density profile is shown in figure 4.4B.

TABLE 4.4: Values of parameters for the diffraction data at T=60°C of the SDS-PTHC-Dodecane-Water system obtained from the fit to the model of lamellar (L_α) phase without background subtraction.

ϕ_s	σ_h(nm)	σ_c(nm)	$(\rho_c)/(\rho_h)$	$z_h(nm)$	η	N	N_d	$d(nm)$	Phase
5.68	0.44±0.03	0.41± 0.03	-1.88±0.09	1.42±0.05	0.28±0.03	2±0	0.7± 0.1	4.584	L_x
10.54	0.34±0.03	0.40±0.02	-1.89±0.09	1.81±0.05	0.26±0.03	2±0	3.3±0.1	5.730	L_x
16.12	0.30±0.03	0.4± 0.02	-1.94± 0.1	2.08±0.04	0.24±0.03	2±0	2.5±0.2	6.520	L_x

Variation of the SAXS data of the L_x phase with ϕ_s at t=60°C of the SDS-PTHC-1-Hexanol-Water system is shown in figure 4.12A along with the fit to the model

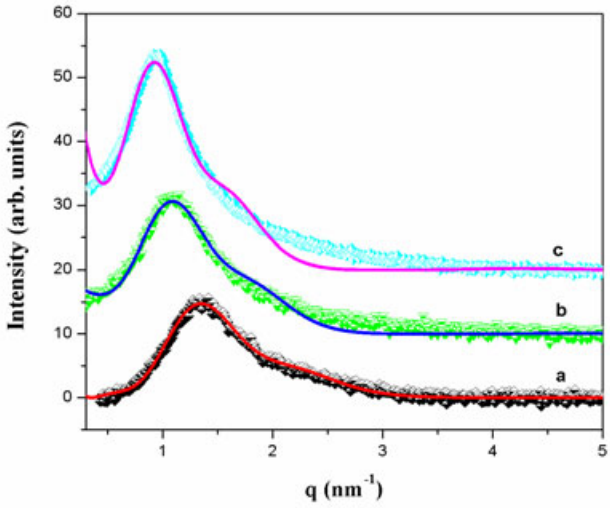

FIGURE 4.15: X-ray diffraction patterns of the L_x phase of the SDS-PTHC-Dodecane-Water without background subtraction for (**a**) ϕ_s=5.68 (**b**), ϕ_s=10.54 (**c**) and ϕ_s=16.12 at T=60°C. The solid lines are fits to the model.

and the parameters obtained from the model are given in table 4.7. Corresponding electron density profiles are shown in figure 4.12B.

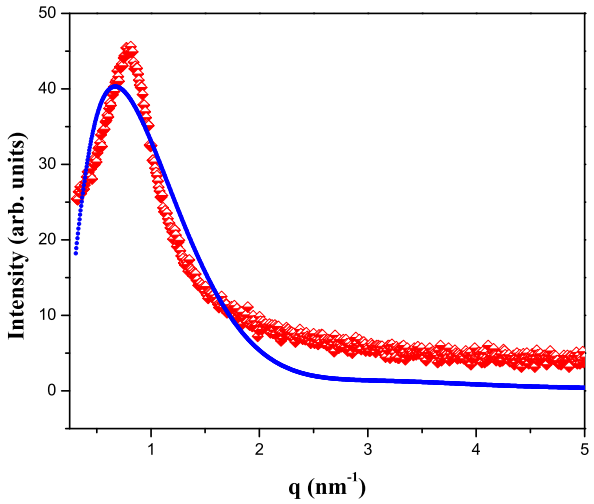

FIGURE 4.16: X-ray diffraction pattern of the L_x phase along with a typical fit to the model of the sponge (L_3) phase. Red and blue colors are represent the data and fit, respectively.

TABLE 4.5: Values of parameters for the diffraction data at ϕ_s=25.04 and T=60°C of the SDS-PTHC-Dodecane-Water system obtained from the fit to the model of sponge (L_3) phase.

ξ_2(nm)	σ(nm)	w(nm)	L(nm)
1.68	4.05	2.26	7.72

TABLE 4.6: Values of parameters for the diffraction data at T=60°C of the SDS-PTHC-Dodecane-Water system obtained from the fit to the model of lamellar (L_α) phase after background subtraction.

ϕ_s	σ_h(nm)	σ_c(nm)	$(\rho_c)/(\rho_h)$	$z_h(nm)$	η	N	N_d	$d(nm)$	Phase
0.00	0.44±0.03	0.41± 0.03	-1.85± 0.09	0.98±0.05	0.36±0.03	2±0	1.6±0.1	3.74	L_x
5.68	0.44±0.03	0.42± 0.03	-1.90±0.09	1.40±0.05	0.27±0.03	2±0	1.4± 0.1	4.58	L_x
10.54	0.48±0.03	0.40±0.02	-1.94±0.09	1.95±0.05	0.25±0.03	2±0	1.9±0.1	5.73	L_x
16.12	0.50±0.03	0.38± 0.02	-1.8± 0.1	2.55±0.04	0.24±0.03	3±0	8.7±0.2	6.52	L_x
19.99	0.51± 0.03	0.38±0.02	-1.8±0.1	2.70±0.04	0.22±0.02	3±0	8.8±0.2	6.75	L_x
25.04	0.56± 0.03	0.38±0.02	1.7±0.1	3.22±0.04	0.20± 0.02	3±0	11.7±0.2	7.72	L_x

TABLE 4.7: Values of parameters for the diffraction data at T=30°C of the SDS-PTHC-1-Hexanol-Water system obtained from the fit to the model of lamellar (L_α) phase.

ϕ_s (°C)	σ_h(nm)	σ_c(nm)	$(\rho_c)/(\rho_h)$	$z_h(nm)$	η	N	N_d	$d(nm)$	Phase
3.56	0.40 ±0.02	0.39±0.02	-1.90±0.08	0.93±0.04	0.35± 0.02	2±0	1.6± 0.3	3.546	L_x
5.36	0.40 ±0.02	0.39±0.02	-1.90±0.08	0.91±0.04	0.36± 0.02	2±0	1.5± 0.3	3.498	L_x
9.79	0.40 ±0.02	0.39±0.02	-1.90±0.08	0.85±0.04	0.36± 0.02	2±0	1.1± 0.3	3.272	L_x
15.47	0.40 ±0.02	0.39±0.02	-1.90±0.08	0.79±0.04	0.36± 0.02	2±0	0.9± 0.3	3.036	L_x
20.70	0.40 ±0.02	0.40±0.02	-1.92±0.08	0.69±0.04	0.37± 0.02	2±0	1.0± 0.3	2.854	L_x
24.92	0.40 ±0.02	0.40±0.02	-1.92±0.08	0.67±0.04	0.38± 0.02	2±0	0.9± 0.3	2.741	L_x
30.06	0.40 ±0.02	0.40±0.02	-1.92±0.08	0.60±0.04	0.38± 0.02	2±0	0.9± 0.3	2.606	L_x
35.15	0.40 ±0.02	0.40±0.02	-1.91±0.08	0.55±0.04	0.39± 0.02	2±0	1.4± 0.3	2.557	L_x
40.45	0.40 ±0.02	0.40±0.02	-1.92±0.08	0.43±0.04	0.40± 0.02	2±0	0.9± 0.3	2.402	L_x

4.5.2 Nature of Lα-L$_x$ transition and the structure of L$_x$ phase

SAXS data of Lα and L$_x$ phases are found to fit very well to the model of L$_\alpha$ phase. The number of correlated bilayers, a fitting parameter, is approximately 10 in the Lα phase and is about 2 in the L$_x$ phase, indicating that inter-bilayer correlations decrease across the L$_\alpha$-L$_x$ transition. Further, we have measured the ionic conductivity of a sample exhibiting the Lα-L$_x$ transition as a function of

temperature (Fig. 4.9B). The observed variation of the conductivity is very similar to that seen across the Lα-sponge transition in other systems [5], where the increased conductivity in the sponge phase has been interpreted in terms of formation of passages between the bilayers. The change in the conductivity occurs over a range of about 5°C, which is consistent with our microscopy observations. Thus the observed decrease in the inter-bilayer correlations and increase in the ionic conductivity across the L_α-L_x transition can be qualitatively understood in terms of the formation of passages between the bilayers, as described in the previous chapter.

High value of conductivity is found in the L_x phase at ϕ_s=0.00 (without dodecane) (Fig. 4.9A), and at high content of dodecane at ϕ_s=30.09 (Fig. 4.9C), which lead us to conclude that L_x phase at low and high content of oils and alcohols has locally a bilayer structure which is connected through passages with continuous water channels.

The measured ratio of slopes of the linear swelling behavior of L_x and L_α phases with oil (Tab. 4.3), is very similar to that seen in the sponge phase further supporting the purposed model for L_x phase.

4.5.3 Stability of L_x phase

Phases exhibited by bilayers can be divided into three broad classes: connected, planar and vesicular (disconnected). These phases are easily explained, to a first approximation, in terms of membrane bending elasticity. The deformation energy of a bilayer is described in terms of two elastic moduli: the bending rigidity κ related to mean curvature of the bilayer and the modulus of Gaussian curvature, $\bar{\kappa}$ related to the Gaussian curvature [6]. Relative stability of these phases are depend on the ratio of $\bar{\kappa}$ and κ [7, 8]. It has been suggested that weakly negative values of this ratio stabilizes a connected network of bilayers.

Oils and alcohols are found to change the rigidity of the bilayer [9, 10]. Bending rigidity (κ) is found to be a discontinuous function of the chain length of the oil

and alcohol due to their differences in penetrating the surfactant chains. Bending rigidity is higher for oils of shorter chain lengths and lower for longer chain lengths [9] while the opposite trend has been seen with alcohols [10]. It has also been found that oils of shorter or comparable chain lengths favor the lamellar phase while longer chain lengths favor sponge phase and bi-continuous phases [9]. However, there are no reports on the direct measurement of the Gaussian rigidity ($\bar{\kappa}$).

In the present study, addition of 1-hexanol to the L_x phase is found to preserve this phase, whereas the addition of a small amount of 1-dodecanol, transforms L_x phase into L_α. L_x is found to reappear at higher concentrations of 1-dodecanol. We also found that addition of tetradecane to the L_x phase preserves this phase, while small amounts of the oil (hexane, decane and dodecane) of chain length equal to or less than the chain length of the surfactant induce the L_α phase. L_x phase reappears at higher concentration of oils. Oils of shorter chain length is found to be more effective in inducing the lamellar (L_α) phase. Figure 4.3F shows the region of stability of the L_α in the phase diagrams. Hexane and 1-dodecanol are found to be comparably effective to induce the formation of the L_α phase followed by decane and dodecane, respectively.

Alcohol has a tendency to anchor at the water-hydrocarbon interface with its $-OH$ group, leaving the chain inside the bilayer leading to a decrease in the effective head group area. In the case of 1-hexanol, which has a shorter chain length compared to the surfactant (SDS), the decrease in the head group area is over compensated by increase in the free space for the chain group. This leads to the thinning the bilayer and a reduction in κ [10], preserving the L_x phase. It has also been seen that incorporation of 1-hexanol or alcohols of smaller chain length compared to the surfactant, helps to form the sponge phase [11, 12]. However, oil (tetradecane) of chain length longer than the surfactant (SDS), is found to preserve the L_x phase.

Addition of alcohol of comparable chain length and oils of chain length smaller or comparable to that of the surfactant to the L_x is found to show the $L_\alpha \rightarrow L_x$ phase sequence as a function of alcohol or oil concentrations (Fig. 4.3). The re-entrant

behavior of the L_x phase can be understood in terms of $\bar{\kappa}$ and κ. The ratio of $\bar{\kappa}$ and κ can be given in terms of ϕ_s as follows.

$$\frac{\bar{\kappa}}{\kappa} = -a(\phi_s) + b(\phi_s)^2 + (\frac{\bar{\kappa}}{\kappa})_{\phi_s=0} \tag{4.1}$$

where a and b are positive constants depending on the system and ϕ_s is the weight fraction of oil or alcohol. The last term is the value of $(\frac{\bar{\kappa}}{\kappa})$ in the L_x phase when no oil or alcohol is added. In the present system, this value is weakly negative. Addition of small amounts of oil or alcohol (at low ϕ_s), the ratio $(\frac{\bar{\kappa}}{\kappa})$ decreases initially up to a minimum negative value which stabilizes the L_α phase and leads to L_x to L_α transition. However, at higher ϕ_s this ratio increases to a weakly negative value which stabilizes the L_x phase and leads to L_α to L_x transition. Clearly further work is needed to substantiate this proposal.

4.6 Conclusion

In conclusion, we have constructed partial phase diagrams of the SDS-PTHC-Oil/Alcohol-Water systems with various chain lengths of oil and alcohol. Only L_α and L_x phases are found to be stable in these systems. High value of ionic conductivity in the L_x phase suggests that this phase has a connected bilayer structure with continuous water channels, which is supported by the swelling data on the L_x and by detailed analysis of the SAXS data. Addition of alcohol of comparable chain length and oils of chain length smaller or comparable to that of the surfactant to the L_x is found to show the $L_\alpha \rightarrow L_x$ phase sequence as a function of alcohol or oil concentrations, ϕ_s. In-order to understand the re-entrant behavior of the L_x phase, a non-monotonic variation of $(\frac{\bar{\kappa}}{\kappa})$ with increasing ϕ_s has been proposed. Clearly further work is needed to clarify this situation.

Bibliography

[1] A. Pal, G. Pabst and V. A. Raghunathan, *Soft Matter*, **8**, 9069 (2012).

[2] S. P. Gupta and V. Raghunathan, (to be submitted).

[3] Thesis by Sajal Kumar Gosh, *Influence of Strongly Bound Counterions on the Phase Behaviour of Ionic Amphiphiles* (2007).

[4] G. Port, J. Marignan, P. Bassereau and R. May, *Europhys. Lett.*, **7**, 713 (1988).

[5] E. Hecht, K. Mortensen and H. Hoffmann, *Macromolecules*, **28**, 5465 (1995).

[6] W. Helfrich, Z. *Naturforsch. C*, **28**, 693 (1973).

[7] L. Golubović, *Phys. Rev. E*, **50**, R2419 (1994).

[8] D. C. Morse, *Phys. Rev. E*, **50**, R2432 (1994).

[9] H. Kellaya, B. P. Binksb, Y. Hendrikxc, L. T. Leed and J. Meunier, *Adv. Colloid Interface Sci.*, **49**, 85 (1994).

[10] C. R. Safinya, E. B. Sirota, D. Roux, and G. S. Smith, *Phys. Rev. Lett.*, **62**, 1134 (1989).

[11] C. A. Miller, M. Gradzielski, H. Hoffmann, U. Krämer, and C. Thunig, *Progr. Colloid. Polym. Sci.*, **84**, 1 (1991).

[12] Ning Lei, C. R. Safinya, D. Roux, and K. S. Liang, *Phys. Rev. E*, **56**, 608 (1997).

Chapter 5

Sponge phase in a cationic surfactant-water systems induced by a polyelectrolyte

5.1 Introduction

Coacervation can be define as a process during which a homogeneous aqueous solution of charged macromolecules, undergoes liquid-liquid phase separation, giving rise to a macromolecules-rich dense phase. It has been proposed that coacervates are at the origin of all life [1]. Coacervates are classified as either simple or complex depending on the process that leads to coacervation [2–4]. Addition of salt normally promotes coacervation in the simple coacervation process, while two oppositely charged macromolecules, e.g., proteins or oppositely charged polyelectrolytes can undergo coacervation through associative interactions, in the process of complex coacervation. Coacervates remain in equilibrium with the dilute supernatant. The charges on the polyelectrolytes must be sufficiently large to cause significant electrostatic interactions, but not so large as to cause precipitation.

Coacervation involves two steps, first, the selective charge neutralization of the polyions dictated by electrostatic interactions and second, the gain in entropy

through random mixing of the polyions in the dense phase plus the gain in entropy due to release of counter ions to the solvent [5, 6]. DNA-lipid complexes which are of biomedical importance as delivery vectors for gene therapy, are examples of complex coacervates [7–10].

Recently, coacervate formation from a single organic compound, a synthetic gemini surfactant has been reported [11]. The authors also proposed that the surfactant phase of sponge morphology, [11–13] should be redefined as coacervates [12]. Further, coacervates of Sponge (L_3) morphology in lipid systems have potential medical and industrial applications and have been used as substrates for the crystallization of membrane proteins, which are very difficult to crystallize using conventional protocols [14].

As, we have discussed in the previous chapters, some ionic surfactants form an isotropic (L_x) phase of bilayers at very high salt concentrations. Our motive is to see whether this behavior is generic or specific to a particular surfactant and salt system. For this purpose, we have studied the phase behavior of aqueous solutions of mixtures of didodecyldimethyl ammonnium bromide (DDAB) and sodium salt of polyacrylic acid (PAANa).

This chapter deals with structures exhibited by complexes of poly acrylic acid, sodium salt (PAANa) with didodecyldimethyl ammonnium bromide (DDAB) and the effect of poly acrylic acid (PAA) on the phase behavior of CPHN (complex of cetylpyridinium chloride (CPC) and 3-hydroxy-2-sodium naphthoate (SHN)). Detailed x-ray diffraction experiments have been carried out on complexes of DDAB with different polyelectrolytes and those of DNA with cationic lipids in recent years, motivated by their potential biomedical applications. These are summarized in section 5.2. Experimental methods and chemicals that we have used are described in section 5.3. We have carried out x-ray, optical microscopy and cryo-SEM studies of DDAB-PAANa complexes, which reveal that the complexes exhibits collapsed lamellar phase as well as a highly swollen sponge phase. In order to reveal the structure in a quantitative way, we fit the scattering data of the sponge, to the model describe by Porcar et al. [15]. We have also studies the

effect of PAA on the phase behavior of CPHN. Interestingly, PAA is found to tune the spontaneous curvature of the micelles, leading to a transition from lamellar phase of bilayers to an inverted isotropic phase of spherical micelles via hexagonal phase of inverted cylindrical micelles. These results are described in section 5.4. We discuss our results in section 5.5. Section 5.6 contains conclusions that can be drawn from these studies.

5.2 Earlier Studies

The phase behavior of aqueous solutions of the cationic double chain surfactant DDAB has been extensively studied in the context of an anomalous attractive interaction between charged bilayers and is found to be strikingly different from those of other double-chain lipid systems [16, 17]. At very high water content, an isotropic phase of unilamellar vesicle (labeled as $^{A}L_3$) is reported. At higher concentration of surfactant, a swollen lamellar (L_α) phase, made up of multilamellar vesicles is found. Interestingly, DDAB-Water system is found to exhibit the coexistence of a swollen lamellar (L_α) phase and a collapsed lamellar phase (L'_α). At 30°C, the coexistence region is found to be stable from ∼40 to ∼85 wt% of DDAB. On increasing the temperature, the coexistence range decreases, leading to a critical point at ∼74°C. At very low water content and low temperature only the collapsed lamellar phase (L'_α) is found. However, at higher temperatures an isotropic (I) phase has been seen. Small angle neutron scattering (SANS) experiments on this phase show only a broad correlation peak. Some authors have reported a flow birefringent phase (L_3) at very low surfactant concentrations [18]. However, didodecyldimethyl ammonnium chloride (DDAC)-Water system shows only a single lamellar phase.

Mixtures of DDAB and the neutral lipid dilauroyl-sn-glycerophosphocholine (DLPC) form lamellar complexes with poly(glutamic acid) (PGA) [19]. By keeping ϕ_{pc} (=

weight of neutral lipid/ total weight of the lipid) fixed and varying the PGA concentration, the lamellar periodicity remains constant at 5nm. Surprisingly, no additional peaks corresponding to PGA-PGA correlations have been observed, which could be explained in terms of the low persistence length of PGA. The swelling behavior observed on increasing ϕ_{pc} at ρ_{iso} (isoelectric point where the positive charges of the DDAB are balanced by the negative charges on the polyelectrolyte DNA) has been also seen in DDAB-DLPC-DNA system [20]. The increase in d-spacing on diluting the charge density of the bilayers, has led to the proposal of a pinched lamellar structure in these systems. This consists of locally pinched regions of DDAB and PGA with the d-spacing away from these regions determined by DLPC. However, the pinching mechanism proposed here has not been well established.

Structures of complexes of DDAB and various polyelectrolytes have been reported [21]. Complexes appear as white precipitates phase separating out from the aqueous solution. The lamellar periodicity of DDAB-dsDNA complexes remain at 4.51 nm, nearly independent of DNA concentration on varying ρ across ρ_{iso}, (ρ, is the ratio between the total number of cationic and DNA charges in the system). X-ray studies have been done on the DDAB-PAA complexes. they also show a lamellar structure, with a spacing of 3.46 nm for $\rho > \rho_{iso}$ and a spacing of 3.22 nm for $\rho < \rho_{iso}$. Lamellar structure is also reported for the complexes of DDAB-poly (vinyl sulfonate) (PVS) system [21].

Bead-on-string structure, which consists of liposomes connected by DNA strands has been reported in early studies on lipid-DNA complexes [22, 23]. Later on x-ray diffraction studies have been done to investigate the structure and morphology of lipid-DNA complexes [7–10]. Three different structures have been reported. The intercalated lamellar ($L^c{}_\alpha$) phase, where DNA strands are sandwiched between the lipid bilayers has been observed with bilayer forming lipids. The inverted hexagonal ($H^c{}_{II}$) structure has been found in systems of flexible bilayers with very low bending rigidity κ, due to the more efficient neutralization of DNA by the lipid head groups, possible in such a structure; it is also found in the case of amphiphilic systems with a negative spontaneous curvature [8]. In this phase, DNA strands

coated by a lipid monolayer is arranged on a two-dimensional hexagonal lattice. $(L^c{}_\alpha) \rightarrow (H^c{}_{II})$ Thermally reversible transition has been observed on heating in some systems [24]. The intercalated hexagonal structure $(H^c{}_I)$, where the hexagonally arranged lipid micelles are surrounded by DNA strands, was first observed in complexes of DNA with cationic surfactants that form cylindrical micelles [9].

Lipid-DNA or surfactant-DNA complex formation is a complex coacervation process, which is entropically driven. In this process the condensed counterions on both the species are released into the solution. The resulting increase in the entropy of these counterions is responsible for the formation of these complexes [5, 6].

There are very few systematic studies on single-chained surfactant-DNA complexes. Studies by R. Ghirlando et. al. on complexes of DNA and single chain surfactant dodecyltrimethylammonium bromide (DTAB) tetradecyltrimethylammonium bromide (TTAB), and cetyltrimethylammoniumbromide (CTAB), had very little structural information [25]. Later on a systematic x-ray diffraction study on CTAB-DNA complexes has been carried out by Krishnaswamy et al. [9, 26], who reported the $(H^c{}_I)$ phase. They also showed that two other phases, namely $(L^c{}_\alpha)$ and $(H^c{}_{II})$ could be induced by changing the spontaneous curvature and flexibility of the bilayer, on addition of hexanol. Recently, studies on the structural details of cetyltrimethylammonium tosylate (CTAT)-DNA complexes have been reported [27]. They have identified a $\sqrt{3}X\sqrt{3}$ super-lattice $(H^c{}_s)$ of an underlying hexagonal lattice $(H^c{}_I)$ and a square lattice $(S^c{}_I)$ from SAXS measurements.

5.3 Experimental

Didodecyldimethylammonium bromide (DDAB), dioctadecyldimethylammonium bromide (DOAB), cetylpyridinium chloride (CPC), polyacrylic acid (PAA) of molecular weight 1800, sodium salt of polyacrylic acid (PAANa) of molecular weight 2100 (PAANa (mw-2100)) and 5100 (PAANa (mw-5100)) were purchased from Sigma-Aldrich. 3-hydroxy-2-sodium-naphthoate (SHN) was prepared by adding equivalent amount of an aqueous solution of sodium hydroxide (NaOH)

to an ethanol solution of HNA as described in the second chapter. CPHN was prepared by mixing equimolar ratios of 3-hydroxy-2-sodium naphthoate (SHN) dissolved in methylisobutyl ketone (MIBK) and CPC in water. The CPHN complex obtained was extracted by vacuum distillation and subsequently dried in a rotary evaporator [28]. Chemical structures of the molecules are shown in figure 5.1.

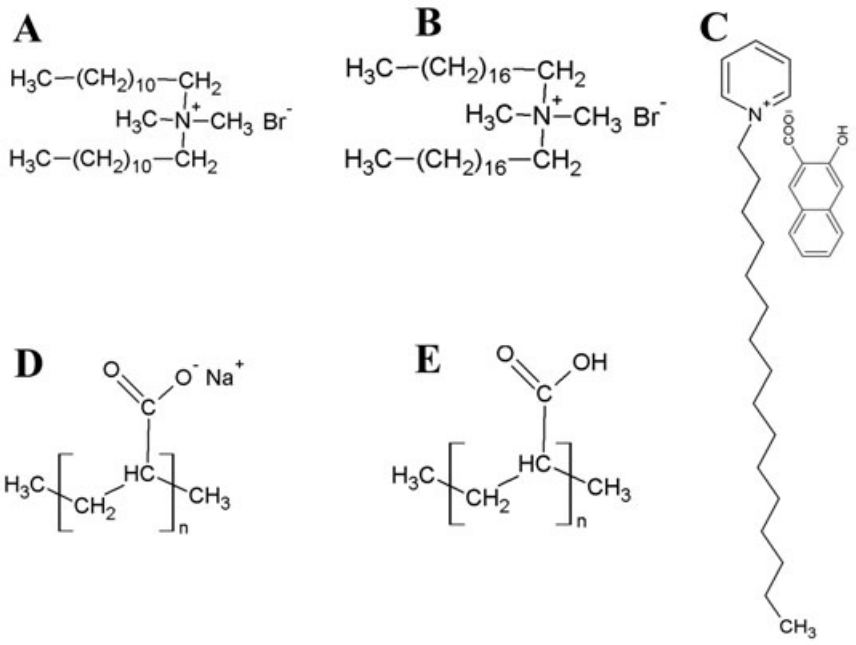

FIGURE 5.1: Chemical structure of surfactants; didodecyldimethylammonium bromide (DDAB) (**A**), dioctadecyldimethylammonium bromide (DOAB) (**B**), CPHN; complex of CPC and SHN (**C**), polyelectrolytes: sodium salt of polyacrylic acid; number of monomers for molecular weight 2100 is (n$\sim$ 22) and for 5100 is (n$\sim$ 54) (**D**) and polyacrylic acid (PAA); number of monomers for molecular weight 1800 is (n$\sim$ 25) (**E**)

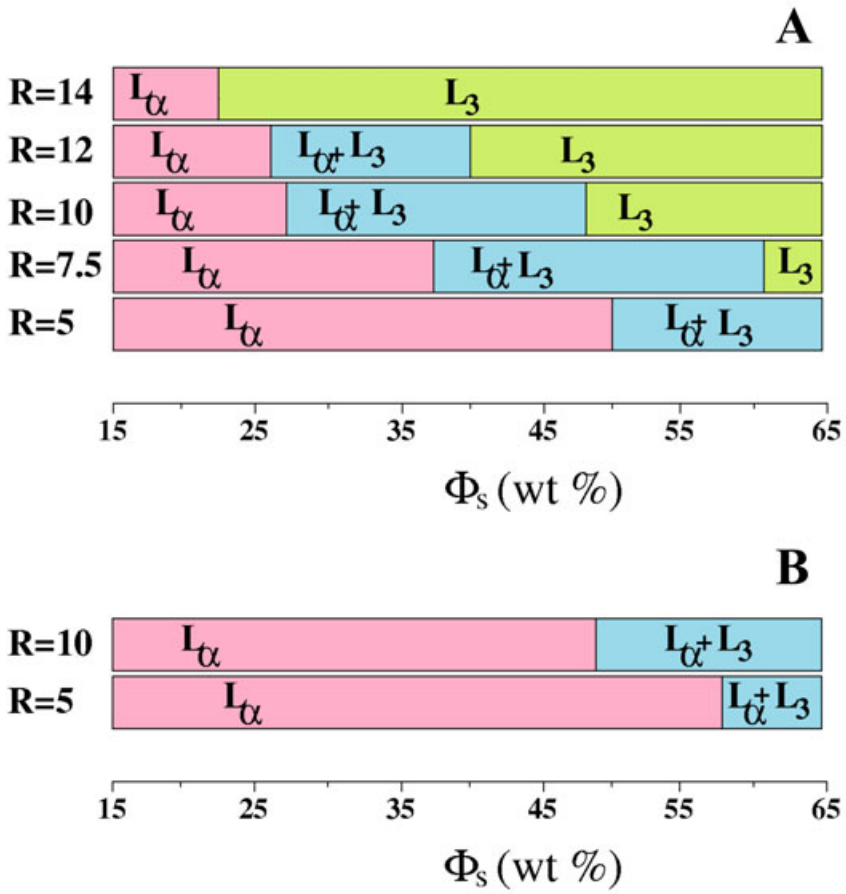

FIGURE 5.2: Partial phase diagrams at 30°C of the; DDAB-PAANa (mw-2100)-water system (**A**) and DDAB-PAANa (mw-5100)-water system (**B**). R is the weight ratio of polyelectrolyte and surfactant, Lα and L_3 are the lamellar and sponge phases respectively.

5.4 Results

5.4.1 DDAB-PAANa-Water system

5.4.1.1 DDAB-PAANa (mw-2100)-Water system

The phase behavior of mixtures of DDAB and PAANa (mw-2100) were studied at different values of the weight ratio (R=$\frac{(PAANa)}{(DDAB)}$) of the two components. For each R the total concentration of the non-aqueous components ($\phi_s = \frac{(DDAB+PAANa)}{(DDAB+PAANa+Water)}$x100) was varied from 20 to 65wt%. The structure of the phases was confirmed by using diffraction studies and polarizing optical microscopy texture of the samples.

Figure 5.2A shows the R−ϕ_s phase diagram of the DDAB-PAANa (mw-2100)-Water system at 30°C. At R=14 and at high water content (at ϕ_s=15 and 20), a whitish turbid complex is found floating in the solution (Fig. 5.3). POM studies of this complex shows oily streak texture (Fig. 5.5A) and SAXS pattern shows two peaks in the small angle region in q ratios 1:2 (Fig. 5.6A), confirming the occurrence of lamellar (L_α) phase. Lamellar periodicity is found to be about 3.7nm. However, at lower water content (at ϕ_s=23), a highly swollen and slightly bluish complex is found (Fig. 5.3), which is optically isotropic. Being a highly swollen phase, its SAXS pattern does not show any peaks within the accessible small angle range. At still lower water content (at ϕ_s=26, 30 and 35) a swollen and slightly yellowish complex is found (Fig. 5.3), which is optically isotropic, and its SAXS pattern (Fig. 5.6B) has similar features as found at ϕ_s=23. However, at still lower water content (at ϕ_s=40), a slightly yellowish complex is found, which is optically isotropic and its SAXS pattern shows a very broad peak at very low q (Fig. 5.7A). SAXS data could be fitted to the model of the sponge (L_3) phase (as described in the chapter 1). Characteristic size of the L_3 phase which corresponds to the broad peak position (Q_1) is about 20.9nm at 30°C and found to decrease with increasing temperature (Tab. 5.1). SAXS patterns obtained at ϕ_s=23, 26, 30 and 35 could be also fitted to the model of sponge (L_3) phase (Fig. 5.6B). At higher ϕ_s (50, 55, 60 and 65), a yellowish complex is found, which is optically isotropic, and its SAXS patterns (Fig. 5.7B-E)exhibit similar feature as found at ϕ_s=40. Also, a good fit is found between data and model of the sponge phase, confirming the occurrence of the sponge (L_3) phase. However, the characteristic size of the sponge phase decreases on decreasing the water content as well as on increasing the temperature (Tabs. 5.2, 5.3, 5.4 and 5.5). The color of the complex in the sponge (L_3) phase changes from light yellowish to yellowish and the apparent viscosity of the supernatant increases on decreasing the water content.

A similar phase behavior has been seen at low R (Fig. 5.4). However, the lamellar (L_α) phase is stable over a wide range of water content and the L_α-L_3 boundary is found shifted towards lower water content (Fig. 5.2A). On increasing the concentration of PAANa (mw-2100) the sponge (L_3) phase is stabilized at the expense

of the lamellar (L_α) phase. The two phase L_α+L_3 region decreases on increasing the PAANa (mw-2100) concentration and finally disappears at higher concentration (R∼14). Lamellar periodicity at ϕ_s=20 is found to be independent of R and remains around 3.8nm. However, it decreases on decreasing the water content, irrespective of R (Tab. 5.6).

5.4.1.2 Cryo-SEM studies

Cryo-SEM experiments have been carried out in the lamellar (L_α) and sponge (L_3) phases. Bilayer features are observed in the micrographs of the lamellar phase (Fig. 5.8(A-D)). Micrograph shows multilamellar vesicles of different sizes. However, in the micrograph of the sponge phase, bilayer features are absent, but a connected structure with water channels of size 10 to 20nm could be seen (Fig. 5.8(E and F)).

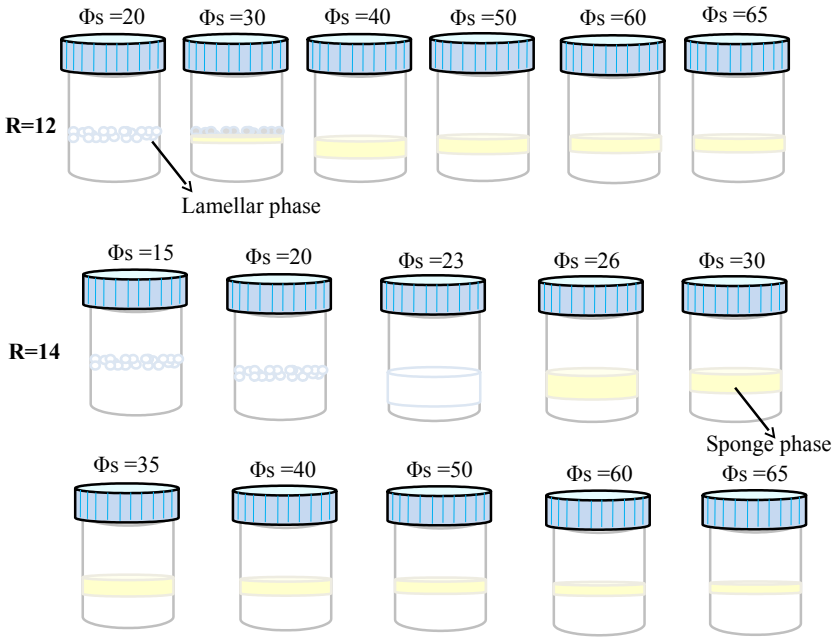

FIGURE 5.3: Different phases in the DDAB-PAANa (mw-2100)-Water system at T=30°C.

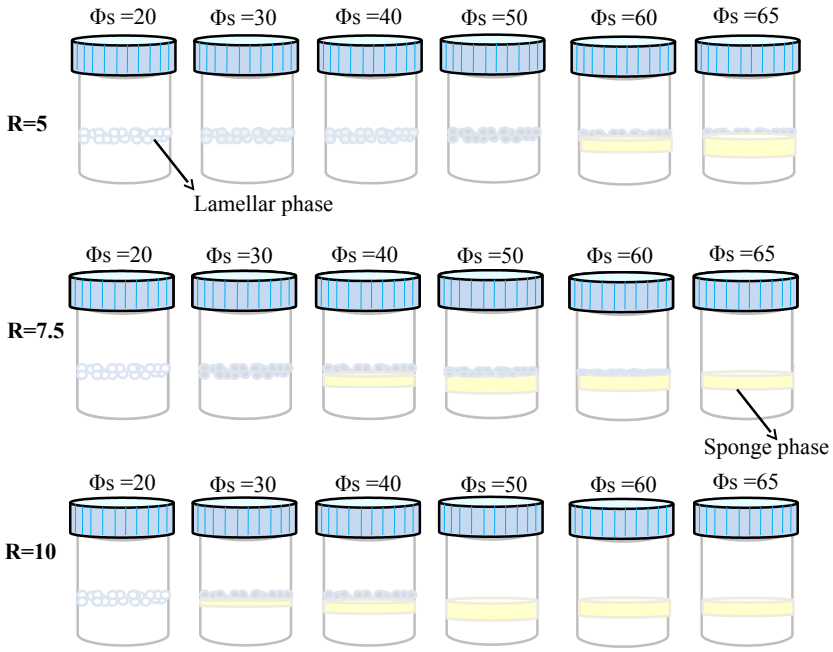

FIGURE 5.4: Different phases in the DDAB-PAANa (mw-2100)-Water system at T=30°C.

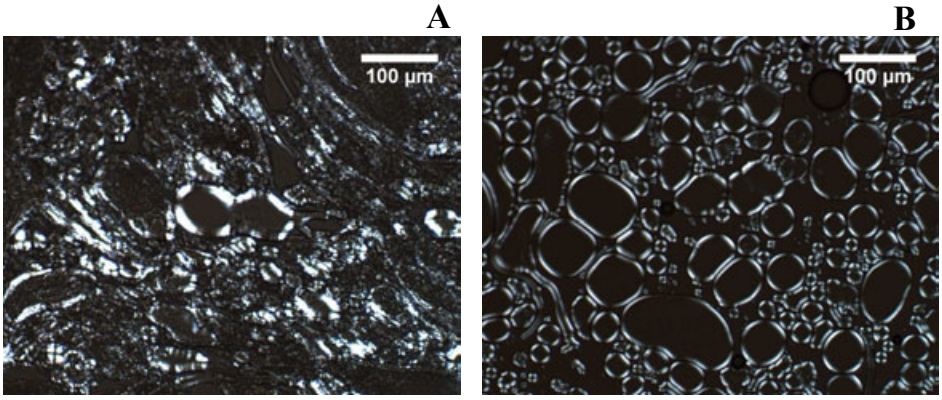

FIGURE 5.5: POM textures of the L_α phase (**A**) at R=5 and ϕ_s=20 and (**B**) at R=10 and ϕ_s=25 in the DDAB-PAANa (mw-2100)-Water system at T=30 °C.

5.4.1.3 DDAB-PAANa (mw-5100)-Water system: Effect of size of polymer

The phase behavior of mixtures of DDAB and PAANa (mw-5100) were studied at different values of the weight ratio (R=$\frac{(PAANa)}{(DAAB)}$) of the two components. For each R

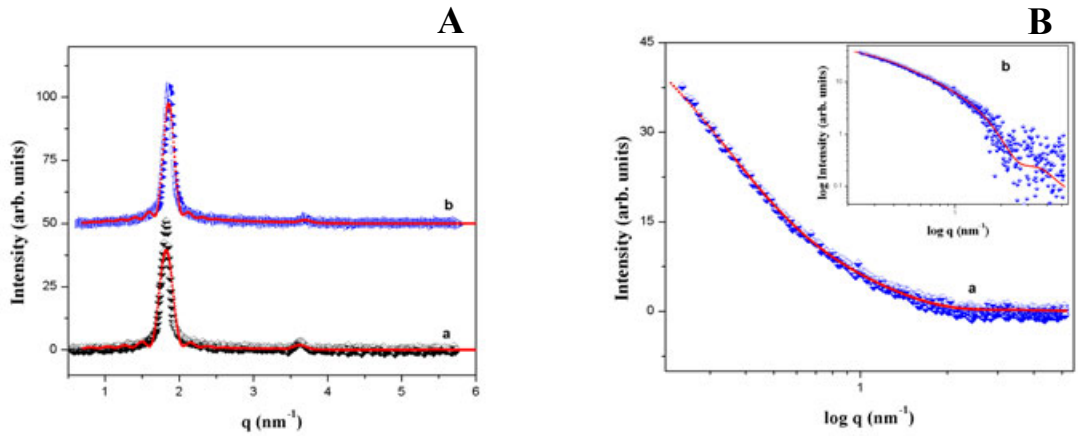

FIGURE 5.6: X-ray diffraction patterns of the L_α phase (**A**) (at ϕ_s=20 and (**a**) T=30°C and (**b**) T=80°C) and L_3 phase (**B**) (at ϕ_s=30 and T=30°C; (**a**) semi log scale and (**b**) log scale, base of log is 10) in the DDAB-PAANa (mw-2100)-Water system. Solid lines are fit to the models.

TABLE 5.1: Values of parameters for the diffraction data at R=14 and ϕ_s=40 of the DDAB-PAANa (mw-2100)-Water system obtained from the fit to the model of sponge (L_3) phase.

T(°C)	ξ_2(nm)	σ(nm)	w(nm)	L(nm)
30	0.53	7.52	2.22	29.92
40	0.56	6.35	2.23	26.18
50	0.85	4.94	2.27	20.67
60	0.75	3.95	2.01	17.45

TABLE 5.2: Values of parameters for the diffraction data at R=14 and ϕ_s=50 of the DDAB-PAANa (mw-2100)-Water system obtained from the fit to the model of sponge (L_3) phase.

T(°C)	ξ_2(nm)	σ(nm)	w(nm)	L(nm)
30	2.19	3.02	2.21	20.94
40	1.81	2.83	2.17	20.94
50	2.02	2.17	2.17	16.98
70	2.09	2.15	1.97	13.37

the total concentration of the non-aqueous components ($\phi_s = \frac{(DDAB+PAANa)}{(DDAB+PAANa+Water)}$x100) was varied from 20 to 65wt%. Structure of the phases was confirmed by using diffraction studies and POM texture of the sample.

Phase behavior is found to be similar to that of the DDAB-PAANa (mw-2100)-Water system as shown in figure 5.2B. At R=10 and at high water content (ϕ_s=20),

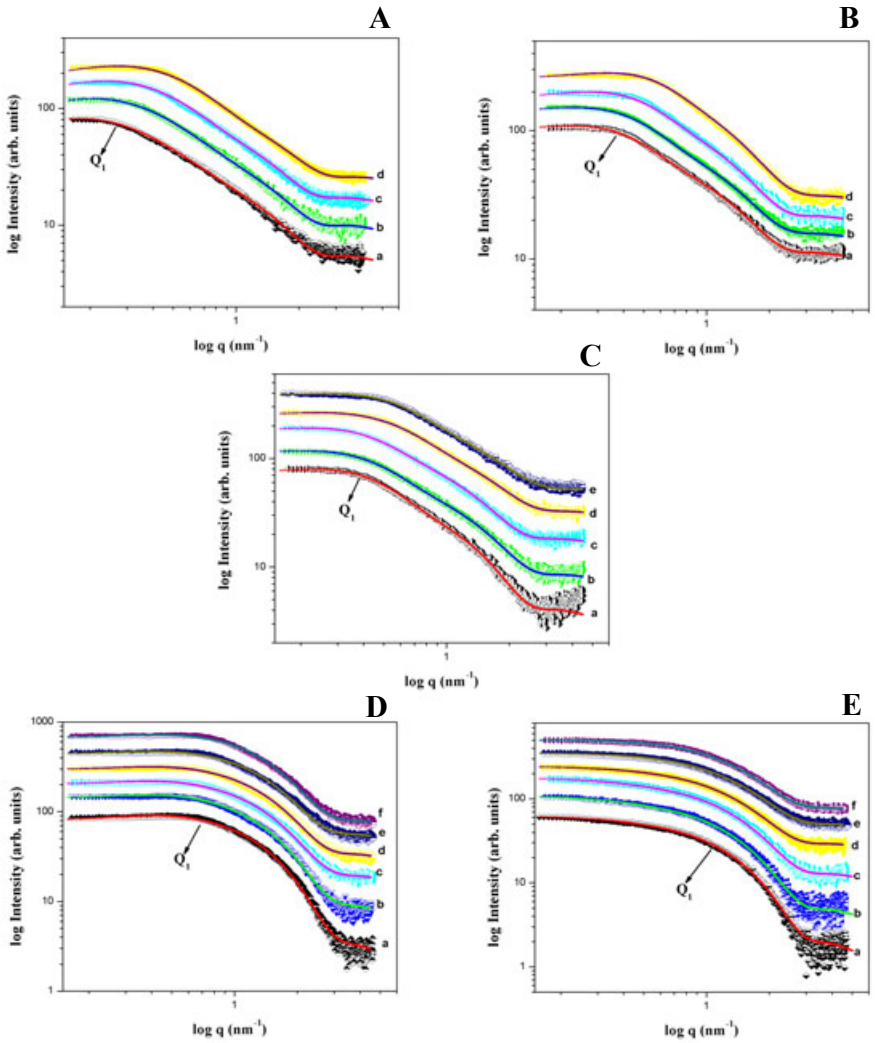

FIGURE 5.7: X-ray diffraction patterns of L_3 phase (**A**) (at ϕ_s=40 and (**a**) T=30°C, (**b**) T=40°C, (**c**) T=50°C and (**d**) T=60°C), (**B**) (at ϕ_s=50 and (**a**) T=30°C, (**b**) T=40°C, (**c**) T=50°C and (**d**) T=70°C), (**C**) (at ϕ_s=55 and (**a**) T=30°C, (**b**) T=40°C, (**c**) T=50°C, (**d**) T=50°C and (**e**) T=70°C), (**D**) (at ϕ_s=60 and (**a**) T=30°C, (**b**) T=40°C, (**c**) T=50°C, (**d**) T=60°C, (**e**) T=70°C and (**f**) T=80°C) and (**E**) (at ϕ_s=65 and (**a**) T=30°C, (**b**) T=40°C, (**c**) T=50°C, (**d**) T=60°C, (**e**) T=70°C and (**f**) T=80°C) in the DDAB-PAANa (mw-2100)-Water system at R=14. Q_1 corresponds to the characteristic size of the sponge phase. Base of log is 10. Solid lines are fit to the model of L_3 phase.

it forms a whitish viscous complex. It shows oily streaks with maltese-cross texture (Fig. 5.10A) under POM, which confirms the occurrence of lamellar (L_α) phase. At (ϕ_s=30, 40 and 45), similar behavior is observed. (similar to Fig. 5.10B). At (ϕ_s=50, 55 and 60), complexes are turbid and less whitish in color, their diffraction pattern show a broad peak in the small q region along with the lamellar peak (Fig.

TABLE 5.3: Values of parameters for the diffraction data at R=14 and ϕ_s=55 of the DDAB-PAANa (mw-2100)-Water system obtained from the fit to the model of sponge (L_3) phase.

T(°C)	ξ_2(nm)	σ(nm)	w(nm)	L(nm)
30	1.79	3.01	2.18	20.27
40	2.07	3.04	2.04	20.27
50	2.24	3.02	2.18	19.64
60	1.14	2.41	1.92	19.64
70	1.59	2.06	1.74	15.71

TABLE 5.4: Values of parameters for the diffraction data at R=14 and ϕ_s=60 of the DDAB-PAANa (mw-2100)-Water system obtained from the fit to the model of sponge (L_3) phase.

T(°C)	ξ_2(nm)	σ(nm)	w(nm)	L(nm)
30	1.90	3.07	1.83	12.32
40	2.46	3.13	1.85	12.08
50	2.91	3.23	1.83	12.08
60	2.59	3.13	1.88	12.08
70	2.47	3.23	1.88	12.08
80	2.55	2.98	1.84	11.86

TABLE 5.5: Values of parameters for the diffraction data at R=14 and ϕ_s=65 of the DDAB-PAANa (mw-2100)-Water system obtained from the fit to the model of sponge (L_3) phase.

T(°C)	ξ_2(nm)	σ(nm)	w(nm)	L(nm)
30	2.87	2.94	1.91	10.83
40	2.92	3.00	1.91	10.65
50	2.37	2.75	1.88	10.65
60	2.33	2.69	1.89	10.30
70	2.19	2.81	1.81	10.30
80	2.02	2.95	1.84	09.97

5.9A and B) and they exhibit maltese-cross texture under POM (Fig. 5.10B and D), which confirms the coexistence of L_α and L_3 phase. Characteristic size of the sponge (L_3) phase decreases on increasing the temperature (Tab. 5.7). However, POM shows less dense maltese-cross texture (Fig. 5.10C) at higher temperatures. It is worth noting that the lamellar periodicity decreases on decreasing the water content (Tab. 5.8) in this coexistence region.

At R=5, phase behavior is very similar to that at R=10. Lamellar (L_α) phase found

TABLE 5.6: Variation of the lamellar periodicity in the DDAB-PAANa (mw-2100)-Water system at T=30°C

ϕ_s	20	30	40	50	60	65
R			d(nm)			
5	3.77	3.50	3.08	2.97	2.90	2.83
7.5	3.73	3.68	3.04	3.00	2.89	2.87
10	3.74	3.08	2.95	–	–	–
14	3.73	–	–	–	–	–

TABLE 5.7: Observed phases and variation of lamellar periodicity/characteristic size with temperature in DDAB-PAANa (mw-5100)-Water system at R=10.

T	ϕ_s**=55**		ϕ_s**=60**	
°C	**Phases**	**d(nm)**	**Phases**	**d(nm)**
30	Lα+L$_3$	2.88, 19.23	Lα+L$_3$	2.87, 17.61
40	Lα+L$_3$	2.87, 18.66	Lα+L$_3$	2.85, 15.94
50	Lα+L$_3$	2.85, 18.25	Lα+L$_3$	2.83, 15.69
60	Lα+L$_3$	2.83, 17.62	Lα+L$_3$	2.81, 13.59
70	Lα+L$_3$	2.83, 16.21	Lα+L$_3$	2.79, 11.94
80	Lα+L$_3$	2.81, 15.01	Lα+L$_3$	2.78, 11.44

TABLE 5.8: Variation of lamellar periodicity/characteristic size with decreasing water content in DDAB-PAANa (mw-5100)-Water system at T=30°C.

ϕ_s	**R=5**		**R=10**	
–	**Phase**	**d(nm)**	**Phase**	**d(nm)**
20	Lα	3.75	Lα	3.68
30	Lα	3.44	Lα	3.42
40	Lα	3.05	Lα	3.06
50	Lα	2.88	Lα+L$_3$	2.87, 20.13
60	Lα+L$_3$	2.86, 17.95	Lα+L$_3$	2.85, 17.61

to more stable at higher water content and the L_α-L_3 boundary shifts towards lower water content (Fig. 5.2B).

5.4.1.4 DOAB-PAANa (mw-2100)-Water system: Effect of chain length of surfactant

Phase behavior of DOAB and PAANa (mw-2100) was studied at R=14 and the total concentration of non-aqueous components ($\phi_s = \frac{(DOAB+PAANa)}{(DOAB+PAANa+Water)}$x100) was varied from 20 to 50wt%.

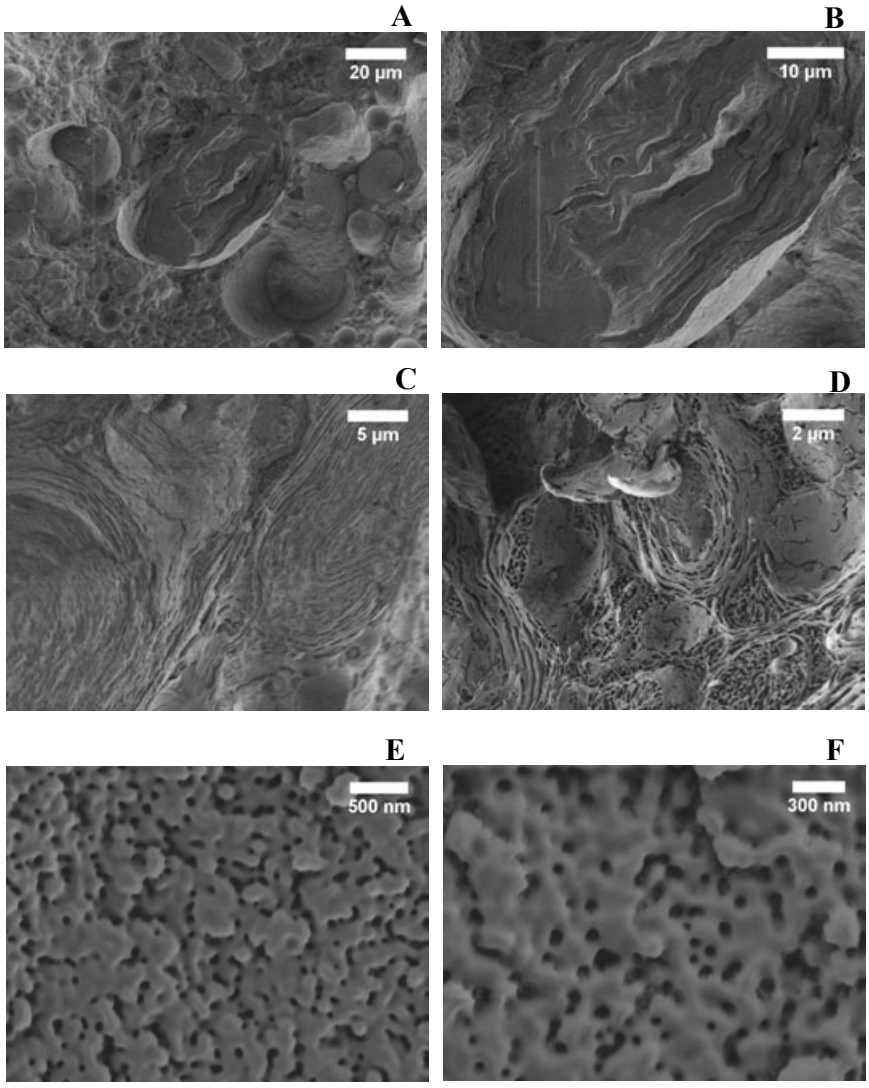

FIGURE 5.8: Cryo-SEM micrographs of (**A, B**) L_α phase at R=5 and ϕ_s=20 and (**C, D**) at R=14 and ϕ_s=20 and (**E, F**) L_3 phase at R=14 and ϕ_s=50 in the DDAB-PAANa (mw-2100)-Water system.

Phase behavior is very similar to that of the DDAB-PAANa (mw-2100)-water system at R=10 at 30°C. For $20 \leq \phi_s \leq 45$, it shows a whitish complex, which shows lamellar phase, confirmed by POM and SAXS studies. Lamellar periodicity is about 3.55nm, irrespective of the water content. However, at ϕ_s=50 and T=30°C, SAXS pattern shows a broad peak at low q region along with a sharp peak at higher q (Fig. 5.11A) and It exhibits maltese-cross texture (similar to figure 5.10B) under POM, confirming the coexistence of lamellar and sponge phases. However, at higher temperatures, a pure sponge phase is found (characteristic size

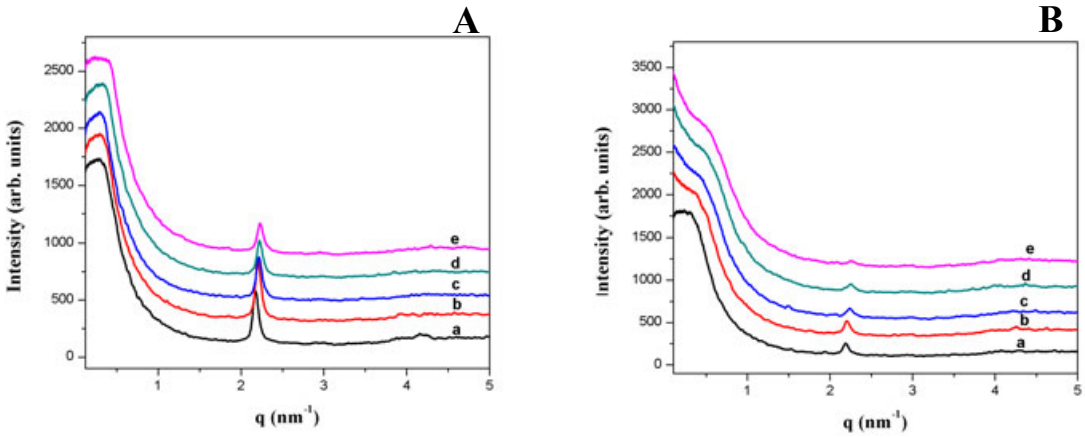

FIGURE 5.9: X-ray diffraction patterns of I+L_3 phase (**A**) (at temperature (**a**) 30°C, (**b**) 50°C, (**c**) 60°C, (**d**) 70°C and (**e**) 80°C; at R=10 and ϕ_s=55) and (**B**) (at temperature (**a**) 30°C, (**b**) 40°C, (**c**) 60°C, (**d**) 70°C and (**e**) 80°C; at R=10 and ϕ_s=60) in the DDAB-PAANa (mw-5100)-Water system.

is given in table 5.9), which is confirmed by fitting the data to the model of the sponge phase (Fig. 5.11B and Tab. 5.10).

TABLE 5.9: Observed phase and lamellar periodicity/ characteristic size in the DOAB-PAANa (mw-2100)-Water system at ϕ_s=50

T(°C)	Phases	d(nm)
30	L_α+L_3	3.55, 12.34
40	L_3	16.10
60	L_3	16.10

TABLE 5.10: Values of parameters for the diffraction data at R=14 and ϕ_s=50 of the DOAB-PAANa (mw-2100)-Water system obtained from the fit to the model of sponge (L_3) phase.

T(°C)	ξ_2(nm)	σ(nm)	w(nm)	L(nm)
60	1.81	3.01	2.31	16.10

5.4.1.5 DDAB-PAANa (mw-2100)-NaBr-Water system: Effect of salt

As we have seen in the present study, two oppositely charged macroions (positively charged bilayer of DDAB and negatively charged PAANa (mw-2100)) form complexes by releasing their condensed counterions (Br^- and Na^+) into the aqueous

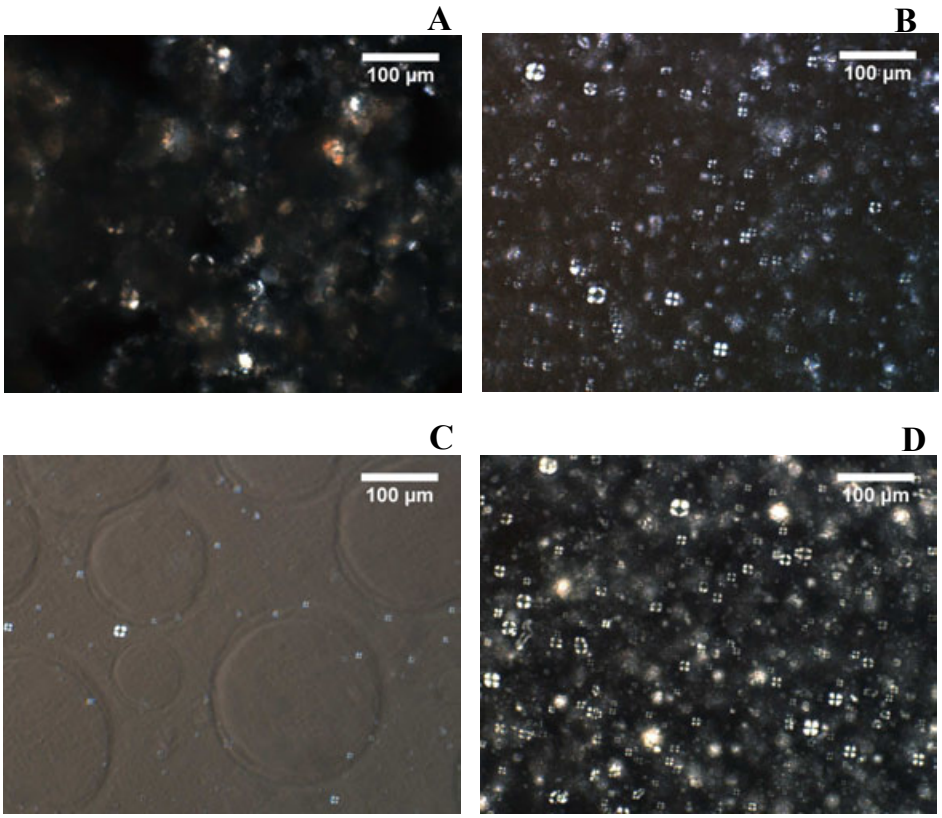

FIGURE 5.10: POM textures of (**A**) L_α phase at R=10 ϕ_s=20 and T=30°C, (**B**) L_α+L_3at R=10 ϕ_s=55 and T=30°C, (**C**) L_α+L_3 at R=10 ϕ_s=55 and T=80°C and (**D**) L_α+L_3 at R=10 ϕ_s=60 and T=30° in the DDAB-PAANa (mw-5100)-Water system.

solution and thereby increasing their entropy. In this way, salt (NaBr) concentration in the aqueous media increases with decreasing water content at particular ratio (R) of PAANa and DDAB. So, the phase behavior of DDAB-PAANa-Water system at particular R, could be realized by increasing the salt (NaBr) concentration and keeping ϕ_s constant.

Salt effect studies were carried out by increasing the salt (NaBr) concentration and keeping ϕ_s=20 and R=14 constant.

Without addition of salt (NaBr), the whitish complex, shows lamellar (L_α) phase. For 50mM (NaBr)- a highly swollen complex of slightly yellowish color is found, which shows optically isotropic texture under POM and its SAXS pattern is similar to that seen at ϕ_s=30 in the DDAB-PAANa (mw-2100)-Water system. However,

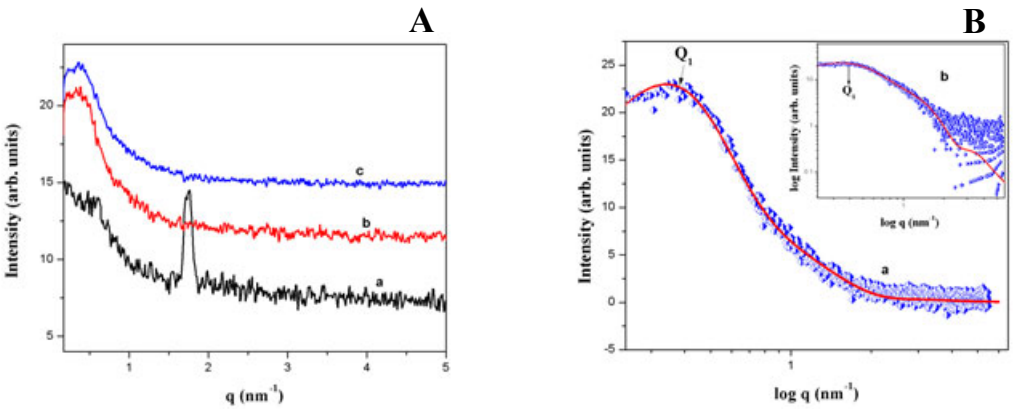

FIGURE 5.11: X-ray diffraction patterns of (**A**) ((**a**) L_α+L_3 phase at T=30°C, (**b and c**) sponge (L_3) phase at T=40°C and T=60°C respectively) and X-ray diffraction pattern of the L_3 phase at T= 60°C (**B**) ((**a**) in semi log plot and (**b**) log plot, base of log is 10; Q_1 is the position of broad peak corresponding to the characteristic size of the sponge phase) in the DOAB-PAANa (mw-2100)-NaBr-Water system at R=14 and ϕ_s=50. The solid lines in (**B**) are fit to the model of L_3 phase.

at 100mM, a whitish complex is found, which shows lamellar phase with a periodicity of about 3.11nm at 30°C. At higher temperatures a lamellar phase coexisting with the sponge phase is observed. The lamellar periodicity increases with increasing the temperature in the coexistence region (Tab. 5.11). Still at higher temperatures, a pure sponge (L_3) phase is observed (Fig. 5.12A), which is confirmed by fitting the SAXS data to the model for the sponge phase (Fig. 5.12B and Tab. 5.12). Characteristic size of the sponge phase is found to be about 11.21nm (Tab. 5.11). At 200mM NaBr concentration, it shows a lamellar phase of periodicity 3.11nm up to 80°C.

5.4.2 CPHN-PAA/NaCl-Water system

5.4.2.1 CPHN-Water system

The phase behavior of CPHN was studied at different water contents. Concentration of CPHN ($\phi_s = \frac{(CPHN)}{(CPHN+Water)}$x100) was varied from 15 to 85 wt%. The

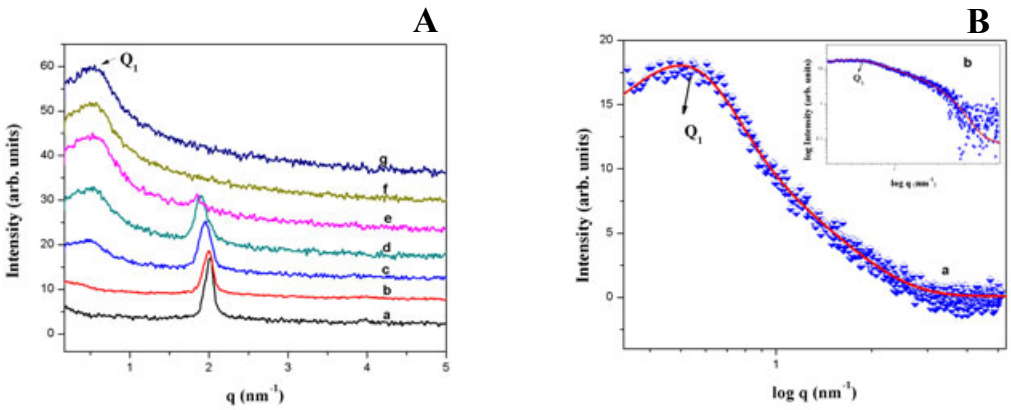

FIGURE 5.12: X-ray diffraction patterns of (**A**)((**a and b**) lamellar (L_α) phase at T=30°C and 40°C respectively, (**c-e**) L_α + L_3 at T=50°C, 60°C and 70°C respectively and (**f and g**) sponge (L_3) phase at T=75°C and 80°C respectively) and X-ray diffraction pattern of the sponge phase at T= 80°C (**B**)((**a**) in semi log plot and (**b**) log plot, base of log is 10; Q_1 is the position of broad peak corresponds to the characteristic size of the sponge phase) in the DDAB-PAANa (mw-2100)-NaBr-Water system at R=14, ϕ_s=20 and [NaBr]=100mM. The solid lines in (**B**) are fit to the model of L_3 phase.

TABLE 5.11: Variation of lattice spacing in different phases with temperature in the DDAB-PAANa (mw-2100)-Water system at NaBr concentration ([NaBr])=100mM and ϕ_s=20

T(°C)	Phase	Lattice spacing(nm)
30	L_α	2.99
40	L_α	3.14
50	L_α+L_3	3.22, 12.68
60	L_α+L_3	3.29, 11.70
70	L_α+L_3	3.39, 11.67
75	L_3	11.50
80	L_3	11.21

structure of the phases was confirmed by using diffraction studies and POM texture of the samples.

Temperature−ϕ_s phase diagram of this system is shown in figure 5.13. Microscopy observations indicate that CPHN forms a lamellar phase coexisting with isotropic phase over a wide range of ϕ_s. POM shows oily streaks with maltese-cross texture under crossed polarizer (Fig. 5.16A) and SAXS patterns show two peaks in the small angle region with their q in the ratio 1:2 (Fig. 5.14a), which confirms the

TABLE 5.12: Values of parameters for the diffraction data at R=14 ϕ_s=20 and [NaBr]=100mM of the DDAB-PAANa (mw-2100)-NaBr-Water system obtained from the fit to the model of sponge (L_3) phase.

T(°C)	ξ_2(nm)	σ(nm)	w(nm)	L(nm)
80	2.29	2.52	2.23	11.21

occurrence of lamellar (Lα) phase with excess water. At higher values of ϕ_s a pure lamellar (Lα) phase observed which is confirmed by POM and SAXS studies. SAXS patterns show three peaks in the small angle region in q ratio 1:2:3 (Fig. 5.14b), which is characteristic of the lamellar (L_α) phase.

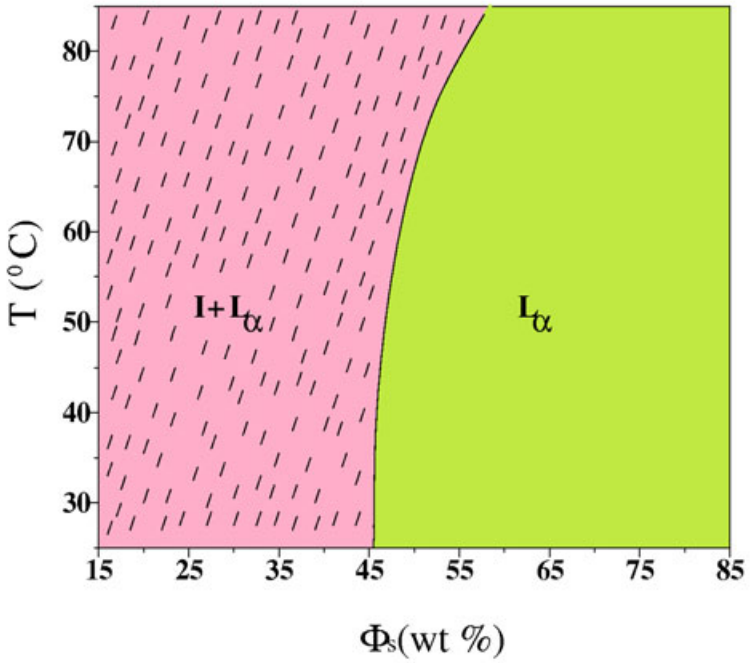

FIGURE 5.13: Partial phase diagram of the CHHN-Water system. I and Lα denote isotropic and lamellar phases respectively.

5.4.2.2 CPHN-NaCl-Water system: Effect of salt

The effect of NaCl on the phase behavior of CPHN was studied over the concentration range of 0.5M to 3.5M. The phase behavior of CPHN-Water system is found not to change much on the addition of NaCl. It is found that the pure lamellar (L_α) phase is more stable on increasing the salt concentration, I+L_α-L_α boundary

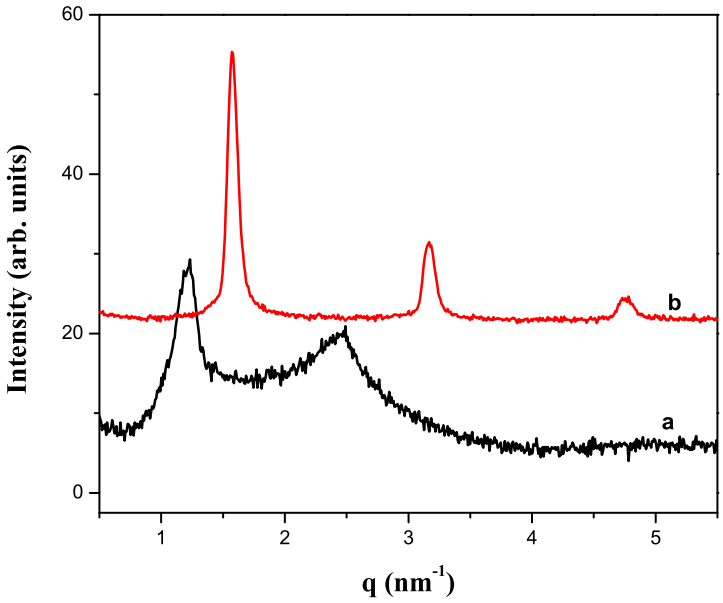

FIGURE 5.14: X-ray diffraction patterns of (**a**) I+L_α at ϕ_s=40 and (**b**) L_α phase at ϕ_s=80 in the CPHN-Water system at T=30°C.

TABLE 5.13: Observed phases and variation of the lamellar periodicity with salt concentration in CPHN-NaCl-water system at T=30 °C.

[NaCl]	ϕ_s=30		ϕ_s=70	
[M]	**Phases**	**d(nm)**	**Phases**	**d(nm)**
0.0	I+Lα	4.79	Lα	4.32
0.5	I+Lα	4.88	Lα	4.32
1.0	I+Lα	5.21	Lα	4.09
1.5	I+Lα	5.46	Lα	4.11
2.0	I+Lα	5.55	Lα	4.33
2.5	I+Lα	5.59	Lα	4.18
3.0	I+Lα	5.70	Lα	4.14
3.5	I+Lα	5.76	Lα	4.23

is shifted towards higher water content. Lamellar periodicity in the I+L_α coexistence region increases on addition of salt (NaCl). However, the lamellar periodicity is found to be more or less constant in the pure lamellar (L_α) phase (Tab. 5.13), on the addition of salt (NaCl).

5.4.2.3 CPHN-PAA-Water system: Effect of polyelectrolyte

The effect of PAA on the phase behavior of CPHN was studied at different values of the weight ratio (R=$\frac{(PAA)}{(CPHN)}$) of the two components. For each R the total concentration of non-aqueous components ($\phi_s = \frac{(CPHN+PAA)}{(CPHN+PAA+Water)}$x100) was kept constant at 30 wt%.

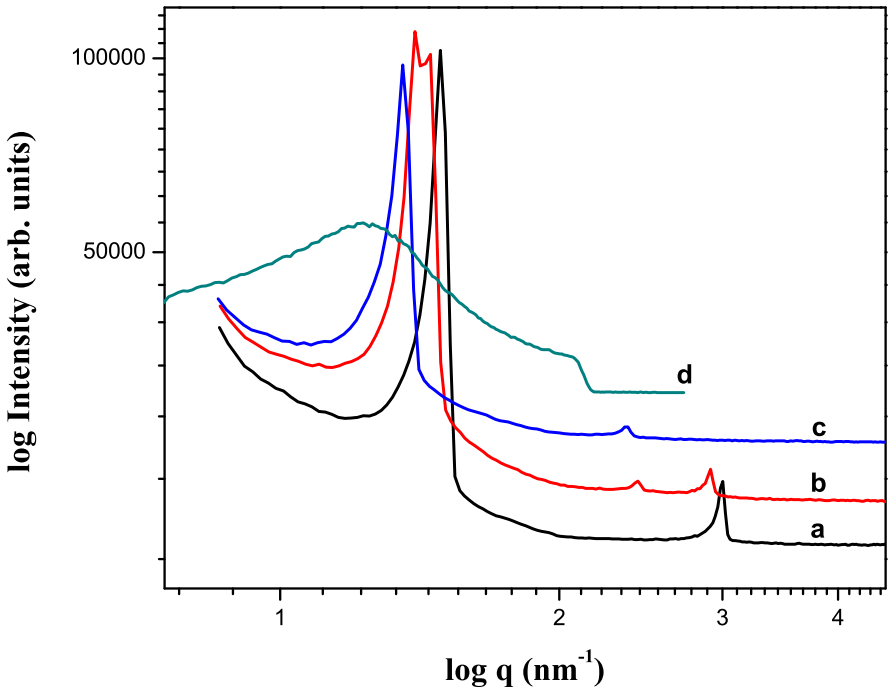

FIGURE 5.15: X-ray diffraction patterns of (**a**) lamellar (L_α) phase, (**b**) lamellar+hexagonal (L_α+H_{II}) phase, (**c**) hexagonal (H_{II}) phase and (**d**) isotropic (I_{II}) phase in the CPHN-PAA system at temperature 30°C.

At ϕ_s=30, without the addition of PAA, it shows a dispersion of multilamellar vesicles. On the addition of small amounts of PAA (R=0.09), the dispersion of multilamellar vesicle i.e. lamellar phase coexisting with excess water, is still stable, as confirmed by POM study, which shows oily streaks with maltese-cross texture (Fig. 5.16B), the lamellar spacing is found to decrease from 4.8nm to 4.3nm. However, at higher concentration of PAA (R=0.31), the surfactant rich part precipitates out in the form of a complex from the solution. Complex shows oily streak texture under crossed POM (Fig. 5.16C) and SAXS pattern shows

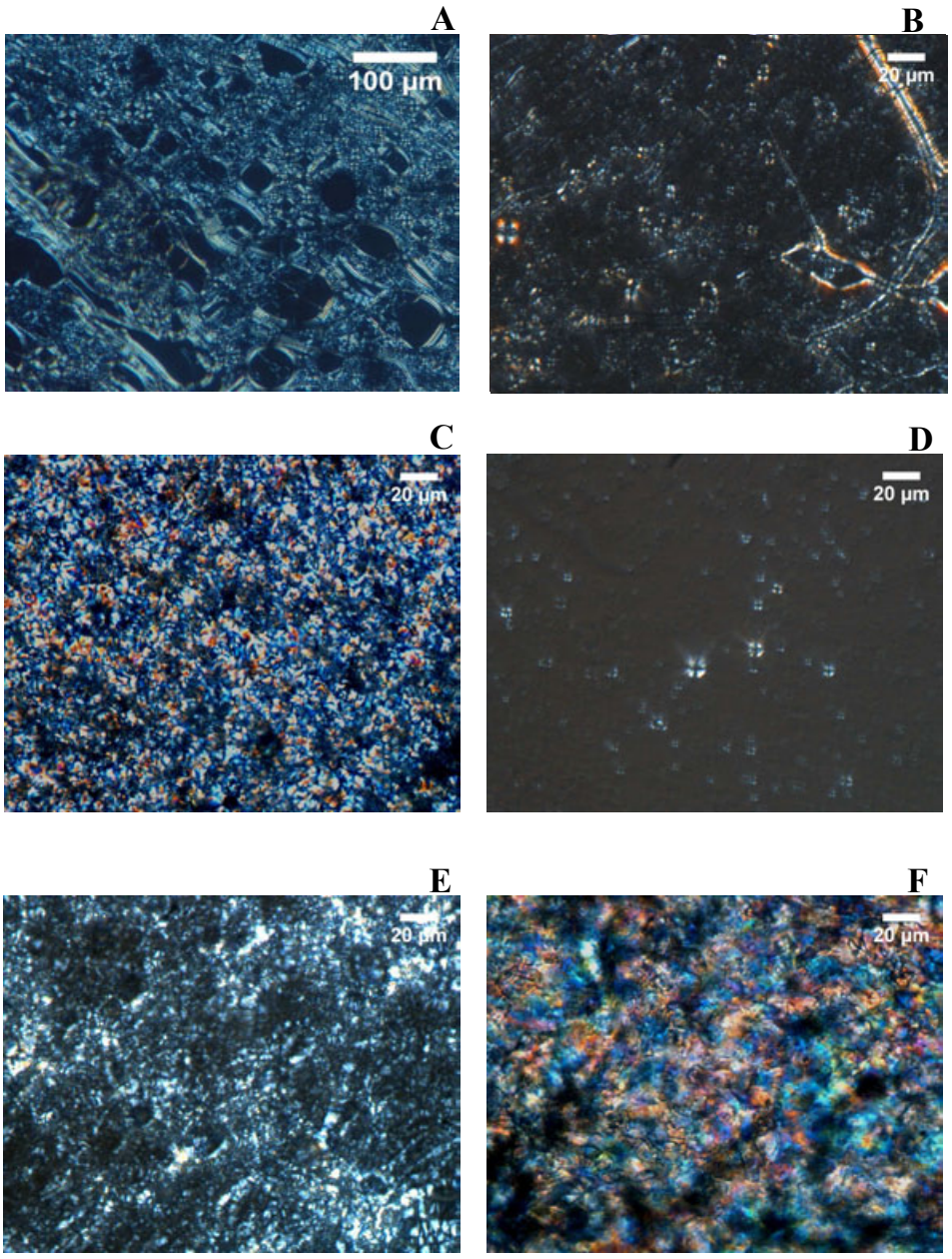

FIGURE 5.16: POM textures of the complex in the (**A**) I+L_α phase in the CPHN-NaCl-Water system, (**B**) I+L_α phase at R=0.09, (**C**) L_α phase, (**D**) MLV in the supernatant at R=0.31, (**E**) L_α phase at R=0.47 and (**F**) H_{II} phase at R=1.18 in the CPHN-PAA-Water system at T=30°C

two peaks in the small angle region with their in the q ratio 1:2 (Fig. 5.15a), which confirms the occurrence of the lamellar phase. Lamellar spacing is found to remain at about 4.3nm. supernatant is whitish in color and shows less dense maltese-cross texture under POM (Fig. 5.16D). However, on further addition of PAA (R=0.47), supernatant is clear and the complex shows lamellar phase with

spacing of about 4.3nm, which is confirmed by POM (Fig. 5.16E) and SAXS studies. On further addition of PAA (R=0.75, when each surfactant molecule corresponds to five monomers of PAA), a different type of complex is found. SAXS pattern shows four peaks, two of them with their q in the ratio 1:2 and the other two in the ratio 1:$\sqrt{3}$ (Fig. 5.15b), confirming the coexistence of lamellar and hexagonal phases. Hexagonal phase appearing here is of the inverted kind (as discussed in the next section). Lamellar spacing remains at about 4.3nm and the lattice spacing in the hexagonal phase is about 5.2nm. supernatant is found to be clear and transparent. Further addition of PAA (R=1.18), leads to the formation of a more stiff complex, which shows a smooth texture (Fig. 5.16F) and its SAXS pattern shows two peaks in the small angle region with their q in the ratio 1:$\sqrt{3}$ (Fig. 5.15c), which confirms the occurrence of the hexagonal phase (H_{II}). Lattice spacing is about 5.3nm. However, on further addition of PAA (at R=3.34, when each surfactant molecule corresponds to ∼24 monomers of PAA), a complex is found which is softer and optically isotropic. Its SAXS patterns shows a broad peak with a spacing of about 5.1nm (Fig. 5.15d), confirming the occurrence of isotropic (I_{II}) phase. Supernatant is still clear transparent and optically isotropic. Apparent viscosity of supernatant increases on the addition of PAA. Results are summarized in table 5.14.

TABLE 5.14: Variation of lattice spacing of the different phases with PAA concentration in the CPHN-PAA(mw-1800)-Water system at T=30°C and ϕ_s=30

$R\frac{(PAA)}{CPHN}$	$\frac{monomer}{surfactant}$	Phase	Lattice spacing(nm)
0.09	0.63	I+L_α	4.25
0.31	2.19	I+L_α	4.26
0.47	3.31	I+L_α	4.27
0.75	5.29	I+L_α+H_{II}	4.32, 5.19
1.18	8.35	I+H_{II}	5.34
2.20	15.57	I+H_{II}	5.41
3.34	23.64	I+I_{II}	5.11

5.5 Discussion

5.5.1 Data analysis

Diffraction data of the lamellar (L_α) phase were analyzed using the procedure described by Pabst et al. [29] as described in chapter 1.

Variation of the SAXS pattern with temperature at R= 14 and ϕ_s=15 is shown in figure 5.6A. The patterns are well described by the model for the L_α phase. Values of the fitting parameters are given in table 5.15. Calculated values of the water layer thickness between the bilayer in the lamellar (Lα) phase is ∼0.66nm, which is about two times the diameter of a water molecule, which confirms the occurrence of collapsed lamellar (L_α) phase.

TABLE 5.15: Values of parameters for the diffraction data at R=14 and ϕ_s=15 of the DDAB-PAANa (mw-2100)-Water system obtained from the fit to the model of lamellar (L_α) phase.

T(°C)	σ_h(nm)	σ_c(nm)	$(\rho_c)/(\rho_h)$	$z_h(nm)$	η	N	N_d	d(nm)	Phase
30	0.28 ±0.02	0.46±0.02	-1.29±0.08	1.10±0.03	0.039± 0.002	10 ±1	1.22 ± 0.02	3.44	L_α
80	0.28 ±0.02	0.46±0.02	-1.29±0.08	1.07±0.03	0.037± 0.002	11 ±1	1.86 ± 0.02	3.38	L_α

The diffraction pattern of the sponge L_3 phase, at larger momentum transfer q, show $q^{-2} - q^{-4}$ behavior, although this region is modified by the background scattering. The $q^{-2} - q^{-4}$ behavior is characteristic of scattering from randomly oriented discs [30], indicating that the local structure of our sample is that of flat membranes. Quantitative values were obtained from the following fit to the data using the procedure described by Porcar [15], as discussed in chapter1.

Variation of the SAXS pattern with temperature for different ϕ_s (40, 50, 55, 60, 65) at R= 14, in the DDAB-PAANa (mw-2100)-Water system is shown in figure 5.7. The patterns are well described by the model for the L_3 phase. The obtained values of radius of gyration of discoids (σ), thickness (w) and cell-cell distance (L) are given in tables 5.1, 5.2, 5.3, 5.4 and 5.5 respectively.

SAXS pattern at R=14, ϕ_s=30 and T=30°C in the DDAB-PAANa (mw-2100)-Water system can be fitted to this model (Fig. 5.6B). However, the cell-cell distance is very large and is not accessible with our SAXS instrument.

The thickness of the discoids obtained from the model varies from 2.3nm to 1.8nm, which is comparable to the reported value for the bilayer thickness of DDAB.

SAXS pattern at R=14, ϕ_s=50 and T=80°C in the DOAB-PAANa (mw-2100)-Water system can also be fitted to this model (Fig. 5.11B). The obtained values of fitting parameters are given in table 5.10. SAXS pattern at R=14, ϕ_s=20 and T=60°C in the DDAB-PAANa (mw-2100)-NaBr-Water system is also fit to this model (Fig. 5.12B). The obtained values of the fitting parameters are given in table 5.12.

The sponge phase found at all the compositions in this system is highly swollen. There are two main possible interactions which can give rise to this swollen sponge phase-electrostatic repulsion and Helfrich repulsion. We will explain the role of each interaction one by one.

At any value of R, increasing ϕ_s increases the concentration of dissociated Na^+ (from PPANa) and Br^- (from DDAB) ions in the solution. The electrostatic potential of the bilayer is given by [31].

$$\psi_x = \psi_o e^{-kx} \tag{5.1}$$

where ψ_o is the potential at the bilayer surface and 1/k is the Debye length. This is the characteristic decay length of the potential. At 25°C the Debye length of aqueous solutions can be written as,

$$\frac{1}{k} = \frac{0.304}{\sqrt{C}}(nm) \tag{5.2}$$

for 1:1 electrolytes. C is the molar concentration of salt. C is estimated from the amount of released counterions (Na^+ and Cl^-) and volume of the water at particular ϕ_s. Amounts of released counterions are estimated from the amounts of

the DDAB and PAA at iso-electric point, by assuming their complete ionization. The presence of large amounts of dissociated salt in the present system makes the Debye length extremely short (Tab. 5.16). Hence, one can ruled out the role of electrostatic interaction in the swelling of the sponge phase.

TABLE 5.16: Variation of Debye length (1/k) in the presence of the dissociated NaBr salt in the DDAB-PAANa (mw-2100)-Water system at R=14 and T=25°C. C[M] is the molar concentration of the salt.

ϕ_s	C[M]	1/k(nm)
20	0.0360	1.602
30	0.0617	1.223
40	0.0961	0.981
50	0.1441	0.801
60	0.2161	0.654

Swelling in the sponge phase might also arise from Helfrich repulsion. This repulsion originates from thermal undulations of the bilayers and is inversely proportional to the bending rigidity of the bilayer. It has been theoretically shown that the homogeneous equilibrium adsorption of polymer on both sides of the bilayer, leads to a decrease in the bending rigidity [32]. Since, in the present system the concentration of polyelectrolyte is very high, which could lead to a drastic decrease in the bending rigidity of the bilayer, which in turn could give rise to a highly swollen sponge phase.

Observation of lamellar phase over an extended range of ϕ_s in the CPHN-Water system is reminiscent of the behavior of mixtures of cationic and anionic surfactants [33–35] and also of some mixtures of cationic surfactants and anionic drugs [36].

CPHN-Water system shows the coexistence of lamellar phase and excess water, at high water content, which transforms to a collapsed lamellar phase on addition of low amounts of PAA and a precipitate is found at higher concentration of PAA, which shows hexagonal phase and isotropic phase on further addition of PAA.

Appearance of precipitates in the hexagonal and isotropic phases indicates that these phase must be of the inverted kind which is further confirmed by finding a

good agreement between the observed intensities of the diffraction patterns and those calculated from a model for the inverted hexagonal phase. The details of modeling are given below. The observed intensity in general can be given as;

$$I(q) = CS(q)P(q) \tag{5.3}$$

where S(q) is the structure factor, P(q) the form factor and C is a constant depending on the experimental geometry [37]. P(q)= $|FT[\rho_m]|^2$, where FT denotes the Fourier transform and ρ_m is the electron density distribution within a repeating unit, which in the present case is a CPHN inverted micelle. S(q) = $|FT[\rho_l]|^2$, where ρ_l is the lattice function, which describes the ordering of the centers of the repeating unit.

The hexagonal phase has long-range positional order in the plane normal to the long axis of the cylindrical micelles. Taking the micelles to be oriented along the z-axis, ρ_l in this case can be taken to be a set of δ functions forming a two-dimensional lattice in the x-y plane. Then S(q) consists of a set of δ functions in the q_x - q_y plane and can be given as,

$$S(q) = \sum_{hk} \delta(q - q_{hk}) \tag{5.4}$$

I(q) is obtained by evaluating P(q) at the corresponding values of q.

In order to find the structural parameters of the CPHN inverted micelle, we first construct a model for the electron density distribution within the micelle. Since the micelles are very long, it is enough to consider the electron density in the plane normal to the micellar axis. We take the cross-section of a CPHN inverted micelle to consists of a circular core of radius r_w and uniform electron density ρ_w corresponding to the aqueous region, surrounded by an annular ring of width δ and electron density ρ_h corresponding to the head-group region (Fig. 5.17). The space between the micelles is filled with hydrocarbon of electron density ρ_c.

Values of ρ_w and ρ_c are taken from the literature to be 332 e/nm3 and 280 e/nm3 respectively [38]. ρ_w, r_w and δ are adjustable parameters in our model.

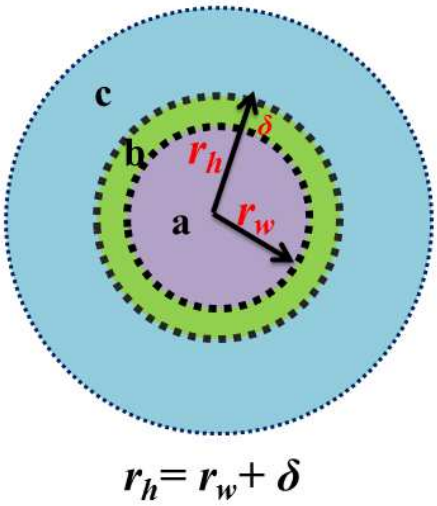

FIGURE 5.17: The electron density model used to calculate the diffraction data of the H_{II} phase. The disc with radius r_w represents the water region (**a**) of the micelles. The shaded annular ring of thickness δ corresponds to the head group region (**b**) and region (**c**) corresponds to the hydrocarbon region.

TABLE 5.17: Observed (I_o) and calculated (I_c) intensities of the different reflections in the inverted hexagonal phase.

Planes(h k)	I_o	I_c
1 0	100	100
1 1	7.26	7.24
2 0	0.76	0.80

The electron density contrast of the micelle with respect to the hydrocarbon background can be written as,

$$\rho_m(r) = \begin{cases} (\rho_w - \rho_c), & r < r_w \\ (\rho_h - \rho_c), & r_w < r < r_w + \delta \\ 0, & r > r_w + \delta \end{cases} \tag{5.5}$$

Taking the Fourier transform of $\rho_m(r)$, we get

$$F = 2\pi(\rho_h - \rho_c)r_h[\frac{J_1(qr_h)}{q}] - 2\pi(\rho_h - \rho_w)r_w[\frac{J_1(qr_w)}{q}] \quad (5.6)$$

Where $J_1(x)$ is the Bessel function of order 1 and

$$r_h = r_w + \delta$$

. The form factor of the inverted micelle, P(q) $=|f(q)|^2$

The intensities of the different peaks in the diffraction pattern of the H_{II} phase at R=1.18, ϕ_s=30 wt% and T=40°C were found by calculating the areas under each peak after subtracting the background and then applying the relevant geometric and multiplicity corrections. The intensities of these reflections were also calculated from the model by evaluating P(q) at values of q corresponding to the observed reflections. Values of the model parameters were then varied over a physically reasonable range to get the best fit between the observed and calculated intensities. Final values of the model parameters were obtained from the best fit of the calculated and observed intensities (Tab. 5.17), are: ρ_h =300.01 e/nm3 , δ = 0.60 nm and r_w = 1.03 nm. The head group size δ obtained from the fit is comparable to that of closely related amphiphiles. The present analysis does confirm that the hexagonal phase of this system is indeed made up of long inverted cylindrical micelles arranged on a two-dimensional hexagonal lattice.

5.6 Conclusion

Phase behavior of complexes of DDAB-PAANa were studied using x-ray diffraction, POM and cryo-SEM techniques, in order to probe their detailed structure. Collapsed lamellar phase is found to be stable at low polyelectrolyte concentration and high water content, in agreement with earlier studies on similar systems. A highly swollen sponge phase is found at high polyelectrolyte concentration and low water content, which was not seen in similar systems earlier. Replacing the

PAANa of smaller molecular weight by the larger molecular weight found to stabilize the collapsed lamellar phase at the expense of sponge phase. Objective of the studies to see the L_x phase in this system. However, swollen sponge phase is found in this system in-place of L_x phase. As discussed, adsorption of polymer on both sides of the bilayer, lead to a change in bending rigidity and that can explain the observed swollen sponge phase. However, further work is needed to clarify this situation. Effect of PAA on the phase behavior of aqueous solutions of CPHN was also studied by using x-ray diffraction and POM techniques. It exhibits lamellar, H_{II} and I_{II} phases, on increasing the concentration of PAA.

Bibliography

[1] A. I. Oparin, *The Origin of Life*, Dover Publications: New York (1953).

[2] H. G. Bungenberg de Jong and J. Bonner, *Protoplasma*, **24**, 198 (1935). .

[3] H. G. Bungenberg de Jong and H. R. Kruyt, *Colloid Polym. Sci.*, **50**, 39 (1939);

[4] H. G. Bungenberg de Jong, *in Colloid Science, Vol.II*, H. R. Kruyt, Ed. Elsevier, New York (1949).

[5] F. Oosawa, *J. Polym. Sci*, **236**, 421 (1957).

[6] R. Bruinsma, *Euro Phys. J.*, **B 4**, 75 (1998).

[7] J. O. Radler, I. Koltover, T. Saldittand and C. R. Safinya, *Science*, **275**, 810 (1997).

[8] I. Koltover, T. Saldittand, J. O. Radler and C. R. Safinya, *Science*, **281**, 78 (1998).

[9] R. Krishnaswamy, V. A. Raghunathan and A. K. Sood, *Phys. Rev. E*, **69**, 031905 (2004).

[10] K. K. Ewert, H. M. Evans, A. Zidovska, N. F. Bouxsein, A. Ahmed and C. R. Safinya, *J. Am. Chem. Soc*, **128**, 3998 (2006).

[11] A. V. Peresypkin and F. M. Menger, *Org. Lett.*, **1**, 1347 (1999).

[12] F. M. Menger, A. V. Peresypkin, K. L. Caran and R. P. Apkarian, *Langmuir*, **16**, 9113 (2000).

[13] F. M. Menger and A. V.Peresypkin, *J. Am. Chem. Soc.*, **123**, 5614 (2001).

[14] Annemarie B. Wóhri, et. al., *Structure*, **16**, 1003 (2008).

[15] L. Porcar, W. A. Hamilton, and P. D. Butler, *langmuir*, **19**, 10779 (2003).

[16] M. Dubois, T. Zemb, N. Fuller, R. P. Rand and V. A. Parsegian, *J. Chem. Phys*, **108**, 7855 (1998).

[17] M. Dubois and T. Zemb, *Langmuir*, **7**, 1352 (1991).

[18] K. Fontell, A. Ceglie, B. Lindman and B. Ninham, *Acta Scand*, **A40**, 247 (1986).

[19] G. Subramanian, R. P. Hjelm, T. J. Deming, G. S. Smith, Y. Li, and C. R. Safinya, *J. Am. Chem. Soc.*, **122**, 26 (2000).

[20] T. Salditt, I. Koltover, J. O. Raedler, and C. R. Safinya, *Phys.Rev.E.*, **58**, 889 (1998).

[21] Thesis in title; Structure of Surfactant-Polyelectrolyte Complexes by Rema Krishnaswamy (2003).

[22] P. L. Felgner, T. R. Gadek, M. Holm, R. Roman, H. W. Chan, M. Wenz, J. Northrop, G. M. Ringold and M. Danielsen, *Proc. Natl. Acad. Sci., U. S. A.*, **84**, 7413 (1987).

[23] P. L. Felgner and G. Rhodes, *Nature*, **349**, 351 (1991).

[24] W. L. Hsu, Y. C. Li, H. L. Chen, W. Liou, U. S. Jeng, H. K. Lin, W. L. Liu and C. S. Hsu, *Langmuir*, **22**, 7521 (2006).

[25] R. Ghirlando, E. J. Watchtel, T. Arad and A. Minsky, *Biochemistry*, **31**, 7110 (1992).

[26] R. Krishnaswamy, G. Pabst, M. Rappolt, V. A. Raghunathan and A. K. Soodn, *Phys. Rev. E*, **73**, 031904 (2006).

[27] A. V. Radhakrishnan, S. K. Ghosh, G. Pabst, V. A. Raghunathan and A. K. Sood, *Proc. Natl. Acad. Sci., U. S. A.*, **109**, 6394 (2012).

[28] R. Oda, J. Narayanan, P. A. Hassan, C. Manohar, R. A Salkar, F. Kern and S. J. Candau, *Langmuir*, **14**, 4364 (1998).

[29] G. Pabst, M. Rappolt, H. Amenitsch, and P. Laggner, *Phys. Rev. E*, **62**, 4000 (2000).

[30] C. F. Schimidt, K. Svoboda, Ning Lei, I. Petsche, L. Berman, C. R. Safinya, and G. Grest, *Science*, **259**, 952 (1993).

[31] J. Israelachvili, *Intermolecular and Surfaces Forces*, 2nd edition, Academic Press, London (1991).

[32] J. T. Brooks, C. M. Marques and M. E. Cates, *J Phys II*, **1**, 673 (1991).

[33] E. W. Kaler, K. L. Herrington, A. K. Murthy and J. A. N. Zasadzinski, *J. Phys. Chem.*, **96**, 6698 (1992).

[34] M. T. Yatcilla, K. L. Herrington, L. L. Brasher and E. W. Kaler, *J. Phys. Chem.*, **100**, 5874 (1996).

[35] K. L. Herrington, E. W. Kaler, D. D. Millar, J. A. Zasadzinski and S. Chiruvolu, *J. Phys. Chem.*, **97**, 13792 (1993).

[36] T. Bramer, M. Paulsson, K. Edwards and K. Edsman, *Pharm. Res.*, **20**, 1661 (2003).

[37] A. Guinier, and G. Fournet, *Small-angle scattering of X-rays*, Wiley: New York (1955).

[38] B. Cabane, *In Surfactant Solutions: New Methods of Investigation*, Zana, R. Ed., Marcel Dekker: New York (1987).

Chapter 6

Salt-induced isotropic phase of worm-like micelles

6.1 Introduction

Worm-like micelles are highly flexible, locally cylindrical aggregates of amphiphilic molecules. Typical radii are 2 to 2.5 nm, with persistence lengths of the order of 15nm and average lengths of the micelles approaching several microns [1, 2]. The presence of worm-like micelles is often reflected in an increase in relative viscosity [2]. These long micelles can entangle with each other to form a transient network which can be highly viscoelastic [3, 4]. The transient networks formed by entangled long micelles exhibit properties similar to those of semi-dilute and concentrated polymer solutions, with an important difference in that micelles can pass through each other, under certain conditions, by opening and re-closing [5–7]. At higher salt concentrations, the entangled linear micelles can transforms into branched and multi-connected micellar networks with highly mobile and fluid connection [7–20].

In this chapter, we study the influence of the hydrotrope, 6-hydroxy-2-sodium naphthoate (SHN2) on the phase behavior of a cationic surfactant, cetylpyridinium chloride (CPC). Earlier studies on this system are described in section 6.2, which

suggest that the addition of hydrotrope to CPC results in an increase in the length of the CPC cylindrical micelles at low surfactant concentration and leads to a highly viscous entangled worm-like micellar solution on further increasing the hydrotropes concentration. At high hydrotrope concentrations, entangled worm-like micelles transform into a low viscous branched and multi-connected network. A brief description of chemicals and experimental techniques are given in section 6.3. Results of these studies are presented in section 6.4. A partial phase diagram of the various structures formed by aqueous solutions of hydrotropes and cationic surfactant as a function of SHN2 and CPC concentrations has been determined from x-ray diffraction data and polarizing optical microscopy textures. At low amounts of SHN2, the phase behavior of CPC-SHN2-Water system is similar to that of the CPC-Water system, which exhibits the hexagonal phase over a wide range of water content, except that the low-viscosity isotropic phase of spherical micelles at higher water content is replaced by high-viscosity worm-like micelles. With increasing concentration of SHN2, hexagonal phase with excess water is found instead of isotropic phase of spherical micelles. A still higher concentration of SHN2, a low viscous isotropic phase is found which seems to be a branched and multi-connected network of cylindrical micelles. This isotropic phase transforms into the hexagonal phase at lower water content and low temperatures. Our results are discussed in section 6.5. The last section contains conclusions that can be drawn from these studies.

6.2 Earlier Studies

CPC forms spherical micelles just above the CMC. Further increase in the concentration of surfactant gives rise to cylindrical micelles and leads to the formation of 2D hexagonal phase. Effect of 3-hydroxy-2-sodium naphthoate (SHN), 2-hydroxy-1-sodium naphthoate (SHN1) and 2, 3 dihydroxy naphthalene (DHN) on the phase behavior of CPC has been investigated [21]. Addition of low amounts of SHN, leads to micellar growth and the formation of a viscous isotropic phase of worm-like micelles at higher water content which transforms first into a nematic phase and then

to the hexagonal phase on decreasing the water content. An intermediate ribbon phase has been found at low water content and low temperature which transform into cubic phase on heating. At moderate concentrations of SHN, mesh-phases (random and ordered), nematic phase of disc-like micelles and lamellar phase have been seen, whereas at equimolar concentration, only the lamellar phase has been reported. At very high concentrations of SHN, a novel isotropic phase of bilayers has been found as discussed in the previous chapter 2. SHN1 is found to induce worm-like micelles at low concentrations and disc-like micelles at higher concentrations. Formation of ribbon, tetragonal ordered mesh phase (T) and lamellar phase has been reported in this system. DHN is found to be very effective in inducing the formation of worm-like micelles.

Influence of hexanol on the phase behavior of CPC in brine has been investigated [22]. Isotropic phase of CPC containing globular micelles is found to transform into rod-like micelles on addition of hexanol and following phase sequence is found: isotropic micellar solution (L_1)$\rightarrow$ lamellar liquid crystal (LLC) $\rightarrow$ sponge phase.

Aqueous mixtures of oppositely charged surfactants exhibit very interesting structures due to electrostatic interaction between their head groups. Coacervates have been seen in equimolar solutions of SDS and CPC [23].

Influence of chaotropic, cosmotropic and hydrotropic anions on the micellar transition and growth of CPC has been investigated by Abezgauz et al. [24]. They have used cryo-TEM, DLS, UV-visible absorption spectroscopy techniques and rheology measurements to quantify the micellar growth and found that hydrotropes induce profound effects by penetrating into the hydrocarbon-water interface and leading to a strong anchoring at the interface which is reflected in both the solution viscosity and micellar structure. NMR and computer simulation studies by other group also find similar results [25, 26]. Chaotropic anions are found to be more effective in inducing the micellar growth in comparison to cosmotropic anions and they follow an order which justifies their locations in the lyotropic series.

Numerous surfactants have been found to form worm-like micelles in the presence of simple salts [27–29] or hydrotropes [30, 31]. Simple salts are primarily involved in decreasing the optimal molecular head group area at the hydrocarbon-water interface by screening the electrostatic repulsion between the head groups and leading to an increase in the end cap energy. Consequently the average micellar length increases dramatically. Hydrotropes are found to inserted between the head groups, thus penetrating deep into the micelles in addition to screening the electrostatic repulsion between the head groups. Worm-like micelles have also been seen in the aqueous solutions of pure surfactants [32, 33].

Worm-like micelles are also seen in mixtures of surfactants and other small molecules such as short chain alcohols [8]. Here alcohol with small head group, reduces the effective head group area per molecule which results in a decrease in the hydrocarbon-water interface curvature, thus leading to micellar growth.

Worm-like micelles have been reported in gemini surfactants [34–37], zwitterionic surfactant [38], in mixtures of ionic-nonionic surfactants [39, 40] and cationic-anionic surfactants [41]. They have been also seen in lipids [42, 43] as well as in block co-polymers [44, 45].

The effect of salt on the worm-like micellar solutions of ionic surfactants has been investigated by many groups. They found significant structural and rheological transitions on the addition of salt and observed multi-connected and branched micellar networks of worm-like micelles [7–19]. Porte et al. [8] reported the formation of branched and multi-connected worm-like micellar networks in ionic micellar solutions with high salt concentrations (CPC/hexanol with [NaCl] = 0.2 M). They proposed that branch-points in the network can slide, yielding high fluidity. Candau et al. [11] carried out rheological measurements on worm-like micellar solutions of CTAB and found that zero-shear viscosity and stress relaxation time reach a maximum and then start decreasing on increasing the salt concentration. This behavior is consistent with a transition from entangled linear micelles to a multi-connected structure on addition of salt. Cappelaere and Cressely [7] have also seen a similar trend in the zero-shear viscosity and stress relaxation time with changes

in the salt concentration. They explain- the reduction of the zero-shear viscosity, in terms of branching of micelles with sliding connections or shortening of the micelles with addition of salt. However, Cappelaere and Cressely [13] observed that plateau modulus decreases with increasing salt content in the worm-like micellar solution of CPC and $NANO_3$. According to them higher concentration of salt could effectively be involved in breaking of the micellar network junctions and leading to shorter micelles. Thus, plateau modulus decreases on increasing the salt concentration. Schubert et al. [17] quantitatively studied the effect of salt on the micellar length of a worm-like micellar solution of CTAT/Sodium Dodecylbenzenesulfonate (SDBS) by using rheology, flow birefringence, and small-angle neutron scattering techniques. They found that both the zero-shear viscosity and stress relaxation time decrease with the addition of the hydrotropic salt sodiumtosylate, which is related to the presence of branched micelles.

Hoffmann et al. [30] have been reported rheology measurements on worm-like micellar solutions of the cetylpyridinium chloride/sodium salicylate (CPC/NaSal) system and found two maxima in the zero-shear viscosity as a function of salt concentration the first one corresponds to low salt concentration and the second maximum occurs when the molar ratio of hydrotrope to surfactant is greater than one (the minimum in viscosity is found at about equimolar conditions). This behavior reflects the reverse progression of structure from branched to ultimately individual unentangled micelles at very high salt concentration. In this progression the net charge of the micelle reverses from positive at low salt concentrations, where the first maximum in viscosity is observed, to negative at higher salt concentrations and passes through zero near the position of the viscosity minimum.

Flow-induced structure formation has also been reported in solutions of worm-like micelles. Rehage and Hoffmann first reported a transient gel-like structure in worm-like micellar solution of cetylpyridinium chloride (CPC) and hydrotrope sodium salicylate (NaSal) under shear flow above a critical shear rate [30]. They referred to this gel-like structure as a shear-induced structure (SIS), because on stopping the flow, the SIS would disappear. SISs consist of highly elongated and

locally concentrated micellar strings. Stable flow-induced structures from worm-like micelles were first reported by Vasudevan et al. [46]. The worm-like micellar solution formed a gel like flow induced structure phase (FISP) after traversing a microfluidic tapered channel packed with micro glass beads. FISP has been reported in many systems after that [47].

6.3 Experimental

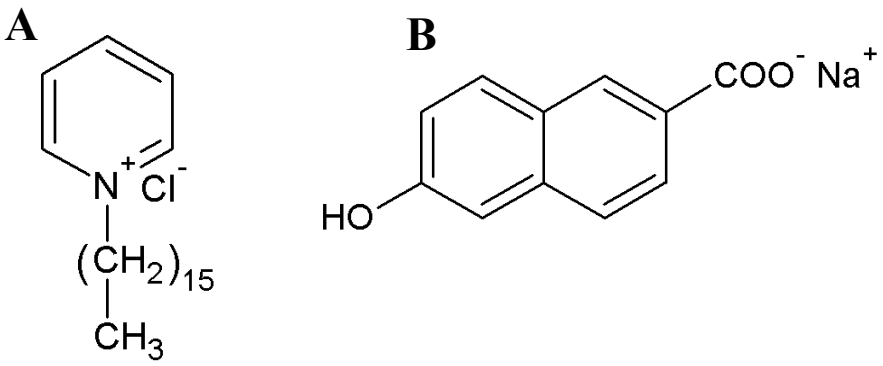

FIGURE 6.1: Chemical structure of the surfactant cetylpyridinium chloride (CPC) (**A**) and the hydrotrope 6-hydroxy-2-sodium-naphthoate (SHN2) (**B**).

Cetylpyridinium chloride (CPC) and 6-hydroxy-2-naphthoic acid (HNA2) were purchased from Sigma-Aldrich. 6-hydroxy-2-sodium-naphthoate (SHN2) was prepared by adding equivalent amount of an aqueous solution of sodium hydroxide (NaOH) to an ethanol solution of HNA2. Chemical structures of the molecules are shown in figure 6.1. Ternary solution were prepared by adding appropriate amounts of deionized water to a mixture of CPC and SHN2. The sample tube was then sealed and left in an incubator at 40°C for more than two weeks to equilibrate. The experimental techniques used to identify the different phases were same as those described in previous chapters. The phase behavior of the systems was probed as a function of the molar ration α of the organic salt to the surfactant, and of the total concentration of the surfactant and salt (ϕ_s)

6.4 Results

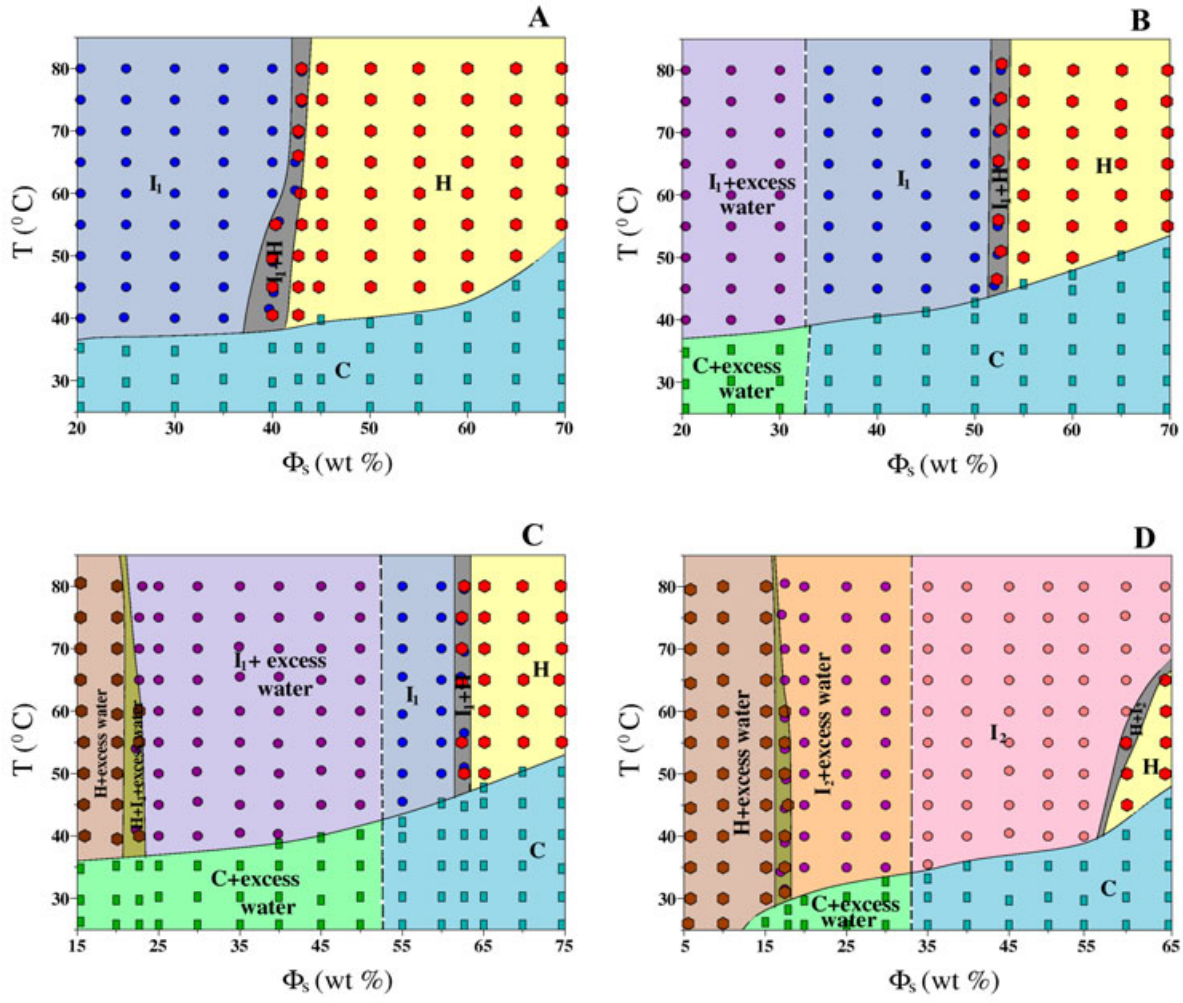

FIGURE 6.2: Partial phase diagrams of the CPC-SHN2-water system at α = 0.25 (**A**), 0.6 (**B**), 1 (**C**) and 1.2 (**D**). I_1, H, I_2 and C denote the isotropic, hexagonal, a different isotropic and crystalline phases, respectively. The dashed line indicates the continuous transition. transitions-I_1+excess water-I_1 and I_2+excess water-I_2 are continuous.

The phase behavior of mixtures of CPC and SHN2 was studied at different values of the molar ratio ($\alpha = \frac{[SHN2]}{[CPC]}$) of the two components. For each α the total concentration of the non-aqueous components ($\phi_s = \frac{(CPC+SHN2)}{(CPC+SHN2+Water)}$x100) was varied from 20 to 80wt%. The microscopy texture of each sample was monitored from 25 to 80°C. The structure of the phases was confirmed by using diffraction studies and texture of the sample.

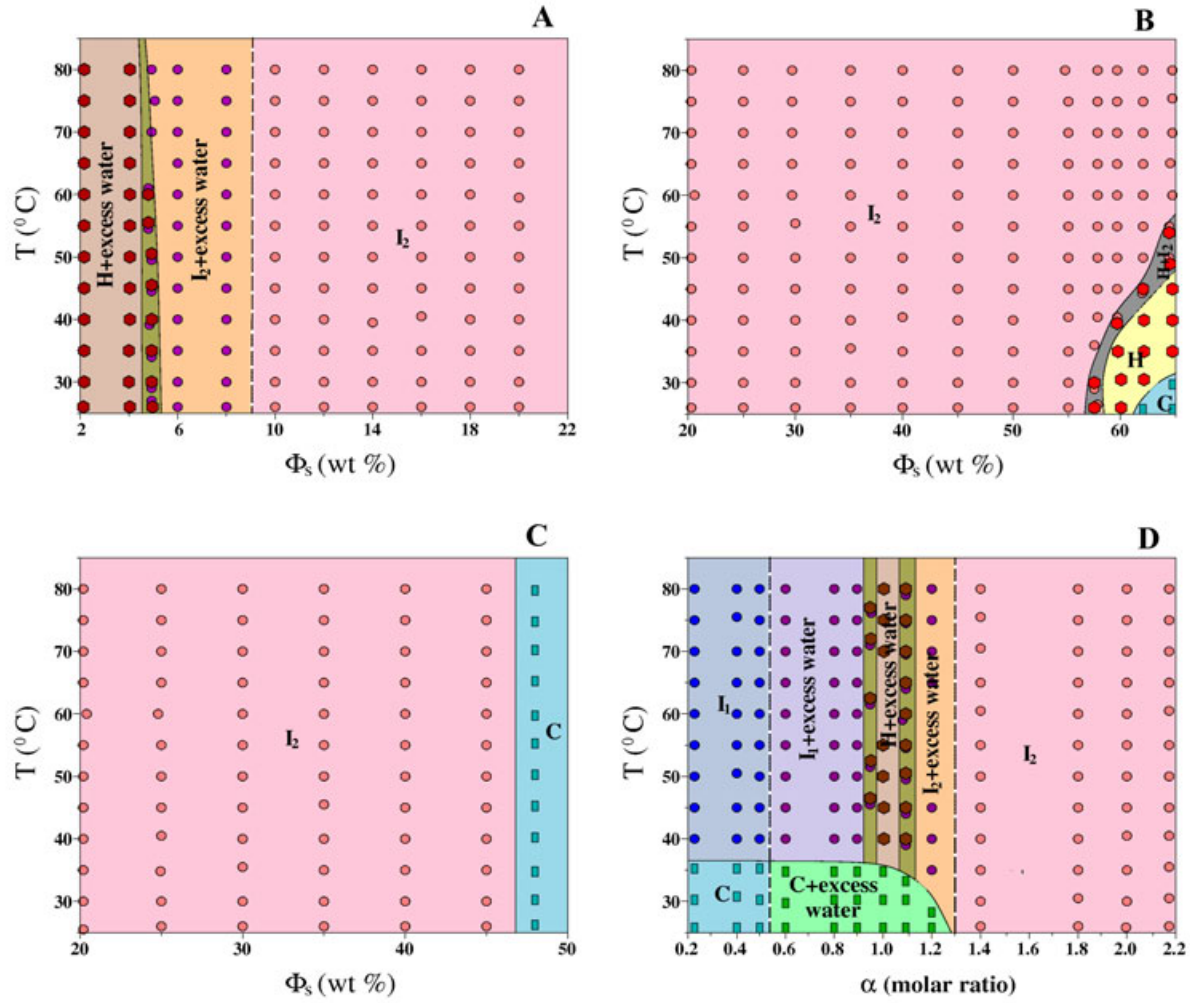

FIGURE 6.3: Partial phase diagrams of the CPC-SHN2-water system at α=1.75 (**A and B**), α=2 (**C**), and ϕ_s=20 (**D**). I_1, H, I_2 and C denote the isotropic, hexagonal, a different isotropic and crystalline phases, respectively. The dashed line indicates the continuous transition. transitions-I_1+excess water-I_1 and I_2+excess water-I_2 are continuous.

6.4.1 CPC-SHN2-Water system

6.4.1.1 Phase behavior at α=0.25

Figure 6.2A shows the temperature−ϕ_s phase diagram of the system at α=0.25. For 20 ≤ϕ_s≤35 and T≤ 40°C, it shows a crystalline (C) phase and above 40°C a visco-elastic isotropic (I_1) phase is found (Fig. 6.4D). Its SAXS pattern shows a broad peak in the small angle region with a shoulder at higher wave vector (q) (Fig. 6.5A(a-c)). For 45<ϕ_s≤70, a crystalline (C) phase is found at low

temperatures which transform into an anisotropic phase at higher temperatures. SAXS pattern of the anisotropic phase shows two peaks with their wave vector (q) in the ratio 1:$\sqrt{3}$ (Fig. 6.5A(d)) and POM shows a fan-like texture (similar to figure 6.4B), confirming the occurrence of 2D hexagonal (H) phase. I_1 phase at low ϕ_s and H phase at higher ϕ_s is separated by a two phase region. Figure 6.6A shows the variation of the lateral spacing (d) of the I_1 phase with ϕ_s. It is found to be described by the relation (d$\sim{\phi_v}^{-s}$) with s$\sim$1/3, where ϕ_v is the volume fraction of the non-aqueous component estimated from ϕ_s, using the densities of the components. The densities of components; CPC, SHN2 and water are taken as 0.98, 1.33 and 0.997g/cm^3, respectively. Variation of lattice spacing (d) of the hexagonal phase with ϕ_s is shown in figure 6.6B. It is found to be described by the relation (d$\sim{\phi_v}^{-s}$) with s$\sim$1/2. The variation of lattice spacing with ϕ_s is also given in table 6.1.

TABLE 6.1: Variation of lattice parameter in the isotropic (I_1) and hexagonal (H) phases of the CPC-SHN2-Water system at α=0.25 and T=60°C

ϕ_s	d_1(nm)	d_2(nm)	Phase	Lattice parameter
20	6.69	–	I_1	–
30	5.87	–	I_1	–
40	5.44	–	I_1	–
45	5.00	2.89	H	5.77
50	4.72	2.73	H	5.45
60	4.52	2.61	H	5.22
70	4.10	2.37	H	4.73

6.4.1.2 Phase behavior at α=0.6

Figure 6.2B shows the temperature−ϕ_s phase diagram of the system at α=0.6. The phase behavior is found to be similar to that observed at α=0.25 except at low ϕ_s. For 20 $\leq\phi_s<$35 a crystalline phase with excess water (C +excess water) is found at low temperatures which transforms into an isotropic phase with excess water (I_1+excess water) at higher temperatures. The amount of excess water decreases with increasing ϕ_s and finally disappears at $\phi_s\sim$ 32. For 35 $\leq\phi_s\leq$50, a crystalline (C) phase is found at low temperatures which transforms into an

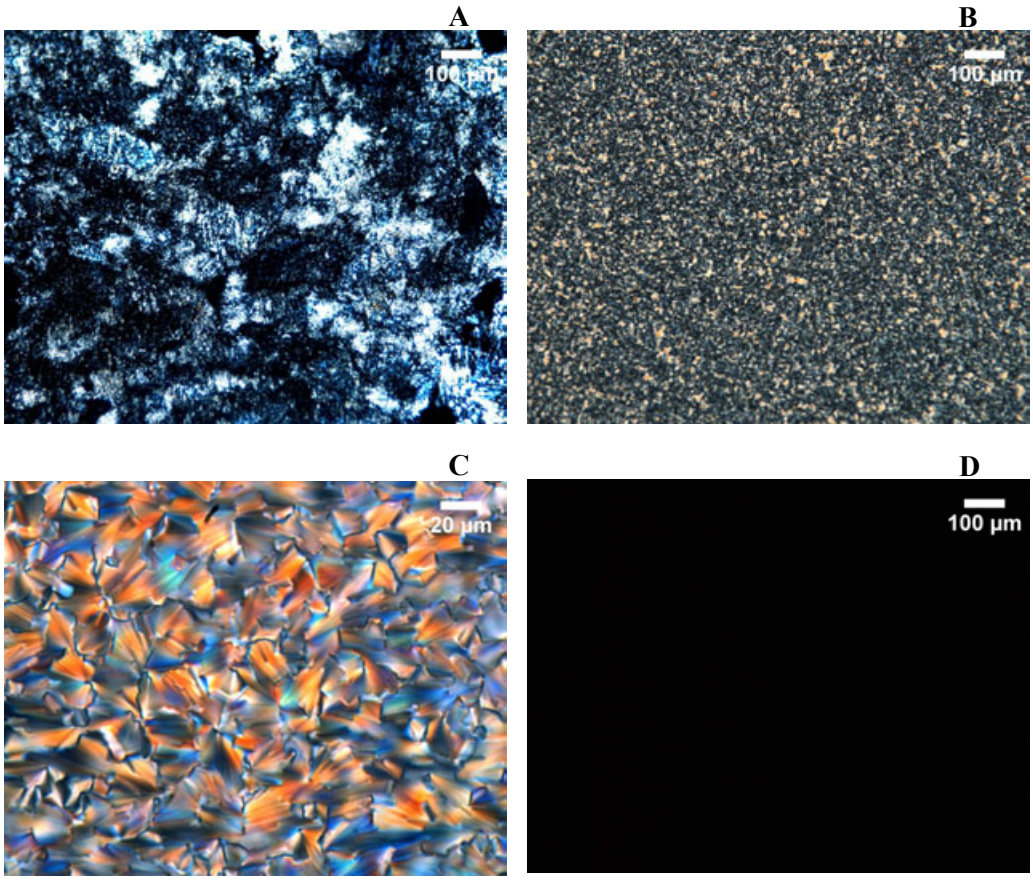

FIGURE 6.4: Polarizing optical microscopy textures of hexagonal phase at (**A**) α=1, ϕ_s=15 and T=50°C, (**B**) α=1, ϕ_s=70 and T=65°C, (**C**) α=1.75, ϕ_s=65 and T=40°C and (**D**) isotropic phase in the CPC-SHN2-Water system.

isotropic (I_1) phase at higher temperatures, whereas for 55 $\leq\phi_s\leq$70 a crystalline phase is found at low temperatures which transforms into an anisotropic phase at higher temperatures. SAXS pattern of this anisotropic phase shows two peaks in the small angle region with their q in the ratio 1:$\sqrt{3}$ and fan-like texture (similar to figure 6.4B) is found under the microscope, which confirms the occurrence of 2D hexagonal (H) phase. I_1 phase and H phase are separated by a two phase region.

6.4.1.3 Phase behavior at α=1

Figure 6.2C shows the temperature−ϕ_s phase diagram of the system at α=1. For 15 $\leq\phi_s<$23, a crystalline phase with excess water (C +excess water) is found at low temperatures which transforms into a hexagonal phase with excess water

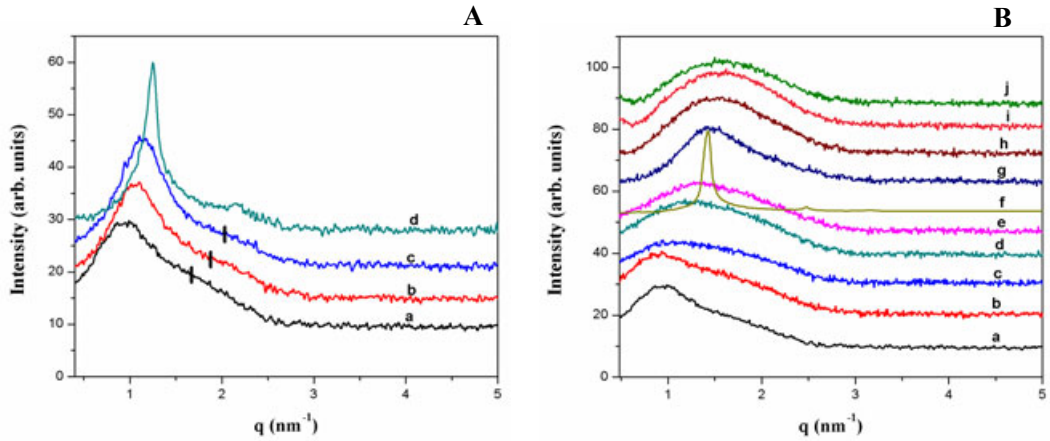

FIGURE 6.5: X-ray diffraction patterns of the CPC-SHN2-Water system (**A**) at α=0.25, T=60°C corresponding to ϕ_s=20 (**a**), ϕ_s=30 (**b**), ϕ_s=40 (**c**) and ϕ_s=45 (**d**). The bars on curves a, b and c indicate secondary peaks at $\sqrt{3}q_o$ where q_o is the position of the primary peak. (**B**) at ϕ_s=20, T=60°C and corresponding to α=0.25 (**a**), α=0.4 (**b**), α=0.6 (**c**), α=0.7 (**d**), α=0.8 (**e**), α=1 (**f**), α=1.2 (**g**), α=1.4 (**h**), α=1.8 (**i**) and α=2.2 (**j**).

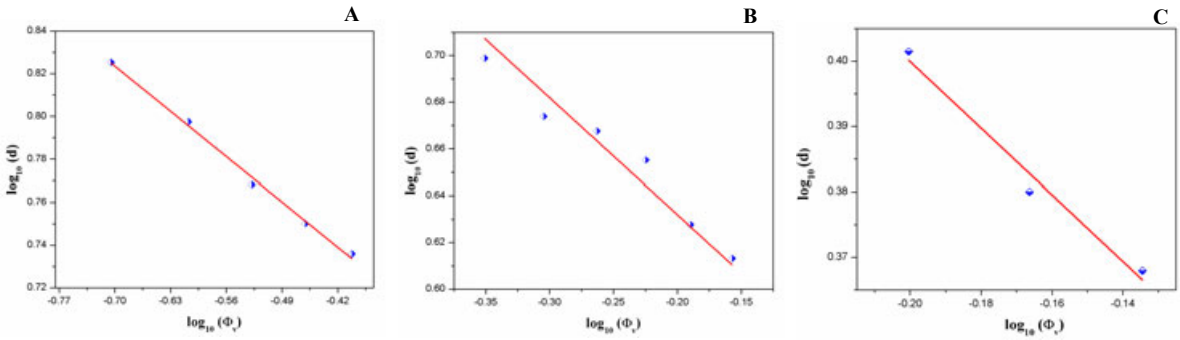

FIGURE 6.6: Variation of the d-spacing with surfactant volume fraction (ϕ_v): (**A**) in the isotropic (I_1) phase of the CPC-SHN2-Water system at α=0.25 and T=60°C (**B**) in the hexagonal phase of the CPC-SHN2-Water system at α=0.25 and T=60°C and (**C**) in the hexagonal phase of the CPC-SHN2-Water system at α=1 and T=60°C.

(H +excess water) at higher temperatures. The SAXS pattern of this hexagonal shows two peaks in the small angle region with their q in the ratio 1:$\sqrt{3}$ (Fig. 6.5B(f)) and a smooth texture (Fig. 6.4A) is found under crossed POM, confirming the occurrence of 2D hexagonal phase. For 23 <ϕ_s≤50, behavior is similar to that seen at α=0.6 for 20 ≤ϕ_s≤35, i.e. isotropic phase coexisting with excess water (I_1+excess water) is found over the temperature range studied. For 55 ≤ϕ_s≤60, a crystalline phase is found at low temperatures which transforms into

an isotropic (I_1) phase at higher temperatures. For 65 $\leq\phi_s\leq$75 a multi-phase region is seen at low temperatures, which transforms into hexagonal (H) phase at higher temperatures (Fig. 6.4B). Figure 6.6C shows the variation of the lattice spacing (d) of the hexagonal phase with ϕ_s. It is found to be described by the relation ($d\sim\phi_v^{-s}$) with s$\sim$1/2. The d-spacing increases from 4.3nm at ϕ_s=15 in the hexagonal(H)+excess water phase to 5.1nm at ϕ_s=55 in the isotropic phase and then decreases to 4.4 nm in the hexagonal (H) phase (Tab. 6.2). Positional correlation length, estimated from the peak width (Fig. 6.7A) is found to be about 60nm in the hexagonal phase and drops to about 7nm in the isotropic phase.

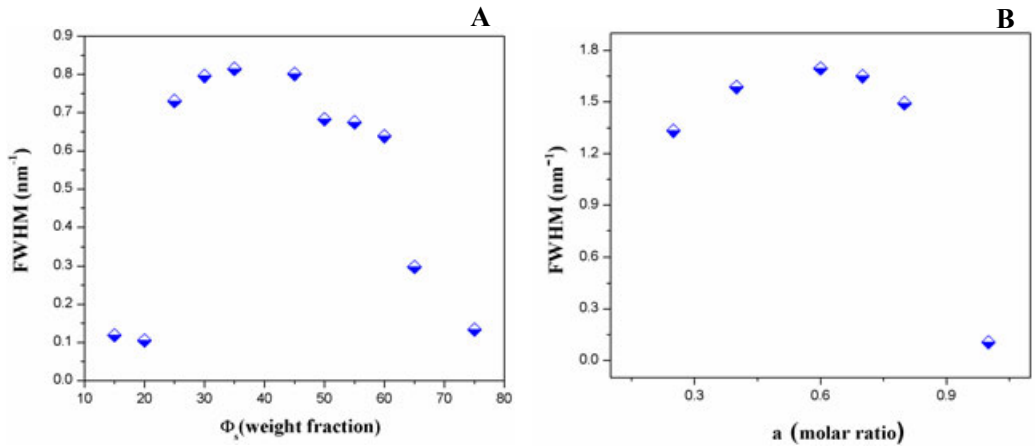

FIGURE 6.7: Variation of full width at half maxima with ϕ_s at (**A**) α=1 and 60°C and with α at (**B**) ϕ_s=20 and 60°C in the CPC-SHN2-Water system.

6.4.1.4 Phase behavior at α=1.2

Figure 6.2D shows the temperature−ϕ_s phase diagram of the system at α=1.2. For 5 $\leq\phi_s\leq$15, it shows hexagonal phase with excess water (H +excess water) over the temperature range studied. For 20$\leq\phi_s\leq$30, a crystalline phase with excess water (C +excess water) is found at low temperatures which transforms into a low viscous isotropic phase with excess water (I_2+excess water) at higher temperatures. For 35$\leq\phi_s\leq$65, it exhibits a crystalline (C) phase at low temperatures which transforms into a low viscous isotropic (I_2) phase at higher temperatures. This isotropic (I_2) phase is found to be different from that of the isotropic phase

TABLE 6.2: (Variation of lattice parameter in the isotropic (I_1) and hexagonal (H) phases of the CPC-SHN2-Water system at α=1 and T=55°C.

ϕ_s	d_1(nm)	d_2(nm)	Phase	Lattice parameter
15	4.27	2.47	H +excess water	4.93
20	4.41	2.55	H +excess water	5.09
25	4.64	–	I_1+excess water	–
30	4.74	–	I_1+excess water	–
35	4.76	–	I_1+excess water	–
40	4.84	–	I_1+excess water	–
45	4.96	–	I_1+excess water	–
50	5.05	–	I_1+excess water	–
55	5.10	–	I_1	–
60	4.92	–	I_1	–
65	4.80	2.77	H	5.54
70	4.57	2.64	H	5.28
75	4.46	2.57	H	5.15

(I_1) found at lower values of α. The SAXS pattern of this isotropic (I_2) phase exhibits a broad peak about 5.0nm at higher water content. The peak position remains the same throughout this phase, however, the positional correlation length is found to develop with decreasing water content. As a result, peak becomes sharper and sharper finally ending with the hexagonal phase at very low water content (Fig. 6.8A). Positions of the broad peak of the isotropic (I_2) phase and the sharp peak of the hexagonal (H) phase are found to be the same (Fig. 6.8B). This hexagonal (H) phase transforms into I_2 phase at higher temperatures, on heating. The transition is found to be reversible on cooling. This indicates a close relationship between the structure of the isotropic (I_2) phase and the hexagonal (H) phase. The spacing corresponding to the structure peak of the isotropic (I_2) phase and the lattice parameter of the hexagonal phase are given in table 6.3.

6.4.1.5 Phase behavior at α=1.75

Figures 6.3A and B show the temperature−ϕ_s phase diagram of the system at α=1.75. For $2 \leq \phi_s \leq 4$ it shows a hexagonal phase with excess water (H +excess water). For $6 \leq \phi_s \leq 8$ it exhibits a low viscous isotropic phase with excess water (I_2+excess water). For $10 \leq \phi_s \leq 55$ a pure isotropic (I_2) phase is found (similar

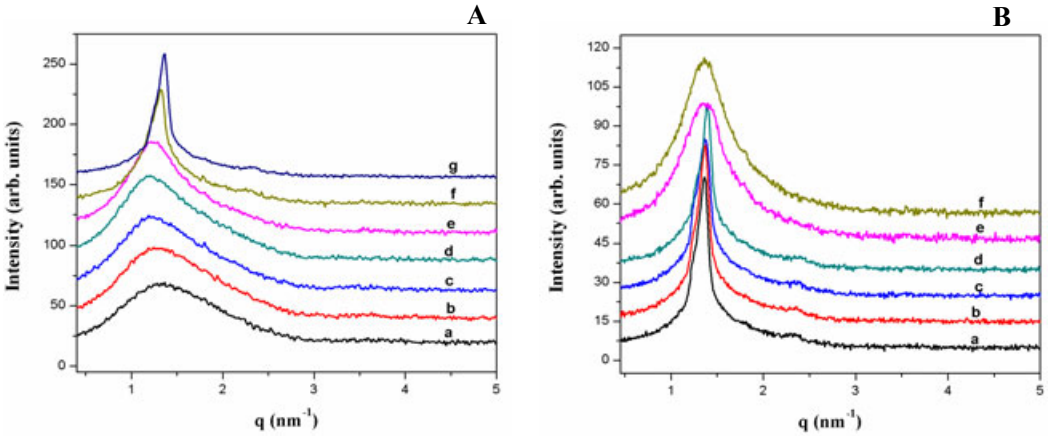

FIGURE 6.8: X-ray diffraction patterns of the CPC-SHN2-Water system (**A**) at α=1.2, T=50°C corresponding to ϕ_s=35 (**a**), ϕ_s=40 (**b**), ϕ_s=45 (**c**), ϕ_s=50 (**d**), ϕ_s=55 (**e**), ϕ_s=60 (**f**) and ϕ_s=65 (**g**). Positional correlation is increasing with increasing ϕ_s. (**B**) at α=1.2, ϕ_s=65 and corresponding to T=50°C (**a**), T=55°C (**b**), T=60°C (**c**), T=65°C (**d**), T=70°C (**e**) and T=75°C (**f**). Hexagonal phase transforms to I_2 phase at higher temperature.

TABLE 6.3: Variation of lattice parameter in the isotropic (I_2) and hexagonal (H) phases of the CPC-SHN2-Water system at α=1.2 and T=50°C.

ϕ_s	d_1(nm)	d_2(nm)	Phase	Lattice parameter
6	4.34	2.51	H +excess water	5.01
10	4.34	2.51	H +excess water	5.01
15	4.34	2.51	H +excess water	5.01
20	4.43	–	I_2+excess water	–
25	4.66	–	I_2+excess water	–
30	4.82	–	I_2+excess water	–
35	4.93	–	I_2	–
40	5.02	–	I_2	–
50	5.06	–	I_2	–
55	5.09	–	I_2	–
60	4.72	2.72	H	5.45
65	4.63	2.67	H	5.35

to the isotropic (I_2) phase that found at α=1.2). The SAXS pattern shows a broad peak at higher water content and positional correlation is found to be developing on decreasing the water content, with a structure peak at about 5.5nm (Fig. 6.9A). At ϕ_s=60 it shows a hexagonal (H) phase at low temperatures which transforms into an isotropic (I_2) phase at higher temperatures on heating. SAXS patterns of the hexagonal (H) and isotropic (I_2) phases are shown in figure 6.9B.

At ϕ_s=65, it shows a crystalline phase at low temperatures which first transforms into a hexagonal (H) phase and then into isotropic (I_2) at higher temperatures, on heating. This hexagonal (H) phase exhibits a nice fan-like texture (Fig. 6.4C) and its SAXS pattern shows two peaks in the small angle region with their q in the ratio 1:$\sqrt{3}$ (Fig. 6.9A(i)). Table 6.4 shows the variation of d-spacing with decreasing water content. At higher water content the d-spacing is about 4.3nm in the hexagonal +excess water (H +excess water) phase, then jumps to about 5.5nm in the isotropic (I_2) phase and then gradually comes to 4.8nm in the hexagonal (H) phase, with decreasing water content.

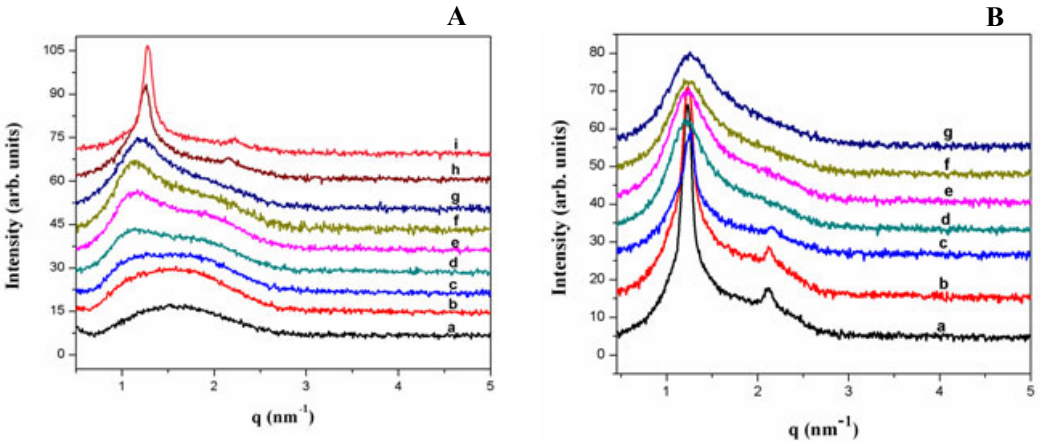

FIGURE 6.9: X-ray diffraction patterns of the CPC-SHN2-Water system (**A**) at α=1.75, T=35°C corresponding to ϕ_s=19.9 (**a**), ϕ_s=28.9 (**b**), ϕ_s=34.1 (**c**), ϕ_s=39.6 (**d**), ϕ_s=45.4 (**e**), ϕ_s=49.9 (**f**), ϕ_s=54.7 (**g**), ϕ_s=59.8 (**h**) and ϕ_s=65.0 (**i**). Positional correlation is increasing with increasing ϕ_s. (**B**) at α=1.75, ϕ_s=59.8 and corresponding to T=25°C (**a**), T=30°C (**b**), T=35°C (**c**), T=40°C (**d**), T=50°C (**e**), T=60°C (**f**) and T=80°C (**g**). Hexagonal phase transforms to I_2 phase at higher temperature.

6.4.1.6 Phase behavior at α=2

Low viscous isotropic (I_2) phase is found over 20≤ϕ_s≤45, similar to the isotropic (I_2) phase at α=1.2 and 1.75 (Fig. 6.3C). SAXS pattern shows a broad peak at higher water content and positional correlations are found to be developing with decreasing water content with a structure peak at about 5.7nm (Fig. 6.10A). At lower water content SHN2 crystallizes out from the solution.

TABLE 6.4: Variation of lattice parameter in the isotropic (I_2) and hexagonal (H) phases of the CPC-SHN2-Water system at α=1.75 at T=35°C.

ϕ_s	d_1(nm)	d_2(nm)	Phase	Lattice parameter
2	4.31	2.49	H+excess water	4.98
4	4.37	2.52	H+excess water	5.05
6	4.43	–	I_2+excess water	–
10.6	–	–	I_2	–
39.6	5.50	–	I_2	–
45.4	5.50	–	I_2	–
49.9	5.50	–	I_2	–
54.7	5.50	–	I_2	–
59.8	5.00	2.89	H	5.77
65.0	4.89	2.82	H	5.65

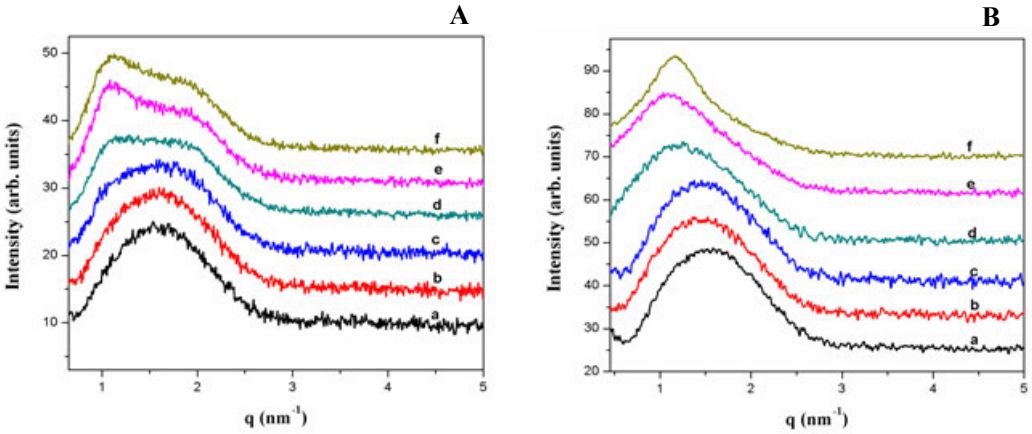

FIGURE 6.10: X-ray diffraction patterns of the (**A**) CPC-SHN2-Water system at α=2, T=30°C corresponding to ϕ_s=20 (**a**), ϕ_s=25 (**b**), ϕ_s=30 (**c**), ϕ_s=35 (**d**), ϕ_s=40 (**e**) and ϕ_s=43.4 (**f**). Positional correlation is increasing with increasing ϕ_s. (**B**) CPC-SHN2-NaCl-Water system at α=1.75 , ϕ_s=20 and T=30°C corresponding to [NaCl]=0.25M (**a**), [NaCl]=0.5M (**b**), [NaCl]=1M (**c**), [NaCl]=2M (**d**), [NaCl]=3M (**e**), and [NaCl]=3.5M). Positional correlation is developing with increasing the salt concentration.

6.4.1.7 Phase behavior at ϕ_s=20

Figure 6.3D shows the temperature−α phase diagram of the system at ϕ_s=20. For $0.2 \leq \alpha \leq 0.5$ it shows a crystalline (C) phase at low temperatures which transforms into an isotropic (I_1) phase at higher temperatures. For $0.5 < \alpha \leq 0.9$ a crystalline phase with excess water (C +excess water) is found at low temperatures which transforms into an isotropic phase with excess water (I_1+excess water) at higher

TABLE 6.5: Variation of lattice parameter in the isotropic (I_1), (I_2) and hexagonal (H) phases of the CPC-SHN2-Water system at ϕ_s=20 and T=50°C.

α	d_1(nm)	d_2(nm)	Phase	Lattice parameter
0.25	6.69	–	I_1	–
0.4	6.74	–	I_1	–
0.6	5.89	–	I_1+excess water	–
0.7	5.50	–	I_1+excess water	–
0.8	4.80	–	I_1+excess water	–
1.0	4.43	2.56	H+excess water	5.12
1.2	4.43	–	I_2+excess water	–

temperatures. For $0.9<\alpha<1.1$ a crystalline phase with excess water (C +excess water) is found at low temperatures which transforms into hexagonal phase with excess water (H +excess water) at higher temperatures. For $1.1<\alpha<1.3$ it shows crystalline phase with excess water (C +excess water) at low temperature which transforms into an isotropic phase with excess water (I_2+excess water)at higher temperatures. For $1.4\leq\alpha\leq2.2$ it exhibits an isotropic (I_2) phase over the temperature range studied. The d-spacing decreases from about 6.8nm at α=0.25 to about 4.4nm at α=1.2 (Tab. 6.5). Positional correlation length estimated from full width half maxima (FWHM) (Fig. 6.7B) is found to be about 4nm in the isotropic phase and about 60nm in the hexagonal phase.

6.4.1.8 Cryo-SEM studies

Cryo-SEM studies have been done in the hexagonal (H) phase. Similar experiments were also carried out in the I_2 phase, both at high water content where SAXS shows a broad peak and at low water content where an additional structure peak is also seen in the SAXS pattern. The experiment were performed in the CPC-SHN2-Water system at α=1.75. Figure 6.11A&B shows cryo-SEM micrographs of the I_2 phase at higher water content. Micrographs show micro-phase separation, where excess water is phase-separated out locally. However, at low water content the micrographs show a different connected structure (Fig. 6.11C&D). However, the resolution of the micrograph is not sufficient to decipher the detailed structure of

the I_2 phase. Figure 6.12 show cryo-SEM micrographs of the hexagonal phase. The cylinder-like features of the hexagonal phase is clearly seen in the micrographs.

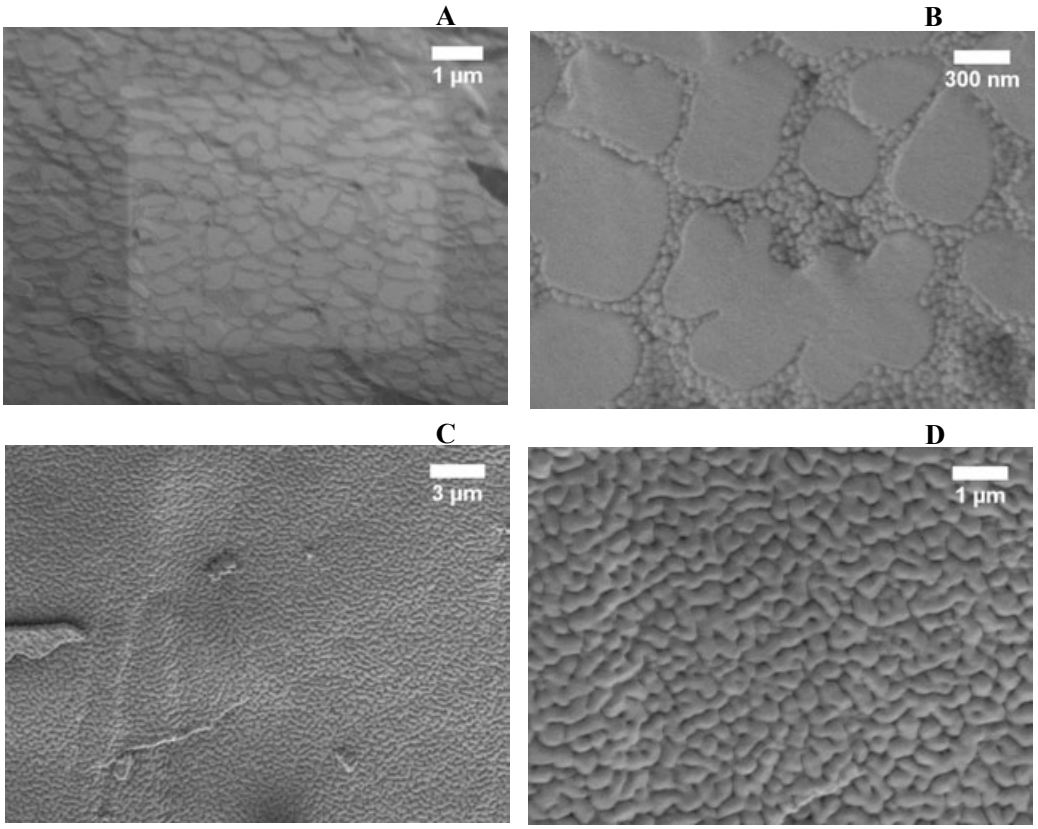

FIGURE 6.11: Cryo-SEM micrographs of I_2 phase in the CPC-SHN2-Water system at (**A and B**) α=1.75 and ϕ_s=20 and (**C and D**) at α=1.75 and ϕ_s=50.

6.4.2 CPC-SHN2-NaCl-Water system: Effect of salt

In-order to find the detailed structure of the I_2 phase, effect of salt (NaCl) on this phase has been studied. These studies have been carried out at α=1.75 and ϕ_s=20 and at various salt (NaCl) concentrations.

Salt is found to have no significant effect on the I_2 phase, at low concentrations, but at moderate concentrations it induces phase separation. Surfactant rich phase is found to be denser initially, but at higher salt concentrations, the water rich phase becomes denser. At still higher salt concentrations, SHN2 crystallizes out (Fig. 6.13) from the solution. At low salt concentration, SAXS patterns show a

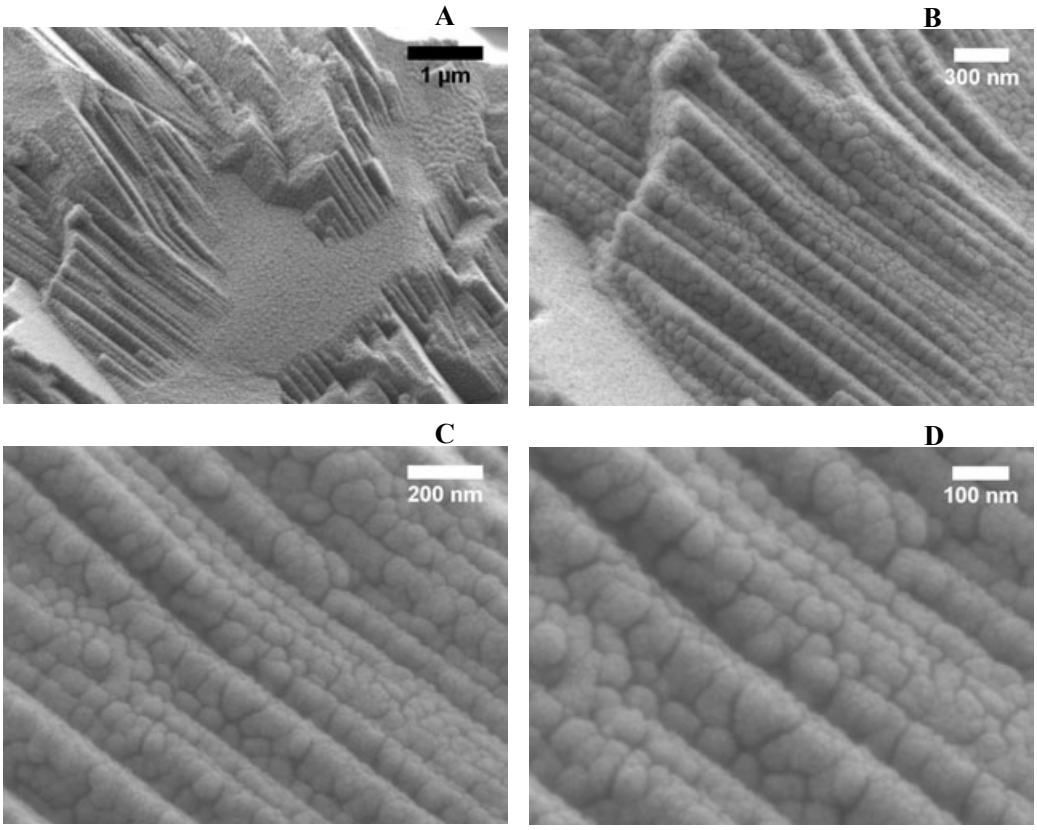

FIGURE 6.12: Cryo-SEM micrographs of hexagonal phase in the CPC-SHN2-Water system at α=1.75 and ϕ_s=60

broad peak whereas at higher salt concentrations an additional structure peak is found at about 5.5nm (Fig. 6.10B) .

6.4.3 UV-visible absorption spectroscopy studies

SHN2 is found to bind much more strongly to the micelles, and is less soluble in water. In order to quantify the relative variation of SHN2 concentration in the excess water part of the different phases, UV-visible absorption spectroscopy studies in the excess water part of the different phases were performed. SHN2 shows a strong absorption peak at around 292nm (Fig. 6.14A) and CPC shows three peaks at 253nm, 259nm and 265nm (Fig. 6.14B). UV spectroscopy studies were performed in the excess water part of the Hexagonal +excess water (H +excess water) phase (at α=1.75 and ϕ_s=10 and 15) and isotropic +excess water (I_2+excess

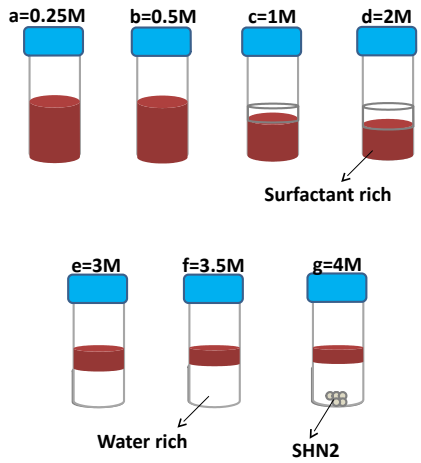

FIGURE 6.13: The different phases in CPC-SHN2-NaCl-water system at α=1.75, ϕ_s=20 and at T=30°C: I_2 phase at 0.25M (**a**), I_2 phase at 0.5M (**b**), isotropic phase floating at the top at 1M (**c**), isotropic phase floating at the top at 2M (**d**), I_2 phase floating at the top at 3M (**e**), I_2 phase floating at the top at 3.5M (**f**) and I_2 phase floating at the top at 4M with the excess SHN2 at the bottom (**g**).

water) phases (at α=1.75 and ϕ_s=19). A strong absorption peak at 292nm with comparable absorbance (Fig. 6.14C) is observed in all these system. The fact that the amount of excess water decreases with increasing ϕ_s, therefore confirms that the amount of SHN2 in the surfactant rich part increases with decreasing water content. Absorption peak corresponding to CPC which is characteristic of the micellar solution is not found, indicating that the concentration of micelles in the water rich part is not significant.

UV spectroscopy study was also performed at α=1.75 and ϕ_s=20 with varying salt (NaCl) concentration, in the excess water part. A strong absorption peak at 292nm which is characteristic of SHN2 is found (Fig. 6.14D) and absorption peak corresponding to CPC is not observed. The absorbance is found to decrease on increasing the salt (NaCl) concentration. The calculated amount of SHN2 is found to decrease in the water rich part with increasing the salt (NaCl) concentration which confirming that SHN2 concentration increases in the surfactant rich part with increasing salt (NaCl) concentration.

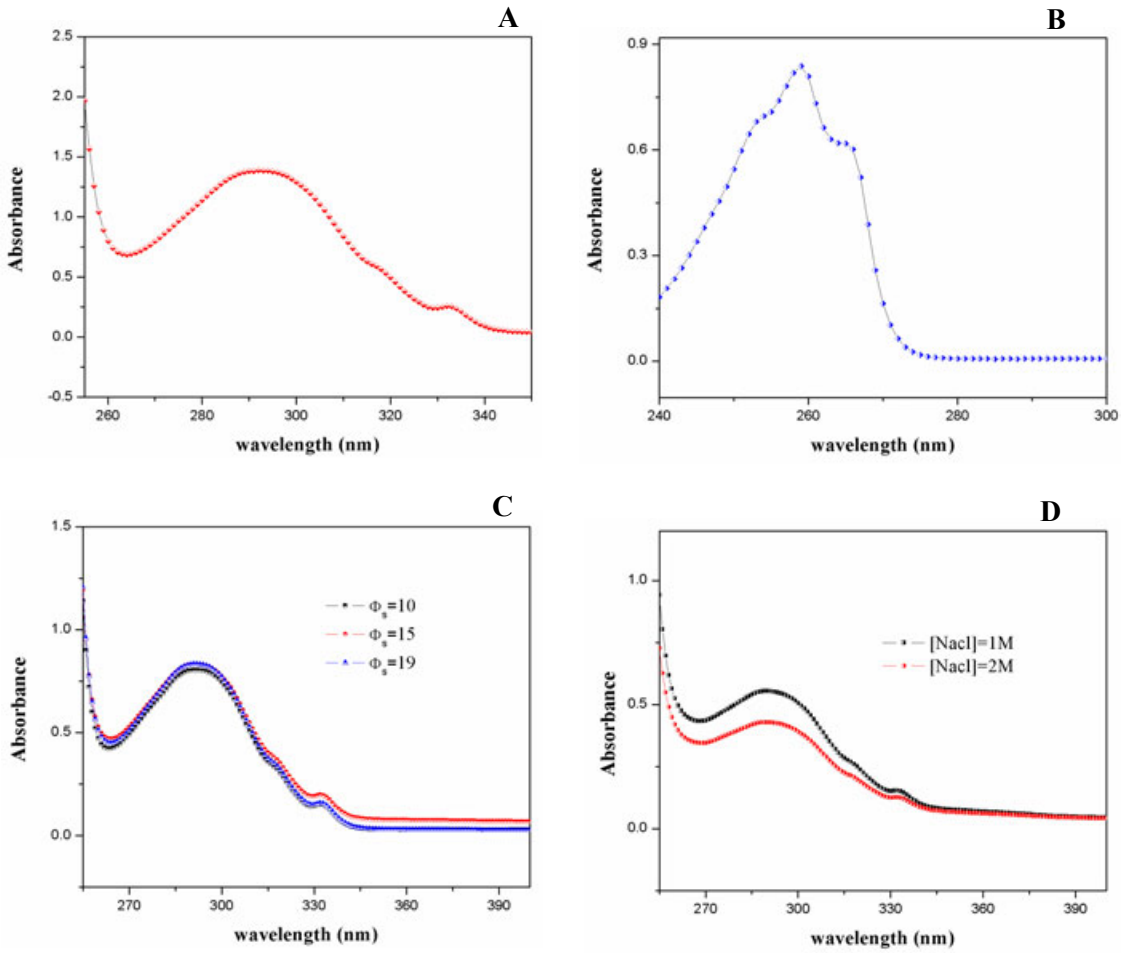

FIGURE 6.14: UV spectra of (**A**) 0.167mM aqueous solution of SHN2, (**B**) 0.174mM aqueous solution of CPC (**C**), water rich part of the CPC-SHN2-Water system at α=1.75 and ϕ_s=10, 15 and 19 and (**D**) water rich part of the CPC-SHN2-NaCl-Water system at α=1.75, ϕ_s=10 and [NaCl]=1M, and 2.

6.5 Discussion

6.5.1 Non-appearance of the lamellar (L_α) phase

In aqueous media, surfactant molecules self-assemble to form aggregates of different micro-structures and shapes depending on the composition, temperature and type of the amphiphile [48]. The aggregate geometry may be predicted on the basis of the packing of the surfactant molecules in the aggregate, usually expressed in terms of shape factor (p), which is defined as $\frac{v}{la}$, where v is the volume of the lipophilic chain having maximum effective length l, and a is the cross-sectional area

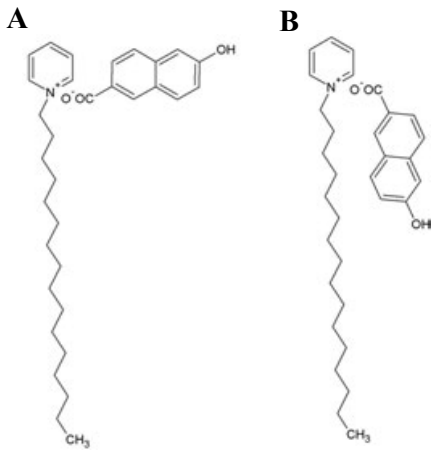

FIGURE 6.15: Schematic drawing of the proposed complexes of CPC and SHN2: (**A**) OH and naphthalene group at the hydrocarbon-water interface and (**B**) OH and naphthalene group in the hydrocarbon region.

of the head group at the interface. For $p \leq \frac{1}{3}$ spherical micelles, when $\frac{1}{3} \leq p \leq \frac{1}{2}$, cylinders, when $p \sim 1$ bilayers and for $p > 1$ inverted micelles are expected [48].

Strongly bound counterions, such as SHN or PTHC, can be considered as an extreme limit of an ionic amphiphile. Although, they do not self-assemble in water to form micelles, they prefer to anchor to the micelles and hence they modify the properties of the micelles-water interface [49]. Such molecules lead to a decrease in the spontaneous curvature of the interface and lead to the formation worm-like micelles (WLM) in many amphiphile systems. In some cases the decrease in spontaneous curvature is large enough to stabilize the bilayer [21].

Lamellar phase made up of bilayers has been seen in equimolar aqueous mixtures of CPC and SHN over an extended range of water content and similar behavior has been found with SHN1 [21]. This is reminiscent of the behavior of mixtures of cationic and anionic surfactants. But this behavior is not seen in the present case, though SHN, SHN1 and SHN2 are isomers. Equimolar aqueous mixtures of CPC and SHN2 form hexagonal phase in place of lamellar phase. This behavior can be understood in terms of shape factor (p).

These strongly bound counterions usually form a complex with the surfactant. In the present case two complexes are possible as shown in figure 6.15. The first one

has a tendency to form cylindrical micelles due to its bulky head group and bilayers are expected in the second case due to its smaller head group. The first case is more favorable, since both the hydrophilic groups are at the interface. As a result cylindrical micelles and hence hexagonal phase is seen at equimolar composition of SHN2 and CPC. In the case of SHN and SHN1, the OH group is at the ortho position. Hence they prefer to form a complex similar to that shown in figure 6.15B but with the OH group at the hydrocarbon-water interface leading to the formation of lamellar phase of bilayers at equimolar composition.

6.5.2 Isotropic Phases (I_1 and I_2)

At low SHN2 concentrations, a viscous isotropic (I_1) phase is found in the present system, indicating the presence of worm-like micelles. This I_1 phase is stable for $\alpha \leq 1$. But for $\alpha > 1$, another isotropic (I_2) phase is found, which is less viscous. SAXS patterns of the I_1 phase shows a broad peak whose position is found to shift towards higher q on decreasing the water content (Fig. 6.5A(a-c)), whereas, the I_2 phase exhibit a broad peak at higher water content and an additional structure peak is found to develop on decreasing the water content (Fig. 6.9A and 6.10A). The position of the structure peak is found to be unchanged on decreasing the water content. The possibility that the I_2 phase is made up of disc-like micelles can be ruled out since this system does not show the lamellar (L_α) phase. It has been seen in many worm-like systems that increasing the salt concentration leads to the formation of entangled linear micelles which transform to branched and multi-connected micellar networks with highly mobile and fluid connection, on further addition of salt. Since, the isotropic (I_2) phase, appears at high salt (SHN2) concentrations and also the fact that this phase is less viscous, indicate that I_2 could be made up of a branched and multi-connected networks of cylindrical micelles. However, we cannot rule out the possibility that this phase is made up of micelles of smaller size, because at higher salt concentration, net charge of the micelle might be reversed, which could lead to the reduction of the micellar size.

6.5.3 Branched and multi-connected network of cylindrical micelles

Branched and multi-connected network of cylinders has been observed in many system, at very high salt concentration, as evidenced by rheological measurements, light scattering techniques, and electron microcopy (EM) imaging [7–20]. Different experimental techniques have been used to deduce the structure of this phase such as, rheology, NMR [25], light scattering [9, 15, 16]. Cryogenic-transmission electron microscopy (cryo-TEM) studies have given direct visual evidence of its multiply connected cylindrical structure [19]. Low viscosity has been found in this phase. This is in fact reminiscent of the highly fluid L_3 (sponge) phase [50], which consist of multi-connected fluid membranes.

Generally, branched and multi-connected cylindrical network appears in the water rich region of the phase diagram. In the present system, branched and muti-connected network appears just above the equimolar concentration (Fig. 6.3D) at low water content and is found to be more stable at higher SHN2 concentration in a wide range of water content (Fig. 6.3).

SAXS pattern of this phase (I_2) shows a broad peak and an additional structure peak is found to develop with decreasing water content which becomes to sharp peaks in the hexagonal (H) phase at lower water content (Figs. 6.8A and 6.9A). Positions of the structure peak of the I_2 phase and the hexagonal phase are found to be identical. Hexagonal phase is found to transform to this phase at higher temperatures (Figs. 6.8B and 6.9B). So, this phase can be considered as a molten hexagonal phase.

6.5.4 Phase transitions

6.5.4.1 From I_1 to I_2

Present investigations have revealed the following transition sequence from I_1 to I_2 in the CPC-SHN2-Water system at ϕ_s=20 (Fig. 6.3D):

$I_1 \rightarrow I_1$+excess water $\rightarrow$ H +excess water $\rightarrow I_2$+excess water $\rightarrow I_2$ as function of increasing counterion concentration.

Relative amounts of excess water increase up to a maximum in the H +excess water coexistence region on increasing the SHN2 concentration and then decrease and finally disappear in the I_2 phase on further addition of SHN2. Apparent viscosity of the surfactant rich phase also increases up to a maximum in the hexagonal phase of the H +excess water and then decreases on increasing SHN2 concentration. SAXS profile (Fig. 6.5A(a)) and apparent high viscosity suggests that the isotropic phase at low concentration of SHN2 is made up of worm-like micelles. The observed phase sequence can be explained as follows. Addition of very low amounts of SHN2 to CPC, transforms the spherical micelles of CPC to worm-like micelles and leads to the formation of a viscous isotropic phase (Fig. 6.16A). Further addition of SHN2, leads to additional growth of the micelles. The $\pi-\pi$ interactions between counterions ($HN2^-$) as well as interactions between the counterions and the cationic head-groups, mediated by the $HN2^-$ counterions embedded within the micelles, become dominant and lead to attractive interaction between the worm-like micelles. This attractive interaction, gives rise to phase separation and the formation of a isotropic phase with excess water (I_1+excess water). Micelles become longer, on further addition of SHN2 and lead to the formation of hexagonal phase with excess water (H +excess water) (Fig. 6.16B). Further addition of SHN2, can lead to either shorting of the micelles or their branching. Micelles of shorter length would be expected to show a uniform dispersion. Phase separation found in this case, therefore, leads us to believe that addition of SHN2 gives rise to branched micelles. Formation of branched micelles destroys positional order of the hexagonal phase, resulting in the isotropic phase with excess water (I_2+excess water) (Fig. 6.16C). Disappearance of excess water and swelling of the I_2 phase might result from the osmotic pressure due to a non-uniform distribution of salt (Fig. 6.16D). So, this sequence of phases suggests a gradual changes in the inter-micellar interaction and in the branching density of the worm-like micelles with increasing concentration of the counterion.(Fig. 6.16).

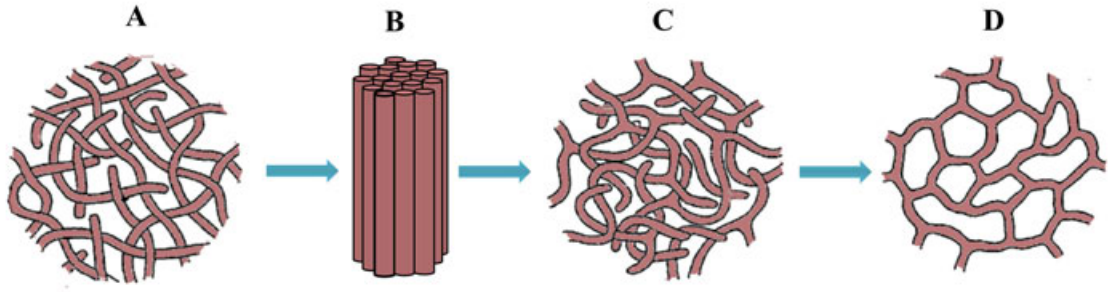

FIGURE 6.16: Schematic drawing of the proposed changes in the CPC aggregate topology with increasing SHN2 concentration (from ref. [11]).

6.5.4.2 Re-entrance of the hexagonal phase

Present investigations have revealed the following transition sequence in the CPC-SHN2-Water system at α 1.2 (Fig. 6.2D) and 1.75 (Figs. 6.3A and B):

H +excess water $\rightarrow$ I_2+excess water $\rightarrow$ I_2 $\rightarrow$ H as a function of increasing ϕ_s.

Relative amount of excess water is found to decreased from H +excess water region to I_2+excess water region and finally disappears in the I_2 phase. The observed transition sequence H +excess water $\rightarrow$ I_2+excess water $\rightarrow$ I_2 can be understood as in the previous case. On increasing ϕ_s, the amount of SHN2 in the micelles increases as confirmed by UV results discussed in section 6.4.3. This helps to melt the hexagonal phase, by inducing the formation of branching and gives rise to I_2 phase. We believe that confinement leads to the I_2 $\rightarrow$ H transition at low water content, due to free energy penalty for branching.

Addition of Salt (NaCl) in the I_2 phase at higher water content is found to induce the phase separation as shown in figure 6.13. However, we have not understood this salt driven phase separation. Further work is needed to clarify this situation.

6.6 Conclusion

The influence of the strongly bound anionic counterion $HN2^-$ on the phase behavior of concentrated aqueous solutions of the cationic surfactant CPC was studied using x-ray diffraction, polarizing optical microscopy and cryo-SEM techniques. At high amounts of SHN2, a low viscous isotropic (I_2) phase is observed. We have seen a transition from I_1 to I_2 through the hexagonal phase. We believe that this I_2 phase is made up of cylindrical micelles similar to seen in the dilute solution of worm-like micelles. Interestingly, on reducing the water content this phase transform into a hexagonal phase. We believe that this is due to confinement similar to the situation as described in chapter 2 for the bilayer forming system. The phase behavior of the surfactant systems mentioned above provides some understanding of the conditions that favor the formation of I_2 phase. On increasing the concentration of the counterion the isotropic (I_1) phase of CPC is found to show the following sequence of transformations: $I_1 \rightarrow I_1$+excess water $\rightarrow$ H +excess water $\rightarrow I_2$+excess water $\rightarrow I_2$. This sequence of phases suggests gradual changes in the inter-micellar interaction and in the branching density of the worm-like micelles with increasing concentration of the counterion.

Bibliography

[1] V. Degiorgio and M. Corti, in Physics of Amphiphiles: *Micelles, Vesicles and Microemulsions*, elsevier scientific publishing company, inc., New York (1985).

[2] M. E. Cates and S. F. Candau, *J. Phys. Condens. Matter*, **2**, 6969 (1990).

[3] H. Rehage and H Hoffmann, *Mol. Phys.*, **74**, 933 (1991).

[4] J. F. Berret, in Molecular Gels: *Rheology of wormlike micelles: Equilibrium properties and shear banding transitions*, eds. R. G. Weiss, P. Terech, Springer, Dordrecht, The Netherlands, pp 667720 (2006).

[5] S. R. Raghavan, *Langmuir*, **17**, 300 (2001).

[6] M. E. Cates, *Macromolecules*, **20**, 2289 (1987).

[7] E. Cappelaere and R. Cressely, *Colloid Polym. Sci.*, **276**, 1050 (1998).

[8] G. Porte, R. Gomati, O. E. Haitami, J. Appell and J. J. Marignan, *J. Phys. Chem.*, **90(22)**, 5746 (1986).

[9] J. Appell, G. Porte, A. Khatory, A. Kern and S. J. Candau, *J. Phys. II*, **2(5)**, 1045 (1992).

[10] A. Khatory, et al., *Langmuir*, **9(4)**, 933 (1993).

[11] S. J. Candau, A. Khatory, F. Lequeux and F. Kern, *J. Phys. IV*, **3(C1)**, 197 (1993).

[12] T. Shikata, H. Hirata, T. Kotaka, *Langmuir*, **4(2)**, 354 (1988).

[13] E. Cappelaere, R. Cressely, *Rheologica Acta.*, **39(4)**, 346 (2000).

[14] I. A. Kadoma and J. W. van Egmond, *Phys. Rev. Lett.*, **76(23)**, 4432 (1996).

[15] I. A. Kadoma, C. Ylitalo and J. W. van Egmond, *Rheologica Acta.*, **36(1)**, 1 (1997).

[16] I. A. Kadoma and J. W. van Egmond, *Langmuir*, **13(17)**, 4551 (1997).

[17] B. A. Schubert, E. W. Kaler and N. J. Wagner, *Langmuir*, **19(10)**, 4079 (2003).

[18] C. Oelschlaeger, G. Waton and S. J. Candau, *Langmuir*, **19(25)**, 10495 (2003).

[19] V. Croce, T. Cosgrove, G. Maitland, T. Hughes and G. Karlsson, *Langmuir*, **19(20)**, 8536 (2003).

[20] C. Oelschlaeger, M. Schopferer, F. Scheffold and N. Willenbacher, *Langmuir*, **25(2)**, 716 (2009).

[21] S. P. Gupta and V. A. Raghunathan, *Phys. Rev. E*, **88**, 012503 (2013).

[22] R. Gomati, J. Appell, P. Bassereau, J. Marignan and G. Porte, *J. Phys. Chem*, **91**, 6203 (1987).

[23] K. Maitia, S. C. Bhattacharyaa, S. P. Moulika and A. K. Panda*Colloids and Surfaces A: Physicochem. Eng. Aspects*, **355**, 88 (2010).

[24] L. Abezgauz, K. Kuperkar, P. A. Hassan, O. Ramon, P. Bahadur and D. Danino, *J. Colloid and Interface Sci.*, **342**, 83 (2010).

[25] U. Olsson, O. Soderman and p. Gudringt, *J. Phys. Chem.*, **90(21)**, 5223 (1986).

[26] Z. Wang Z and R. G. Larson, *J. Phys. Chem. B*, **113(42)**, 13697 (2009).

[27] S. J. Candau, E. Hirsch, R. Zana and M. Adam, *J. Colloid and Interface Sci.*, **122**, 430 (1988).

[28] P. Debye and E. W. Anacker, *J. Phys. Colloid Chem.*, **55**, 644 (1950).

[29] F. Quirion and L. J. Magid, *J. Phys. Chem.*, **90**, 5435 (1986).

[30] H. Hoffmann and H. Rehage, *J. Phys. Chem.*, **92**, 4712 (1988).

[31] K. Nakamura and T. Shikata, *Langmuir*, **22**, 9853 (2006).

[32] F. R. Husson and V. Luzzati, *J. Phys. Chem.*, **68**, 3504 (1964).

[33] P. Ekwall, L. Mandell and P. Solyom, *J. Colloid Interface Sci.*, **35**, 519 (1971).

[34] E. Buhler, E. Mendes, P. Boltenhagen, J. P. Munch, R. Zana and S. J. Candau, *Langmuir*, **13**, 3096 (1997).

[35] C. Oelschlaeger, G. Waton, S. J. Candau and M. E. Cates, *Langmuir*, **18**, 7265 (2002).

[36] A. Bernheim-Groswasser, R. Zana and Y. Talmon, *J. Phys. Chem. B*, **104**, 4005 (2000).

[37] R. Oda, I. Huc, J. C. Homo, B. Heinrich, M. Schmutz and S. Candau, *Langmuir*, **15**, 2384 (1999).

[38] H. Hoffmann, A. Rauschera, M. Gradzielski and S. F. Schulz, *Langmuir*, **8**, 2140 (1992).

[39] S. Bucci, C. Fagotti, V. Degiorgio and R. Piazza, *Langmuir*, **7**, 824 (1991).

[40] J. Penfold, E. Staples and I. Tucker, *J. Phys. Chem. B*, **106**, 8891 (2002).

[41] S. R. Raghavan, G. Fritz and E. W. Kaler, *Langmuir*, **18**, 3797,(2002).

[42] P. Schurtenberger and C. Cavaco, *J. Phys. II*, **3**, 1279 (1993).

[43] Y. A. Shchipunov, *Colloids Surf., A*, **183**, 541 (2001).

[44] Y. Y. Won, H. T. Davis and F. S. Bates, *Science*, **283**, 960 (1999).

[45] I. W. Hamley, J. S. Pedersen, C. Booth and V. M. Nace, *Langmuir*, **17**, 6386 (2001).

[46] M. Vasudevan, et al., *Nat. Mater*, **9(5)**, 436 (2010).

[47] J. J. Cardiela, A. C. Dohnalkovab, N. Dubasha, Ya Zhaoa, P. Cheunga, and A. Q. Shena, *PNAS*, **110**, E1653 (2013).

[48] J. Israelachvili, *Intermolecular and Surface Forces*, 2nd edition, Academic Press, London (1991).

[49] P. A. Hassan, S. R. Raghavan and E. W. Kaler, *Langmuir*, **18**, 2543 (2002).

[50] M. Cates, D. Roux, D. Andelman, S. C. Milne and S. Safran, *Europhys. Lett.*, **5**, 733 (1988).

Chapter 7

Phase behavior of the SDS-PTHC-Water system and effect of chirality on the phase behavior

7.1 Introduction

Hydrotropes are a class of amphiphilic molecules that cannot form well organized structures, such as micelles, in water but do increase the aqueous solubility of organic molecules. When such molecules, combine with surfactants, they decrease the spontaneous curvature of the micellar surface leading to the formation of long worm-like micelles (WLM) [1]. At higher concentrations, they first promote the formation of entangled linear micelles and then branched and multi-connected micellar networks [1, 2].

In this chapter, we describe the influence of a hydrotrope p-toluidine hydrochloride (PTHC), on the phase behavior of the anionic surfactant sodium dodecyl sulfate (SDS). Earlier studies on similar systems are described in section 7.2. A short description of chemicals used is given in section 7.3. Experimental results are

described in section 7.4. Phase behavior of SDS-PTHC-Water system is studied at various molar ratio (α) of PTHC to SDS. This system is found to exhibit- isotropic, nematic, hexagonal, lamellar and cubic phases. At $\alpha > 0.14$ the phase diagrams is dominated by the lamellar phase. Two nematic phases are also observed, with the one at lower values of α consisting of cylindrical micelles (N_c) and the other seen at higher values of α being made up of disc-like micelles (N_d). At α=0.14, N_c and N_d phases are found at higher and at lower water content, respectively. A possible transition between the nematic and hexagonal phases via the hexatic phase is found at α=0.1 and ϕ_s=40. Detailed discussion of our results is given in section 7.5, and the conclusions that can be drawn from this study are given in section 7.6.

7.2 Earlier Studies

Detailed phase behavior of aqueous solutions of sodium dodecylsulfate (SDS) is reported in the literature by kekchif [3]. It exhibits an isotropic phase of rod like micelles at room temperature up to a surfactant concentrations of ∼35 wt%. 2D hexagonal phase is observed in a wide range of intermediate concentration. At very high surfactant concentrations a lamellar phase has been found. A variety of intermediate phases, such as ribbon, ordered mesh and bicontinuous cubic, are found in between the lamellar and hexagonal phases in narrow range of composition.

Effect of strongly bound counterions on the growth of SDS micelles has been studied by Hassan and co-workers [4, 5]. NMR studies of these system reveal that p-toluidine hydrochloride (PTHC) has a strong affinity to sit at the water-hydrocarbon interface, reducing its spontaneous curvature and leading to the growth of cylindrical micelles. Growth of the micelle is found to be very sensitive to the position of the methyl substituent in the benzene ring of the aromatic salt. p-toluidine hydrochloride (PTHC) and m-toluidine hydrochloride (MTHC) induce much longer micelles than aniline hydrochloride (AHC) and o-toluidine

hydrochloride (OTHC) at similar salt concentrations [6], which is confirmed by dynamic light scattering (DLS) studies.

An unusual phase sequence (hexagonal → nematic → isotropic → nematic → lamellar) has been reported in the SDS-PTHC-Water system with increasing PTHC concentration [7] and this sequence of phases has been understood in-terms of a gradual prolate to oblate change in the aggregate morphology with increasing counterion concentration. A possible nematic to hexatic to hexagonal phase transition has also been observed this system [8].

7.3 Experimental

Sodium dodecyl sulfate (SDS), p-toluidine hydrochloride (PTHC) and cholesterol were purchased from Sigma-Aldrich. The chemical structures of the molecules are shown in figure 7.1.

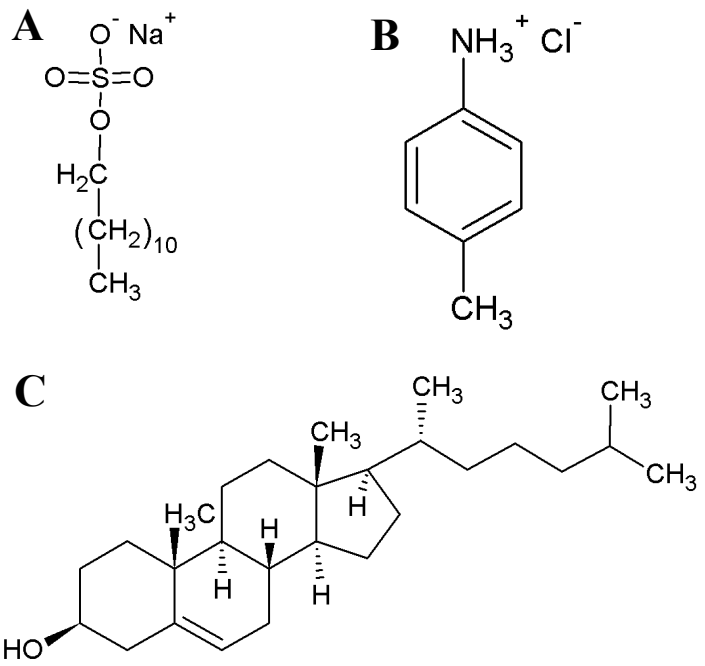

FIGURE 7.1: Chemical structures of Sodium dodecyl sulfate (SDS) (**A**), p-toluidine hydrochloride (PTHC) (**B**) and cholesterol (**C**)

7.4 Results

7.4.1 SDS-PTHC-Water system

The phase behavior of mixtures of SDS and PTHC were studied at different values of the molar ratio (α=$\frac{[SDS]}{[PTHC]}$) of the two components. For each α, the total concentration of the non-aqueous components ($\phi_s = \frac{(SDS+PTHC)}{(SDS+PTHC+Water)}$x100) was varied from 20 to 60wt%.

7.4.1.1 Phase behavior at α=0.05

Figure 7.2A, shows the temperature−ϕ_s phase diagram of the SDS-PTHC-Water system at α=0.05. For 20≤ ϕ_s ≤30, a viscoelastic isotropic phase is found which exhibits flow birefringence. At low ϕ_s, diffraction pattern of isotropic (I) phase shows a broad peak (Fig. 7.3A). At ϕ_s=32.5 a nematic phase is found over the temperature range studied. It exhibits schlieren texture under crossed polarizers (Fig. 7.4A). For 35≤ ϕ_s ≤40, at low temperatures, nematic phase is found, which goes into hexagonal phase at higher temperatures, on heating via a two phase region. Diffraction pattern in the hexagonal phase shows two peaks with corresponding d-spacings in the ratio 1:1/$\sqrt{3}$ (similar to figure 7.5B) and fan-like texture is found under the microscope (Fig. 7.4B). For 45≤ ϕ_s ≤55, the hexagonal (H) phase is found over the temperatures range studied. Figure 7.3B shows the variation of the lattice parameter (d) of the H phase with ϕ_s. It is found to be described by the relation (d∼ ϕ_v^{-s}) with s∼0.5, where ϕ_v is the volume fraction of the non-aqueous component estimated from ϕ_s, using the densities of the components. Densities of SDS, PTHC and water have been taken as 1.010, 1.167 and 1.000g/cm^3 to calculate ϕ_v. For 57.5≤ ϕ_s ≤60, at low temperatures, a crystalline phase is found which transforms into an optically isotropic phase, on heating. Diffraction pattern of this isotropic phase shows four peaks in the small angle region (Fig. 7.5A) with their wave vector (q) in the ratio $\sqrt{6}$:$\sqrt{8}$:$\sqrt{10}$:$\sqrt{22}$, which could be indexed on a cubic lattice of space group Pn3m (Tab. 7.1). This cubic (Q) phase transforms into

the hexagonal phase at higher temperatures on heating. This hexagonal phase is similar to that observed at low ϕ_s, and its diffraction pattern consists of two peaks in small q region with their q in the ratio 1:$\sqrt{3}$ which correspond to reflections from the (1 0) and (1 1) planes of the hexagonal lattice (Fig. 7.5B). Hexagonal phase is found over a wide range of water content. Variation of lattice parameters of the different phases with increasing ϕ_s is given in table 7.2.

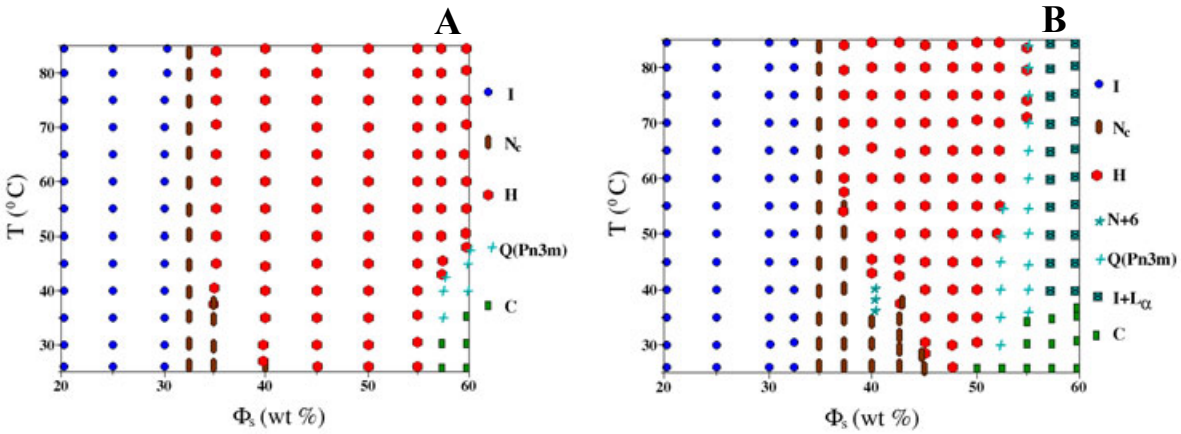

FIGURE 7.2: Partial phase diagrams of the SDS-PTHC-Water system at (**A**) α=0.05 and (**B**) α=0.1. I, N, N+6, H, Q(Pn3m), Lα and C, denote the isotropic, nematic, hexatic, hexagonal, cubic (Pn3m), lamellar and crystalline phases, respectively.

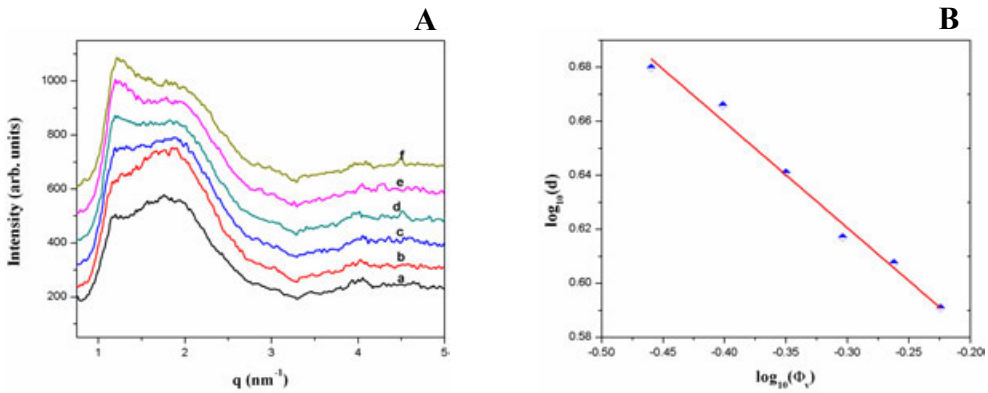

FIGURE 7.3: X-ray diffraction patterns of the isotropic phases (**A**) at α=0.05, ϕ_s=20 and corresponding to T=30°C (**a**), T=40°C (**b**), T=50°C (**c**), T=60°C (**d**), T=70°C (**e**) and T=80°C (**f**) in the SDS-PTHC-Water. (**B**) Variation of the lattice parameters of the Hexagonal phase in the SDS-PTHC-Water system at α=0.05.

TABLE 7.1: X-ray diffraction data from the cubic phase of the SDS-PTHC-water system at $\alpha = 0.05$, $\phi_s = 60$ and T= 40°C and T= 45°C, indexed on a cubic lattice corresponding to the space group Pn3m. The calculated spacings (d_c) are obtained from the relation $1/d^2 = (h^2 + k^2 + l^2)/a^2$, with $a = 11.36$nm and $a = 10.95$nm respectively.

T(°C)	d_o(nm)	d_c(nm)	(hkl)	Intensity
40	4.66	4.64	(211)	32
	3.98	4.02	(220)	20
	3.58	3.59	(310)	100
	2.42	2.42	(332)	0.6
45	4.49	4.47	(211)	32
	3.99	3.71	(220)	42
	3.63	3.65	(300)	100

TABLE 7.2: The lattice parameters and polarizing optical microscopy textures of the different phases in SDS-PTHC-water system at α=0.05 and T=30°C.

ϕ_s	d_1(nm)	d_2(nm)	POM texture	Phase	Lattice parameter (nm)
25	4.90	–	Isotropic	I	–
30	4.88	–	Isotropic	I	–
35	4.87	–	Schlieren texture	N_c	–
40	4.76	2.75	Fan-like texture	H	5.50
45	4.56	2.63	Fan-like texture	H	5.27
50	4.14	2.39	Fan-like texture	H	4.78

7.4.1.2 Phase behavior at α=0.1

At α=0.1, the phase behavior is very similar to that observed at α=0.05 (Fig. 7.2B). At low values of ϕ_s, a flow-birefringent isotropic and nematic phases observed (For 20$\leq \phi_s \leq$35). However, phase behavior at higher ϕ_s is slightly different. At ϕ_s=37.5, a nematic phase is found at low temperatures which goes to the hexagonal phase on increasing the temperature via a two phase region. At ϕ_s=40, also a nematic phase is observed at low temperatures, which seems to transform into a hexagonal at higher temperatures on heating via an intermediate hexatic phase. For 42.5$\leq \phi_s \leq$45, a nematic phase found at low temperatures, goes to hexagonal phase on heating via a two phase region. This hexagonal phase shows striated fan-like texture (Fig. 7.4C). At ϕ_s=47.5, a hexagonal phase is found over

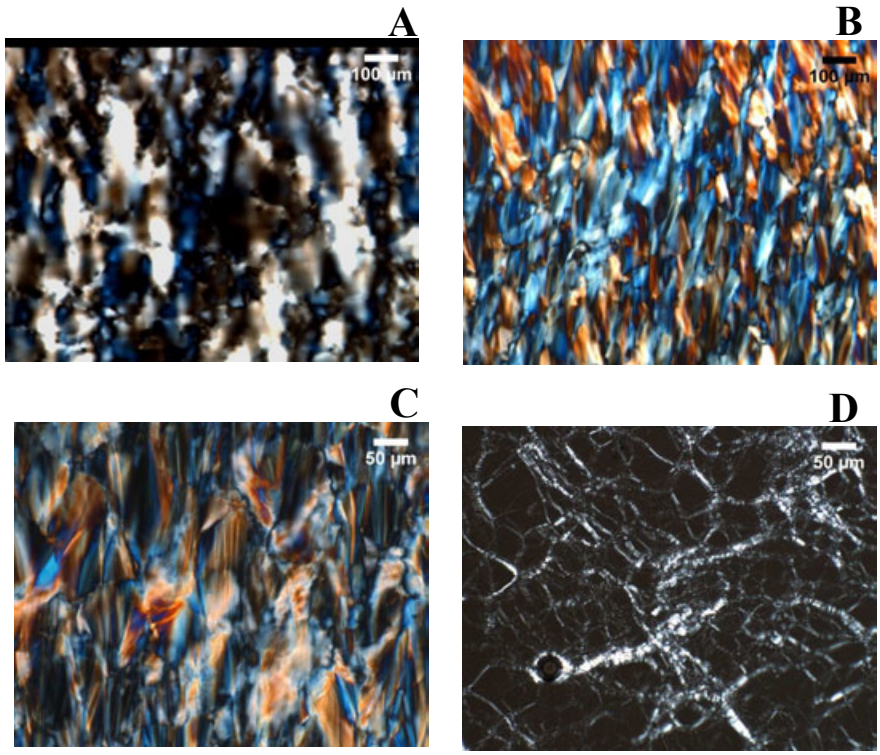

FIGURE 7.4: POM textures of (**A**) nematic phase at α=0.05, ϕ_s=32.5 and T=30°C, (**B**) hexagonal phase at α=0.05, ϕ_s=40 and T=70°C, (**C**) hexagonal phase at α=0.1, ϕ_s=42 and T=45°C and (**D**) I+Lα phase at α=0.1, ϕ_s=60 and T=60°C in the SDS-PTHC-Water system.

the temperatures range studied. At ϕ_s=50, phase behavior is similar to that observed at ϕ_s=47.5, except at low temperature a crystalline phase is found. The concentration range of the hexagonal phase is considerably reduced compared to that observed at α=0.05. Lattice spacings of hexagonal and other phases are given in table 7.3. At ϕ_s=52.5, a crystalline phase is found at low temperatures, which first transforms into a cubic phase then into a hexagonal phase on heating. However, at ϕ_s=55, a cubic phase is found to coexist with hexagonal phase at higher temperatures. Cubic phase shows six reflections (Fig. 7.5C) in the small angle region, with their q in the ratio $\sqrt{6}$:$\sqrt{8}$:$\sqrt{9}$:$\sqrt{10}$:$\sqrt{10}$:$\sqrt{12}$:$\sqrt{16}$, which could be indexed on a cubic lattice of space group Pn3m (Tab. 7.4). Lattice constant (a) of the cubic phase is found to decrease on increasing the temperature (Tab. 7.5). For 57.5$\leq \phi_s \leq$60, a crystalline phase coexisting with excess solvent is observed at low temperatures, which goes to a lamellar phase coexisting with excess solvent on

heating. This lamellar phase exhibits typical oily streak texture under POM (Fig. 7.4D) and its diffraction pattern shows two peaks with corresponding d-spacings in ratio 1:1/2 (Fig. 7.5D and Tab.7.3).

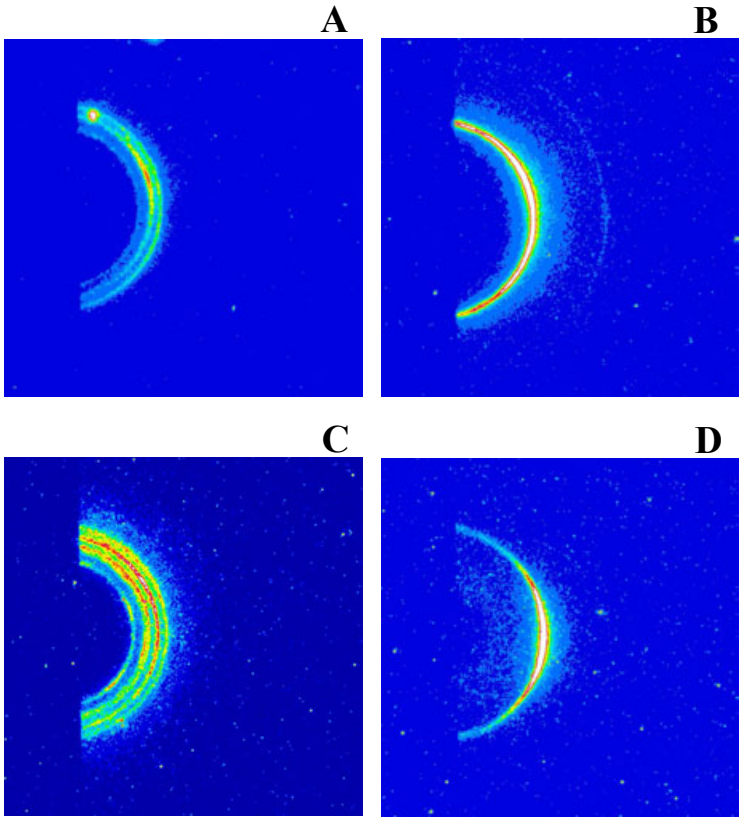

FIGURE 7.5: 2D-X-ray diffraction patterns of (**A**) cubic phase at α=0.05, ϕ_s=60 and T=40°C, (**B**) hexagonal phase at α=0.05, ϕ_s=60 and T=70°C, (**C**) cubic phase at α=0.1, ϕ_s=55 and T=40°C and (**D**) I+Lα phase at α=0.1, ϕ_s=60 and T=60°C in the SDS-PTHC-Water system.

7.4.1.3 Phase behavior at α=0.14

Figure 7.6, shows temperature−ϕ_s phase diagram of the SDS-PTHC-Water system at α=0.14. For 20≤ ϕ_s ≤35, sample is viscous and exhibits an isotropic phase, which shows birefringence under shear. Small angle x-ray scattering (SAXS) pattern at low ϕ_s shows a broad peak, which is very similar to that found in the isotropic phases at α=0.05 and 0.1 (Fig. 7.3A(a)). At ϕ_s=37.5, sample is viscous and translucent, and shows an isotropic phase at low temperatures. This isotropic phase exhibits flow birefringence and first goes into a nematic phase via a two

TABLE 7.3: The lattice parameters and polarizing optical microscopy textures of the different phases in SDS-PTHC-water system at α=0.10 and T=50°C.

ϕ_s	d_1(nm)	d_2(nm)	d_3(nm)	POM texture	Phase	Lattice parameter
20	diffuse broad peak	–	–	Isotropic	I	–
25	4.99	–	–	Isotropic	I	–
30	4.93	–	–	Isotropic	I	–
35	4.79	–	–	Schlieren texture	N_c	–
40	4.67	2.69	2.33	Fan-like texture	H	5.39
45	4.39	2.53	2.19	Fan-like texture	H	5.07
50	4.26	2.46	2.13	Fan-like texture	H	4.92
60	3.61	1.81	–	Oily streak texture	I+L_α	–

TABLE 7.4: X-ray diffraction data from the cubic phase of the SDS-PTHC-water system at α = 0.1, ϕ_s = 55 and T= 45°C, indexed on a cubic lattice corresponding to the space group Pn3m. The calculated spacings (d_c) are obtained from the relation $1/d^2 = (h^2 + k^2 + l^2)/a^2$, with a = 12.60nm.

d_o(nm)	d_c(nm)	(hkl)	Intensity
5.14	5.14	(211)	45
4.45	4.45	(220)	58
4.23	4.20	(300)	100
3.94	3.98	(310)	75
3.61	3.64	(222)	49
3.14	3.15	(400)	15

TABLE 7.5: Variation of lattice parameter of the cubic phase in SDS-PTHC-Water system at α=0.1.

ϕ_s=**52.5**		ϕ_s=**55**	
T(^{0}C)	**a(nm)**	**T(°C)**	**a(nm)**
30	13.29	40	12.71
35	12.89	45	12.60
40	12.79	50	12.34
45	12.64	55	12.15
–	–	60	12.03
–	–	65	11.92

phase region and then transforms into hexagonal phase via two phase region, on heating. This nematic phase is viscous and shows schlieren texture (Fig. 7.7A) under the microscope. Fan-like texture is observed under POM in the hexagonal phase (Fig. 7.7B). Behavior at ϕ_s=40 is similar to that observed at ϕ_s=37.5. However, isotropic to nematic and nematic to hexagonal transition temperatures are found to be lower than the corresponding transition temperatures at ϕ_s=37.5.

SAXS pattern of isotropic shows a diffuse broad ring, a slightly less diffuse ring is found in the nematic phase and hexagonal phase exhibits two sharp peaks in the small q region with their respective d-spacings in the ratio 1:1/$\sqrt{}$(3) (Figs. 7.8A-C respectively, Tabs. 7.6 and 7.7). Yet, at ϕ_s=42.5, a low viscous isotropic phase is found which does not show flow birefringence. This isotropic phase transforms into a nematic phase via a two phase region, with the transition temperature higher than that at ϕ_s=40. On further increasing the temperature, nematic phase goes to hexagonal phase via a two phase region. At ϕ_s=45, a low viscous isotropic phase is found at low temperatures, which transforms into a hexagonal phase on heating; the nematic phase is not found. At ϕ_s=47.5, at low temperatures, a low viscous nematic phase is found. Typical schlieren texture is found under the microscope. Texture contains large pseudo-isotropic patches where the nematic director aligns perpendicular to the substrate (Fig. 7.7C). This phase first goes to an isotropic phase via a two phase region and then transforms into a hexagonal phase at higher temperatures (Tab. 7.7). At ϕ_s=50, a nematic phase is found at low temperatures, which is similar to that observed at ϕ_s=47.5. This nematic phase transforms into an isotropic phase at higher temperatures. For 55$\leq$ ϕ_s $\leq$60, a lamellar phase is found to coexist with an isotropic phase over the temperature range studied except at low temperatures and higher ϕ_s, where a crystalline phase coexisting with excess solvent is found which transform into lamellar phase coexisting with excess solvent, on heating. The diffraction pattern of the lamellar shows two sharp peaks with the corresponding spacings in the ratio 1: 1/2 (Tab. 7.6 and 7.7) and oily streaks texture is found under microscope (Fig. 7.7D).

7.4.1.4 Phase behavior at α=0.175

At low surfactant concentrations (ϕ_s $\leq$40) an isotropic phase is found which does not show flow birefringence (Fig. 7.9A) and its apparent viscosity is low. SAXS pattern shows a broad peak at higher water content. However, an additional broad peak is found to develop on decreasing the water content (Fig. 7.10A(a-c)) and also with increasing the temperature. On increasing ϕ_s (at 42.5 and 45) a nematic phase appears which shows the typical schlieren texture under the microscope.

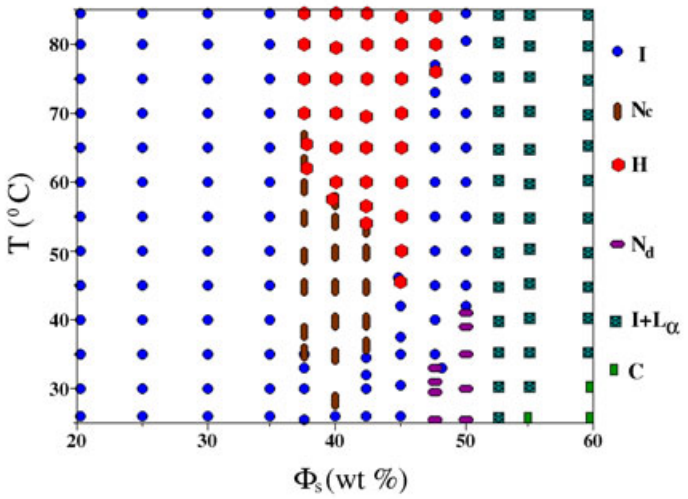

FIGURE 7.6: Partial phase diagram of the SDS-PTHC-Water system at α=0.14. I, N, H, Lα and C, denote the isotropic, nematic, hexagonal, lamellar and crystalline phases, respectively.

TABLE 7.6: The d-spacings and polarizing optical microscopy textures of the different phases in SDS-PTHC-water system at α=0.14 and T=35°C.

ϕ_s	d_1(nm)	d_2(nm)	POM texture	Phase
25	diffuse broad peak	–	Isotropic	I
30	4.72	–	Isotropic	I
35	4.69	–	Isotropic	I
40	4.68	–	Schlieren texture	N_c
45	4.42	–	Isotropic	I
50	4.03	–	Schlieren texture	N_d
55	3.90	1.95	Oily streak texture	I+L_α
60	3.66	1.84	Oily streak texture	I+L_α

The texture contains large pseudo-isotropic patches where the nematic director aligns perpendicular to the substrate (Fig. 7.11A). Its SAXS pattern shows two broad peaks, with their q in the ratio 1:2 (Figs. 7.10A(d) and 7.12A). This phase goes to an isotropic phase through a two phases region, on heating. On further increasing ϕ_s,(46.98 $\leq \phi_s \leq$52.5) at low temperatures, a turbid solution is found, which shows the oily streak texture characteristic of a lamellar phase (Fig. 7.11B). This lamellar phase coexists with excess solvent. The coexistence of the lamellar and isotropic phases is found over a wide range of surfactant concentrations. The

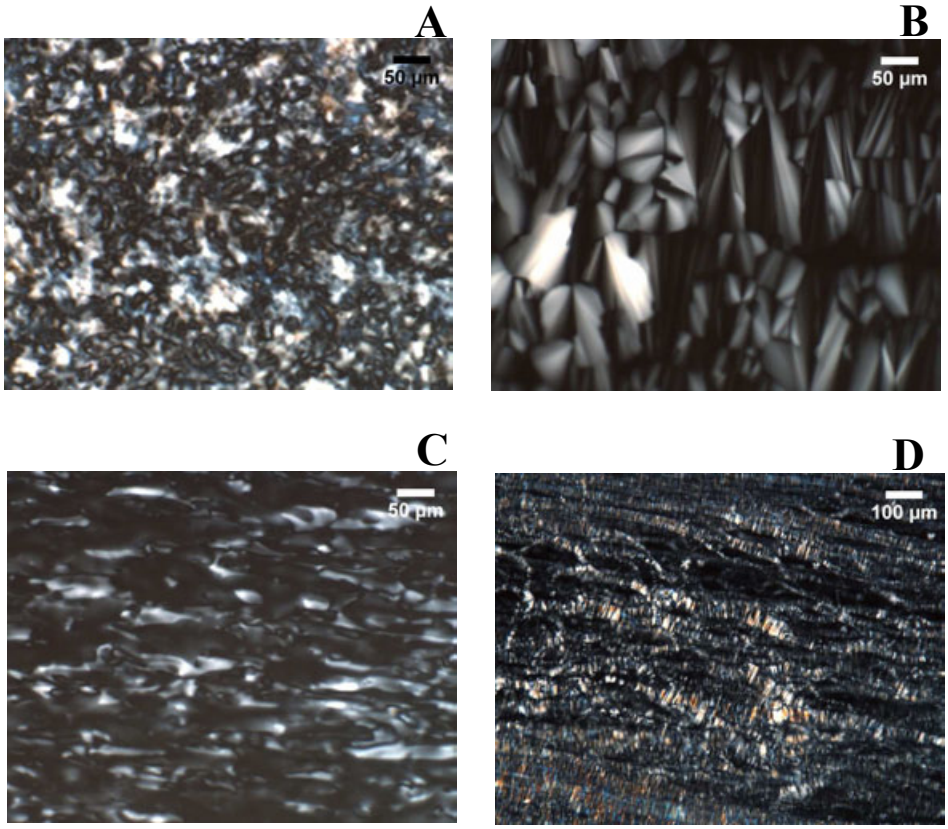

FIGURE 7.7: POM textures of (**A**) nematic (N_c) phase at α=0.14, ϕ_s=37.5 and T=54°C, (**B**) hexagonal phase at α=0.14, ϕ_s=37.5 and T=80°C, (**C**) nematic (N_d) phase at α=0.14, ϕ_s=47.5 and T=25°C and (**D**) I+Lα phase at α=0.14, ϕ_s=55 and T=44°C in the SDS-PTHC-Water system.

lamellar phase first transforms into a nematic and then to an isotropic phase on heating at ϕ_s=46.98. Nematic phase exhibits schlieren texture characteristic of this phase (Fig. 7.11C). For 55 $\leq$ ϕ_s $\leq$60, at low temperatures, a crystalline phase coexisting with excess water is found, which transforms to a lamellar phase coexisting with excess solvent, at higher temperatures. Lamellar phase shows two sharp peaks with the corresponding spacings in the ratio 1: 1/2 (Fig. 7.12B and Tab. 7.8)

7.4.1.5 Phase behavior at α=0.22

Phase behavior at α=0.22 is very similar to that observed at α=0.175. But the phase boundaries are found to shift towards higher water content (Fig. 7.9B). For

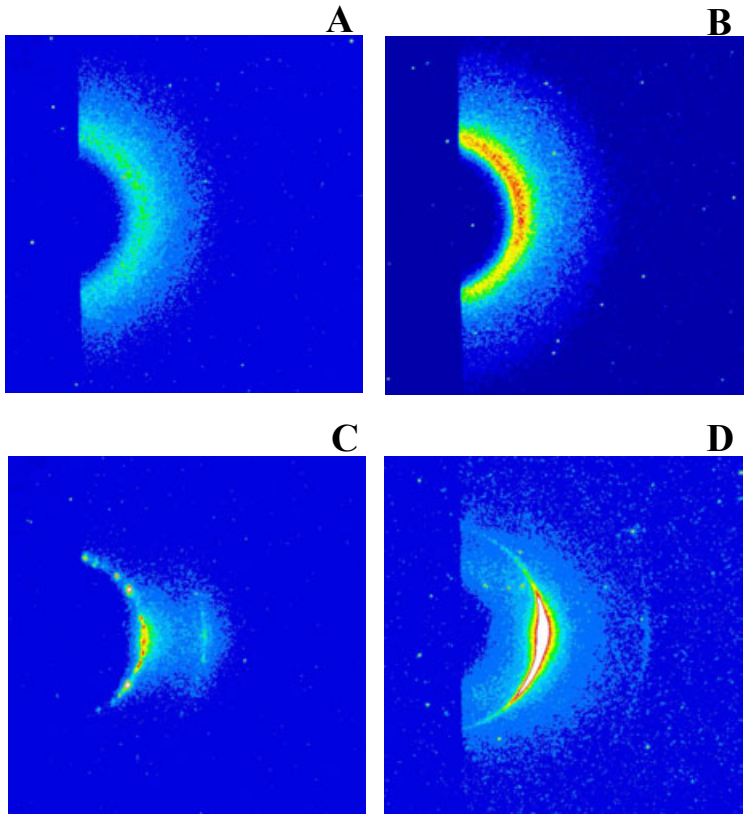

FIGURE 7.8: 2D-X-ray diffraction patterns of (**A**) isotropic phase at α=0.14, ϕ_s=40, and T=25°C, (**B**) nematic (N_c) phase at α=0.14, ϕ_s=40, and T=46°C and (**C**) hexagonal phase at α=0.14, ϕ_s=40, and T=65°C and (**D**) I+Lα phase at α=0.14, ϕ_s=60 and T=70°C in the SDS-PTHC-Water system.

$20 \leq \phi_s \leq 35$, a translucent sample with low apparent viscosity is found which exhibits an isotropic phase. This phase does not show flow birefringence. SAXS pattern at higher water content shows broad peaks (Fig. 7.10B(a-d)). For $37.5 \leq \phi_s \leq 42.5$, sample is translucent and exhibits nematic phase. This phase shows typical schlieren texture under POM with large pseudo-isotropic patches (Fig. 7.11D). SAXS pattern shows two broad peaks with their q in the ratio 1:2, due to short-range lamellar arrangement of the disc-like micelles (Fig. 7.10B(e)). This phase goes into an isotropic phase through a two phase region on heating. At ϕ_s=45, sample is turbid and exhibits a lamellar phase coexisting with excess solvent (Fig. 7.11E). Diffraction pattern of this phase shows a sharp peak (Fig. 7.12C). This phase transforms into an isotropic phase via a nematic phase. Nematic phase exhibits the schlieren texture under microscope (Fig. 7.11F) and a narrow peak

TABLE 7.7: The d-spacings and polarizing optical microscopy textures of the different phases in SDS-PTHC-water system at α=0.14 and T=80°C.

ϕ_s	d_1(nm)	d_2(nm)	POM texture	Phase
25	4.80 (weak structure peak)	–	Isotropic	I
30	4.72	–	Isotropic	I
35	4.69	–	Isotropic	I
40	4.64	2.68	Fan-like texture	H
45	4.53	2.62	Fan-like texture	H
50	4.28	–	Isotropic	I
55	4.01	1.99	Oily streak texture	I+L_α
60	3.68	1.84	Oily streak texture	I+L_α

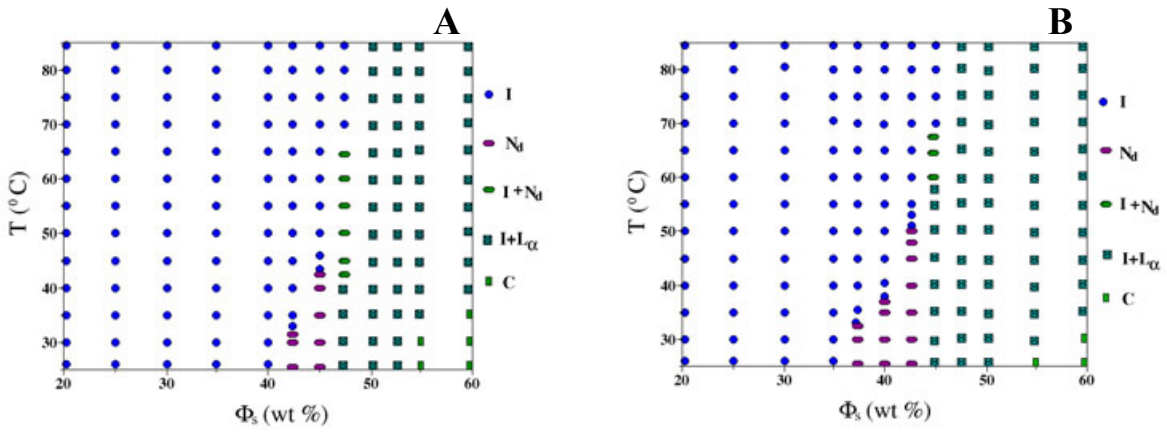

FIGURE 7.9: Partial phase diagrams of the SDS-PTHC-Water system at (**A**) α=0.175 and (**B**) α=0.22.

in the diffraction pattern (Fig. 7.12D) and isotropic phase shows a diffuse ring (Fig. 7.12E). Lamellar phase is found to coexist with excess solvent over a wide range of water content. For 47.5 $\leq \phi_s \leq$50, lamellar phase coexists with excess solvent over the temperature range studied. For 55 $\leq \phi_s \leq$60, a crystalline phase coexisting with excess solvent is found at low temperatures, which transform into lamellar phase coexisting with excess solvent (I+L_α), on heating. The typical diffraction pattern of this L_α phase is shown in figure 7.12F. The observed phases and corresponding d-spacings are given in the table 7.9.

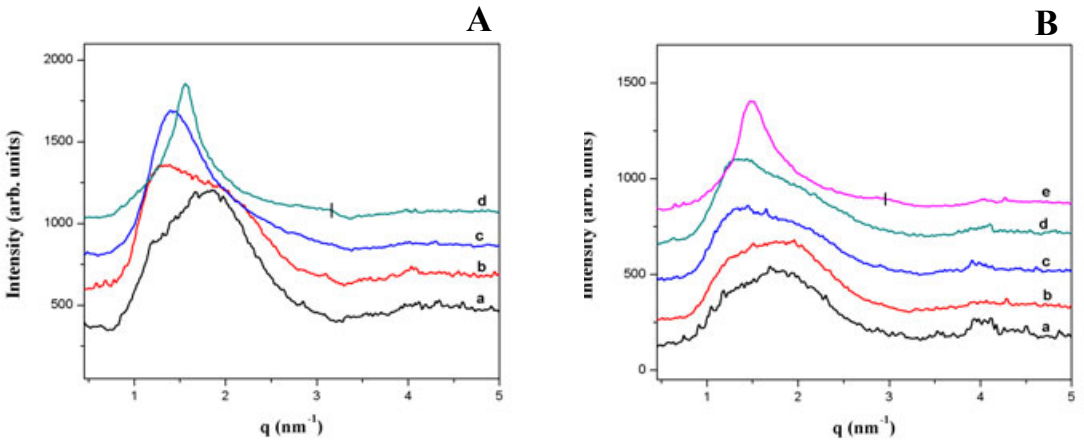

FIGURE 7.10: X-ray diffraction patterns of (**A**) isotropic phases at α=0.175, T=30°C corresponding to ϕ_s=20 (**a**), ϕ_s=30 (**b**), ϕ_s=40 (**c**) and nematic N_d phase at α=0.175, T=30°C and ϕ_s=45 (**d**). The bar on curve d indicates the secondary peak at $2q_o$, where q_o is the position of the primary peak. (**B**) Isotropic phases at α=0.22, T=30°C corresponding to ϕ_s=20 (**a**), ϕ_s=25 (**b**), ϕ_s=30 (**c**), ϕ_s=35 (**d**) and nematic N_d phase at α=0.22, T=30°C and ϕ_s=40 (**e**) in the SDS-PTHC-Water system. The bar on curves e indicates the secondary peak at $2q_o$, where q_o is the position of the primary peak.

TABLE 7.8: The d-spacings and polarizing optical microscopy textures of the different phases in SDS-PTHC-water system at α=0.175 and T=30°C.

ϕ_s	d_1(nm)	d_2(nm)	POM texture	Phase
25	diffuse (form factor)	–	Isotropic	I
30	4.78	–	Isotropic	I
35	4.63	–	Isotropic	I
40	4.39	–	Isotropic	I
45	4.01	–	Schlieren texture	N_d
50	3.89	1.94	Oily streak texture	I+L_α
52.5	3.72	1.85	Oily streak texture	I+L_α

7.4.2 Phase behavior at α=0.1 and ϕ_s=40

Nematic phase found at low temperatures goes to hexagonal phase at higher temperature on heating via a possible intermediate hexatic phase (Fig. 7.2B). In-order to confirm the occurrence of the hexatic phase, we have measured the variation of translational (positional) correlation length with temperature.

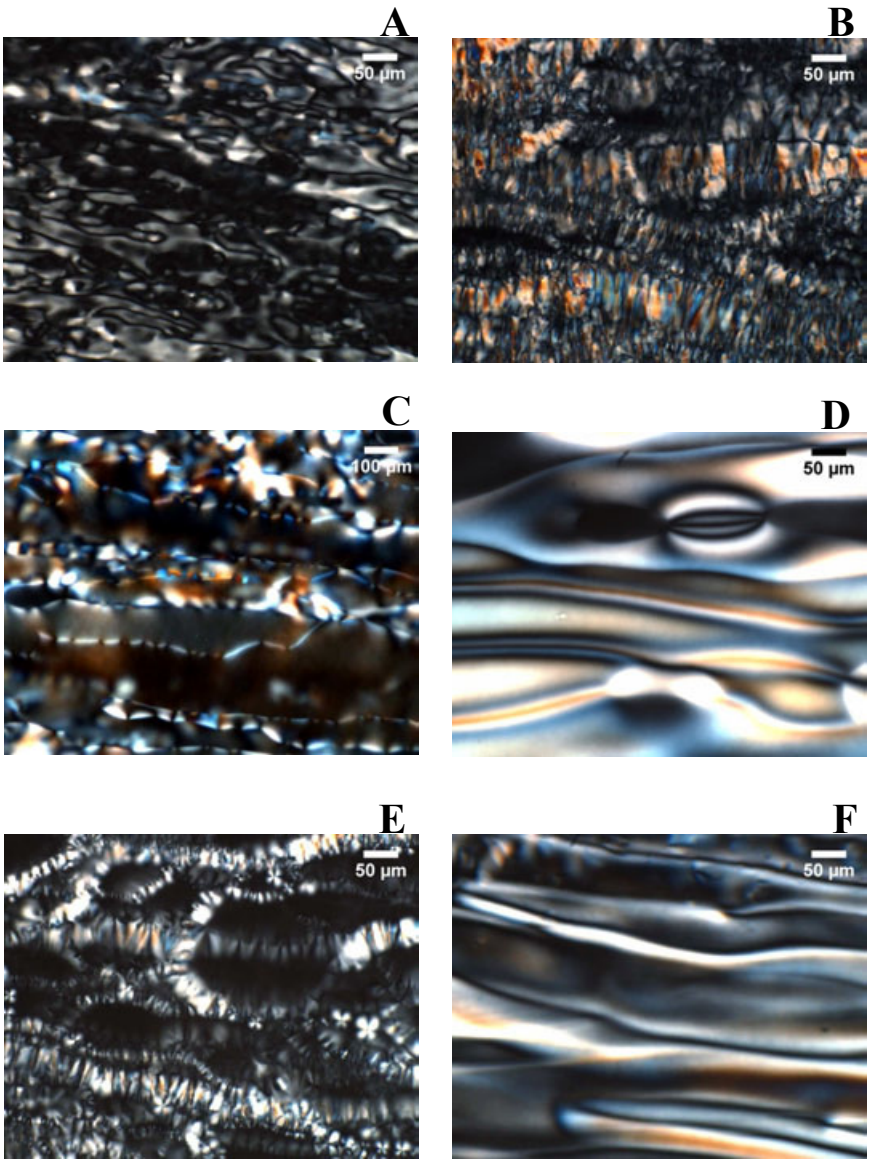

FIGURE 7.11: POM textures of (**A**) nematic N_d phase at α=0.175, ϕ_s=45 and T=26°C, (**B**) I+L_α phase at α=0.175, ϕ_s=46.98 and T=30°C and (**C**) I+N_d phase at α=0.175, ϕ_s=46.98 and T=60°C, (**D**) nematic N_d phase at α=0.22, ϕ_s=40 and T=26°C, (**E**) I+L_α phase at α=0.22, ϕ_s=45 and T=45°C and (**F**) I+N_d phase at α=0.22, ϕ_s=45 and T=60°C in the SDS-PTHC-Water system.

To measure the in-plane (perpendicular to the nematic director) positional correlation length ξ, the incoming X-ray beam is aimed perpendicular to the principal axis (perpendicular alignment) of the SDS-PTHC micelles and diffraction patterns have been recorded at different temperatures starting from 26°C in the nematic phase and progressively heating the sample to 60°C. Diffraction patterns obtained

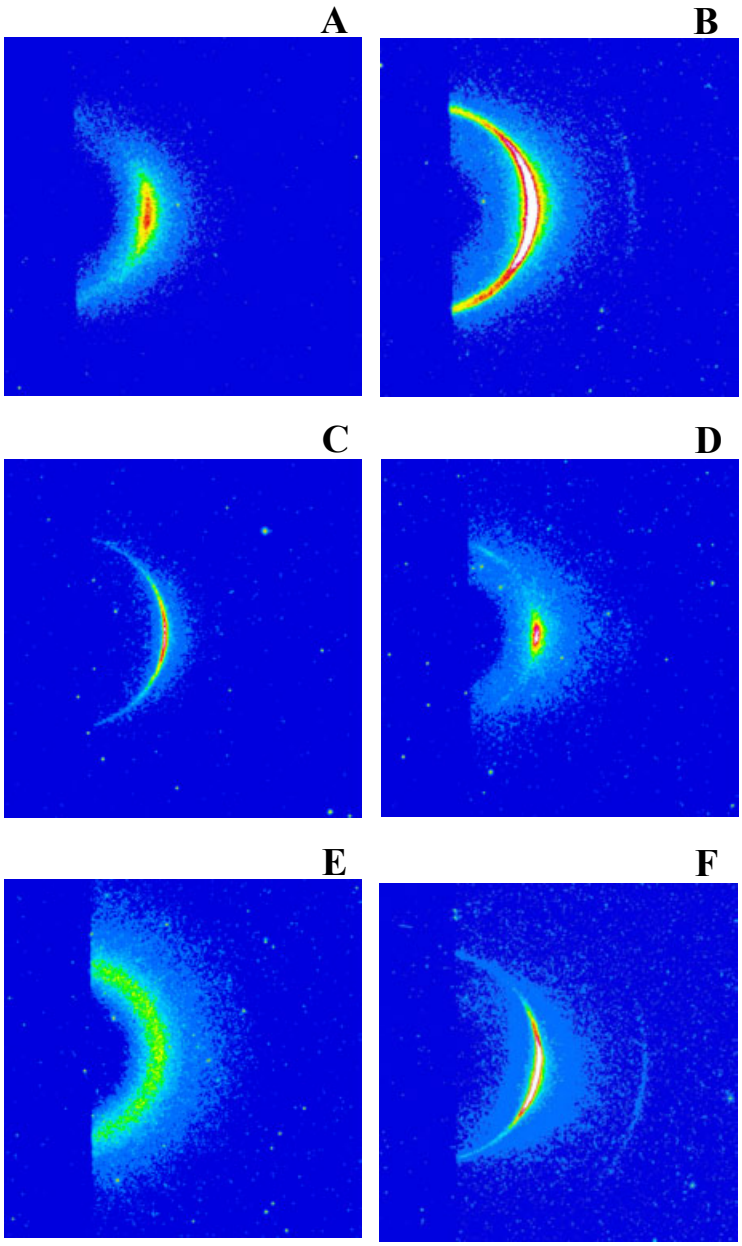

FIGURE 7.12: 2D-X-ray diffraction pattern of (**A**) nematic N_d phase at α=0.175, ϕ_s=45 and T=30°C, (**B**) I+L_α phase at α=0.175, ϕ_s=60 and T=50°C, (**C**) I+L_α phase at α=0.22, ϕ_s=45 and T=25°C, (**D**) I+N_d phase at α=0.22, ϕ_s=45 and T=60°C, (**E**) isotropic phase at α=0.22, ϕ_s=45 and T=80°C and (**F**) I+L_α phase at α=0.22, ϕ_s=60 and T=25°C in the SDS-PTHC-Water system.

for different phases are presented in figure. 7.13. It shows that at low temperature, in the nematic phase, the peak is quite broad and becomes progressively narrower as the temperature is increased (Fig. 7.13 and 7.14A). The two sharp peaks obtained in the small angle region above 40°C with their q in the ratios

TABLE 7.9: The d-spacings and polarizing optical microscopy textures of the different phases in SDS-PTHC-water system at α=0.22 and T=30°C.

ϕ_s	d_1(nm)	d_2(nm)	POM texture	Phase
25	diffuse (form factor)	–	Isotropic	I
30	4.72	–	Isotropic	I
35	4.70	–	Isotropic	I
40	4.22	–	Schlieren texture	N_d
45	4.12	2.05	Schlieren texture	I+L_α
50	3.82	1.92	Oily streak texture	I+L_α
55	3.62	1.81	Oily streak texture	I+L_α

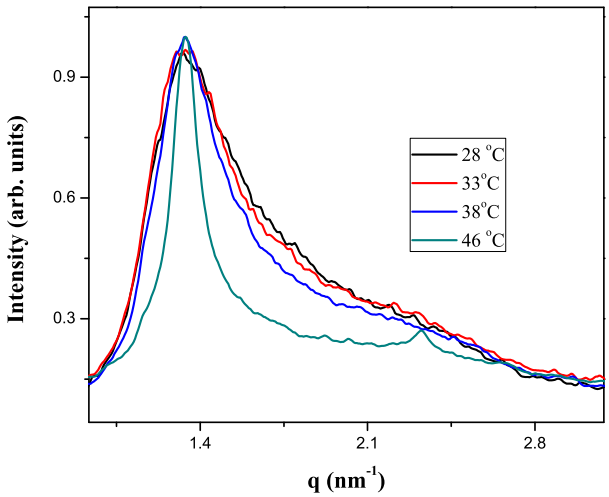

FIGURE 7.13: Diffraction patterns of the nematic N_c phase at α=0.1, ϕ_s=40 and T=28°C and T=33°C, hexatic phase at α=0.1, ϕ_s=40 and T=38°C and hexagonal phase at α=0.1, ϕ_s=40 and T=46°C)

1:$\sqrt{(3)}$, corresponds to (1 0) and (1 1) planes of the hexagonal phase (Fig. 7.13 and 7.14C). For intermediate temperatures, (Fig. 7.13 and 7.14B), a less narrow peak is found, compared to that observed in the hexagonal phase.

The correlation length, ξ, which is inversely proportional to the FWHM of the diffraction peak can be calculated as a function of temperature. Figure 7.15A shows the variation of correlation length (ξ) with temperature. It shows that in the nematic phase the positional correlation is of the order of 2nm and it continuously evolves with temperature and finally reaches 8nm in the hexagonal

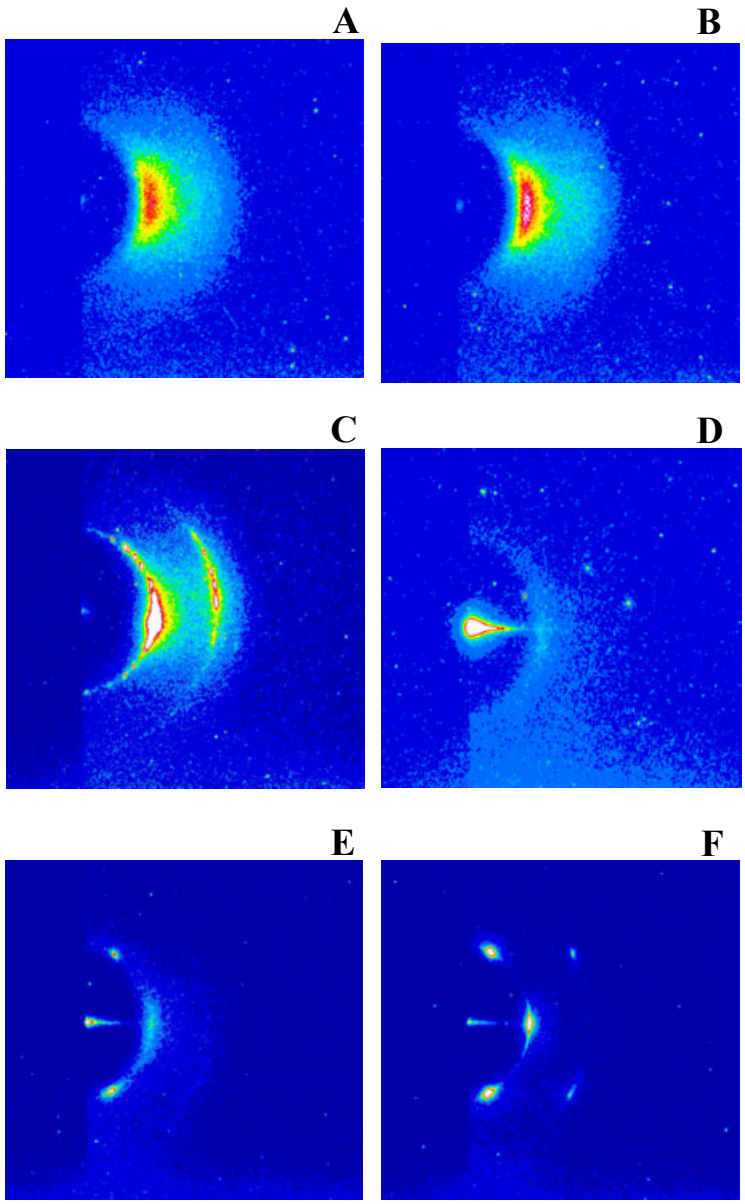

FIGURE 7.14: Oriented diffraction patterns of ((**A**) nematic N_c phase, (**B**) hexatic phase and (**C**) hexagonal phase at α=0.1 and ϕ_s=40 in the perpendicular alignment) and ((**D**) nematic N_c phase, (**E**) hexatic phase and (**F**) hexagonal phase at α=0.1 and ϕ_s=40 in the parallel alignment) in the SDS-PTHC-Water system.

phase. Variation of positional correlation length suggests the presence of a hexatic phase in between the nematic and hexagonal phases.

We have also recorded the x-ray diffraction patterns at different temperature when the principal axis of the micelles lie in a direction parallel to the incoming X-ray

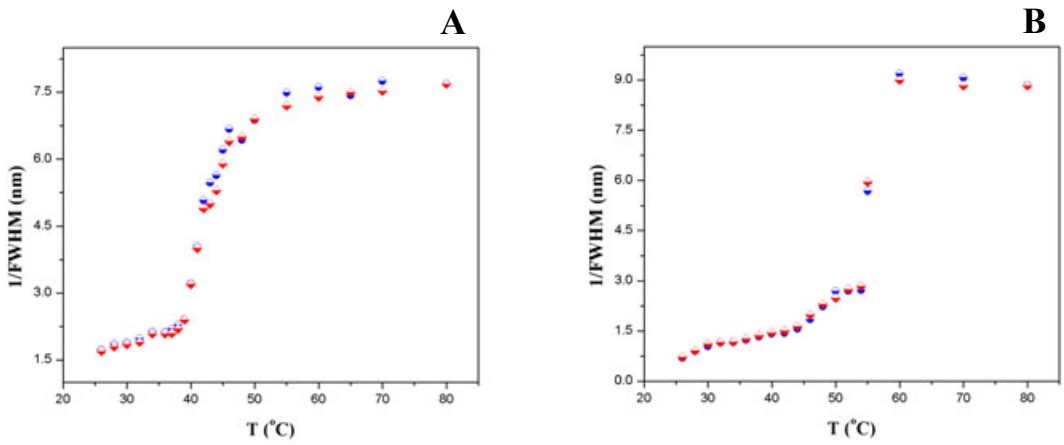

FIGURE 7.15: Variation of positional correlation length with temperature for the (**A**) achiral and (**B**) chiral system. Red and blue colors show the heating and cooling cycle respectively.

beam (parallel alignment). Except for fluctuations, momentum transfer q was in the plane perpendicular to the micellar axis. A diffuse ring is found in the nematic phase (Fig. 7.14D) which reflects the liquid-like translational and bond orientational correlations in the plane normal to the nematic director. In the high temperature hexagonal phase, a single-domain pattern with sharp peaks having six-fold symmetry is found (Fig. 7.14F). Figure 7.14E shows the 2D x-ray scattered intensity distribution with pronounced six-fold angular modulation in the hexatic phase.

In order to check the stability of the hexatic phase obtained in this system, nematic to hexatic to hexagonal transitions has been investigated thoroughly, both on heating and subsequent cooling. The results obtained show that the transitions are reversible with almost no hysteresis establishing that the hexatic phase is thermodynamically stable phase. However, only one transition which corresponds to the hexatic-hexagonal transition is seen under POM.

In-order to check the effect of chirality on the nematic to hexatic and hexatic to hexagonal transitions, chirality has been induced by adding cholesterol in the system. Present studies have been done on the SDS-PTHC-Cholesterol-Water system with composition α=0.1 β=0.03 and ϕ_s=40, where β=[Cholesterol]/[SDS]. This

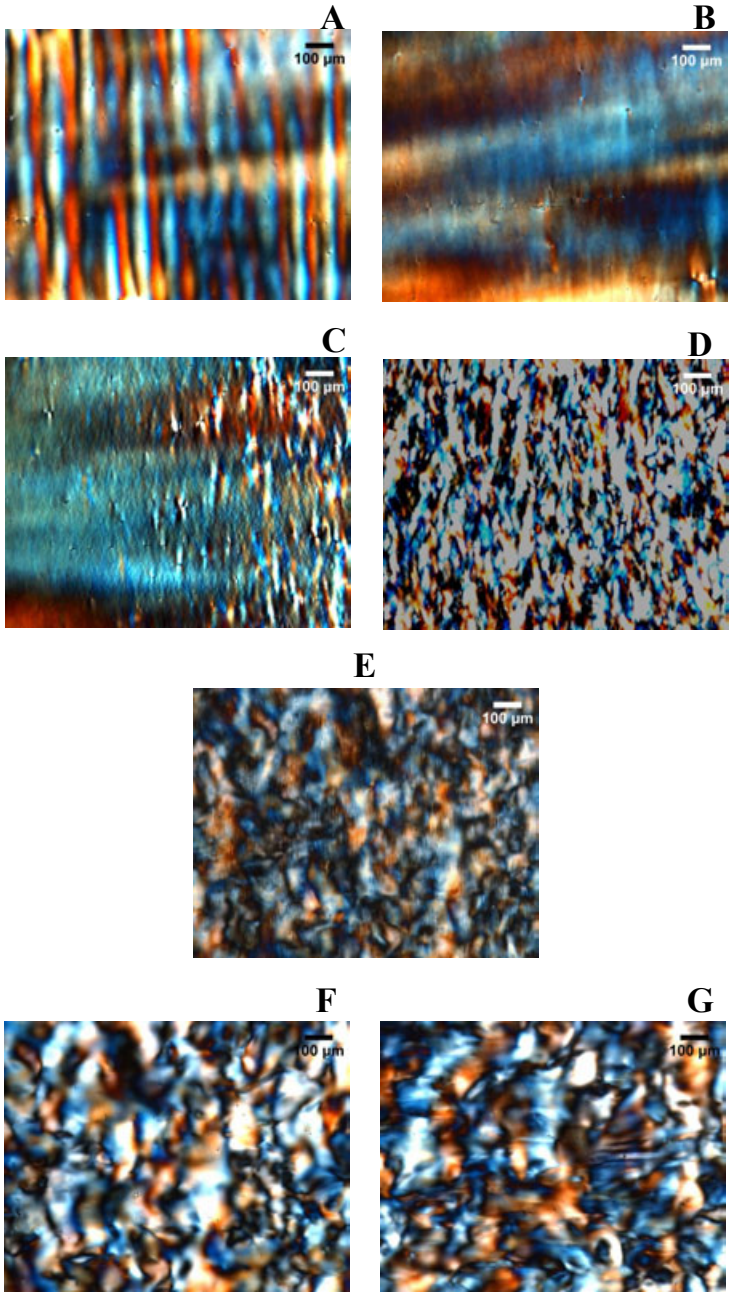

FIGURE 7.16: POM textures of ((**A**) nematic N_c phase, (**B**) hexatic phase (**C**) hexatic+ hexagonal phase and (**D**) hexagonal phase on heating) and ((**E**) hexatic+ hexagonal phase, (**F**) hexatic phase and (**G**) nematic N_c phase on cooling) in the SDS-PTHC-Cholesterol-Water system at α=0.1, ϕ_s=40 and β=0.03.

sample shows a cholesteric phase in the low temperature range (26°C≤T≤42°C), hexatic phase in the middle temperature range (43°C≤T≤49°C) and hexagonal phase at higher temperature range (T≥51°C), which is confirmed by POM and SAXS studies. For POM study, sample has been taken in a flat capillary of

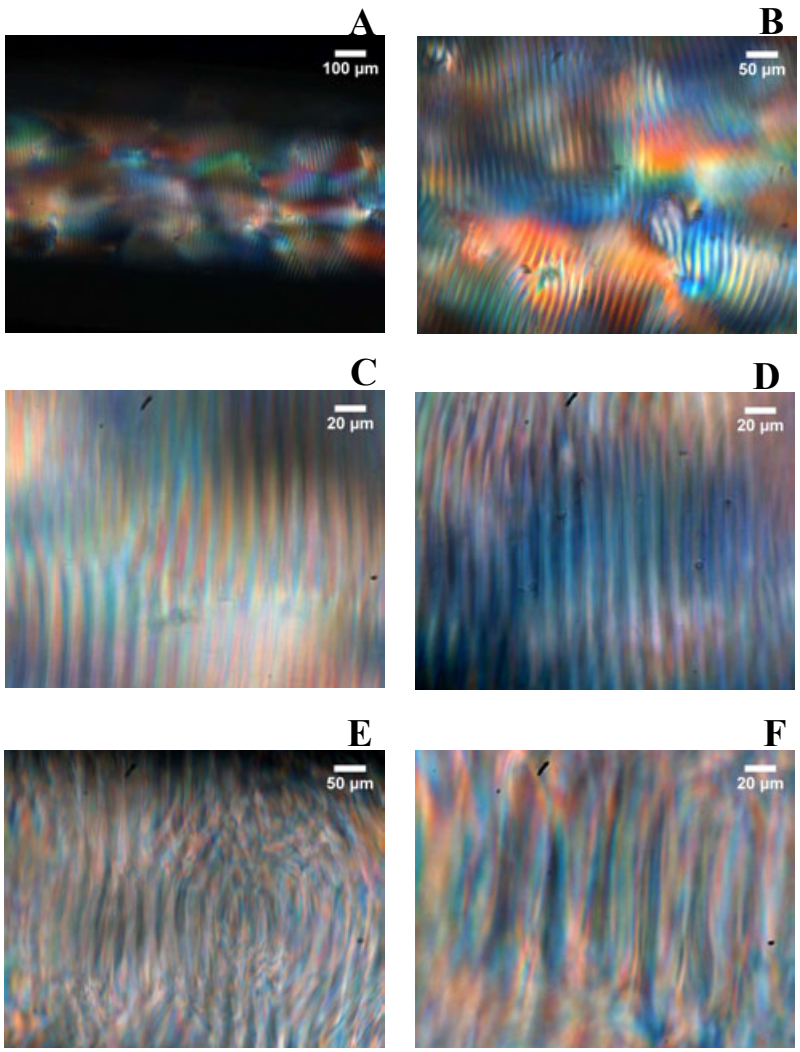

FIGURE 7.17: Fingerprint textures of cholesteric phase in the SDS-PTHC-Cholesterol-Water system at α=0.1, ϕ_s=40, β=0.05 (**A-D**) and β=0.03 (**E and F**).

thickness 0.2mm and both sides of the capillary have been sealed properly. POM textures have been recorded at different temperatures starting from 26°C in the nematic phase and progressively heating the sample through the nematic-hexatic and the hexatic-hexagonal transition to 60°C. At low temperatures, in the cholesteric phase, a striated pattern is found (Fig. 7.16A). However, in the hexatic phase a smooth texture is found (Fig. 7.16B) and a two phase region is not found in between hexatic and cholesteric phase. At higher temperatures, a fan-like texture is found to grow at the expense of the smooth texture (Fig. 7.16C) and finally

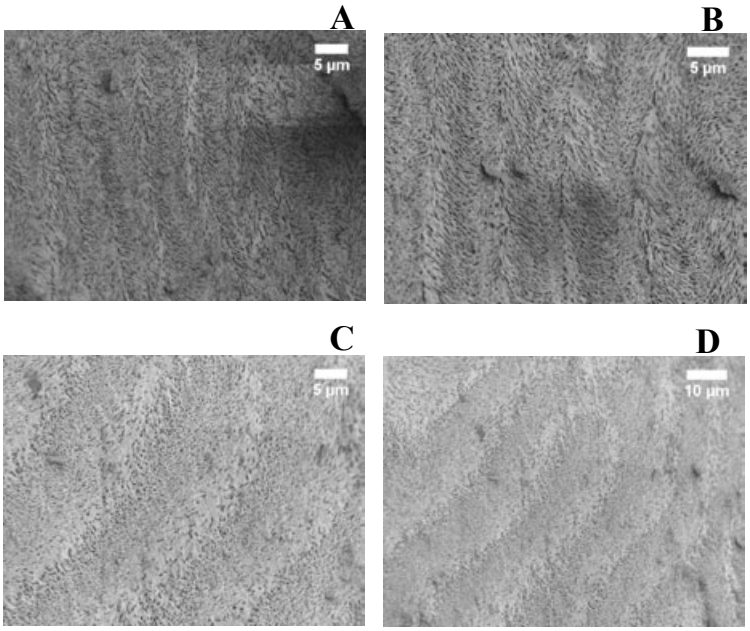

FIGURE 7.18: Cryo-SEM micrographs of the cholesteric phase (equilibrated for two weeks in a cylindrical capillary) in the SDS-PTHC-Cholesterol-Water system at α=0.1, ϕ_s=40 and β=0.05.

the fan-like texture covers the entire sample (Fig. 7.16D), indicating that a region of coexistence of the hexatic and hexagonal phases. However, on cooling, the textures of the hexatic and cholesteric phase are quite different from that observed on heating (Fig. 7.16E-G). Yet, the transition temperatures corresponding to the hexagonal to hexatic and hexatic to cholesteric transitions are found to be unchanged. It is worthwhile to note that the fingerprint texture which is the trademark of the cholesteric phase takes about two week to form in these samples. Fingerprint texture found in the cholesteric phase at β=0.03 has a pitch of 62μm, whereas that found at β=0.05 has a lower pitch of 28μm (Fig. 7.17). Interestingly, cryo-SEM micrographs of the same sample, show striation patterns of same pitch (Fig. 7.18). However, samples which are not equilibrated long enough, show cryo-SEM micrographs with different features as shown in figure 7.19.

Figures 7.20A-C; show the 2D diffraction patterns of the chiral system in perpendicular alignment. An aligned pattern with a broad peak is observed in the cholesteric phase (Fig. 7.20A), similar to that found in the achiral sample. However, this aligned pattern takes about two weeks to transform to a diffuse ring

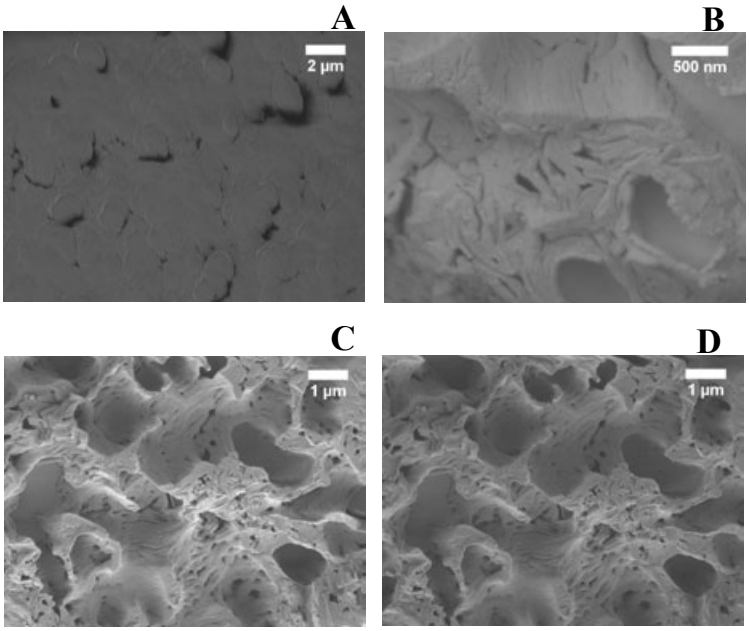

FIGURE 7.19: Cryo-SEM micrographs of the cholesteric phase (equilibrated for 20minutes in a cylindrical capillary) in the SDS-PTHC-Cholesterol-Water system at α=0.1, ϕ_s=40 and β=0.05.

pattern. In the hexatic phase, again, an aligned pattern with a narrower peak is found (Fig. 7.20B). Yet, in the hexagonal phase a align pattern with two sharp peaks is observed with their q in the ratio1:$\sqrt{3}$ (Fig. 7.20C). We have again plotted the in-plane positional correlation length ξ as a function of temperature (Fig. 7.15B), which does not show much of a difference from that of the achiral system.

Figures 7.20D-F; show the 2D diffraction patterns of the chiral system in the parallel alignment. In the temperature range where we find the hexatic phase in the achiral system, in perpendicular alignment we find aligned diffraction pattern whereas in parallel alignment it shows a broad ring (Fig. 7.20E). At still higher temperature, in the hexagonal phase, the system shows a strong six fold intensity modulation (Fig. 7.20F).

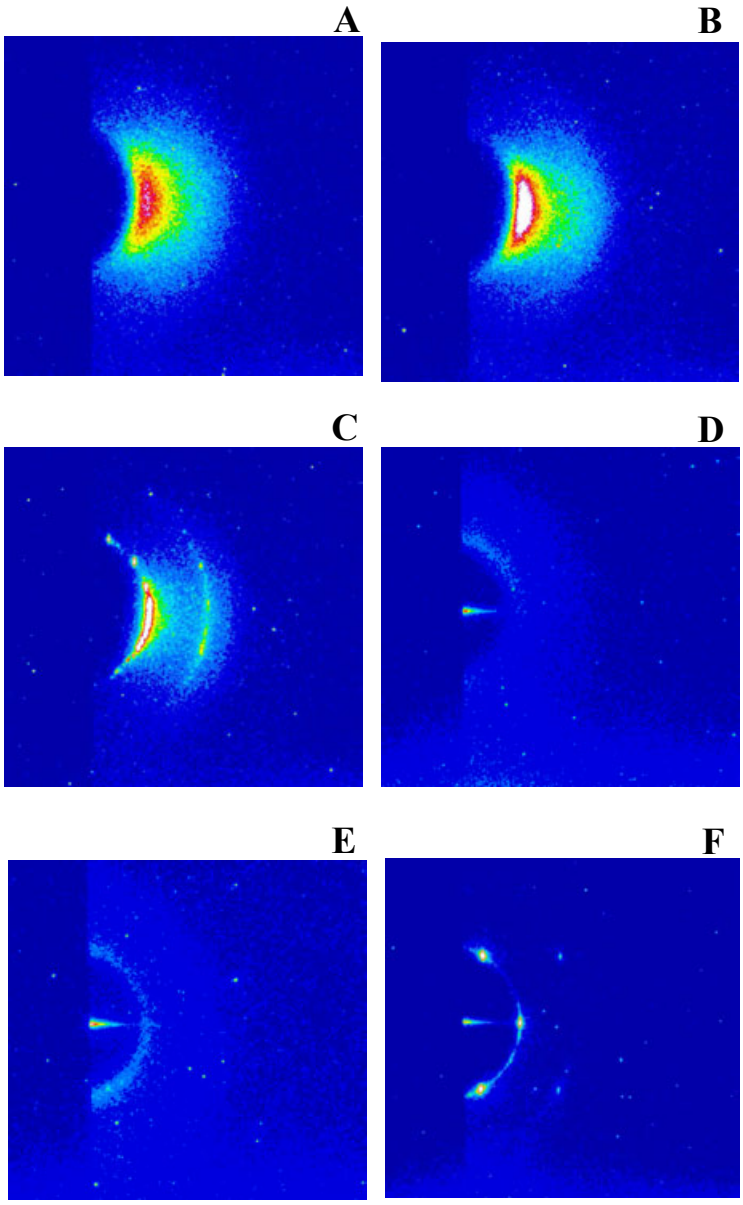

FIGURE 7.20: Oriented diffraction pattern of ((**A**) cholesteric phase, (**B**) hexatic phase and (**C**) hexagonal phase at α=0.1 and ϕ_s=40 in the perpendicular alignment) and ((**D**) cholesteric, (**E**) hexatic phase and (**F**) hexagonal phase at α=0.1 and ϕ_s=40 in the parallel alignment) in the SDS-PTHC-Cholesterol-Water system.

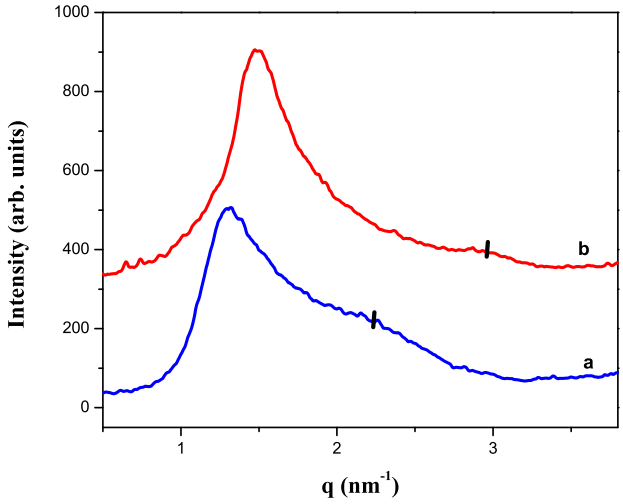

FIGURE 7.21: Typical diffraction patterns of the N_c (**a**) and N_d phases of the SDS-PTHC-Water system. The bars on curves b and c indicate secondary peaks at $\sqrt{3}q_o$ and $2q_o$, respectively, where q_o is the position of the primary peak.

7.5 Discussion

7.5.1 Nematic phases (N_c and N_d)

The nematic (N_c) phase that occurs in the SDS-PTHC-Water system at low values of α (α<0.14 i.e. α=0.05 and 0.1) is made up of worm-like micelles that have a cylindrical shape on average. This conclusion is supported by the following observations. This phase occurs close to the hexagonal phase and is highly viscous. POM textures of this phase do not exhibit any homeotropic regions, where the optic axis is normal to the bounding plates (Figs. 7.4A and 7.7A). The x-ray diffraction patterns of this phase show a secondary maximum near $\sqrt{3}q_o$, where q_o is the wave vector of the primary peak, which indicates short-range hexagonal order (Fig. 7.21a). A further increase in ϕ_s brings the cylindrical micelles closer, forcing them to order on a 2D hexagonal lattice. Further, an isotropic phase (I) found near to this phase is highly viscous and shows flow birefringence, indicating the presence of long cylindrical micelles.

In contrast, the nematic (N_d) phase that occurs at higher values of α (α>0.14 i.e. α=0.175 and 0.22) in the SDS-PTHC-Water system is made up of micelles that have a disc-like shape on average. This phase has a much lower viscosity in comparison and occurs close to the lamellar phase. POM textures of this phase show homeotropic regions, where the optic axis is normal to the bounding plates (Figs. 7.7C and 7.11A&D). The x-ray diffraction patterns of this phase show a secondary maximum near $2q_o$, indicating short-range lamellar order (Fig. 7.21b). Further at α=0.175 and 0.22, a transition from lamellar to isotropic via nematic phase is observed which confirms the presence of disc-like micelles. This kind of phase transition on heating has been observed in caesium pentadecafluoro-octanoate (CsPFO)-water system where the nematic phase is well established to be made up of disc-like micelles [9–11]. Further, an isotropic phase (I) found near to this phase has lower viscosity in comparison to that observed in the isotropic phase (I) near to N_c phase, indicating that this isotropic phase is made up of small aggregates.

However, at α=0.14, both nematic phases are found, one (N_c phase) at higher water content and other(N_d phase) at lower water content

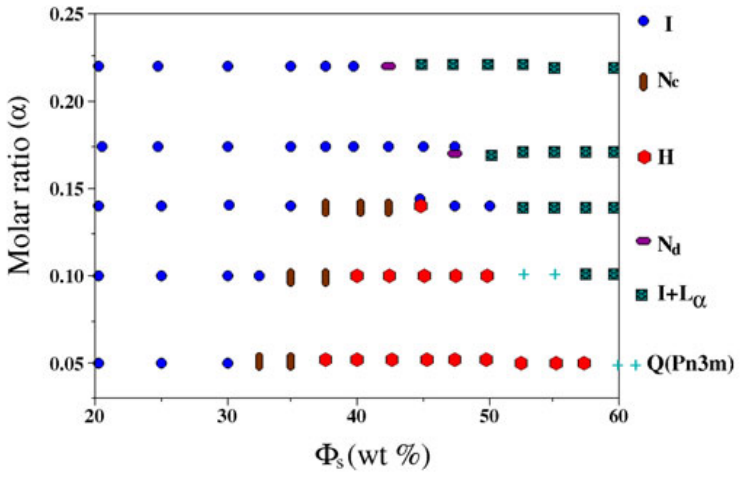

FIGURE 7.22: α-temperature phase diagram of the SDS-PTHC-Water system at T=45°C.

Following phase sequence is seen in the SDS-PTHC-Water system at α=0.14. *Isotropic (I)* $\rightarrow$ *Nematic* (N_c) $\rightarrow$ *Hexagonal(H)* $\rightarrow$*Isotropic (I)*$\rightarrow$ *Lamellar* (L_α) as a function of increasing ϕ_s (Fig. 7.22).

This phase sequence is unusual and consistent with a gradual transformation of the aggregate shape from cylindrical to disc-like with increasing ϕ_s. The apparent viscosity of the sample also shows a non-monotonic behavior. It found to increase gradually upto a maximum in the hexagonal phase and then decreases in the isotropic phase, on decreasing the water content. This is consistent with an initial gradual increase in the length of the cylindrical micelles and then a subsequent decrease. This sequence of phases suggests a gradual prolate to oblate change in the aggregate morphology with increasing ϕ_s. Such a morphological change seems to prevent the formation of other intermediate phases usually seen between the hexagonal and lamellar phases. Further experiments are needed to understand the proposed change in the morphology of the aggregates.

7.5.2 The possible existence of a hexatic phase

Theories of two-dimensional melting predict the existence of an intermediate phase, so called hexatic phase in between the crystal and liquid [12–15]. The hexatic phase exhibits short range translational order but does retain quasi long range bond-orientational order. Bond-orientational order describes the relative orientation of nearest neighbors of a given molecule in a medium. Bond-orientational order defined by the order parameter ψ_6 defined as:

$$\psi_6 = \rho_6 e^{i6\phi_6}$$

, ρ_6 is the amplitude of the order parameter and the ϕ_6 indicates the rotation of a group of atoms with respect to an axis (schematic is shown in figure 7.23). Melting can occur via two continuous transitions with the first from crystal to hexatic driven by dislocation unbinding and the second from hexatic to liquid driven by disclination unbinding.

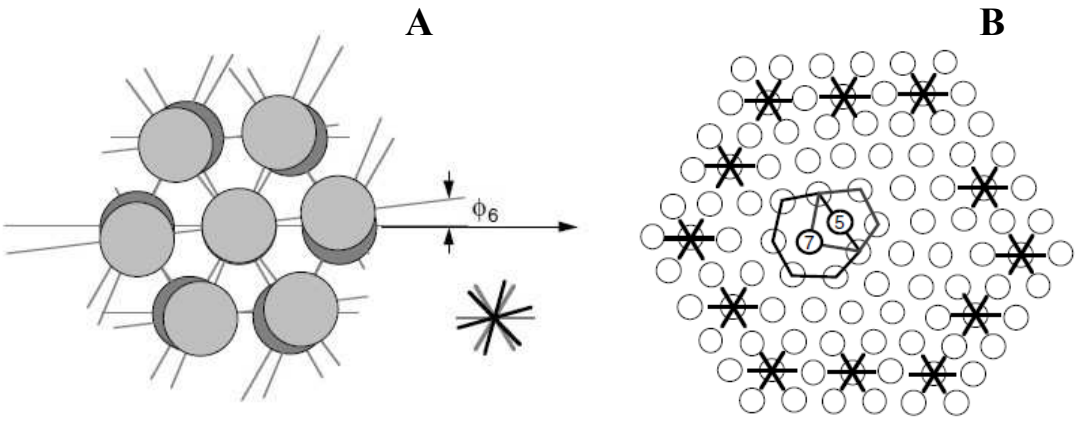

FIGURE 7.23: Schematic of bond orientational order. (**A**) Definition of the bond-orientational order parameter in a crystal of hexagonal symmetry. The phase ϕ_6 of the hexatic order parameter indicates the rotation of a group of atoms with respect to an axis. Six-arm star denotes the hexatic order parameter and (**B**) The variation in the phase ϕ_6 of the hexatic order parameter on a circuit enclosing a dislocation is zero; the dislocations do not destroy the orientational order of the bonds between nearest-neighbor molecules (from ref. [16]).

The line hexatic or N+6 phase, characterized by long range nematic (orientational order), long range bond orientational order and short range positional order is the three dimensional analog of the two dimensional hexatic phase [13]. In fact, any cut through the line hexatic phase perpendicular to the local director reveals a collection of points exhibiting canonical 2D hexatic order.

Lekkerkerker et al. [18] have reported a hexatic phase, spontaneously formed by colloidal plate-like particles with a high diameter polydispersity. This system consists of 1D columns, which two dimensionally pack into a (1+2)D hexatic structure. This structure is distinctly different from the (2 +1)D hexatic smectic liquid crystals, which consist of 2D hexatic layers stacked one dimensionally. Their results imply that geometric frustration related to the size polydispersity of the particles destroys long-range translational order and therefore promotes the formation of this novel phase. (1+2)D hexatic has also been reported in DNA molecules [19].

In the present study, positional and bond orientational order are found to be gradually increasing from nematic to hexagonal phase in the SDS-PTHC-Water

system which suggests the existence of hexatic phase in between nematic and hexagonal phases.

The phase sequence seen in this system can be explained as follows. This system is made up of worm-like micelles and worm-like micelles are known to show a non-monotonic trend in their zero shear viscosity with increasing salt concentration, showing a pronounced peak first, followed by a trough [12–14, 20–25]. The hypotheses dominating the literature is that the micelles grow while staying linear up to the peak, where as beyond the peak, they transform into a branched network [17, 20, 23, 25–30] with mobile inter-micellar junctions, that lead to a decrease in the viscosity [31].

In the our system, the higher temperature hexagonal phase is more viscous compared to the lower temperature nematic phase which suggests that the micelles in the nematic phase are highly branched. This high branch point density in the nematic phase results in its positional order short being ranged. As the temperature is increased, for organic salts such as PTHC, the solubility in water decreases and hence the quantity of salt in the micelles increases. The increase in the salt concentration at the water-micellar interface, leads to a decrease in the branch point density leading to the formation of the more ordered hexagonal phase.

The nematic phase transforms into a cholesteric phase in the presence of chirality and one would expect a diffuse ring in its diffraction pattern. However, these samples show an aligned diffraction pattern which transforms into a diffuse ring in about two weeks. Interestingly, this is also the time scale taken by these samples to show the fingerprint texture under polarizing microscope, which is the characteristic texture of this phase. We can understand these observation as follows. When we draw the sample into the capillary the micelles align parallel to the axis of the capillary due to the flow. It takes a very long time for these samples to organize into the helical cholesteric due to their extremely high viscosity.

Hexatic phase of the chiral system also shows an aligned diffraction pattern in the perpendicular alignment and a broad diffuse ring in parallel alignment. This could be understood as follows. Chirality can affect the hexatic phase in two different

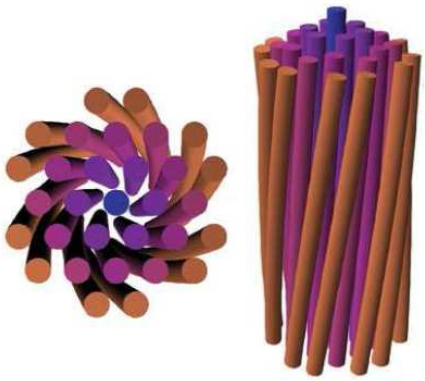

FIGURE 7.24: Schematic of Moiŕe phase (from ref. [32]).

ways. It can twist either the nematic order leading to the formation of a TGB-like phase or the bond-orientational order to form a Moiŕe phase (schematic is shown in figure 7.24).

The TGB-like structure of the hexatic phase would consist of domains, with the micelles within each domain oriented along a preferred direction. This preferred direction in adjacent domains is twisted by a specific angle. Such a structure would give rise to a diffuse ring in its diffraction pattern both in the parallel and perpendicular alignments. As we discussed above, the micelles might take a long time to get into a twisted state and that may be the reason to see an aligned pattern in the hexatic phase in the perpendicular alignment. On the other hand, since in the Moiŕe phase it is only the bond orientational order which is getting twisted, the twist axis is parallel to the micellar rods or the axis of the capillary. This would then result in a diffuse ring in the parallel alignment, as observed. In the perpendicular alignment, one would still expect the inter micellar orientational correlations manifested in the form of a broad aligned pattern, again as observed. Thus the observed diffraction patterns of the chiral hexatic phase is consistent with the theoretically predicted Moiŕe structure.

7.6 Conclusion

Phase behavior of SDS-PTHC-Water system was studied using polarizing optical microscopy and x-ray diffraction techniques. Two nematic phase are found, one (N_c) at low salt concentration and other (N_d) at high salt concentration. At intermediate (α), an unusual phase sequence *Isotropic (I)* $\rightarrow$ *Nematic* (N_c) $\rightarrow$ *Hexagonal(H)* $\rightarrow$*Isotropic (I)*$\rightarrow$ *Lamellar* (L_α) is found. This sequence of phases suggests a gradual prolate to oblate change in the aggregate morphology with increasing counterion concentration. Such a morphological change seems to prevent the formation of other intermediate phases usually seen between the hexagonal and lamellar. Our results suggest the formation of an intermediate line hexatic phase in between the nematic and hexagonal phases over a narrow temperature and composition range. These transitions seem to be driven by a change in the degree of branching of the worm-like micelles with temperature. Further, the structure of the chiral line hexatic phase is consistent with the theoretically predicted Moiŕe structure. However, further detailed measurement of the evolution of the hexatic order parameter is needed to unambiguously confirm the existence of the hexatic phase.

Bibliography

[1] G. Porte, J. Appel, P. Bassereau and J. Marignan, *J. Phys.*, **50**, 1335 (1989).

[2] E. Cappelaere and R. Cressely, *Colloid Polym. Sci.*, **276**, 1050 (1998).

[3] P. Kekicheff and B. Cabane, *Acta Cryst*, **44**, 395 (1988).

[4] P. A. Hassan, S. R. Raghavan and W. Kaler, *Langmuir*, **18**, 2543 (2002).

[5] P. A. Hassan, G. Fritz and E. W. Kaler, *J. Colloid Int. Sci*, **257**, 154 (2003).

[6] G. Garg, P. A. Hassan, V. K. Aswal and S. K. Kulshrestha, *J. Phys. Chem. B*, **109**, 1340 (2005).

[7] S. K. Ghosh, V. Rathee, R. Krishnaswamy, V. A. Raghunathan and A. K. Sood, *Langmuir*, **25**, 8497 (2009).

[8] Thesis by A. Pal (2013).

[9] M. S. Leaver and M. C. Holmes, *J. Phys. II France*, **3**, 105 (1993).

[10] M. C. Holmes, A. M. Smith and M. S. Leaver, *J. Phys. II France*, **3**, 1357 (1993).

[11] M. C. Holmes, P. Sotta, Y. Hendrix and B. Deloche, *J. Phys. II France*, **3**, 1735 (1993).

[12] J. M. Kosterlitz and D. J. Thouless, *J. Phys. C*, **6**, 1181 (1973).

[13] B. I. Halperin and D. R. Nelson, *Phys. Rev. Lett.*, **41**, 121 (1978); D. R. Nelson and B. I. Halperin, *Phys. Rev. B*, **19**, 2457 (1979).

[14] A. P. Young, *Phys. Rev. B*, **19**, 1855 (1979).

[15] For an extensive overview, see D. R. Nelson, *Defects and Geometry in Condensed Matter Physics*, Cambridge University Press, Cambridge, England, (2002).

[16] P. Oswald and P. Pieranski, in *Smectic and columnar liquid crystals*, (CRC Press, Boca Raton, FL), of *The liquid crystal book series*, (2006).

[17] J. Toner, *Phys. Rev. A*, **27**, 1157 (1983).

[18] A. V. Petukhov, D. van der Beek, R. P. A. Dullens, I. P. Dolbnya, G. J. Vroege, and H. N. W. Lekkerkerker, *Phys. Rev. Lett.*, **95**, 077801 (2005).

[19] H. H. Strey, J. Wang, R. Podgornik, A. Rupprecht, L. Yu, V. A. Parsegian, and E. B. Sirota, *Phys. Rev. Lett.*, **84**, 3105 (2000).

[20] R. Pindak, D. E. Moncton, S. C. Davey, and J. W. Goodby, *Phys. Rev. Lett.*, **46**, 1135 (1981).

[21] W. H. de Jeu, B. I. Ostrovskii, and A. N. Shalaginov, *Rev. Mod. Phys.*, **75**, 181 (2003).

[22] D. Van Winkle, M. Davidson, and R. L. Rill, *J. Chem. Phys.*, **97**, 5641 (1992).

[23] A. Le Forestier, and F. Livolant, *Biophys. J.*, **65**, 56 (1994).

[24] R. B. Meyer, F. Lonberg, V. Tarututa, S. Fraden, S. D. Lee, and A. J. Hurd, *Disc. Faraday Chem. Soc.*, **79**, 125 (1985).

[25] V. Luzatti, and A. Nicolaieff, *J. Mol. Biol.*, **1**, 127 (1959); 7, 142 (1963); M. Feughelman, R. Langridge, W. E. Seeds, A. R. Stokes, H. R. Wilson, M. H. F. Wilkins, R. K. Barclay, and L. D. Hamilton, *Nature* (London) 175, 834 (1955).

[26] J. Lapault, J. Dubochet, W. Baschong, and E. Kellenberger, *Eur. Mol. Biol. Organ. J.*, **6**, 1507 (1987).

[27] R. J. Birgeneau and J. D. Litster, *J. Phys. (Paris) Lett.*, **39**, 399 (1978).

[28] J. W. Goodby and R. Pindak, *Mol. Cryst. Liq. Cryst.*, **75**, 233 (1981).

[29] J. W. Goodby, *Mol. Cryst. Liq. Cryst.*, **72**, 95 (1981).

[30] G. Albertini, S. Melone, G. Poeti, F. Rustichelli, and G. Torquati, *Mol. Cryst. Liq. Cryst.*, **104**, 121 (1984).

[31] M. C. Marchetti and D. R. Nelson, *Phys. Rev. B*, **41**, 1910 (1990).

[32] Gregory M. Grason and Robijn F. Bruinsma, *Phys. Rev. Lett.*, **99**, 098101 (2007)

Chapter 8

Undulation instability in the nematic phase of worm-like micelles

8.1 Introduction

Aggregation of amphiphilic molecule leads to the formation of spherical or rod-like micelles above the critical micellar concentration [1]. An increase in surfactant concentration, change in temperature or pH, addition of inorganic or strongly binding organic salt or addition of an oppositely charged surfactant can all promote micellar growth [2–12]. This growth generally leads to a highly viscous solution and the formation of an entangled network of flexible worm-like micelles. Equilibrium statics and dynamics of worm-like micelles resemble those of a polymer solution.

Worm-like micelles have potentially wide range of applications including drag reduction, enhanced oil recovery, food emulsion, cosmetics, paints, pharmaceuticals and many household products [13]. They also used as soft templates for growing nano wires [14], which rely on the formation of ordered arrays. Therefore it is important to understand the stability of aligned worm-like micelles in thin films.

This chapter deals with the undulation instability in worm-like micelles due to dilation. Earlier studies on this instability are described in section 8.2. A short description of chemicals used is given in section 8.3. The experimental results are described in section 8.4. In section 8.5, possible reasons for the large characteristic length found in the nematic phase of the worm-like micelles are discussed. Finally section 8.6 contains the conclusions that can be drawn from these studies.

8.2 Earlier Studies

It has been theoretically predicted that layers of SmA and cholesteric liquid crystals can undulate when subjected to external electric or magnetic fields [15, 16]. A magnetic or electric field applied along the normal to of the molecular orientational axis, in the case of a homeotroprically aligned SmA sample and along the helical axis in the case of a cholesteric sample, tends to reorient the layers. This effect competes against both the elastic deformation and surface anchoring at the bounding plates. There exists a critical applied field beyond which the layers undergo undulation instability. this phase transition is called the Helfrich-Hurault effect. The instability has never been observed in an ordinary SmA due to the very high value of the critical magnetic field but is easily seen in the cholesteric system as long as the sample thickness is much larger than the natural pitch [17].

Layer undulation in SmA may also be triggered through a mechanically induced dilation of the layers [18–21]. This remarkable deformation appears only under dilation not in compression. The imposed dilation can be relaxed by two possible ways. One must either add new layers or tilt them if their number is kept constant in-order to fill space. If the dilation is too sudden for the system to be able to adjust the number of layers. It has no other choice but to tilt the layers with respect to the bounding plates. This fast process leads to undulation of layers.

A characteristic length, proportional to square root of the ratio of the bending and compression moduli can be directly estimated from the wavelength of the undulation. It is found to be of order of thickness, in thermotropic systems [18]

and most lyotropic lamellar phases [22, 23]. But there are some systems where it is found to be very small, of the order of a few angstroms [24].

Auernhammer et al. [25] have investigated the undulation instability of smectic A liquid crystal under shear flow. Within the frame-work of irreversible hydrodynamics, they predicted that the layers have a tendency to reduce their vertical thickness due to the tilt of the nematic director in the direction of the flow. The layers can accommodate this tendency above a critical shear rate by developing undulations in the direction perpendicular to the velocity and velocity gradient directions.

For surfactant lamellar systems, Marlow et al. [26] have calculated in detail the effect of shear flow on the Helfrich interaction. They demonstrated that non-permeable or slowly permeating membranes can be susceptible to an undulatory instability and speculated that such an instability could be one source of a transition to multilamellar vesicles. Courbin et al. [27] recently, found experimentally the formation of multi-lamellar vesicles by an undulation instability in a surfactant lamellar phase. A similar instability is also seen in the hexagonal phase.

Hexagonal phase of lyotropic systems usually exhibit striated fan texture developing spontaneously in the samples as they are heated or cooled [28–32]. Quantitative study confirms that these striations are due to undulation or zig-zag configuration of columns. The angle of zig-zag is of the order of a few degrees and the wavelength of striations varies as square root of the sample thickness [33]. These striations are also visible in the columnar phase of discotic liquid crystals. They nucleate by the sudden dilation of planer samples perpendicular to the columns [36]. The columns then undulate above some critical thickness with well defined wavelength. From the measurement of undulation wavelength as a function of the sample thickness, Gharbia et al. [36] found that the apparent curvature elastic modulus of the columns is anomalously large in discotic liquid crystals ($\sim$ six order of magnitude larger than in SmA, N). They found a similar value by measuring the threshold of column buckling under compression along the columns [28].

As such there is no report of the undulation instability in the nematic phase of lyotropic or thermotropic systems.

8.2.1 Theoretical Studies

8.2.1.1 Linear regime

Kleman and Oswald have purposed the theory to understand a undulation instability in the hexagonal phase [37].

The elastic energy density (f) in the columnar hexagonal phase can be expressed as [37].

$$f = \frac{1}{2}B(U_{xx} + U_{yy})^2 + \frac{1}{2}C(U_{xy}^2 - U_{xx}U_{yy})^2 + \frac{1}{2}K[(\frac{\partial^2 u}{\partial z^2})^2 + (\frac{\partial^2 v}{\partial z^2})^2] \tag{8.1}$$

Where the first two terms describe the strain of the hexagonal lattice and the last one describes the deformation of the director field. B is the compression modulus, C the shear modulus and K the curvature elastic constant of the column. In the reference state, the columns are aligned along the z direction and the lattice is not distorted, x-axis is perpendicular to the plates. u and v are the x and y components of the displacement vector of the columns. U_{ij} are the components of the deformation tensor given by,

$$U_{xx} = (\frac{\partial u}{\partial x}) - \frac{1}{2}(\frac{\partial u}{\partial z})^2 + \frac{1}{2}(\frac{\partial v}{\partial x})^2 \tag{8.2}$$

$$U_{yy} = (\frac{\partial v}{\partial y}) - \frac{1}{2}(\frac{\partial v}{\partial z})^2 + \frac{1}{2}(\frac{\partial u}{\partial y})^2 \tag{8.3}$$

and

$$U_{xy} = \frac{1}{2}(\frac{\partial u}{\partial y} + \frac{\partial v}{\partial x}) - \frac{1}{2}(\frac{\partial u}{\partial x}\frac{\partial v}{\partial x} + \frac{\partial u}{\partial y}\frac{\partial v}{\partial y} + \frac{\partial u}{\partial z}\frac{\partial v}{\partial z}) \tag{8.4}$$

Strong anchoring is assumed at the surfaces and the deformation of the columnar lattice is taken to be of the type $u = \gamma x$ and $v = \gamma y$ where γ is the dilation. To study the stability of the deformed state, the value γ_c of the dilation is to be determined above which a solution of the type

$$u = \gamma x + u_0 sin(q_z z) sin(q_x x) \tag{8.5}$$

$$v = \gamma y + v_0 sin(q_z z) sin(q_x x) \tag{8.6}$$

becomes energetically favorable. In this expression, $q_z = 2\pi/\lambda$ is the wave vector of the undulation and $q_x = \pi/d$ enforces the strong anchoring condition at the plates, d is thickness of the sample and λ is the wavelength of undulation.

putting these solutions in equation 8.1 and integrating over unit area lead to two uncoupled equations corresponding to instability in horizontal and vertical planes respectively. The threshold wavelength and strain in the vertical and horizontal planes are given by

$$\lambda_{uc} = 2\sqrt{\pi m d} \tag{8.7}$$

$$\gamma_{uc} = \frac{m q_x}{1 - A} \tag{8.8}$$

in vertical (x, z) plane and

$$\lambda_{vc} = (2\sqrt{\pi m d})/\sqrt[4]{A} \tag{8.9}$$

$$\gamma_{vc} = (\frac{m q_x}{1 - A})\sqrt{A} \tag{8.10}$$

in horizontal (y, z) plane; where m=$\sqrt{\frac{K}{B}}$ is the characteristic length which is usually of the order of the distance between columns and A=$\frac{C}{4B}$ is a dimensionless number characterizing the elastic anisotropy of the hexagonal lattice.

Experimental value of A is in between (0.025, 0.075) as found in the $C_{12}O_6$-Water system [38]. For instance, one gets $\gamma_c \sim 10^{-5}$ for A=0.05 in the $C_{12}O_6$-Water

system. Values of the dilation coefficient (dilation per unit temperature) for lyotropic [29, 31] and thermotropics [32] of the order of 10^{-3} per kelvin have been reported. It becomes apparent that the striations are almost always observed far from the threshold, in the strongly nonlinear regime. So using the formula (eq. 8.7 and 8.9) is questionable.

8.2.1.2 Non-linear regime

The non linear model was developed by Oswald et al. [33], in order to explain the striation pattern far from the threshold. The main assumption of this model is that the columns form a zigzag rather than a sinusoid. This model is meaningful if m/θ where θ is the angle made by column to z axis, is small with respect to the width $\lambda/2$ of a stripes. This condition is generally fulfilled in practice. Final results of the model are given below.

wavelength of the zigzag is practically independent of the dilation, remaining equal to its threshold value λ_c and given by

$$\lambda \approx (2\sqrt{\pi m d})/\sqrt[4]{A} \tag{8.11}$$

and angle

$$\theta \approx (1.92 \pm 0.01)\sqrt{\gamma} \tag{8.12}$$

8.3 Experimental

Sodium dodecyl sulfate (SDS), cetyltrimethylammonium tosylate (CTAT), p-toluidine hydrochloride (PTHC) and cholesterol were purchased from Sigma-Aldrich, and were used without further purification. The chemical structures of the molecules are shown in figure 8.1. Samples were prepared by adding deionized water to the mixture of the surfactant and organic salt and then sealed. The composition of the samples are specified in terms of the parameters α, β and ϕ_s, where $\alpha = \frac{[PTHC]}{[SDS]}$,

β=$\frac{[Cholesterol]}{[SDS]}$ and ϕ_s is the weight fraction of the non-aqueous components. The sample were kept in an oven at 40°C for equilibration.

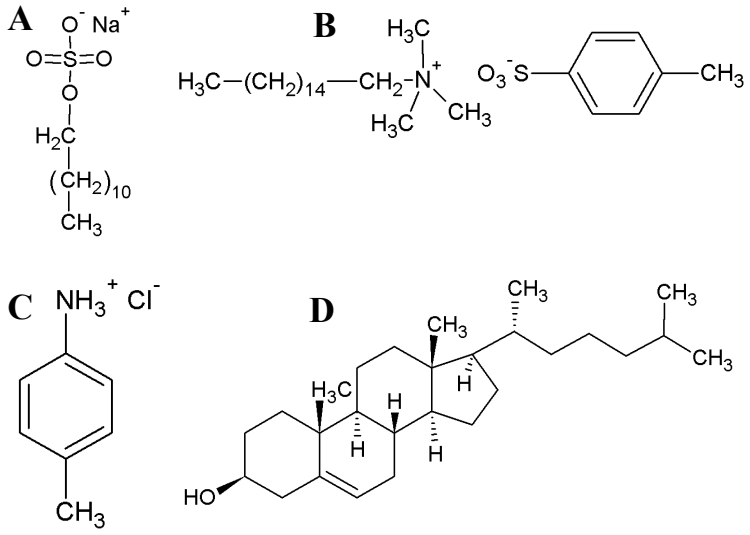

FIGURE 8.1: Chemical structures of Sodium dodecyl sulfate (SDS) (**A**), cetyltrimethylammonium tosylate (CTAT) (**B**), p-toluidine hydrochloride (PTHC) (**C**) and cholesterol (**D**).

Samples were taken in a rectangular capillary with the help of a syringe and both sides of the capillary were flame sealed. The sealed rectangular capillary was placed under a polarizing optical microscope to study the undulation instability induced.

8.4 Results

Studies were carried in the nematic phase of the SDS-PTHC-Water system at α=0.1 and ϕ_s=40, the CTAT-Water system at ϕ_s=40, the SDS-PTHC-Cholesterol-Water system at α=0.1, β=0.03 and ϕ_s=40 and also in the hexagonal phase of the SDS-PTHC-Water system at α=0.05 and ϕ_s=49. Rectangular capillaries of the thickness 0.02mm, 0.05mm, 0.1mm and 0.2mm and 0.2mm were used in the nematic phase whereas, capillaries of thickness 0.3mm and 0.4mm were used in the hexagonal phase due to its higher viscosity.

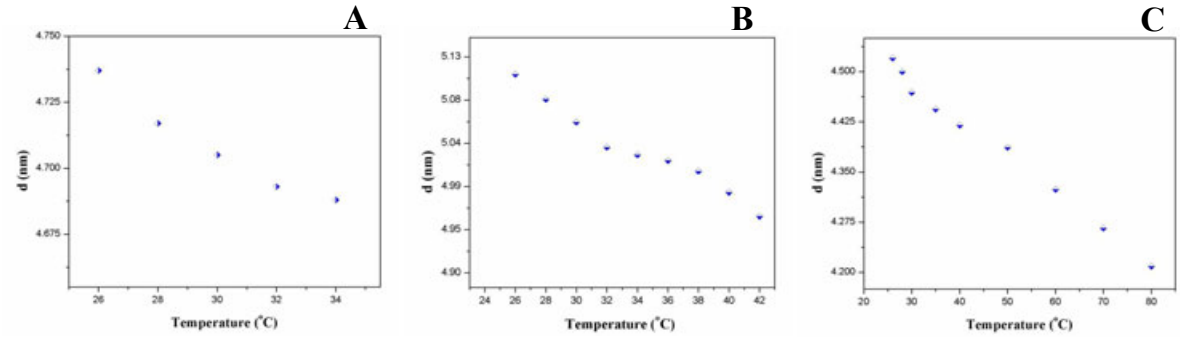

FIGURE 8.2: Variation of lateral separation (d) with temperature in the (**A**) nematic phase of the SDS-PTHC-Water system (**B**) chiral nematic phase of the SDS-PTHC-Cholesterol-Water system and (**C**) hexagonal phase of the SDS-PTHC-Water system.

8.4.1 Nematic phase of the SDS-PTHC-Water system

Sample of composition α=0.1 and ϕ_s=40 was used. It shows nematic phase in the temperature range 23°C-35°C as confirmed by small angle x-ray scattering (SAXS) and polarizing optical microscopy (POM) studies (as discussed in chapter 7). This nematic phase is made up of worm-like micelles. Figure 8.2A shows the variation of lateral separation (d) between the micelles in the nematic phase. d decreases monotonically with increasing the temperature.

These worm-like micelles were shear aligned along the long axis of the rectangular capillary while being drawn into the capillary. A dilation strain was applied by decreasing the lateral spacing by increasing the temperature. Samples were equilibrated at 29°C till we got a uniform texture under the polarizing optical microscopy. Then the temperature was suddenly increased to 30°C.

Striation were observed perpendicular to the long axis of the rectangular capillary/long axis of the worm-like micelles, with an optical contrast depending on the specimen orientation in the polarizing microscope. Striation were more clear in capillaries with smaller thickness.

Figure 8.3 shows the striation pattern under crossed polarizers. These striations are also visible without the analyzer which confirms the occurrence of undulations in the vertical as well as in the horizontal plane. The wave length is measured from

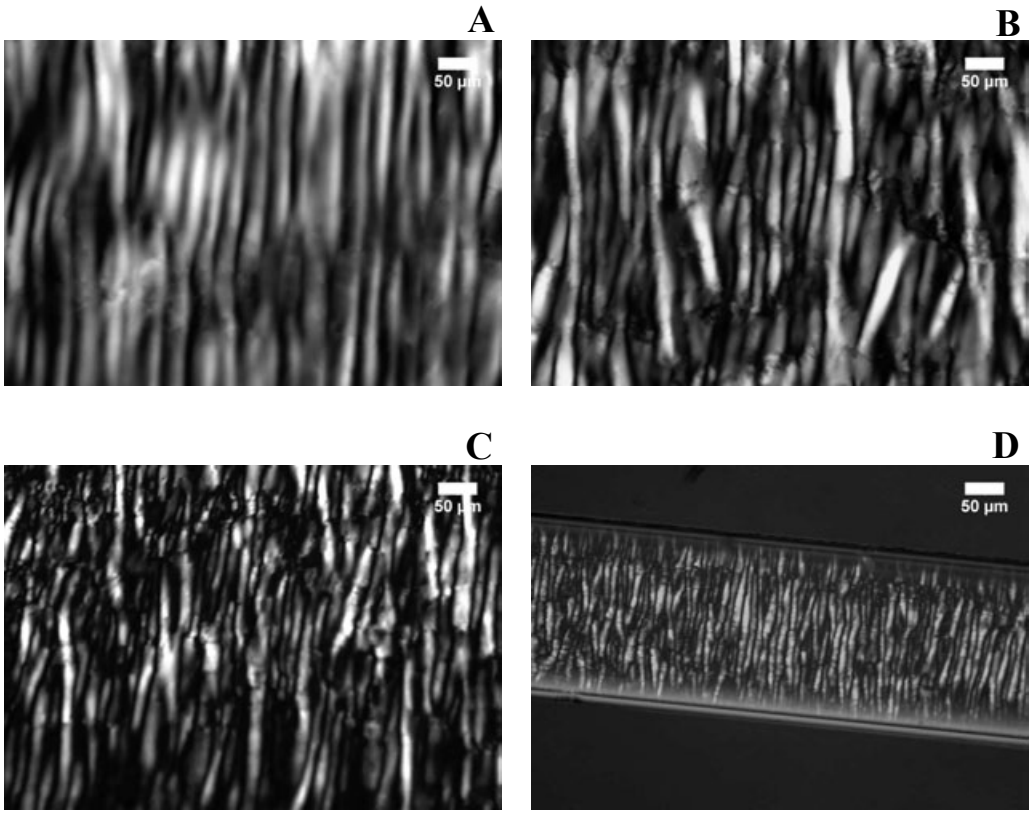

FIGURE 8.3: Striation patterns in achiral nematic phase of the SDS-PTHC-Water system with sample thickness: 0.2mm (**A**), 0.1mm (**B**), 0.05mm (**C**) and 0.02mm (**D**).

the photograph of the texture by using box integration which gives the variation of intensity long a direction parallel to the striation wavevector (Fig. 8.7A). Finally, wavelength is calculated by averaging about 6 striations. The distance between two dark (or bright) lines corresponds to half a wavelength which is verified by observing dislocations of these lines, where four dark (or bright) lines collapse into two dark (or bright) lines.

Figure 8.8A shows the variation of logλ with logd. Slope of the plot is about 0.5, which confirms the predicted $\sqrt{d}$ dependence of λ. The value of characteristic length (m) is obtained from the slope of the λ^2 vs d plot (Fig. 8.9A) by using eq. 8.11 and taking A=0.05. Because, experimental value of A is in between (0.025, 0.075) as found in the $C_{12}O_6$-Water system [38]. Also, wavelength is inversely proportional to the fourth root of A. So, the effect of A in the measurement of m will be less, hence the exact value of A is not crucial. m is expected to be the

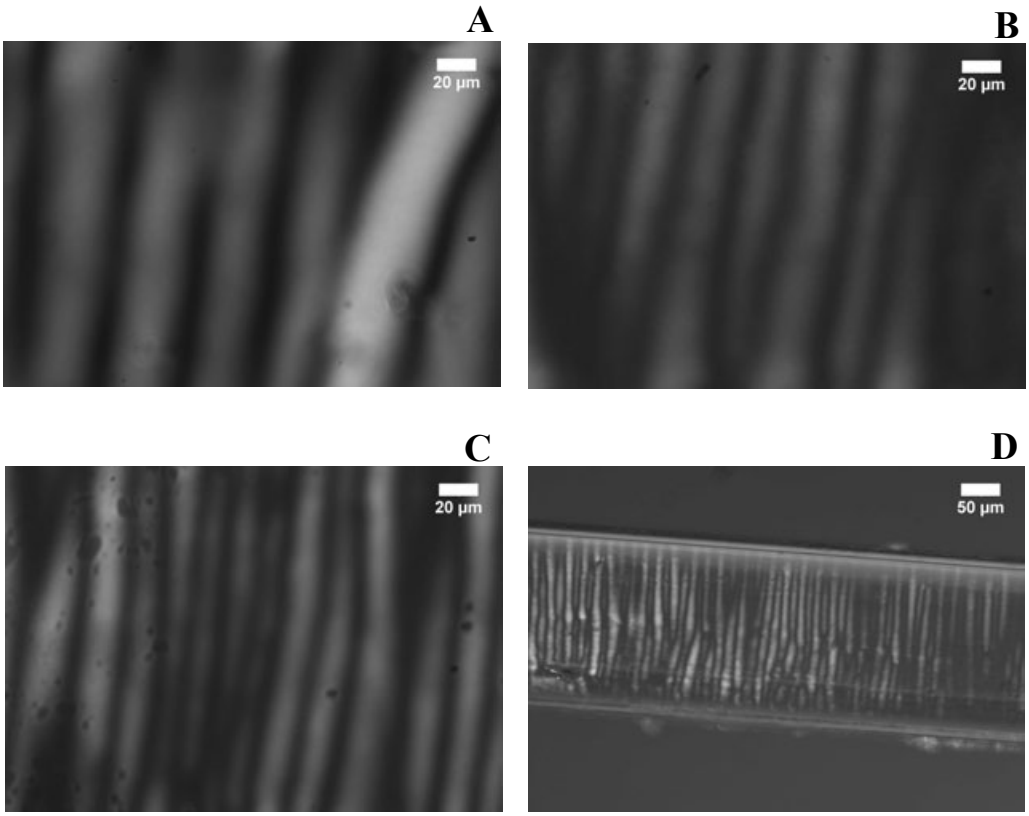

FIGURE 8.4: Striation patterns in chiral nematic phase of the SDS-PTHC-Cholesterol-Water system with sample thickness: 0.2mm (**A**), 0.1mm (**B**), 0.05mm (**C**) and 0.02mm (**D**).

order of the diameter of the worm-like micelles ≈ 2.5nm. The calculated value of m is 285.90 nm which is about two orders of magnitude larger than the diameter of the worm-like micelles.

8.4.2 Chiral nematic phase of the SDS-PTHC-Cholesterol-Water system

In-order to check the effect of chirality on the wavelength of the striation, cholesterol was added to the system. Sample of composition α=0.1, β=0.03 and ϕ_s=40 was used for this study. This sample is less viscous than the achiral one. It shows nematic phase made up of worm-like micelles, in the temperature range 23°C-42°C as confirmed by small angle x-ray scattering and POM studies. Figure 8.2B shows

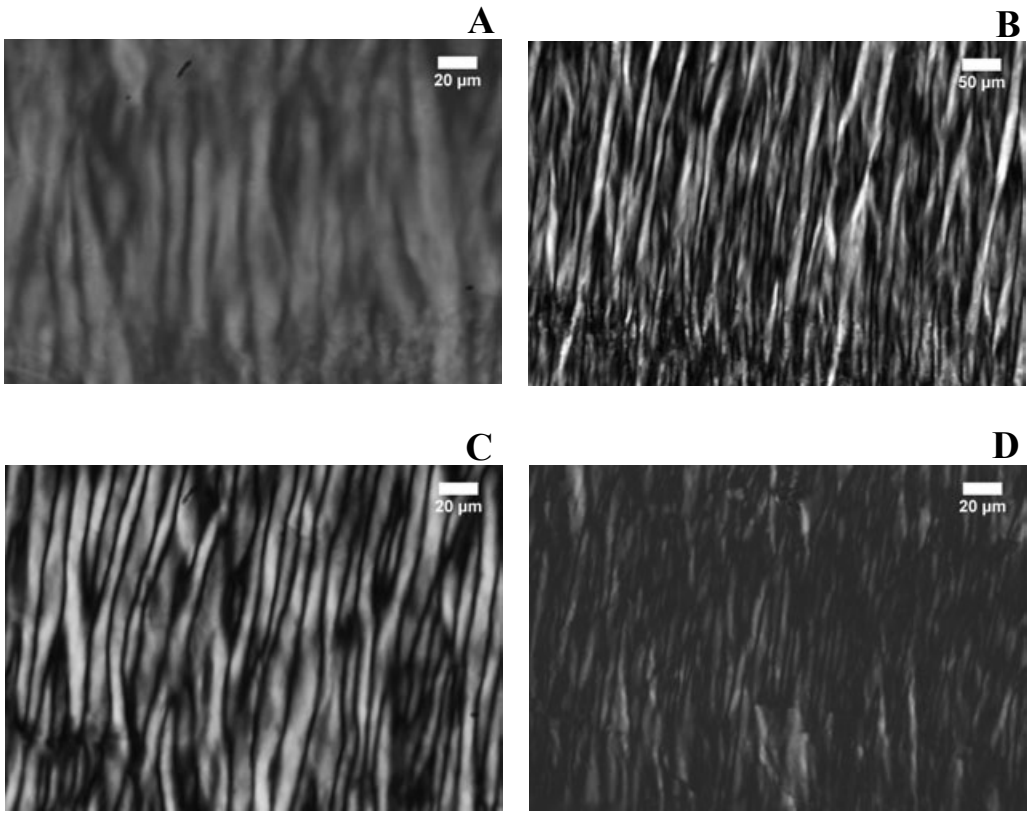

FIGURE 8.5: Striation patterns in nematic phase of the CTAT-Water system with sample thickness: 0.2mm (**A**), 0.1mm (**B**), 0.05mm (**C**) and 0.02mm (**D**).

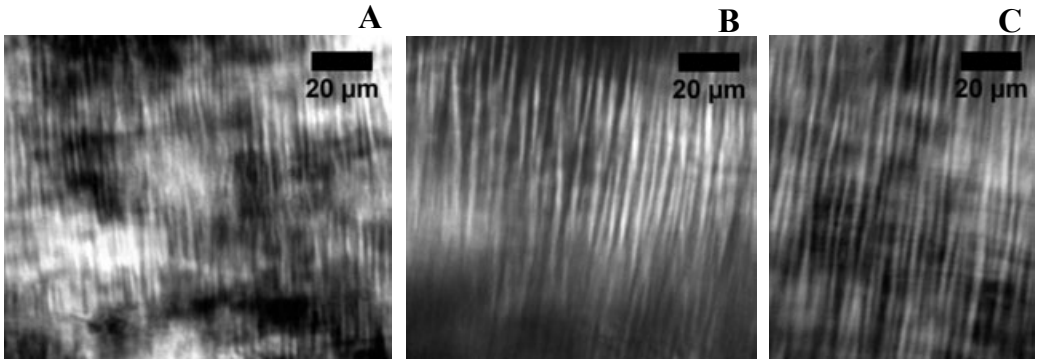

FIGURE 8.6: Striation pattern in hexagonal phase of the SDS-PTHC-Water system with sample thickness: 0.2mm (**A**), 0.3mm (**B**) and 0.4mm (**C**).

the variation of lateral spacing (d) in the nematic phase. d decreases monotonically with increasing the temperature. Striations were very clear as shown in figure 8.4. Undulations are in the vertical as well as in the horizontal plane as confirmed by POM studies. Wavelength is calculated from the intensity profile (Fig. 8.7B).

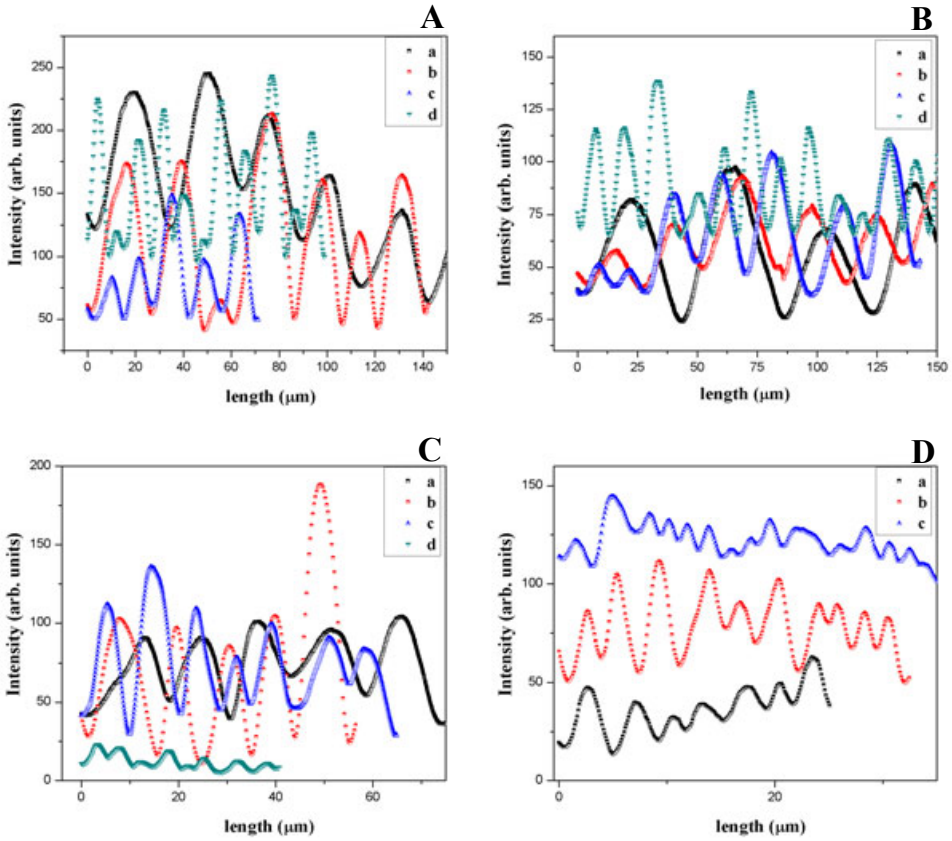

FIGURE 8.7: Patial variation of intensity along the striation wavevector: (**A**) nematic phase of the SDS-PTHC-Water system with the sample thickness: 0.2mm (**a**), 0.1mm (**b**), 0.05mm (**c**) and 0.02mm (**d**). (**B**) chiral nematic phase of the SDS-PTHC-Cholesterol-Water system with the sample thickness: 0.2mm (**a**), 0.1mm (**b**), 0.05mm (**c**) and 0.02mm (**d**). (**C**) nematic phase of the CTAT-Water system with the sample thickness: 0.2mm (**a**), 0.1mm (**b**), 0.05mm (**c**) and 0.02mm (**d**) and (**D**) hexagonal phase of the SDS-PTHC-Water system with the sample thickness: 0.2mm (**a**), 0.3mm (**b**) and 0.4mm (**c**).

Slope of the logλ vs logd plot is about 0.5, which confirms the $\sqrt{d}$ dependence of λ (Fig. 8.8B). m is calculated from the slope of λ^2 vs d plot (Fig. 8.9B), which is 593.96 nm, about twice the value found in the achiral system and about two orders of magnitude larger than the diameter of the worm-like micelles.

8.4.3 Nematic phase of the CTAT-Water system

In-order to check if the observed instability is generic to the nematic phase of worm-like micelles, we studied the nematic phase of CTAT-Water system. For this

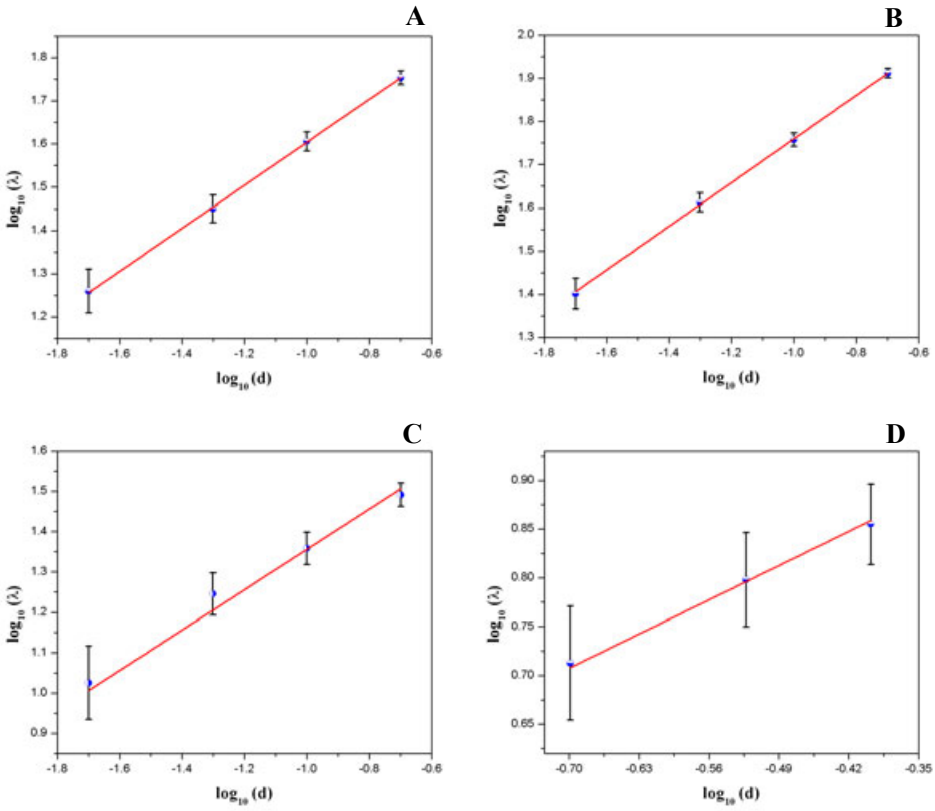

FIGURE 8.8: Variation of log of wavelength with log of sample thickness in the (**A**) nematic phase of the SDS-PTHC-Water system, (**B**) chiral nematic phase of the SDS-PTHC-Cholesterol-Water system, (**C**) nematic phase of the CTAT-Water system and (**D**) hexagonal phase of the SDS-PTHC-Water system.

study, sample of composition ϕ_s=40 was used. This sample is more viscous than previous two samples and exhibits nematic phase in the temperature range 23°C-64°C [39]. This nematic phase is again made-up of worm-like micelles and lateral spacing is found to decrease with increasing the temperature [39]. Striations are not very uniform in this system, as shown in figure 8.5. Wave length is calculated by averaging over 6 striations (Fig. 8.7C). Slope of the plot logλ vs logd is about 0.5 which confirms the $\sqrt{d}$ dependence of λ (Fig. 8.8C). Slope of the plot λ^2 vs d gives m=85.76 nm which is about forty times the diameter of the micelles (Fig. 8.9C).

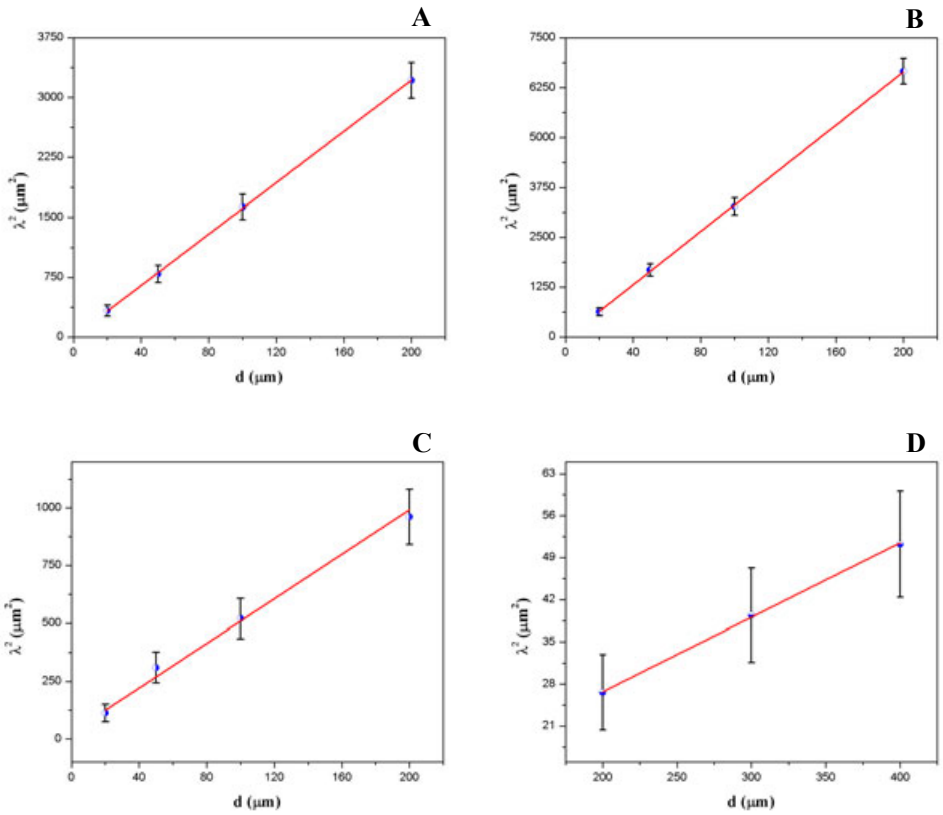

FIGURE 8.9: Variation of the square of the wavelength with the sample thickness in the (**A**) nematic phase of the SDS-PTHC-Water system, (**B**) chiral nematic phase of the SDS-PTHC-Cholesterol-Water system, (**C**) nematic phase of the CTAT-Water system and (**D**) hexagonal phase of the SDS-PTHC-Water system.

8.4.4 Hexagonal phase of the SDS-PTHC-Water system

Nematic phase shows long range orientational order and short range positional order, on the other hand hexagonal phase exhibits long range orientational order and long range positional order. In-order to examine how the wave length of the undulation is changing from nematic phase (higher symmetry phase) to the hexagonal phase (lower symmetry phase). For this study, sample of the composition α=0.05 and ϕ_s=49 was used. This sample is viscous. It shows Hexagonal phase over all the temperature range studies, as discussed in the chapter 7. Figure 8.2C shows the variation of lateral separation (d) in the hexagonal phase. d decreases monotonically with increasing the temperature. Striations are sharp and clear as shown in figure 8.6. Wavelength is calculated from the intensity profile

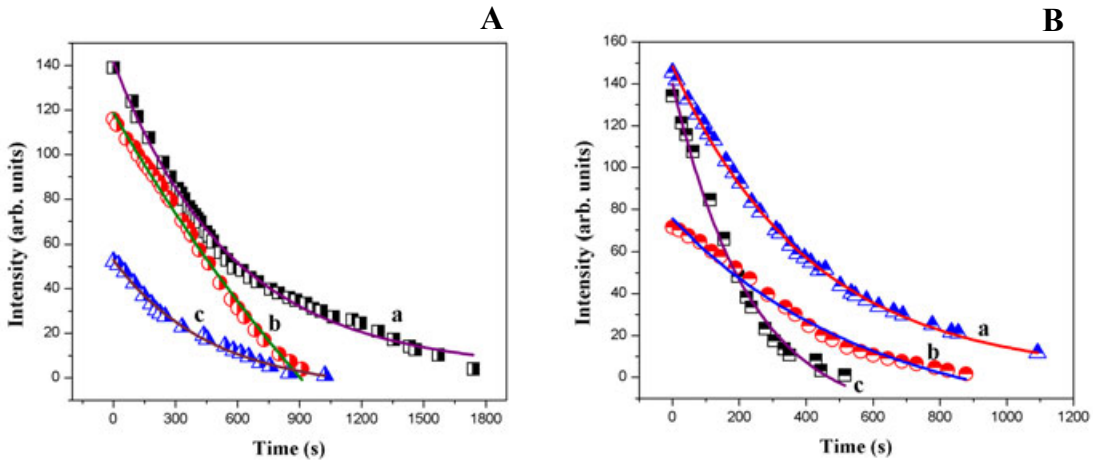

FIGURE 8.10: Variation of intensity with the time in the (**A**) nematic phase of the SDS-PTHC-Water system: t_1=568.20s (**a**), t_1=2156.06s (**b**) and t_1=468.17s (**c**) and (**B**) chiral nematic phase of the SDS-PTHC-Cholesterol-Water system: t_1=413.65s (**a**), t_1=599.49s (**b**) and t_1=231.01s (**c**).

(Fig. 8.7D). Slope of the plot logλ vs logd is about 0.5, which confirms the $\sqrt{d}$ dependence of λ (Fig. 8.8D). The value of characteristic length (m) is obtain from the slope of the λ^2 vs d plot (Fig. 8.9D). The calculated value of m is 2.20 nm, which is comparable to the diameter of the worm-like micelles

8.4.5 Relaxation of undulation

It found that striations visible for few minutes and then relax slowly. To quantify the relaxation process of the undulation instability, variation of intensity of the striations (average over about 5 striations) with time is measured at constant temperature 30°C. It follows exponential decay ($I = a + I_0 exp(-t/t_1)$). The characteristic time (t_1) is in the range of 450s to 2150s and 230s to 600s in the nematic phase of achiral and chiral system respectively (Figs. 8.10A and B).

8.5 Discussion

All the systems that we discussed above, are made up of worm-like micelles. On increasing the temperature, lateral/lattice spacing decreases in all theses systems which leads to a sudden dilation (rate of heating is faster than relaxation of the columns of the worm-like micelles). As a result undulation instability is takes place, similar to that observed in the case of SmA.

There are two possible ways of relaxing the imposed dilation. One must either add new cylinders of worm-like micelles or tilt them if their number is maintained constant to fill space. Since the dilation is too sudden for the system to be able to adjust the number of cylinders. It has no other choice but to tilt the cylinders with respect to plate. This fast process leads to the cylinder undulation instability. However, this undulation is not seen in nematics made up of small micelles or molecules. As compared to the nematic phase of small rod or disc-like micelles, the nematic phase of worm-like micelles has Frank splay elastic constant much larger than the those corresponding to twist and bend. Also, there is a free energy cost for locally compressing/dilating these liquid crystal composed of long flexible chains (worm-like micelles), which is described in terms of osmotic compressibility. The osmotic compressibility of the macromolecules is the main difference between these systems, including the present one, and small molecule [34, 35]. This is the reason why the present system shows undulation instability.

The calculated value of the characteristic length (m) is found to be of the order of the diameter of worm-like micelles in the hexagonal phase. However, in the case of nematic phase, it is atleast two order of magnitude larger than the expected value (diameter of worm-like micelles).

Similarly, a very large value of the characteristic length (m) has also been reported, in the hexagonal phase of discotic thermotropic liquid crystal [28, 36]. A possible explanation for this is given by J. Prost [40] by assuming large density of lock in fault defect (Fig. 8.11). These defect elastic constant which is consistent with

large value of m. This explanation support its Rayleigh scattering [41, 42]. But there no experimental evidence of the existence of these defects so far.

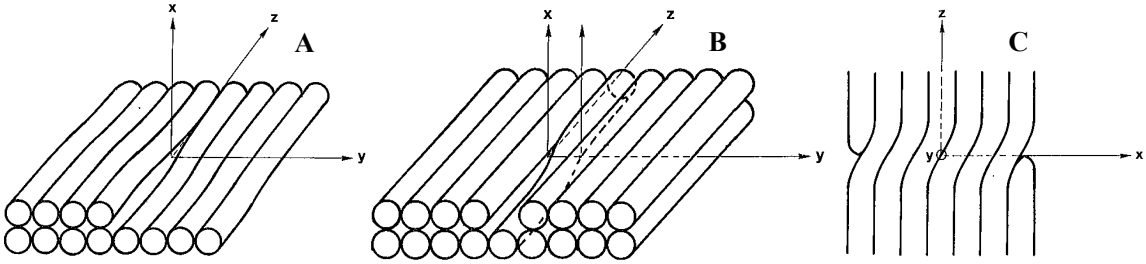

FIGURE 8.11: A screw dislocation **(A)**, lock-in fault line **(B)** and Lock-in fault line in xz plane **(C)**. [40]

Lock in fault defects could also be explain the results of the present study though this study is differ by thermotropic one in many ways. Undulations observed in this case, are both in the horizontal as well as in the vertical plane, undulations are only in the vertical plane in the thermotropic system. However, independent measurements of the two elastic constants are necessary to clarify the situation.

The characteristic time found in the chiral system is lesser than that in the achiral one (Fig. 8.10). This can be understood in terms of defect density, as follows. The apparent viscosity of the chiral system is found to be less than that of the achiral one. It is well known that worm-like micelles can cross-link to form fluid-like mobile inter-micellar junctions, so called branch points [2] that lead to a decrease in the viscosity. This suggests that branch point (defect) density is less in the achiral system than the chiral system. Since, the dilation imposed by thermal dilation relaxes by proliferation of defects, it would be easier and faster to relax the dilation in the chiral system.

8.6 Conclusion

The undulation instability has been observed in both the nematic and hexagonal phases of worm-like micelles under dilation strain induced by temperature. The

characteristic length, estimated from the striation wavelength is comparable to diameter of worm-like micelles in the case of hexagonal phase but is about two order of magnitude larger in the case of nematic phases. The large value of characteristic length (m) could be related to the density of branch points or the distance between the lock in fault defects. Independent measurement of K and B are required for a better understanding of the origin of the large value of m obtained from these studies.

Bibliography

[1] J. Israelachvili, *Intermolecular and Surface Forces*, 2nd edition, Academic Press, London (1991).

[2] S. J. Candau, E. Hirsch and R. Zana, *J. Colloid Interface Sci.*, **105**, 521 (1985).

[3] F. Reiss-Husson and V. Luzzati, *J. Phys. Chem.*, **68**, 3504 (1964,).

[4] P. Ekwall, L. Mandell and P. Solyom, J. Colloid Interface Sci., **35**, 519 (1971).

[5] K. Fontell, A. Khan, B. Lindström, D. Maciejewska and S. Puan-Ngern, *Colloid Polym. Sci.*, **269**, 727 (1991).

[6] G. Porte, Y. Poggi, J. Appell and G. Maret, *J. Phys. Chem.*, **88**, 5713 (1984).

[7] S. J. Candau, E. Hirsch, R. Zana and M. Adam, *J. Colloid Interface Sci.*, **122**, 430 (1988).

[8] P. Debye and E. W. Anacker, *J. Phys. Colloid Chem.*, **55**, 644 (1950).

[9] P. A. Hassan, S. R. Raghavan and E. W. Kaler, *Langmuir*, **18**, 2543 (2002).

[10] G. Porte, R. Gomati, O. El Haitamy, J. Appell and J. Marignan, *J. Phys. Chem.*, **90**, 5746 (1986).

[11] M. Bergström and J. S. Pedersen, *Langmuir*, **15**, 2250 (1999).

[12] R. D. Koehler, S. R. Raghavan and E. W. Kaler, *J. Phys. Chem. B*, **104**, 11035 (2000).

[13] J. Yang, *Curr. Opin. Colloid Surface Sci.*, **7**, 276 (2002).

[14] Y. Song, R. M. Garcia, R. M. Dorin, H. Wang, Y. Qiu, E. N. Coker, W. A. Steen, J. E. Miller and J. A. Shelnutt, *nano Lett.*, **7**, 3650 (2007).

[15] W. Helfrich, *J. Chem. Phys.*, **55**, 839 (1971).

[16] J. P. Hurault, *J. Chem. Phys.*, **59**, 2068 (1973).

[17] F. Rondelez, J. P. Hulin, *Solid State Commun.*, **10**, 1009 (1972).

[18] M. Delaye, R. Ribotta, and G. Durand, *Phys. Lett.*, **44A**, 139 (1973).

[19] R. Ribotta, G. Durand, and J. D. Litster, *Solid State Commun.*, **12**, 27 (1973).

[20] R. Ribotta, and G. Durand, *J. Physique (France)*, **38**, 179 (1977).

[21] N. A. Clark and R. B. Meyer, *Appl. Phys. Lett.*, **22**, 10 (1973).

[22] C. R. Safinya, D. Roux, G. S. Smith, S. K. Sinha, P. Dimon, N. A. Clark and A.-M. Bellocq, *Phys. Rev. Lett.*, **57**, 2718 (1986).

[23] D. Roux and C. R. Safinya, *J. Physique (France)*, **49**, 307 (1988).

[24] P. Oswald and M. Allain, *J. Physique (France)*, **46**, 831 (1985).

[25] G. K. Auernhammer, H. R. Brand, and H. Pleiner, *Rheol. Acta*, **39**, 215 (2000); *Phys. Rev. E*, **66**, 061706 (2002).

[26] S. W. Marlow and P. D. Olmsted, *Eur. Phys. J. E*, **8**, 485 (2002).

[27] L. Courbin, J. P. Delville, J. Rouch, and P. Panizza, *Phys. Rev. Lett.*, **89**, 148305 (2002).

[28] M. Cagnon, M. Gharbia and G. Durand, *Phys. Rev. Lett.*, **53**, 938 (1984).

[29] J. Rogers, and P. A. Winsor, *J. Coll. Int. Sci.*, **30**, 500 (1969).

[30] F. Livolant, A. -M. Levelut, J. Doucet and J. P. Benoit, *Nature*, **339**, 724 (1989).

[31] D. Constantin, P. Oswald, M. Impéror-Clerc, P. Davidson and P. Sotta, *J. Phys. Chem. B*, **105**, 668 (2001).

[32] J. M. Buisine, R. Cayuela, C. Destrade and H. T. Nguyen, *Mol. Cryst. Liq. Cryst.*, **144**, 137 (1987).

[33] P. Oswald, J. C. Géminard, L. Lejcek and L. Sallen, *J. Phys. II (France)*, **6**, 281, (1996).

[34] Ivan I. Smalyukh, Olena V. Zribi, John C. Butler, Oleg D. Lavrentovich and Gerard C. L. Wong, *Phys. Rev. Lett.*, **96**, 177801 (2006).

[35] H. Finkeimann, I. Kundier, E.M. Terentjev and M. Warner, *J. Phys. II (France)*, **7**, 1059 (1997).

[36] M. Gharbia, M. Cagnon and G. Durand, *J. Phys. Lett. France*, **46**, L-683 (1985).

[37] M. Kléman and P. Oswald, *J. Phys. France*, **43**, 655 (1982).

[38] Clerc M., Etude de transition de phase vers les phases cubiques des systémes eau-surfactant, Ph.D. Thesis, University of Paris XI, Orsay (1992).

[39] Antara Pal, Rose Mary and V. A. Raghunathan, *Journal of Molecular Liquids*, **174**, 48 (2012).

[40] J. Prost, *Liq. Cryst.*, **8**, 123 (1990).

[41] M. Gharbia, T. Othman, A. Gharbi, C. Destrade, and G. Durand, *Phys. Rev. Lett.*, **68**, 2031 (1992).

[42] J. F. Palieme, These de 3eme Cycle, Universite de Paris-Sud (1983).

Chapter 9

Summary

In this thesis we have explored the rich phase behavior of concentrated aqueous solutions of ionic amphiphiles in the presence of strongly binding counterions. A variety of intermediate phases are observed. In this case, concentration of the strongly binding counterion (SHN) is a control parameter to tune the spontaneous curvature of the micellar aggregates and stabilize different intermediate phases. However, detailed theoretical understanding of the stability of these intermediate phases is presently lacking. The system studied here being multicomponent, theoretical analysis is complicated by the likely existence of a coupling between local curvature and composition. Undoubtedly, this feature makes the phase behavior very much richer than that of pure amphiphiles. We feel that computer simulations of systems such as the one studied here will lead to a better understanding of the stability of different intermediate phases. We hope that the present study will motivate future work in that direction.

The CPC-SHN-Water system also exhibits a novel isotropic (L_x) phase of bilayers characterized by small average inter-bilayer spacing and short-range positional correlations, at higher concentration of SHN. Although theoretical studies indicate that (quasi) long-range positional order of the lamellar phase can be destroyed by the proliferation of edge dislocations, the occurrence of a phase such as the L_x reported here has not been theoretically predicted. This phase is somewhat analogous to the sponge phase, which is made up of a network of bilayers. All the

theoretical investigations on the sponge phase hitherto have been confined to sterically stabilized bilayers. These studies show that the sponge phase is stable when the ratio of the moduli of Gaussian and mean curvature of the bilayer becomes weakly negative or positive. It would be interesting to see if the structure presented here can be accounted for by extending the existing models of the sponge phase to the attraction dominated regime.

Addition of oils of shorter or comparable chain length to that of the surfactant is found to show a $L_x \rightarrow L_\alpha \rightarrow L_x$ transition sequence as a function of increasing oil concentration ϕ_s. Alcohols of comparable or longer chain length are also found to have a similar effect. In-order to understand the re-entrant behavior of the L_x phase, a non-monotonic variation of $(\frac{\bar{\kappa}}{\kappa})$ with increasing ϕ_s to be assumed. It would be interesting to probe the effect of oils and alcohols on the sponge phase. Such studies will be helpful to understand the effect of these additives on the elastic moduli of bilayers and the relative stability of the lamellar and sponge/L_x phases.

A polymer or polyelectrolyte that adsorbs on the bilayer can be considered as an extreme case of a strongly binding counterion. An earlier study had reported the L_x phase in a system of this kind. We have therefore studied complexes of sodium salt of polyacrylic acid and the bilayer forming surfactant DDAB to see if the L_x is generic to such systems. Complexes of DDAB-PAANa exhibit a collapsed lamellar phase and swollen sponge phase. However, L_x phase is not found in this system. Interestingly, this seems to be the first observation of a polymer induced $L_\alpha \rightarrow$ sponge transition in a amphiphile-water system. Addition of simple salts such as NaBr is found to transform the sponge phase back into L_α. The mechanism driving this transition is not clear at present. It is possible that the nature of the amphiphile counterion and the molecular weight of the polyelectrolyte are important parameters in this problem. Further work by varying these parameters should lead to a better understanding of these transitions.

Addition of SHN2 instead of SHN to the CPC-water system does not lead to the formation of bilayers, and only cylindrical micelles are observed. Interestingly,

two isotropic phases with very different viscoelastic properties are found in this system. The one occurring at low SHN2 concentrations is made up of entangled worm-like micelles, whereas the one at high SHN2 concentration seems to be made up of a branched network of cylindrical micelles. Such a structure is the analogue of the L_x phase, with the bilayers replaced by cylindrical micelles. It would be interesting to study the density of branch points as a function of SHN2 concentration. Measurement of the amphiphile self-diffusion coefficient using NMR would be one way to estimate it.

An instability analogous to the Helfrich-Hurualt instability in lamellar and columnar liquid crystals has been observed under dilation for the first time in a nematic made up of worm-like micelles. A characteristic length can be estimated from the wavelength of this spatially periodic instability, which is proportional to the ratio of the bending and compression moduli of the system. Instead of being comparable to the micellar diameter, It is found to be a few orders of magnitude larger. The reason for this difference is unclear. Independent estimates of the two elastic moduli would be useful to understand the origin of this behavior.